Radiation Damage in Silicon

- Defect Analysis and Detector Properties -

Dissertation
zur Erlangung des Doktorgrades
des Department Physik
der Universität Hamburg

vorgelegt von

Frank Hönniger

aus Hamburg

Hamburg
2007

Gutachter der Dissertation:	Prof. Dr. R. Klanner
	Prof. Dr. J. Mnich
Gutachter der Disputation:	Prof. Dr. P. Schleper
	JProf. Dr. J. Haller
Datum der Disputation:	8. Januar 2008
Vorsitzender des Prüfungsausschusses:	Prof. Dr. C. Hagner
Vorsitzender des Promotionsausschusses:	Prof. Dr. G. Huber
Dekan der Fakultät MIN:	Prof. Dr. A. Frühwald
Departmentleiter Physik:	Prof. Dr. R. Klanner

Abstract

Silicon microstrip and pixel detectors are vital sensor-components as particle tracking detectors for present as well as future high-energy physics (HEP) experiments. All experiments at the Large Hadron Collider (LHC) are equipped with such detectors. Also for experiments after the upgrade of the LHC (the so-called Super-LHC), with its ten times higher luminosity, or the planned International Linear Collider (ILC) silicon tracking detectors are forseen. Close to the interaction region these detectors have to face harsh radiation fields with intensities above the presently tolerable level. Defect engineering of the used material, e.g. oxygen enrichment of high resistivity float zone silicon and growing of thin low resistivity epitaxial layers on Czochralski silicon substrates has been established to improve the radiation hardness of silicon sensors.

This thesis will focus mainly on the investigation of radiation induced defects and their differences observed in various kinds of epitaxial silicon material. Comparisons with other materials like float zone or Czochralski silicon are added.

Deep Level Transient Spectroscopy (DLTS) and Thermally Stimulated Current (TSC) measurements have been performed for defect characterization after γ-, electron-, proton- and neutron-irradiation.

The differences in the formation of vacancy and interstitial related defects as well as so-called clustered regions were investigated for various types of irradiation. In addition to the well known defects VO_i, C_iO_i, C_iC_s, VP or V_2 several other defect complexes have been found and investigated. Also the material dependence of the defect introduction rates and the defect annealing behavior has been studied by isothermal and isochronal annealing experiments. Especially the IO_2-defect which is an indicator for the oxygen-dimer content of the material has been investigated in detail.

On the basis of radiation induced defects like the bistable donor (BD) defect and a deep acceptor, a model has been introduced to describe the radiation induced changes in macroscopic detector properties as affected by the microscopic defect generation. Finally charge collection measurements have been performed at high radiation doses.

Zusammenfassung

Silizium-Mikrostreifen- und Pixel-Sensoren sind zentrale Komponenten der sowohl für heutige als auch für zukünftige Spurdetektoren in der Hochenergiephysik (HEP). Alle Experimente am *Large Hadron Collider* (LHC) sind mit derartigen Detektoren ausgestattet. Auch für die Experimente am aufgerüsteten LHC (dem sogenannten S-LHC), mit seiner dann zehnmal höheren Luminosität, oder dem *International Linear Collider* (ILC) sind Spurdetektoren vorgesehen. In der Nähe der Wechselwirkungszone sind diese Detektoren intensiven Strahlungsfeldern ausgesetzt. Um unter derartigen Bedingungen einsetzbar zu bleiben ist ein angemessenes *Defectengeneering* für die Siliziummaterialien notwendig. Verbesserungen bezüglich der Strahlenhärte wurden durch Sauerstoffanreicherungen in zonengezogenem Silizium und durch epitaktisches Silizium auf einem Czochralski Siliziumsubstrat erreicht.

Einen Schwerpunkt dieser Arbeit bilden Untersuchungen zu strahlungsinduzierten Defekten und ihre Unterschiede in diversen epitaktischen Materialien. Vergleiche mit zonengezogenem und Czochralski Silizium ergänzen diese Untersuchungen.

Deep Level Transient Spectroscopy (DLTS) und *Thermally Stimulated Current* (TSC) Messungen wurden zur Defektcharakterisierung nach Gamma-, Elektronen, Protonen und Neutronenbestrahlungen durchgeführt.

Die Unterschiede in der Generation von Leerstellen- und Zwischengitterplatz-Defekten wie auch von Defektclustern, hervorgerufen durch die jeweiligen Bestrahlungen, wurden untersucht. Neben den gut bekannten Defekten VO_i, C_iO_i, C_iC_s, VP und V_2 wurden mehrere andere Defekte gefunden and untersucht. Auerdem wurden die Materialabhängigkeiten der Genrationsraten und das Ausheilverhalten der Defekte in isothermalen und isochronalen Ausheilexperimenten studiert. Besonders der IO_2-Defekt, der ein Indikator für den Gehalt an Sauerstoffdimeren ist, wurde detailliert untersucht.

Auf der Basis der Generation strahlungsinduzierter Defekte, wie einen bistabilen Donator (BD) und einen tiefen Akzeptor, wurde ein Model zur Beschreibung der strahlungsinduzierten Änderung der makroskopischen Detektoreigenschaften eingeführt. Abschließend wurden Messungen zur Ladungssammlung bei hohen Strahlungsdosen durchgeführt.

Contents

1 Introduction **1**

2 Damage Induced Defects in Silicon **3**
2.1 Generation of defects . . . 3
2.2 The NIEL scaling hypothesis . . . 4
2.3 Classification of defects . . . 6
2.3.1 Point defects . . . 7
2.3.2 Cluster . . . 8
2.4 Electrical properties of point defects . . . 8
2.4.1 Electrical properties of semiconductors . . . 8
2.4.2 Defect occupation . . . 10
2.4.3 Energy and enthalpy . . . 10
2.4.4 Carrier generation and recombination . . . 11
2.4.5 Occupation of traps under reverse bias . . . 13
2.4.6 Occupation of traps under forward bias . . . 14
2.4.7 Poole-Frenkel shift . . . 14
2.4.8 Negative-U systems . . . 15
2.5 Annealing of defects . . . 15
2.5.1 Reaction kinetics . . . 15
2.6 Impurities . . . 17
2.6.1 Oxygen . . . 17
2.6.2 Thermal Donors (TD's) . . . 19
2.6.3 Carbon . . . 20
2.6.4 Hydrogen . . . 20
2.7 Important point defects . . . 20
2.7.1 Vacancy related defects . . . 21
2.7.2 Vacancy oxygen clusters . . . 23
2.7.3 Interstitial related defects . . . 24
2.8 Damage Modeling . . . 25
2.9 Cluster . . . 27
2.10 Radiation induced change of detector properties . . . 27
2.10.1 The oxygen effect . . . 29

3 Experimental Methods and Equipment **30**
3.1 Materials and devices . . . 30
3.1.1 Float zone material (FZ) . . . 30
3.1.2 Czochralski silicon (Cz) . . . 31

3.1.3 Epitaxial silicon . . . 31
3.1.4 Used devices . . . 31
3.2 Radiation sources . . . 33
3.2.1 Brookhaven National Laboratory ($^{60}Co - \gamma - photons$) . . . 33
3.2.2 Stockholm (6 MeV electrons) . . . 34
3.2.3 Trieste (900 MeV electrons) . . . 34
3.2.4 Karlsruhe (26 MeV protons) . . . 34
3.2.5 CERN (23 GeV protons) . . . 35
3.2.6 Ljubljana (reactor neutrons) . . . 35
3.3 C/V- and I/V-measurements . . . 35
3.4 Deep Level Transient Spectroscopy (DLTS) . . . 37
3.4.1 DLTS principle . . . 38
3.4.2 Classical DLTS method . . . 38
3.5 DLTFS method . . . 40
3.5.1 Principle . . . 40
3.5.2 Fourier transformation . . . 42
3.5.3 Defect concentration . . . 44
3.6 Capture measurements . . . 45
3.7 Refolding method . . . 46
3.8 Thermally Stimulated Current (TSC) . . . 48
3.8.1 Principle of operation . . . 48
3.8.2 Determination of defect parameters . . . 49
3.9 The DLTS and TSC set-up . . . 52
3.9.1 The cryostat system . . . 52
3.9.2 The electrical set-up . . . 53

4 Microscopic Investigations - Particle Dependence of Radiation Induced Defects 55
4.1 ^{60}Co-γ irradiation . . . 56
4.2 6 MeV electron irradiation . . . 57
4.3 900 MeV electron irradiation . . . 59
4.4 26 MeV proton irradiation . . . 60
4.5 23 GeV proton irradiation . . . 61
4.6 Reactor neutron irradiation . . . 63
4.7 Comparison . . . 64
4.7.1 The A-center (VO_i) . . . 64
4.7.2 The divacancy (V_2) . . . 65
4.7.3 The E(170K)-defect . . . 68
4.7.4 The C_i-defect . . . 70
4.7.5 The C_iO_i-defect . . . 70
4.7.6 The VP-defect . . . 71
4.8 Main results for epi-50-diodes . . . 72

5 Microscopic Investigations - Material Dependence of Radiation Induced Defects 74
5.1 ^{60}Co-γ irradiation . . . 74
5.2 900 MeV electron irradiation . . . 79

5.3 26 MeV proton irradiation . . . 84
5.4 23 GeV proton irradiation . . . 92
5.5 Reactor neutron irradiation . . . 96

6 Annealing of Radiation Induced Defects 101
6.1 Defects after ^{60}Co-γ irradiation . . . 102
6.1.1 Isochronal annealing of Epi-72-St silicon . . . 102
6.1.2 Isochronal annealing of Epi-72-DO silicon . . . 106
6.1.3 Isochronal annealing of MCz-100 silicon . . . 108
6.1.4 Isochronal annealing of FZ-50 silicon . . . 112
6.1.5 Isothermal annealing of the divacancy-defect . . . 114
6.2 Defects after 900 MeV electron irradiation . . . 122
6.2.1 Isothermal annealing of FZ silicon . . . 122
6.2.2 Isothermal annealing of DOFZ silicon . . . 124
6.2.3 Isothermal annealing of Cz silicon . . . 126
6.2.4 Isothermal annealing of epitaxial silicon . . . 128
6.3 Defects after 26 MeV proton irradiation . . . 129
6.3.1 Isochronal annealing of epi-72-St-silicon . . . 130
6.3.2 Isochronal annealing of epi-72-DO-silicon . . . 132
6.3.3 Comparison . . . 134
6.4 Defects after 23 GeV proton irradiation . . . 136
6.4.1 Isochronal annealing of epi-25 silicon . . . 136
6.4.2 Isochronal annealing of epi-75 silicon . . . 138
6.4.3 Comparison . . . 140
6.5 Investigation of the IO_2-defect . . . 142
6.5.1 Suppression of the IO_2-signal . . . 142
6.5.2 Annealing characteristics of IO_2 . . . 143

7 Comparison of Macroscopic Detector Properties and Microscopic Defects 145
7.1 High energy proton irradiation . . . 145
7.2 Reactor neutron irradiation . . . 155

8 Summary 161

9 Outlook 165

A Constants and Silicon properties 166

B Discrete Fourier Transformation 168
B.1 Signal processing . . . 168
B.1.1 Fourier transformation . . . 168
B.2 Folding . . . 169
B.3 Correlator functions . . . 169

C Used devices 170

D Detected defects 172

Chapter 1

Introduction

The ambition of all high energy physics (HEP) experiments is to comprehend the elemental constituents of matter and the forces between them. This aim experimentally requires acceleration and collision of particles at sufficient high energy. The products of these collisions are measured by large detectors build around the interaction point.

The Standard Model (SM) of particle physics provides a largely verified theory of the elementary particles including the strong and the electro-weak interaction between quarks and gluons. All particles of the SM have been detected except the particle associated with the generation of mass the Higgs boson. In its present form the SM is also known to fail at the TeV scale. The search for the Higgs boson and possible extensions of the SM, e.g. with super-symmetric particles (SUSY) are the main impetus for the LHC and the ongoing construction of future colliders.

The momenta of charged particles are measured by precise tracking detectors in a magnetic field. Silicon sensors (microstrip and pixel detectors) are presently used in HEP experiments for such tracking applications. Because of their high position resolution, their fast signal response, and their large signal-to-noise ratio they are used in experiments like CMS [CMS] and ATLAS [ATL] at the forthcoming *Large Hadron Collider* (LHC) at CERN, and they are as well a viable and promising solution for future experiments, like the planned upgrade of the LHC the so-called SuperLHC (SLHC) [SLHC] and the *International Linear Collider* (ILC).

For the LHC with its center of mass energy of 14 TeV and a luminosity of up to 10^{34} cm^{-2}s^{-1} the particle fluence over the lifetime of expected 10 years will be in the range of $3 \cdot 10^{14}$cm^{-2} (1 MeV neutron equivalent) per year. The main contribution for the pixel detectors is coming from charged hadrons. Oxygen enriched silicon detectors are able to operate up to these fluences, but for the SLHC a ten times higher luminosity is planned which will lead to a 1 MeV neutron equivalent fluence of about $1.5 \cdot 10^{16}$cm^{-2} within 5 years of operational time. The corresponding deterioration of the performance of float zone silicon detectors, as investigated by the RD48 collaboration, is beyond the limits required for a useful operation after such high fluences.

For the present CERN collaboration, RD-50 [RD50], the main task to cope with is the search for more radiation hard silicon devices for very high luminosity colliders. Part of the work presented in the following was performed in the framework of this collaboration.

The radiation induced changes of the detector performance, the increase of the leakage current, the change of the depletion voltage and a decrease of the lifetime of charge carriers, are caused by microscopic defects. Many of them are well characterized by different microscopic methods like the *Deep Level Transient Spectroscopy* (DLTS) or the *Thermally Stimulated Current* (TSC). Several defects have been identified to be responsible for the change of the detector performance. But up to now a final model has not been developed. New materials like Czochralski silicon, thin epitaxial silicon with and without additional oxygen enrichment, thin wafer-bonded float-zone silicon and materials with different resistivity opened a new field of possible materials for future applications and of course a lot of questions about the radiation hardness of and the corresponding defect generation in these devices.

The aim of this work is to understand the defect-generation in different materials as well as the differences in the generation of defects caused by different particles. Also the defect evolution at elevated temperatures (so-called annealing effects) is investigated. Of comparable interest is the correlation of the defects with the macroscopic detector properties build from these new materials. Since the start of the development of radiation hard materials defect engineering of the starting material is known as an important key towards this goal.

This thesis is organized in eight chapters. In the following chapter an introduction into the generation of defects in silicon is given. Chapter 3 follows with an overview of the materials presented in this work, the radiation sources are introduced and the experimental techniques mainly used in this work are explained, focussing on the DLTS and the TSC method. In chapter 4 the differences in defect generation by various particles are shown in case of identical devices. In chapter 5 this investigation is extended by the observation of several other materials and a comparison of the defect generation in different devices is included. In chapter 6 different annealing experiments, performed at elevated temperatures, are presented to investigate the kinetics of several defects in different materials. Therefore a more detailed insight into the role of impurities like e.g. oxygen, oxygen-dimer, carbon or phosphorus on the generation of defects is achieved. In chapter 7 a model for the correlation of macroscopic detector properties and microscopic defects is introduced. Chapter 8 summarizes the work presented here. Finally in chapter 9 an outlook is given towards possible investigations to be performed in the nearby future.

Chapter 2

Damage Induced Defects in Silicon

The radiation induced damage in silicon detectors can be divided into two main parts, surface damage and bulk damage. The surface damage creates ionization at the $Si - SiO_2$ interface. In high energy physics (HEP) experiments the damage in silicon detectors close to the interaction point of colliding accelerated beams is bulk damage. This is caused by displacement of silicon atoms out of their lattice sites and can be divided into point defects and cluster defects. The following work will focus on bulk damage which is the limiting factor for silicon tracking detectors used in HEP-experiments. This chapter starts with the description of the basic mechanisms of defect generation, the formation of point defects and clusters caused by the interaction of high energy particles (photons, leptons, hadrons) in the silicon crystal. The comparison of damage caused by different particles with different energies is explained by introduction of the so called "Non Ionizing Energy Loss (NIEL) hypothesis" and the concept of the hardness-factors. A classification of defects by their electrical properties is given and leads to an overview of important point defects and the cluster model. The defect kinetics or the change of defect parameters by annealing is introduced as the change of the electrical properties of detectors even after irradiation.

2.1 Generation of defects

Radiation induced damage in silicon caused by impinging particles which impart an energy higher than the displacement threshold energy of about E_R = 20 eV can knock out a single silicon atom from its lattice site [Huh02]. By this effect an interstitial (I) and a vacancy (V) are created (Frenkel pair). They are both mobile at room temperature. The displaced silicon atom is called PKA (primary knock-on atom). If the imparted energy on the PKA is high enough, further silicon atoms can be knocked out and a defect cascade can be formed. At the end of the path of the knocked off atoms the density of vacancies and interstitials is very high. These disordered regions are called clusters. With a recoil-energy of E_R = 50 keV a PKA is able to create about 1000 interstitial-vacancy pairs. In Fig. 2.1 a simulation of a spatial distribution of vacancies in the silicon lattice after an impinging 1 MeV neutron which imparts E_R = 50 keV on a PKA is shown. A typical structure which includes several subclusters can be seen. A recombination of interstitial-vacancy pairs is very likely if their distance is smaller than the lattice constant. This effect

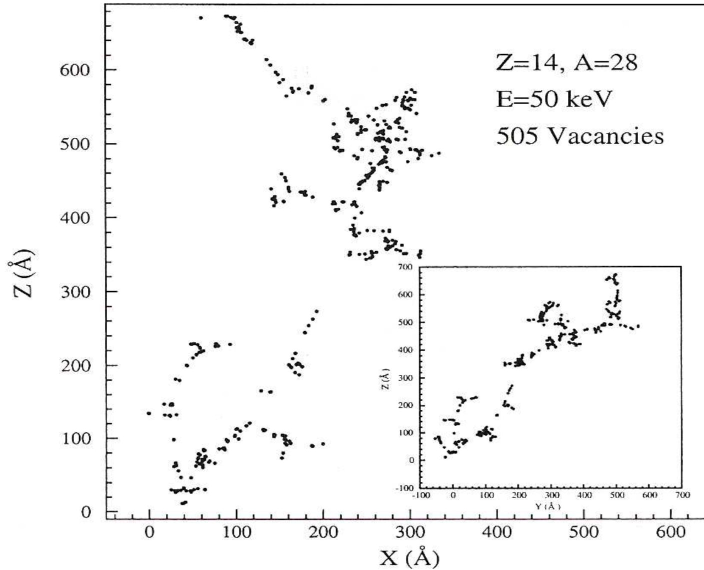

Figure 2.1: *Spatial distribution of vacancies created by an 1 MeV neutron imparting $E_R = 50\ keV$ on a silicon atom. The inset shows the transverse projection of the same event after [Huh02].*

occurs with a rate of about 60% of the overall produced Frenkel pairs [Wun92]. In disordered regions this level can be between 75% and 95% [Shi90]. The vacancies and interstitials which have not recombined migrate through the silicon lattice and perform reactions with each other or with impurity atoms. The defects produced by these reactions (point defects) and the defects within the clusters are the real damage of the silicon bulk material. Their electrical properties are the reason for the change of macroscopic parameters of the detector.

2.2 The NIEL scaling hypothesis

The interaction of particles with the silicon crystal depends on the kind of particle and its energy. At low energies a big part of the particle energy is lost due to ionization of silicon atoms in the lattice. This ionization is fully reversible. The non-ionizing energy loss (NIEL) for charged particles is mainly due to Coulomb interaction, while neutrons interact mainly via elastic scattering with the nucleus, i.e. the probability of interaction between neutrons and matter is quite low [Wun92]. Above 1.8 MeV neutrons are able to split the nucleus [Lin80], and the fragments are interacting with the silicon lattice mainly via Coulomb interaction. The maximal energy imparted to the recoiled silicon atom E_{max} can be calculated in case of a central interaction. For high energy particles the calculation has to be done relativistically

$$E_{max} = 2\frac{E_k + 2m_pc^2}{Mc^2}E_k, \tag{2.1}$$

where M is the mass of the silicon atom, E_k is the kinetic energy of the impinging particle and m_p is its rest mass. For neutrons and protons, with a mass almost

identical, the calculated energy is almost the same, but protons more likely impart their energy in small fractions to the lattice because of Coulomb interaction. By this way protons will much more create point defects than neutrons do. A simulation of the defect generation for 10 MeV protons, 24 GeV/c protons and 1 MeV neutrons is shown in Fig. 2.2. With increasing energy of the impinging proton the energy

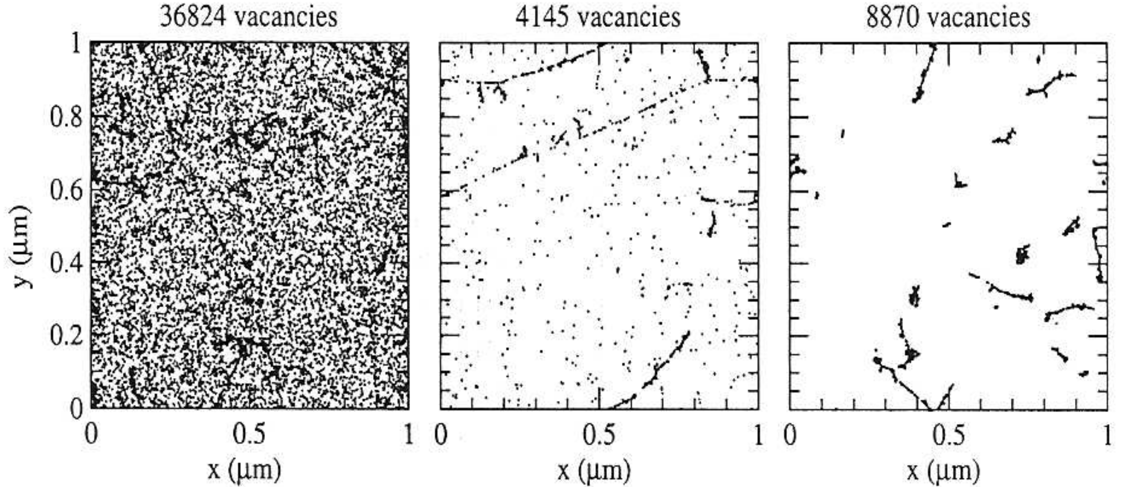

Figure 2.2: *Initial distributions of vacancies by 10 MeV protons (left), 24 GeV/c protons (middle) and 1 MeV neutrons (right). The plots are projections over 1 μm of depth (z) and correspond to a fluence of 10^{14} cm^{-2} after [Huh02].*

Particle	Energy	κ	
protons	23 GeV	0.62	[Lin01b]
protons	26 MeV	2.53	[Huh93a]
neutrons	reactor neutrons (average 1 MeV)	0.91	[Gri96, Zon98]
electrons	900 MeV	$8.25 \cdot 10^{-2}$	[Sum93]
electrons	6 MeV	$4.20 \cdot 10^{-2}$	[Sum93]
$^{60}Co - \gamma$	1.25 MeV	$4.9 \cdot 10^{-5}$	[Akk01]

Table 2.1: *Hardness factors for the different particles used in this work.*

of the PKA becomes higher and higher and it becomes more likely that protons are also able to split the nucleus directly and hence the mixing between cluster damage and point defects will look more similar to neutron irradiation.
In each interaction leading to displacement damage a PKA with a specific recoil energy E_R is produced. The radiation damage scales with the non ionizing energy loss of the impinging particle. This can be expressed by the displacement damage function

$$D(E) := \sum_{\nu} \sigma_{\nu}(E) \cdot \int_0^{E_R^{max}} f_{\nu}(E, E_R) P(E_R) dE_R \qquad (2.2)$$

The index ν indicates all possible interactions between the incoming particle with the Energy E and the silicon atoms in the lattice leading to displacements in the lat-

tice. σ_ν is the cross section corresponding to the reaction with index ν and $f_\nu(E, E_R)$ gives the probability for the generation of a PKA with recoil energy E_R by a particle with Energy E undergoing the indicated reaction ν. $P(E_R)$ is the so called *Lindhard partition function* with which the portion of recoil energy that is deposited in form of displacement damage can be calculated analytically [Laz87, Wun92]. The integration is done over all possible recoil energies E_R and below the displacement threshold the partition function is set to zero $P(E_R < E_d)= 0$. In Fig. 2.3 the displacement damage functions for neutrons, protons, pions and electrons in a range from 10 GeV down to some meV for the thermal neutrons is shown. A thorough discussion of these functions can be found in [Vas97, Huh93b]. However some remarks should be made. The minimum kinetic neutron energy needed to transfer enough energy for displacements by elastic scattering is $\approx$ 185 eV [Mol99]. However the damage function rises below that value with decreasing energy like it is displayed in Fig. 2.3. This fact can be explained by neutron capture, for which the emitted gamma rays result in a recoil energy of about 1 keV. This is much higher than the displacement threshold energy of $\approx$ 20 eV (see section 2.1). Therefore this part of the displacement damage function can not be neglected. For neutrons with energies in the MeV range an increasing number of nuclear reactions opens up adding to the displacement function. The proton damage function is on the other hand dominated by Coulomb interaction at lower energies and therefore much larger than that for neutrons [Sum93]. For very high energies in the GeV range both damage functions converge almost to a common value. In this case the contribution of Coulomb interaction becomes very small and the nuclear reactions are practically the same for neutrons and protons (see insert of Fig. 2.3). To compare the damage generated by different particles with individual energy spectra $\phi(E)$ a hardness factor κ is defined by normalizing the different radiation fields to that of 1 MeV neutrons:

$$\kappa = \frac{\int D(E)\phi(E)dE}{D(E_n = 1MeV) \cdot \int \phi(E)dE} \tag{2.3}$$

The displacement damage function value caused by 1 MeV neutrons is calculated to

$$D_n(1MeV) \qquad = \qquad 95MeVmb. \tag{2.4}$$

The hardness factors for different particles are given in Tab. 2.1. The damage caused by γ-rays is due to electrons from the photoelectric effect, Compton scattering or pair production. The γ-rays, with energies of 1.17 and 1.33 MeV (in case of the ^{60}Co-source used in this work), produce secondary electrons chiefly by the Compton effect. These electrons with an energy of about 1 MeV are not able to generate clusters, but only point defects. Therefore γ-rays are a perfect radiation source for investigation of point defects.

2.3 Classification of defects

After irradiation with high energy particles two different kind of defects are basically generated, namely clusters and point defects.

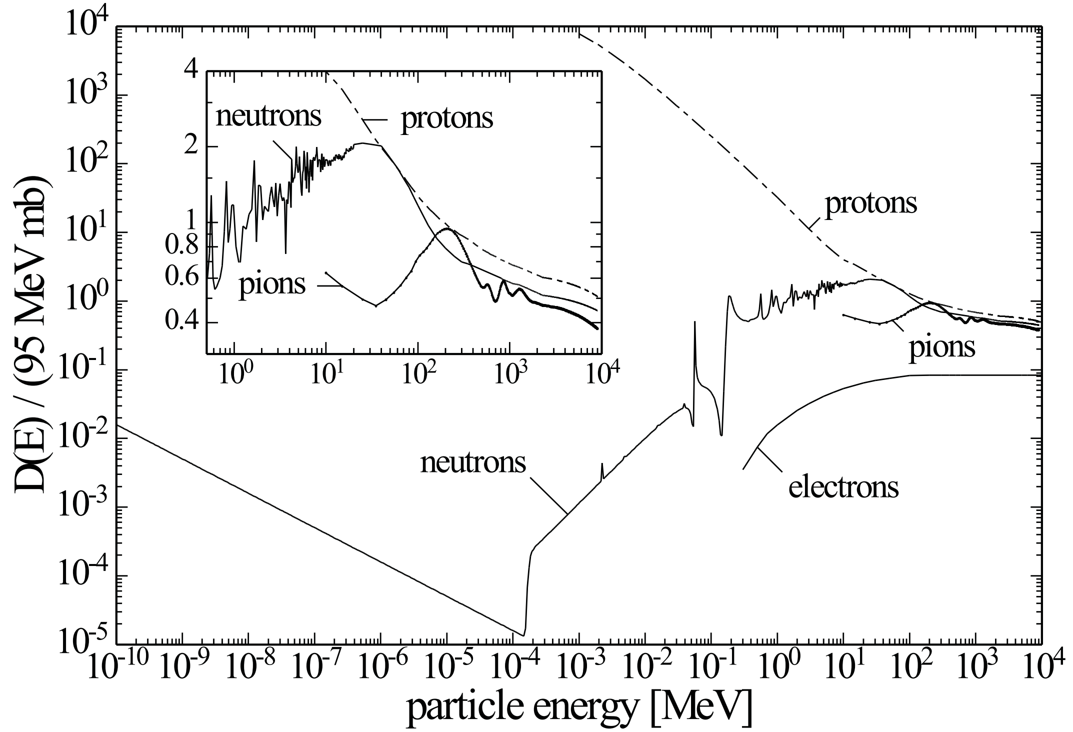

Figure 2.3: *Displacement damage functions D(E) normalized to 95 MeVmb for neutrons (10^{-10} bis 20MeV [Gri96], 20 bis 400MeV [Kon92], 805 MeV bis 9 GeV [Huh93b]), protons [Huh93b, Sum93, Huh93a], pions [Huh93b] and electrons [Sum93].*

2.3.1 Point defects

Primary induced vacancies and interstitials can react with themselves or other impurities inside the lattice. Some of these created point defects are electrically active

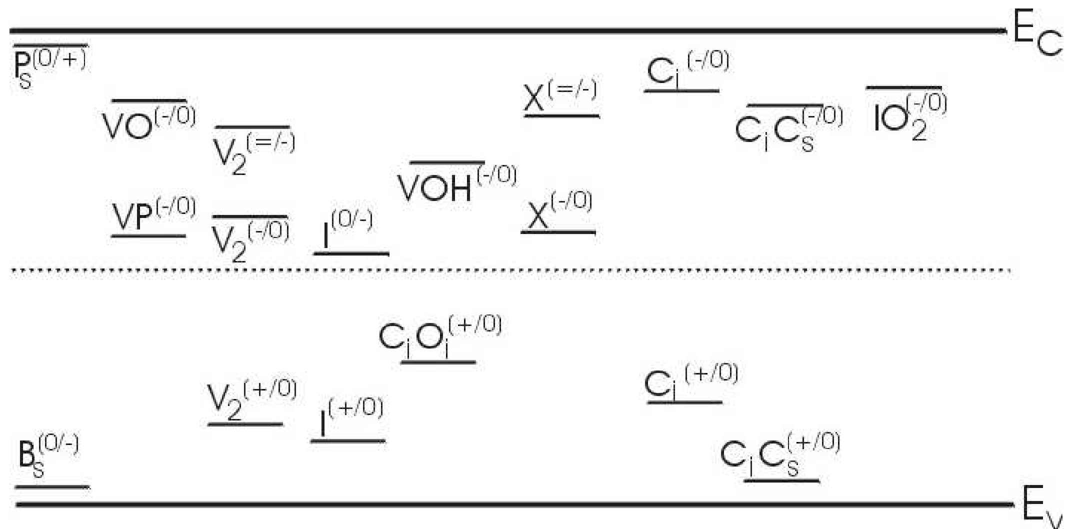

Figure 2.4: *Different defect states in the bandgap (taken from [Sta04]).*

and have energy states in the bandgap. The trap energy E_t is usually put in relation

to the edges of the bandgap, $E_t = E_C - E_a$ for defect states in the upper half in the bandgap, and $E_t = E_V + E_a$ for defect states in the lower half of the bandgap. E_a is the energy to excite an electron from the state E_t into the conduction band, respectively a hole into the valence band. Some defects have more than one level in the bandgap. If defects have levels which can act as donors or acceptors they a called amphoteric defects. In Fig. 2.4 an overview of different defect states is given.

2.3.2 Cluster

In order to explain the very high minority carrier recombination rate observed after irradiation with heavy particles compared to the one observed after gamma or electron irradiation the cluster model was proposed [Gos59]. Besides their composition of vacancies and interstitials no information about their exact nature or their electrical properties within the space charge region or in thermal equilibrium is known. The suppression of the DLTS-signal of the doubly charged divacancy (see Chapter 4) was attributed to strain fields arising from the close conglomeration of defects inside the clusters [Sve91]. Furthermore the high leakage current in silicon detectors after fast hadron irradiation was attributed to the so called "intercenter charge transfer model" caused by interactions between divacancies within the clusters [Wat96, Mac96, Gil97]. Indications for the introduction of negative space charge by clusters were given by [Mol99].

2.4 Electrical properties of point defects

2.4.1 Electrical properties of semiconductors

For an explanation of the electrical properties of point defects the electrical properties of semiconductors have to be introduced first.

Intrinsic semiconductor

Intrinsic silicon has a negligibly small amount of impurities [Sze81]. The number of free electrons in the conduction band can therefore be approximated by

$$n = N_C \cdot exp\left(-\frac{E_C - E_F}{k_B T}\right), \quad (2.5)$$

where k_B is the Boltzmann constant, T the absolute temperature and N_C is the effective density of states in the conduction band, which is given by

$$N_C = 2\left(\frac{2\pi m_{de} k_B T}{h^2}\right)^{3/2}. \quad (2.6)$$

m_{de} is the effective mass of conduction band state density, which is for silicon

$$m_{de} = (m_l^* m_t^{*2})^{1/3}. \quad (2.7)$$

In this equation m_t^* and m_l^* are the transverse and longitudinal effective masses associated with the ellipsoidal constant energy surfaces. E_C and E_F are the energies

of the conduction band edge and the Fermi level. The Fermi level is also known as the chemical potential usually for T = 0 K. In semiconductor physics the term Fermi level is also used for T > 0 K.

This calculation can also be done for holes with the result for the free concentration of holes in the valence band

$$p = N_V \cdot exp\left(-\frac{E_F - E_V}{k_B T}\right) \tag{2.8}$$

with N_V the effective density of states in the valence band given by

$$N_V = 2\left(\frac{2\pi m_{dh} k_B T}{h^2}\right)^{3/2}, \tag{2.9}$$

where m_{dh} is the density-of-state effective mass of the valence band

$$m_{dh} = (m_{lh}^{*3/2} + m_{hh}^{*3/2})^{2/3}. \tag{2.10}$$

In this equation m_{lh}^* and m_{hh}^* refer to the light and heavy hole masses. With the equations 2.5 and 2.8 the position of the Fermi level in an intrinsic semiconductor can be calculated

$$E_F = E_i = \frac{E_C + E_V}{2} + \frac{k_B T}{2} ln\left(\frac{N_V}{N_C}\right). \tag{2.11}$$

The position of the Fermi level in an intrinsic semiconductor is generally very close to the middle of the bandgap. The intrinsic carrier density n_i can also be obtained using equations 2.5 and 2.8:

$$np = n_i^2 = N_C N_V exp\left(-\frac{E_g}{k_B T}\right) \tag{2.12}$$

with the energy bandgap $E_g = E_C - E_V$. Equation 2.12 is also called the law of mass action, which is also valid for extrinsic semiconductors. At room temperature the intrinsic carrier density in silicon is about $6.1 \cdot 10^9\ cm^{-3}$, which is small compared to the amount of dopants usually built into the lattice. The intrinsic carrier density is strongly dependent on the temperature. It doubles about every 11°C.

Extrinsic semiconductor

With impurities in the lattice the silicon material cannot be regarded as intrinsic anymore, and the Fermi level has to adjust to preserve charge neutrality. For temperatures much higher than the ionization temperatures of the added impurities, almost all donors and acceptors are ionized, and the neutrality condition can be approximated by [Sze81]

$$n_e + N_A = p_e + N_D, \tag{2.13}$$

where n_e and p_e are the concentrations of free electrons and holes in the extrinsic semiconductor and N_D and N_A are the concentrations of donors and acceptors assumed to be ionized. With the equations 2.12 and 2.13 the concentrations of electrons in the conduction band and holes in the valence band can be calculated. For electrons in an n-type semiconductor it is given by

$$n_e = \frac{1}{2}[(N_D - N_A) + \sqrt{(N_D - N_A)^2 + 4n_i^2}]. \tag{2.14}$$

If the concentration of donors is much larger than the concentration of acceptors ($N_D \gg N_A$) and the intrinsic concentration ($N_D \gg n_i$), the concentration of free electrons is almost equal to the concentration of donors $n_e \approx N_D$. The concentration of holes is then given by

$$p_e = n_i^2/n_e \approx n_i^2/N_D. \tag{2.15}$$

The position of the Fermi level in an extrinsic semiconductor can be calculated by

$$E_C - E_F = k_B T \cdot ln\left(\frac{N_C}{N_D}\right). \tag{2.16}$$

In most doped semiconductors the concentration of free carriers at room temperature is determined by the doping and not by thermal excitation of carriers.

Extrinsic semiconductors are used to build up so-called p-n-junctions. They are realized by bringing together positively and negatively doped semiconductors. This structure is the basic building plan for diodes used in this work. The p-n-junctions are widely described in different publications and a well known standard in science, therefore no detailed discussion about p-n-junctions will be given here. For such an introduction into p-n-junctions as well as the capacitance and the leakage current of diodes see e.g. [Sze85, Mol99].

2.4.2 Defect occupation

In thermal equilibrium the electron occupation probability of a defect state with energy E_t is described by the Fermi-Dirac distribution function

$$F(E_t) = \frac{1}{1 + exp\left(\frac{E_t - E_F}{k_B T}\right)} \tag{2.17}$$

with E_F as the Fermi level [Lut96]. Using the Fermi function the occupation of the defects, with a total concentration N_t, with electrons (n_t), respectively holes (p_t) can be calculated by

$$n_t = N_t F(E_t) = N_t \frac{1}{1 + exp\left(\frac{E_t - E_F}{k_B T}\right)} \tag{2.18}$$

$$p_t = N_t(1 - F(E_t)) = N_t \frac{1}{1 + exp\left(-\frac{E_t - E_F}{k_B T}\right)} \tag{2.19}$$

It has to be taken into account that the totality condition $N_t = n_t + p_t$ has to be fulfilled, i.e. each defect state is either occupied by an electron or a hole. For the calculation of the effective doping concentration N_{eff} the occupation of the defects has to be included. At room temperature an acceptor occupied with an electron would contribute with negative space charge to the effective doping concentration.

2.4.3 Energy and enthalpy

From the point of the thermodynamical definition the energy E used should be labeled as Gibbs free energy G [Vec76]. The number of free electrons in the conduction

band is therefore given by

$$n = N_C \cdot exp\left(-\frac{\Delta G}{k_B T}\right) \tag{2.20}$$

with $\Delta G = \Delta H - T\Delta S$. H is called the enthalpy and S is the entropy. With this relation equation 2.20 can be written as

$$n = X_n N_C \cdot exp\left(-\frac{\Delta H}{k_B T}\right). \tag{2.21}$$

with the entropy factor $X_n = exp(\Delta S/k_B)$ which is temperature independent. The majority of defect measurements in this work have been done with the electrical technique of DLTS. Using this method in addition to the change in Gibbs free energy also the change in enthalpy during the emission of carriers is determined (see chapter 3). In the following chapters in most cases no difference between energy and enthalpy is made and the entropy factor is not measured. It is assumed $X_n = 1$.

2.4.4 Carrier generation and recombination

For indirect-bandgap semiconductors like silicon the dominant recombination process is a transition via localized energy states in the forbidden energy bandgap [Sze85]. These states act as stepping stones between the conduction band and the valence band. Because the transition probability depends on the energy differences between the step and the conduction and valence band edges, these intermediate states can substantially enhance the recombination process. The possibilities for such interactions are shown in Fig. 2.5. The four different processes are electron capture (a), electron emission (b), hole capture (c), and hole emission (d). The change in the occupation of a level can be written as

$$\frac{dn_t}{dt} = R_a - R_b - R_c + R_d. \tag{2.22}$$

Only one electron can occupy a given defect center. Thus, the rate of electron capture is proportional to the concentration of centers which are occupied with holes and not occupied with electrons. The concentration of centers available for electron capture is given by equation 2.19, i.e. the rate of electron respectively hole capture is given by

$$R_a = c_n n N_t (1 - F) \tag{2.23}$$

$$R_c = c_p p N_t F \tag{2.24}$$

where c_n and c_p are the capture coefficients for electrons and holes. The emission rate from a defect state is the inverse of the capture process, i.e. the electron (hole) emission is proportional to the number of defect states occupied by electrons (holes)

$$R_b = e_n N_t F \tag{2.25}$$

$$R_d = e_p N_t (1 - F). \tag{2.26}$$

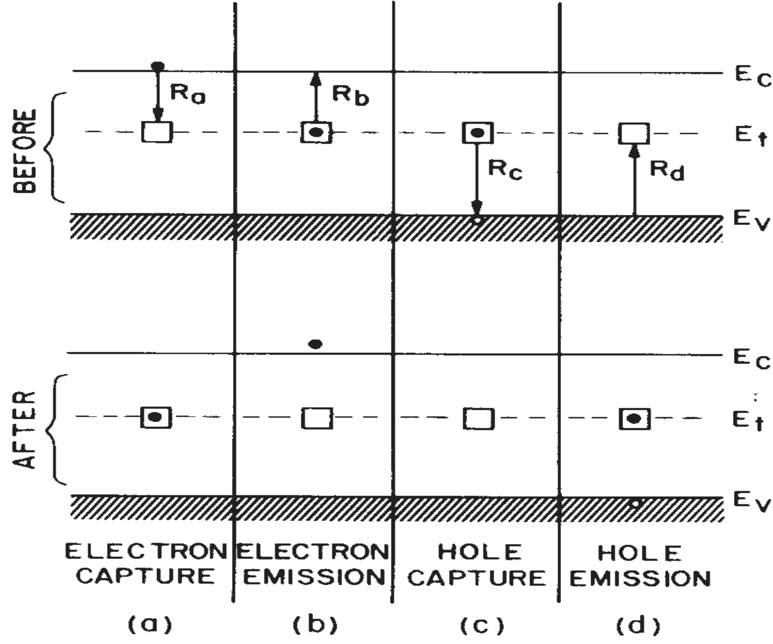

Figure 2.5: *Indirect generation-recombination processes at thermal equilibrium.(taken from [Sze85]).*

Here the proportionality constants e_n and e_p are called emission rates. In case of thermal equilibrium the capture and emission rates have to be equal ($R_a = R_b$) and the emission rate can be expressed using the capture coefficient

$$e_n = \frac{c_n n(1-F)}{F}. \tag{2.27}$$

With the Fermi function (see equation 2.17) the results for the emission rates can be written as

$$e_n = c_n n_i \cdot exp\left(\frac{E_t - E_i}{k_B T}\right) \tag{2.28}$$

$$e_p = c_p n_i \cdot exp\left(-\frac{E_t - E_i}{k_B T}\right). \tag{2.29}$$

With the entropy factor X and the intrinsic carrier density N$_C$ introduced in the previous sections the emission rates can be rewritten as

$$e_{n,p} = c_{n,p} N_{C,V} \cdot exp\left(\pm\frac{E_t - E_{C,V}}{k_B T}\right) \tag{2.30}$$

$$e_{n,p} = c_{n,p} N_{C,V} X_{n,p} \cdot exp\left(-\frac{\Delta H_{n,p}}{k_B T}\right). \tag{2.31}$$

Usually the capture rates $c_{n,p}$ are expressed by capture cross sections $\sigma_{n,p}$ [Sze85].

$$X_{n,p} c_{n,p} = \sigma_{n,p} v_{th,n,p}, \tag{2.32}$$

with $v_{th,n,p}$ as the thermal velocity which is given by:

$$v_{th,n,p} = \sqrt{\frac{3k_BT}{m^*_{dC,V}}} \tag{2.33}$$

Where $m^*_{dC,V}$ represents the density-of-state effective masses for electrons m^*_{dC} and holes m^*_{dV} (see also appendix A). The capture cross sections can be substituted, which leads to a description of the emission rates by

$$e_{n,p} = \sigma_{n,p} v_{th,n,p} N_{C,V} exp\left(-\frac{\Delta H'_{n,p}}{k_BT}\right), \tag{2.34}$$

where ΔH has been replaced by $\Delta H'$ in order to indicate that the enthalpy was obtained under the assumption of a constant capture cross section.

2.4.5 Occupation of traps under reverse bias

To build up a depleted zone in a diode, which is nearly empty of free carriers it is necessary to apply a reverse bias [Mol99]. Inside of this so called space charge region (SCR) with a volume of V_{SCR} a non equilibrium condition exists, in which the equations 2.18 and 2.19 can no longer be used for calculation of the trap occupation.

Because of the very low concentration of free carriers in the SCR ($n \approx p \approx 0$) the capture of such free carriers into defect states can be neglected. This assumption simplifies equation 2.22

$$\frac{dn_t}{dt} = -R_b + R_d = -e_n n_t + e_p p_t. \tag{2.35}$$

This leads to an occupation of defect states inside the SCR given by

$$n_t = N_t \frac{e_p}{e_n + e_p} \qquad and \qquad p_t = N_t \frac{e_n}{e_n + e_p}. \tag{2.36}$$

Summing up over all donors occupied by holes and all acceptors occupied by electrons the effective doping concentration can be calculated

$$N_{eff} = \sum_{donors} p_t - \sum_{acceptors} n_t. \tag{2.37}$$

In this equation impurity atoms are also seen as occupied defect levels. With phosphorous as a shallow donor completely occupied with holes at room temperatures there is one possible impurity which contributes with positive space charge.

Defect states are able to generate electron-hole pairs. The generation rate G_t is given by

$$G_t = e_n n_t = e_p p_t \tag{2.38}$$

$$G_t = N_t n_i \frac{c_n c_p}{c_n \exp(\frac{E_t - E_i}{k_BT}) + c_p \exp(-\frac{E_t - E_i}{k_BT})}. \tag{2.39}$$

If only one of the capture cross sections is known, it is usual to assume both captures cross sections to be equal ($\sigma_n = \sigma_p = \sigma$) and equation 2.39 simplifies to

$$G_t = \frac{N_t n_i c_n}{2\cosh(\frac{E_t - E_i}{k_BT})}. \tag{2.40}$$

The bulk generation current caused by defect states in the SCR is given by:

$$I = \sum_{traps} q_0 G_t V_{SCR}. \tag{2.41}$$

This current is calculated by summing up the contribution of all defects. Equation 2.40 reflects the situation that only deep levels, i.e. defect states with an energy level close to the intrinsic Fermi level strongly contribute to the bulk generation current.

The assumption $n \approx p \approx 0$ is not valid after high radiation damage. In this case also free carriers inside the SCR have to be taken into account, which leads to an occupation of defect states given by

$$n_t = N_t \frac{c_n n + e_p}{e_n + c_p p + c_n n + e_p}. \tag{2.42}$$

2.4.6 Occupation of traps under forward bias

When it is needed to provide a large amount of free carriers to fill the traps in the bulk with electrons and holes for the microscopic measuring methods DLTS (see section 3.4) and TSC (see section 3.8) a forward bias is used. Injecting such a high number of carriers into the silicon bulk the emission rates become small compared to the capture rates ($e_n << c_n n$ and $e_p << c_p p$). In such a case the capture rates are the main factor for the occupation of the defect states which is then given by

$$n_t = N_t \frac{1}{1 + \frac{c_p p}{c_n n}} \qquad and \qquad p_t = N_t \frac{1}{1 + \frac{c_n n}{c_p p}}. \tag{2.43}$$

From equation (2.43) it can be seen that a defect state is only filled with holes when the capture coefficient $c_n \cdot n$ for electrons is smaller than the capture coefficient for holes $c_p \cdot p$, or vice versa for the filling with electrons.

2.4.7 Poole-Frenkel shift

An electron emitted from a donor state of an n-type semiconductor has to overcome the electric field of the afterwards positively charged donor level [Wei91]. This potential barrier can be lowered by a superposition with an external electrical field E_e (ΔE: $E_a(E_e) = E_{a,0} - \Delta E$). This is called the Poole-Frenkel effect. The energy change ΔE can be approximated by

$$\Delta E = \sqrt{\frac{q_0^3 E_e}{\pi \epsilon_0 \epsilon}} \tag{2.44}$$

Also the emission time constant is influenced by the change in activation energy:

$$\tau_e(E_e) = \tau_{e0} exp\left(-\frac{\Delta E}{k_B T}\right) \tag{2.45}$$

The observation of the Poole-Frenkel shift with activation energy of an electron trap is an indication for a defect being a donor.

2.4.8 Negative-U systems

When point defects introduce more than one electrically active level in the bandgap of a semiconductor it is often found that if one electron is trapped, a raise in energy of the level position of the second trapped electron is observed. A defect has negative-U properties if the second of two trapped electrons is bound more strongly than the first. The remarkable feature of a defect with negative-U properties is that there is an attractive interaction between electrons at the defect [Wat81]. This interaction is assumed to be due to an attractive potential between up-spin and down-spin electrons at the same bond site. The complete interaction can be modeled as the sum of the repulsive Coulomb interaction U and the interaction caused by the attraction of the two atoms in the bond [And75]. These defects can show bistability. In one state the electrons are emitted as in a normal positive U-system with two levels (0/+) and (+/++), and in the other state the two electrons can only be emitted at the same time (0/++). The actual state of the system is determined by the filling conditions. The Thermal Double Donors TDD1 and TDD2 (see section 2.6.2) are examples for bistable negative-U systems.

2.5 Annealing of defects

The characterization of defects can be done not only by their electrical properties ($\Delta H, \sigma_{n,p}$), in this work done by using the DLTS and the TSC methods, but also by their annealing behavior. Annealing and identification of their electrical properties lead to a possible comparison of defect data with data from other measurement techniques (EPR, IR-absorption) and to an identification of defects. If also the macroscopic properties of the detector ($\Delta N_{eff}, \Delta I$) are monitored during the annealing, correlations between the microscopic detector properties and the macroscopic detector behavior can be studied.

Migration and dissociation are roughly the two main annealing mechanisms which have to be taken into account. The defects become mobile at a certain temperature. These defects can have a very simple structure, like single vacancy or interstitial or they are more complex like the divacancy (V_2) or the vacancy oxygen complex (VO_i). Vacancies and interstitials are mobile at room temperature, while others like divacancies become mobile between 250 °C and 300 °C. These defects can be gettered at sinks or they can form more complex defects, which can have a higher thermal stability, e.g. $VO_i + H \rightarrow VOH$. An other possibility is the dissociation of a defect into its components, like the dissociation of the E-center ($VP \rightarrow V + P$). This happens if the annealing temperature is high enough to overcome the binding energy of the defect. The vacancy is very likely captured by another impurity or a self-interstitial.

2.5.1 Reaction kinetics

The rate equation for defects which disappear during a first order process, which can happen through migration or dissociation, can be described by

$$-\frac{d[N_X]}{dt} = k[N_X], \tag{2.46}$$

where N_X is the defect concentration and k the rate constant [Sve86, Mol99]. It is characteristic for a first order process that each individual defect complex anneals out independently of the rest. Dissociation and also the formation of more complex defects is given by

$$N_X + N_Y \rightarrow N_X N_Y \tag{2.47}$$

and can be calculated with equation 2.46. The defect or impurity N_X combines with the defect N_Y into a more complex structure $N_X N_Y$. The concentration of the defect N_Y has to be much bigger than the concentration of N_X ($[N_Y] \gg [N_X]$).The corresponding rate equation according to a diffusion limited reaction becomes:

$$-\frac{d[N_X]}{dt} = 4\pi RD[N_Y]_{t=0}[N_X] \tag{2.48}$$

with R being the capture radius, D being the sum of the diffusion coefficients for N_X and N_Y, and $[N_Y]_{t=0}$ being the starting concentration of the defect N_Y. It can be seen from equation 2.46 and 2.48, that the rate constant k equals $4\pi RD[N_Y]_{t=0}$. It also depends on the temperature and therefore can be expressed by an Arrhenius relation

$$k = k_0 exp\left(-\frac{E_a}{k_B T}\right), \tag{2.49}$$

where k_0 denotes the frequency factor and E_a the activation energy for migration or dissociation. The frequency factor is related to the attempt-to-escape frequency that can be estimated by the most abundant phonon frequency ($\approx k_B T/h = 2.1 \cdot 10^{10}$ x T[K]s^{-1} [Cor66]).

In case of two reaction partners the temperature dependence is associated with the sum of the two diffusion coefficients D, which is usually dominated by one of the two diffusion coefficients. The result of the integration of equation 2.48 leads to an exponential decreasing defect concentration

$$[N_X](t) = [N_X]_{t=0} exp(-kt). \tag{2.50}$$

During annealing new defects N_Z can be formed by annealing of defect N_X via equation 2.47, the result can be written as N_Z=$N_X N_Y$. The time dependence of defect N_Z is given by

$$[N_Z](t) = [N_X]_{t=0}(1 - exp(-kt)). \tag{2.51}$$

In some cases a defect N_X can anneal out in two different first order processes, for example the VO_i complex which can dissociate or form higher order defect complexes like VO_2. With comparable but different rate constants for the two processes the corresponding rate equation becomes

$$\frac{dN_X}{dt} = -k_2[N_X] - 4\pi RD[N_X][N_Y]_{t=0} = -[N_X](k_1 + k_2). \tag{2.52}$$

The solution of this differential equation is given by

$$[N_X](t) = [N_X]_{t=0} exp(-(k_1 + k_2)t), \tag{2.53}$$

and the result for the concentration of the new defect N_Z is

$$[N_Z](t) = [N_X]_{t=0} \frac{(1 - exp(-(k_1 + k_2)t))}{1 + k_1/k_2}. \tag{2.54}$$

With different activation energies for the rate constants k_1 and k_2 the maximum concentration of the defect N_Z varies with annealing temperature.

A more common expression for the reaction kinetics is given by

$$-\frac{\delta[N_X]}{\delta t} = k_\gamma [N_X]^\gamma, \tag{2.55}$$

where γ stands for the order of reaction, which does not have to be an integer number. In a second order reaction, where $\gamma = 2$, the concentration of both reaction partners are supposed to be the same. For this reaction the concentration is given by

$$\gamma = 1 \quad : \quad [N_X](t) = [N_X]_{t=0} exp(-k_1 t) \tag{2.56}$$

$$\gamma = 2 \quad : \quad [N_X](t) = [N_X]_{t=0} \frac{1}{1 + k_2 [N_X]_{t=0} t}. \tag{2.57}$$

The main difference between these reactions is displayed in the half life periods ($[N_X]_{\tau_{1/2}} = [N_X]_{t=0}/2$)

$$\gamma = 1 \quad : \quad \tau_{1/2} = \frac{ln2}{k} \tag{2.58}$$

$$\gamma = 2 \quad : \quad \tau_{1/2} = \frac{1}{k[N_X]_{t=0}}. \tag{2.59}$$

From 2.58 it can be seen that for a first order process the annealing is independent of the defect concentration. However, the speed of reaction for a second order process is determined by the momentary defect concentration $N_X(t)$ and therefore for higher initial defect concentration $[N_X]_{t=0}$ a lower half life period is found.

2.6 Impurities

The main impurities in silicon introduced during crystal growth or processing are oxygen, carbon and hydrogen.

2.6.1 Oxygen

Oxygen is the main impurity in detector grade silicon. It is present in float zone silicon (FZ) due to the oxidation process which is performed to passivate the open bonds at the silicon surface. In addition the oxygen content can be enriched by the *Diffusion oxygenation process* (DOFZ). The oxygen is present in silicon crystals grown by the Czochralski (Cz) pulling technique from the crucible. Therefore it is also present in Epitaxial silicon which is grown on Czochralski silicon due to diffusion. Infrared absorption measurements show that most of the oxygen present in as-grown Cz silicon at room temperature is in a dispersed form, as interstitial oxygen (O_i). Near the melting point of silicon (1418°C) the solubility of oxygen is estimated to be $2 \cdot 10^{18}$ atoms/cm^3. It has been observed that the presence of dispersed oxygen

produces a small increase in the average lattice spacing, proportional to the oxygen concentration. This increase indicates a local expansion near the isolated O-atom. Therefore, the presence of oxygen in silicon always leads to an expansion of the material and to built-in stress [Shi94].

Oxygen interstitial

The observation of its vibrational modes proofs the existence of interstitial oxygen in silicon [Shi94].

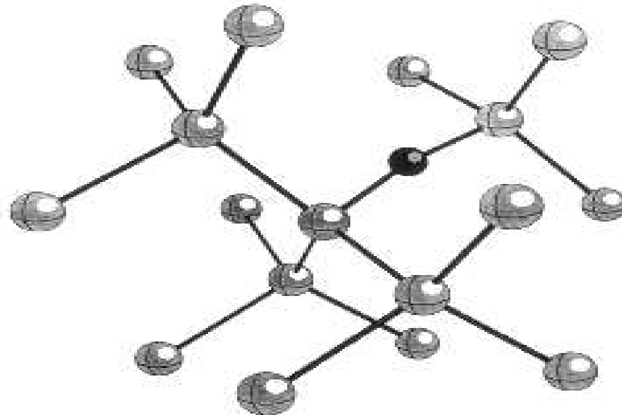

Figure 2.6: *Oxygen interstitial in the silicon lattice (taken from [Shi94]).*

These modes have first been measured via infrared absorption. These studies showed that three vibrational features are associated with oxygen in as-grown silicon. They are attributed to the three modes of a non-linear Si-O-Si pseudo molecule embedded in the silicon lattice. In this pseudo-molecule, the Si-atoms are nearest neighbor atoms of the crystal, and the bridging with the O-atom results from breaking the Si-Si bond. In this configuration, the interstitial O-atom is located in a (111) plane equidistant between the two Si atoms and its exact position depends on the Si-O-Si angle, as can be seen in Fig. 2.6.

Oxygen dimer

Also the oxygen dimer O_{2i} is observed in the silicon lattice. While an oxygen molecule is not stable in the silicon lattice the oxygen dimer can be stable in a certain configuration [Mur98]. The concentration of dimers in oxygenated silicon is usually two to three orders of magnitude less than the concentration of oxygen interstitials, therefore dimers can exist up to an amount of a few 10^{15} cm^{-3} in Cz material. Vibration modes of the oxygen dimer can be detected by IR-absorption measurements. It was found that there are two possible structures of the oxygen dimer with nearly similar energies [Obe98]. These consist of a pair of oxygen atoms at neighboring bond-center sites sharing a common silicon atom (staggered dimer), and a pair lying on a hexagonal ring, but separated by a Si-Si bond (skewed dimer). Both constellations of the dimer are shown in figure 2.7. The lower diffusion energy of

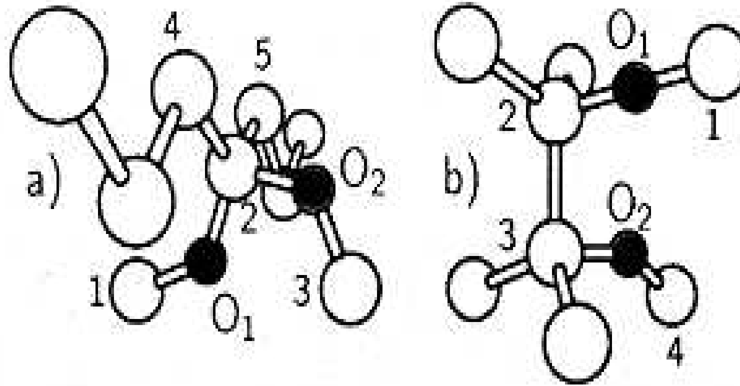

Figure 2.7: *Two possible configurations of the oxygen dimer. In the left hand side the staggered configuration is shown, while the right hand side shows the skewed configuration after [Cou00].*

the dimers (1.5 eV) compared with oxygen interstitials (2.5 eV) lead to the general assumption that oxygen dimers play a key role in the formation of Thermal Donors [Ram98],[Cou00],[Cou01],[Lee02]. Additional dimers in the silicon diodes can be generated by irradiation with γ-rays or electrons at 300° C [Lin97].

2.6.2 Thermal Donors (TD's)

Oxygen in its usual configuration is electrically inactive. But in silicon with high oxygen concentration the formation of thermal donors due to heat treatments can seriously change the effective doping concentration, e.g. as-grown Cz silicon displays an n-type electrical activity related to oxygen [Shi94]. This electrical activity is caused by a series of donor centers, the so-called Thermal Donors (TD's). The Thermal Donors were discovered in 1954 by Fuller et al. [Ful54], when upon heat treatment in the range of $300° - 550°$ C electrically active centers were formed in oxygen rich silicon. Three groups of Thermal Donors are discovered so far, the early Thermal Double Donors (TDD's), Shallow Thermal Donors (STD's), and New Donors (ND's). Only the TDD's are of interest in this work. The important factors that control the formation of TDD's are the annealing temperature and time, which also influences the energy of the charge states. For a 0.75 h annealing at 450^oC, two ionization energies of 60 and 130 meV were found, while for an annealing time of 7.5 hours the energies were 55 and 120 meV. From this results it is suggested that the TDD complexes grow in size with increasing annealing duration. Up to 16 different TDD's have been found so far. The TDD1, which has the largest binding energy is formed first. The formation kinetics of Thermal Donors present a significant problem for the direct involvement of oxygen. The diffusity of oxygen required for the formation of TDD's is two to three orders larger than generally accepted. The activation energy of the transformation from TDD(N) to TDD(N+1) varies from

1.2 eV for N=1, to 1.7 eV for larger N. This rules out a model where single oxygen atoms O_i diffuse to an oxygen cluster, because of their diffusion energy of 2.5 eV [Cou01]. To explain the formation of Thermal Donors a fast diffusion oxygen species is necessary. Theoretical calculations have shown that the oxygen dimer O_{2i}, and even oxygen chains with more than two oxygen atom have a lower migration energy than the interstitial and can therefore act as fast diffusion species (FDS) [Lee01].

The formation of Thermal Donors is influenced by the presence of carbon and hydrogen [Lin94]. It could be shown that for carbon concentrations smaller than $3 \cdot 10^{17}\ cm^{-3}$, there is only a small effect on the TDD generation. However, if the carbon concentration is larger, the maximum TDD concentration is reduced by two or more orders of magnitude. This effect was explained by the formation of carbon oxygen-pairs and other carbon related defects that capture oxygen atoms, and therefore inhibit the TDD formation.

On the other hand it was discovered that the TDD formation is enhanced by exposure to a hydrogen plasma during annealing. The hydrogen plasma annealed sample shows a significant increase in TDD concentration, the strongest enhancement was found for an annealing temperature of 350°C [Shi94].

2.6.3 Carbon

In silicon diodes two main configurations of carbon can be present. The substitutional carbon C_s or the interstitial C_i. The interstitial C_i is mobile at room temperature and will form higher order defect complexes (see section 2.7). The C_i is electrically active, while the carbon substitutional C_s is electrically inactive and will not influence the electric properties of the silicon material.

2.6.4 Hydrogen

Mainly to passivate dangling bonds in the silicon crystal or on the SiO_2-Si interface hydrogen is introduced into silicon. It is present in the atomic form, but also the formation of hydrogen molecules H_2 is possible. The H-Si-bonds are stronger than the Si-Si-bonds. Therefore the bandgap in SiH is larger than that of crystalline silicon, i.e. 1.7 eV vs. 1.1 eV [Pan91]. Also the dangling bonds of vacancies and impurities can be passivated with hydrogen, thus it is possible to passivate vacancies (VH_4) and divacancies (V_2H_6). Even other impurities like gold and silver which are known to cause deep levels in the bandgap, can be deactivated with hydrogen [Pan91]. It has been demonstrated that the electrical activity of Thermal Donors can be reduced by hydrogen treatment of the material. Due to the combination of hydrogen and impurities also electrical active defects can be introduced.

2.7 Important point defects

This section will give an overview of the point defects important for this work. The defects can be generated during the processing of the material, induced by radiation or later be formed during annealing.

2.7.1 Vacancy related defects

The single vacancy (V)

It has been shown by [Wat00] that the single vacancy defect takes on five different charge states in the silicon bandgap ($V^{++}, V^{+}, V^{0}, V^{-}, V^{--}$), with the two donor levels $V^{++/+}$ and $V^{+/0}$ showing a negative U-behavior. Their positions in the bandgap are E_V+0.13 eV for the $V^{++/+}$ and E_V+0.05 eV for the $V^{+/0}$. The thermally activated migration of the vacancy strongly depends on its charge state with activation energies of 0.18 ± 0.02 eV for the $V^{=}$, 0.32 ± 0.02 eV for V^{-} and 0.45 ± 0.04 eV for the V^{0}. This is displayed in 2.8. At room temperature the vacancies are mobile and their main traps are the interstitial oxygen, other substitutional atoms like phosphorus or boron, or other vacancies to form the divacancy. The vacancy can also form different vacancy-hydrogen complexes like VH, VH_2, VH_3, and VH_4. The first three of these defects are also electrically active. In Fig. 2.8 the thermal stability of the vacancies and several of the vacancy defect pairs is shown after 15 - 30 min isochronal annealing studies.

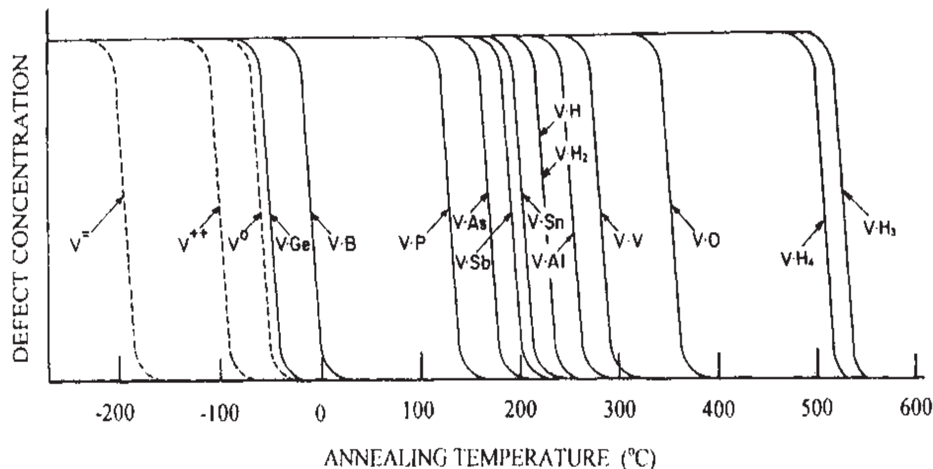

Figure 2.8: *Annealing temperature of vacancy related defects after [Wat00].*

The divacancy (V_2)

The divacancy can be formed in two different ways. It is either created directly by a displacement of two adjacent silicon atoms or it is formed by pairing of two single vacancies. This mechanism can be due to a creation of two single vacancies directly by a particle-atom collision or indirectly by a recoil-atom-atom collision [Sve92]. It was shown, that the formation rate of the divacancy strongly depends on the kind of impinging particles and their energies [Wat65]. Three levels in the bandgap and four charge states of the divacancy are introduced. The levels are the two acceptor levels $V_2(=/-)$ at $E_C - 0.22$ eV and $V_2(-/0)$ at $E_C - 0.42$ eV, and a donor state $V_2(+/0)$ at $E_V + 0.2$ eV. The model of the divacancy is given as two vacancies sitting at the adjacent sites of a silicon atom [Wat64]. The divacancy starts to anneal out

at about 250°C. The divacancy becomes mobil and combines with other impurities, therefore the annealing strongly depends on the material and its composition of impurities. At about 350°C also the dissociation of the divacancy was observed. A minimum binding energy of about 1.6 eV has been calculated for the the divacancy [Wat65]. Higher order vacancy defects like V_3, V_4, etc. in various configurations are very likely important structural components of clusters but have up to now only been investigated in a few experiments (see e.g. [Lee73] for V_4 and V_5). Molecular-dynamic simulations predict a gain of energy by forming an aggregate of n vacancies out of an isolated vacancy plus an aggregate of (n-1) vacancies [Has97].

The E-center (VP)

The E-center is a defect combined out of a vacancy and a phosphorus dopant atom P. In case of antimony doped silicon also the VSb defect would be called "E-center". The VP-defect has an energy level at $E_C - 0.45$ eV in the bandgap. Forming the E-center has two significant effects on n-type silicon. First the VP-defect is introducing an acceptor-level. But secondly there is the removal of the phosphorus doping, i.e. P is deactivated after forming the VP-defect. This mechanism is known as the "donor removal". A picture of the atomic configuration of the E-center can be seen on the left hand side of Fig. 2.9. Since the phosphorous atom as a dopant has an extra

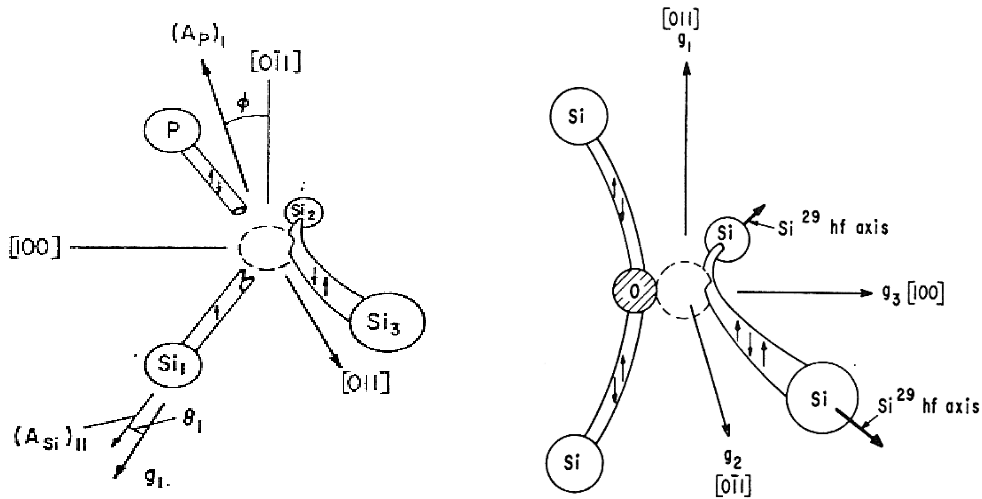

Figure 2.9: *Atomic model of the E-center (VP) [Wat64] and the A-center (VO_i)[Cor64].*

nuclear charge, it can take two electrons in its broken orbital with their spins paired off [Wat64]. Two of the remaining broken bonds form an electron pair bond between two silicon atoms, which pulls them together, one electron pair bond is left, leaving a single unpaired electron in the orbital of a silicon atom. A complete annealing of the E-center at 150°C can be observed [Kim76]. The annealing is either due to diffusion with the formation of higher order defect complexes, or due to dissociation. In case of dissociation the single-vacancy is most likely to be trapped by an oxygen atom to form the VO_i-defect.

2.7.2 Vacancy oxygen clusters

VO_i **and** VO_2

Since vacancies are mobile it is very likely that they are trapped by other impurities. One major possibility is the trapping of vacancies by oxygen to form the A-center (VO_i) or by oxygen dimers to form VO_2. The A-center is not a primarily radiation induced defect [Wat60]. Its energy level is 170 mV below the conduction band. In case of high radiation doses the A-center, sometimes also labeled "oxygen substitutional" depends on the oxygen concentration in the material. The atomic model is shown on the right hand side of Fig. 2.9. There are four broken bonds around the vacancy. In contrast to the E-center here the oxygen is bridging two of the broken bonds, forming a Si-O-Si molecule, while two silicon bonds pull together to form a Si-Si molecular bond. In the neutral charge state, the two electrons are paired off in the bonding orbital. If an additional electron gets trapped, it goes into the antibonding orbital and causes the level at E_C - 0.17 eV [Cor61]. The VO_i-center starts to anneal out at 300° C. In case of a high hydrogen content the transformation into VOH is observed, which has an acceptor level at $E_C - 0.32$ eV [?].
In contrast to the VO_i-defect the VO_2-defect is not electrically activ and has a higher binding energy. The most stable complex of one vacancy and two oxygen atoms is a complex, where the two oxygen atoms are inserted into the two dimer bonds of the vacancy. This complex corresponds to an A-center which has bound one additional oxygen atom with an additional binding energy of 1.0 eV [Cas00]. The VO_2-defect is also suspected to be bistable [Lin03].

V_2O **and** V_2O_2

The V_2O- and V_2O_2-defect, with very similar electrical properties, have been discovered by EPR-measurements [Lee76]. They have not been detected by methods which can give information about their capture cross section so far. Different results suggest an identification of the so-called X-defect with either the V_2O-defect [Mon02] or the V_2O_2-defect [Sta04]. The predicted model for the V_2O-defect is shown in the left hand side of Fig. 2.10. It consists of a divacancy and a nearly substitutional oxygen which is trapped near a vacancy site forming the Si-O-Si bond structure. Two main channels are responsible for the formation of the V_2O-defect. The first one is VO_i+V which could occur during irradiation, when the created VO_i-defect captures a single vacancy V which is mobile at room temperature. An other possible formation channel is via the divacancy ($V_2 + O_i$). Because neither the divacancy nor the oxygen interstitial is mobile at room temperature, this channel is only possible during annealing at temperatures higher than 250°C, where the divacancy becomes mobile. Both formations are second order processes. The V_2O-defect itself is stable up to 325°C. It is expected that the V_2O defect does not dissociate, it will either catch an other vacancy to form V_3O or catch an other oxygen atom to form V_2O_2.

The structure of the V_2O_2-defect is shown in the right hand side of Fig. 2.10. The two oxygen impurities are trapped at the two vacancy sites, respectively giving Si-O-Si structures. Beside the formation already mentioned above there are other possible ways of creating the V_2O_2-defect. One would be via the annealing of V_2 interacting with an oxygen dimer at high temperature. Another possibility can be

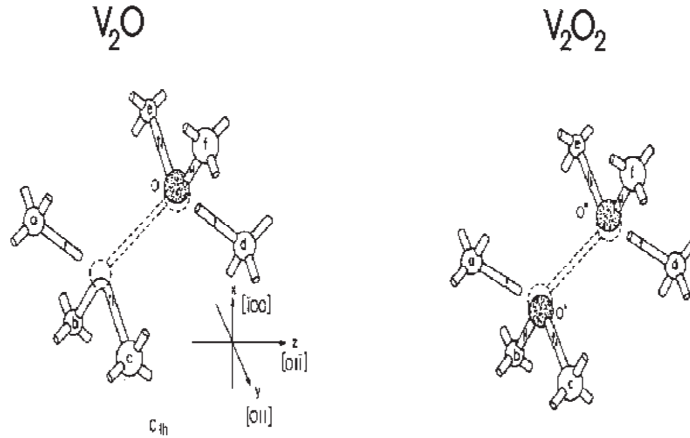

Figure 2.10: *Structures of the deep defects V_2O and V_2O_2 (taken from [Lee76]).*

found at room temperature via VO_2 +V which would also be a second order reaction as the formation of V_2O. V_2O_2 is slightly more stable than V_2O and will also anneal out by forming more complex defects, either it transforms to V_3O_2 by trapping a vacancy or to V_3O_3 by trapping a vacancy and an interstitial oxygen atom.

2.7.3 Interstitial related defects

The silicon interstitial (I)

EPR-experiments in p-type silicon have shown no evidence of isolated silicon interstitial atoms after electron irradiation at cryogenic temperature [Wat00]. Only defects which are identified as interstitials trapped at impurities are observed in a similar concentration to that of isolated vacancies. From that it has been concluded that the isolated interstitial atoms must be highly mobile even at 4.2 K, and therefore their activation energy for migration is very low. It is estimated to be around 0.07 eV [Hal99]. By the so called Watkins replacement mechanism the silicon interstitial can interact with other impurities like carbon or boron (in case of p-type silicon) by kicking the substitutional atom out of its lattice site and produces an interstitial carbon or boron atom. The silicon interstitial can also react with the oxygen interstitial and form the IO complex, which is stable up to about 200 K [Khi01]. Capturing another interstitial will lead to the formation of the I_2O complex which anneals out at room temperature [Her01]. By interacting directly with oxygen dimers the interstitials can also form the IO_2-defect which anneals out at about 400 K. In Fig. 2.11 the stability of the interstitial related defects is shown, after $15 - 30$ min isochronal annealing studies.

The Carbon interstitial (C_i)

The C_i-defect is an amphoteric defect with an acceptor state at E_C - 0.11 eV and a donor state at $E_V + 0.28$ eV. It is generated via the Watkins replacement mechanism. It is mobile at room temperature but much less than the silicon interstitial. It will

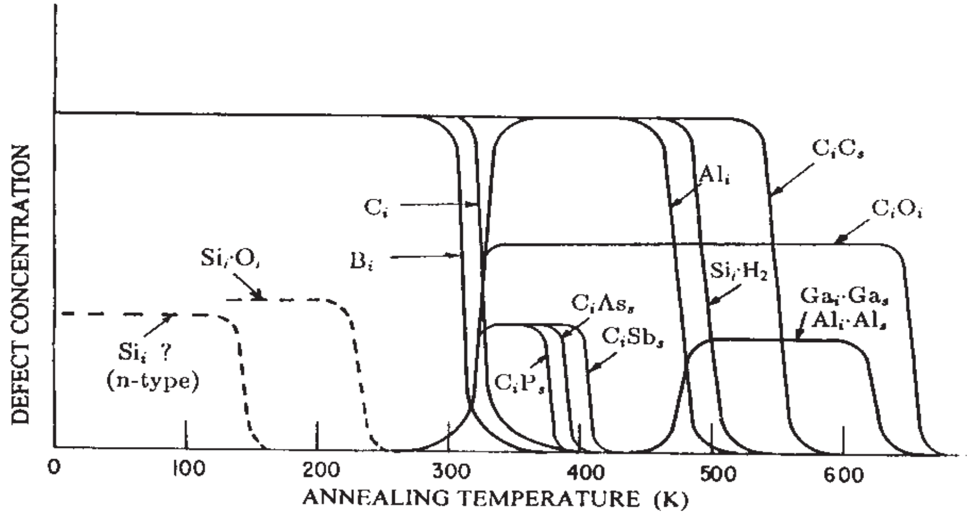

Figure 2.11: *Annealing temperature of interstitial related defects after [Wat00].*

react with other impurities like C_S to form C_iC_S or with O_i to form C_iO_i. The carbon interstitial can also react with hydrogen to form C_iH [Lea98].

The C_iC_s-defect

The C_iC_S-defect is a bistable defect with amphoteric character in both defect configurations. The transition from configuration A to B and vice versa is possible by a simple bond switching transformation [Son88, Son90]. In the A^- state the energy levels are at E_C - 0.17 eV and at E_V + 0.09 eV, in the B^- state at E_C - 0.11 eV and at E_V + 0.05 eV. The barrier for the transition from B^- to A^- is about 0.15 eV.

The C_iO_i-defect

As mentioned above it is most likely that the C_i will form the C_iO_i-defect, which has a donor state at E_V + 0.360 eV. This defect is stable up to 350°C.

Other carbon related defects

The carbon interstitial can also form defects like the C_iP_s-defect, which is a metastable defect with up to five different configurations observed so far [Gur92]. The C_iO_i-defect can react with silicon interstitials to form C_iO_iI, C_iO_iII or combinations with hydrogen (C_iO_iH, $C_iO_iH_2$) [Cou01]. Most of these defects are electrically inactive.

2.8 Damage Modeling

In 1987 Davies et al. [Dav87] were introducing a model for defect evolution after low energy electron irradiation, where only point defects are created. Vacancies,

self-interstitials and divacancies are created by this kind of irradiation. Most of the displaced interstitials (> 90%) recombine directly with the vacancies. The other 10% are able to move through the lattice at room temperature. Depending on the concentration of impurities the vacancies can make a certain number of jumps before meeting an impurity and being captured by forming a stable defect complex. The number of jumps strongly depends on the oxygen concentration, which is the main impurity in the silicon material. For Cz silicon this number of jumps is estimated to 5×10^4. For float zone silicon, where the amount of oxygen is lower, the number of jumps would be much higher. The typical capture time for vacancies is in the order of 0.025 seconds. The self-interstitial is even more mobile and therefore it is trapped more quickly. The Watkins replacement mechanism gives a possibility for self-interstitials to exchange with carbon atoms in the lattice $I + C_s \rightarrow Si + C_i$. The carbon interstitial has a much lower migration speed at room temperature and therefore the formation of higher order carbon related defects takes days after irradiation. The defect reactions proposed by Davies et al. are given in the first part of Tab. 2.2. In its second part the extensions made in 1995 by MacEvoy et al. [Mac95] are given. The model was adapted for γ-irradiation and extended by reactions with phosphorus atoms and higher order vacancy-oxygen complexes. In the last years it has been shown that also oxygen dimers are important for the radiation hardness of silicon materials [Kra03, Sta04]. Therefore reaction channels including oxygen dimers are presented in the third part of Tab. 2.2. In addition the model was extended by reactions with unknown impurities, labeled Y. These impurities can either trap vacancies or interstitials or form higher order complexes.

I reactions	V reactions	C_i reactions
$I + C_s \rightarrow C_i$	$V + V \rightarrow V_2$	$C_i + C_s \rightarrow CC$
$I + CC \rightarrow CCI$	$V + V_2 \rightarrow V_3$	$C_i + O_i \rightarrow CO$
$I + CCI \rightarrow CCII$	$V + O \rightarrow VO$	
$I + CO \rightarrow COI$	$V + VO \rightarrow V_2O$	
$I + COI \rightarrow COII$		
$I + V_2 \rightarrow V$		
$I + VO \rightarrow O$		
$VP + I \rightarrow P$	$V + P \rightarrow VP$	
$V_3O + I \rightarrow V_2O$	$V_2O + V \rightarrow V_3O$	
$VO_2 + I \rightarrow O_2$	$V + O_2 \rightarrow VO_2$	
$V_2O_2 + I \rightarrow VO_2$	$V + VO_2 \rightarrow V_2O_2$	
$I + O_2 \rightarrow IO_2$	$V + Y \rightarrow VY$	
$VY + I \rightarrow Y$	$V + VY \rightarrow V_2Y$	
	$V + I \rightarrow Si_s$	

Table 2.2: *Defect kinetics according to the Davies Model [Dav87] (first part). MacEvoy extension [Mac95] (second part). Oxygen dimer extension [Kra03] (third part).*

2.9 Cluster

Clusters are introduced to describe so-called disordered regions with 10^5 to 10^6 atoms. This results in a cluster size of 150 Å to 200 Å. The electric structure of the semiconductor is disturbed in the clustered regions and the electric bands are bent. The model introduced in the previous section can explain the change in the effective doping and the generated current only in case of point defect generation. If the model is applied to hadron, especially neutron, irradiation strong deviations between the predicted and the measured values can be observed [Mac99]. The main difference between hadron and γ-irradiation is the introduction of clusters. Inside these clusters the density of divacancies is assumed to be up to 10^{20}cm^{-3} [Gil97]. The V_2 contribution to the generation current can therefore be enhanced if the charge reaction $V_2^0 + V_2^0 \rightarrow V_2^+ + V_2^-$ occurs. This so-called inter-defect charge exchange is only possible if the defect density is very high inside a small volume [Mac02]. Also other defects inside the clusters are suspected to participate in the inter-defect charge transfer. Within the clusters the standard Shockley Read Hall statistics is not the fundament of charge carriers anymore [Mac02].

2.10 Radiation induced change of detector properties

Effective doping

The effective doping directly influences the depletion voltage of a silicon detector, therefore its one of its main parameters. Radiation induced donor- and acceptor-like defects influence the effective doping of the detector. Considering the occupation of the defect levels the effective space charge density N_{eff} can be written as (see equation 2.36).

$$N_{eff} = \sum_{Donors} p_t - \sum_{Acceptors} n_t = \sum_{Donors} N_t \frac{e_{n,t}}{e_{n,t} + e_{p,t}} - \sum_{Acceptors} N_t \frac{e_{p,t}}{e_{n,t} + e_{p,t}} \quad (2.60)$$

The so-called donor removal will influence the effective space charge. After the formation of the E-center the phosphorous atoms cannot act as donors anymore. A typical example for the change of the effective doping due to irradiation is given in Fig. 2.12.

Here the starting material is n-type silicon, doped with phosphorus donors. Irradiation leads to a deactivation of the donors which is due to the creation of E-centers (donor removal). Additionally deep acceptors are created. Both effects lead to a reduction of the initial negative space charge and above a certain fluence value to a space charge sign inversion. After the exhaustion of the initial doping concentration a linear increase of negative space charge is observed. With a maximum voltage supply of 600 V the detectors cannot be fully depleted anymore, after a fluence of about $2 \cdot 10^{14}\ cm^{-2}$.

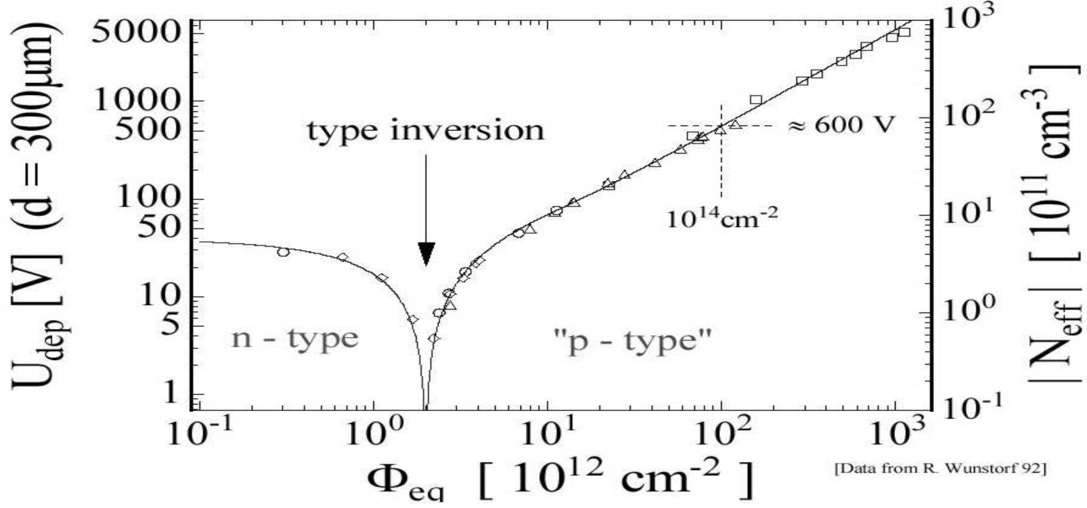

Figure 2.12: *Absolute effective doping concentration as measured immediately after irradiation [Wun92].*

Reverse Current

Another important effect of radiation induced damage is the increase of the reverse current. In case of fast hadron irradiation it was shown that this increase is proportional to the fluence and independent of the silicon material [Mol99]. The measured increase in current can be written as

$$\Delta I = \alpha \Phi_{eq} V \tag{2.61}$$

where α is called current related damage rate, Φ_{eq} is the fluence normalized to 1 MeV neutrons and V is the volume of the detector. The α-value depends on the annealing time and temperature (see [Mol99]). When comparing different kind of irradiation by the reverse current one has to respect the fact, that only defects close to the middle of the bandgap are efficient electron-hole pair generation centers. Therefore one can compare fluences of different particles by observation of the leakage current only when it is clear that the ratio of the introduction rate for current generation centers and all other defects are nearly the same. This is true for fast hadrons, but for gammas or low energy electrons it is not true anymore (see chapter 4).

Charge Collection Efficiency - Trapping

Electrons and holes generated by an ionizing particle in the silicon bulk drift to the electrodes due to the applied electric field (charge collection). Some of the charge carriers are captured (trapped) by deep defects during their drift through the detector. If it takes longer than the shaping time of the read-out electronic to re-emit the charge carrier the trapping results in a decrease of charge collection efficiency.

2.10.1 The oxygen effect

Oxygen rich silicon material has been established to be radiation harder than standard silicon material after irradiation with charged particles and photons [Lin01] with respect to the change of their effective doping. This oxygen effect is most pronounced after γ-irradiation. Defect models attribute this effect to a deep acceptor, which is suppressed in oxygen rich material. The simulation model predicts an energy level for this deep acceptor of $E_C - 0.5 \pm 0.05$ eV [Mac99] and a ratio of capture cross section of σ_p/σ_n=3 [Mac00]. A good candidate for this acceptor is the V_2O defect. According to the model, a high oxygen concentration suppresses the formation of V_2O, because the reaction $V + O_i \rightarrow VO_i$ is preferred instead of $VO_i + V \rightarrow V_2O$. It is also expected that the oxygen dimer O_{2i} has a strong influence on the radiation hardness of the silicon material. It was found that shallow bistable donors (BD's) are created by radiation in diodes, supposed to be oxygen-dimer rich, compensating the build up of negative space charge by deep acceptors [Pin05, Pin06]. In [Pin05, Pin06] it is suggested that the radiation induced formation of BD's might be connected with the presence of oxygen dimers O_{2i}.

Chapter 3

Experimental Methods and Equipment

In this chapter the experimental techniques and the setups are presented. In the first part an overview about the used materials and devices is given. Thereafter the used irradiation facilities are shortly described. Subsequently the used experimental methods are introduced. After a short description of the measurements of the current and capacitance (I/V - C/V) characteristics a more detailed introduction of the Deep Level Transient Spectroscopy (DLTS) and the Thermally Stimulated Current (TSC) technique, used for the investigation of radiation induced defect levels in the forbidden bandgap, are given in more detail. At the end of the chapter a short overview of the setup for these microscopic measurements is presented.

3.1 Materials and devices

Basically three different kind of silicon materials (float zone (FZ), Czochralski (Cz) and epitaxial layers on Czochralski substrate (Epi)) have been used for the fabrication of the diodes investigated in this work. All materials are n-type silicon doped with phosphorus and were processed by CiS [CiS] except the wafer bonded FZ devices which were processed by MPI [MPI]. For more information about the used planar processing technology see [Kem80, Lut99].

3.1.1 Float zone material (FZ)

One possibility to grow silicon is the float zone method [Sze85]. This material is usually less contaminated than the material produced with the Cz method (see below). The starting material is polysilicon, already formed in a rod and put into a vertical holder. A radio frequency is used to partly melt the silicon. The molten silicon is touched from below with a seed crystal. Both are rotating. The molten zone is than moved slowly along the rod and the silicon solidifies in a single crystal. This process can be repeated several times in order to obtain a very pure material.

3.1.2 Czochralski silicon (Cz)

Most of the silicon used for electronics is grown via the Czochralski method. Again the starting material is poly-silicon, which is melted in a rotating quartz crucible via a radio frequency field [Sze85]. The dopants are added into the crucible. A single seed crystal is placed from above on the surface of the liquid silicon and slowly drawn upwards while being rotated and the silicon solidifies in a single crystal.

In this work also MCz (magnetic field applied Cz) material is used. The MCz method is the same as the Cz method except that it is carried out within a strong horizontal or vertical magnetic field. This serves to control the convection fluid flow, allowing e.g. to minimize the mixing between the liquid in the center of the bath with that at the edge. This effectively creates a liquid silicon crucible around the central silicon bath, which can trap contaminations and slow its migration into the crystal. Compared to the standard Cz a lower oxygen concentration can be obtained and the impurity distribution is more homogeneous.

3.1.3 Epitaxial silicon

Epitaxial layers are grown as thin films on a single crystal substrate [Dez97]. The crystal structure of the epi-layer is defined by the lattice structure and surface orientation of the substrate. During the crystal growth impurities from the substrate (in this work Cz material) migrate into the epitaxial layer. Thus it is possible to find high concentrations of oxygen in epitaxial silicon.

The layers used in this work were manufactured by ITME [ITM] using the CVD (chemical vapor deposition) process.

3.1.4 Used devices

In this section an overview of the the used devices and their labeling is given. The test structures were designed by the semiconductor laboratory of the MPI München [MPI]. For further information see [Sta04].

The used float zone silicon was grown by Wacker [WAC]. The thickness of the devices is of about 285 μm. Four different kind of thick float zone material has been used, the standard float zone (StFZ), which got no extra oxygen diffusion, and three kind of diffusion oxygenated float zone (DOFZ), which got an extra oxygen diffusion at 1150°C for 24, 48 and 72 hours. A fifth thin float zone material (50 μm) has been processed by MPI using the wafer bonding technique [And04]. These thin devices have an area of 10 mm^2 while all other samples have an area of 25 mm^2.

Three kind of Czochralski material have been used in this work. While a standard material was fabricated by Sumitomo [SIT], two magnetic Czochralski (MCz) devices were processed on material from Okmetic [OKM] one with a thickness of 280 μm and a thinned one with a thickness of 100 μm.

Five different types of epi-devices were used in this work. They were all grown on low ohmic Cz-substrates but with different thickness. Epi-layers with resistivity of about 0.05 kΩcm were grown with thicknesses of 25, 50 and 75 μm. In a second production step epi-layers with a resistivity of about 0.15 kΩcm were grown. Part of the epi-layers underwent a preceding oxygen enrichment by a heat treatment for 24

hours at 1100°C (denoted as epi-72-DO) before pad diodes were processed on them using the CiS process technology. The other did not undergo these heat treatment (labeled as epi-72-St).

Information about the different properties and the labeling of the used devices can be found in Tab. 3.1. Since the presented oxygen content strongly depends on the different oxygen diffusion mechanisms the given values for $[O_i]$ have more a statistical meaning and for a more clear information oxygen profiles will be given below.

Wafer labeling	Producer of material	orient.	Layer [μm]	$[O_i]$ [10^{16}cm^{-3}]	N_{eff} [10^{12}cm^{-3}]	ρ [kΩcm]	Comments
CA	Wacker	<111>	285	< 0.5	1.1	2-5	
CB	Wacker	<111>	285	6	1.1	2-5	DOFZ 24h
CC	Wacker	<111>	285	10	1.1	2-5	DOFZ 48h
CD	Wacker	<111>	285	12	1.1	2-5	DOFZ 72h
Cz	Sumitomo	<100>	285	80	3.3	1.2	
MCz	Okmetic	<100>	280	60	4.4	0.8	
MCz-100	Okmetic	<100>	100	60	4.3	0.8	thinned
epi-25	ITME	<111>	25	12	60	0.05	ox. profile
epi-50	ITME	<111>	50	9	68	0.05	ox. profile
epi-75	ITME	<111>	75	5	62	0.05	ox. profile
epi-72-St	ITME	<111>	72	5	25	0.15	ox. profile
epi-72-DO	ITME	<111>	72	70	25	0.15	DO-EPI
FZ-50	Wacker	<100>	50	3	33	0.10	wafer bonded / area 10 mm^2

Table 3.1: Properties and labeling of the used materials

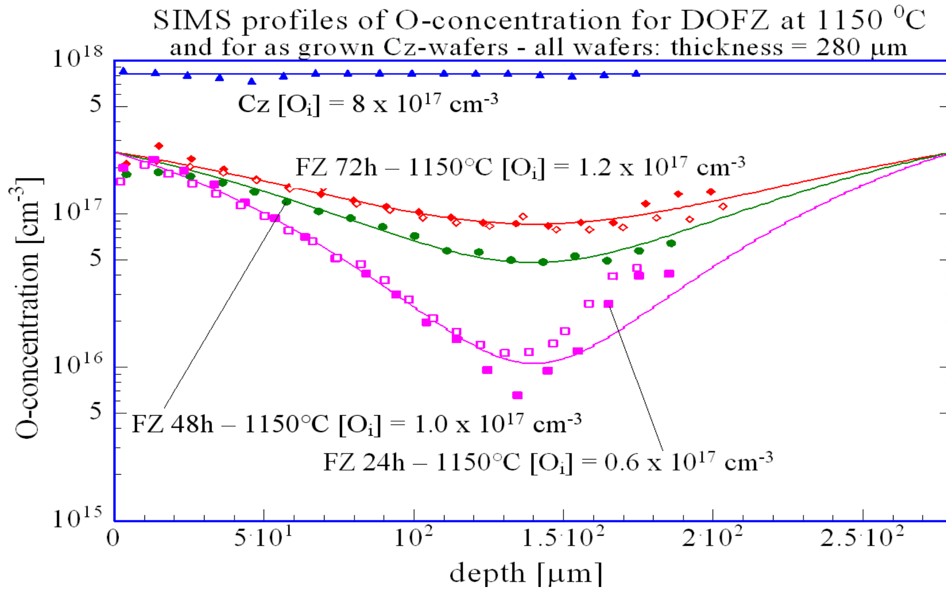

Figure 3.1: *SIMS measurements of the oxygen concentration for different DOFZ and Cz materials.*

Since it is well known that the oxygen content of the diodes plays an important role on the defect formation during irradiation as well as during annealing several materials have been investigated by the Secondary Ion Mass Spectroscopy (SIMS) in order to get information about the homogeneity and the concentration of oxygen

inside of the diodes. To get a good depth profiles for thick devices the samples are beveled an an angle and the surface of the beveled area is scanned [Bar03]. While for thin devices the SIMS measurements can be done by directly sputtering the samples. The oxygen profiles of the different devices are shown in Fig. 3.1 and 3.2. In all cases also the carbon concentration has been measured and found to be below the detection limit.

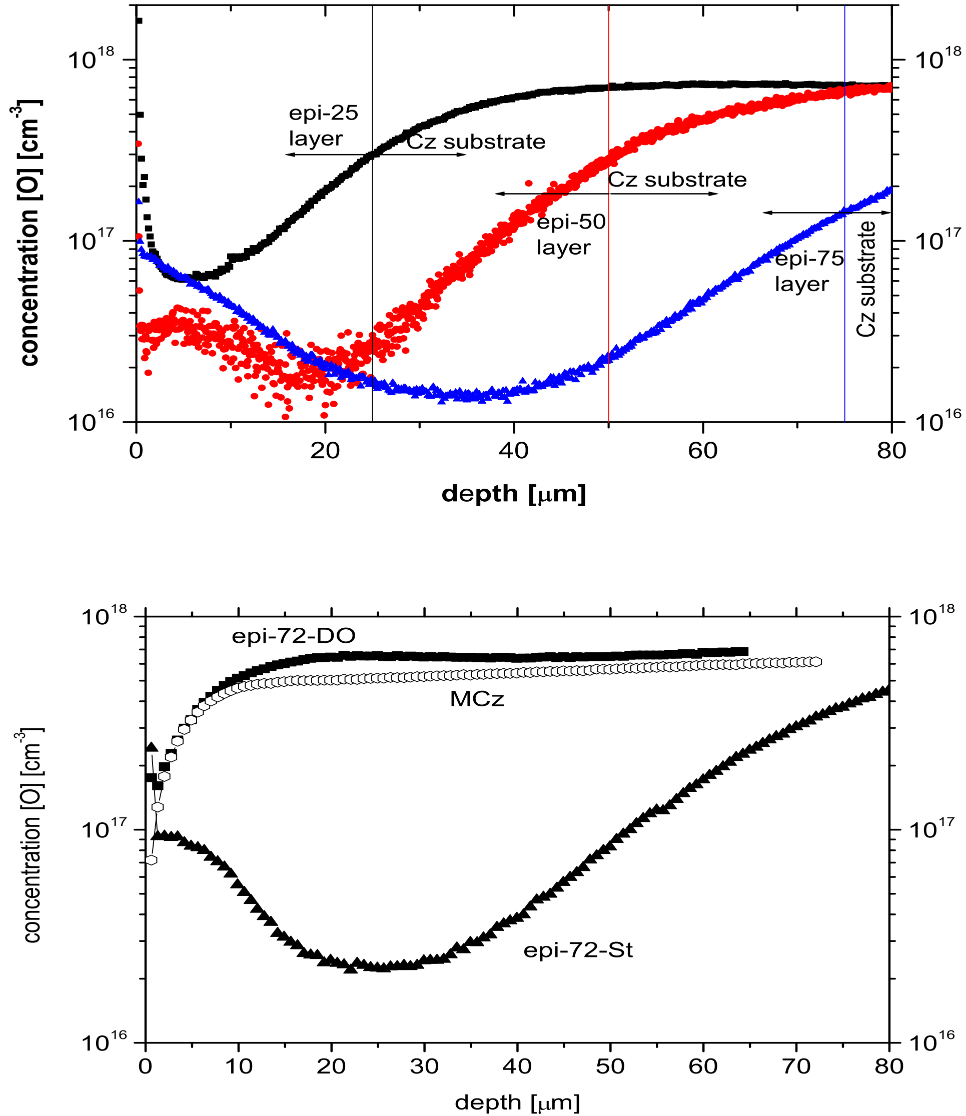

Figure 3.2: *SIMS measurements for epi-25, epi-50 and epi-75 diodes (upper part) and for epi-72-St, epi-72-DO and MCz samples (lower part)*

3.2 Radiation sources

3.2.1 Brookhaven National Laboratory ($^{60}Co - \gamma - photons$)

Several samples used in this work were irradiated with $^{60}Co - \gamma$-rays using the $^{60}Co - \gamma$-source of the Brookhaven National Laboratory (BNL). $^{60}_{27}Co$ has a half-life

of 5.27 years and it decays in a β^- decay into $^{60}_{28}Ni$, where two γ photons (1.17 MeV and 1.33 MeV) are emitted. The dose rate at the position of irradiation is about 1.5 kGy/hour, and the irradiations are performed at temperatures between 25°C and 30°C. After exposure the samples were stored at room temperature.

The dose is measured with a calibrated dosimeter at the position of irradiation. The error of the dose measurement is estimated to be 5-10 %. The biggest source of error is the temperature, which increases during the irradiation due the heating-up of the equipment. The elevated temperature lead to a start of annealing effects. This error does not affect the dose but the concentration of some measurable defects.

3.2.2 Stockholm (6 MeV electrons)

The irradiation with 6 MeV electrons has been performed at the Alvén laboratory at the KTH, Stockholm, Sweden. The irradiation has been performed at room temperature. The fluence of about 10^{14}cm^{-2} has been reached within 1000 seconds.

3.2.3 Trieste (900 MeV electrons)

The irradiations with high energy electrons were performed with the electron beam of the LINAC injector at the synchrotron light facility Elettra in Trieste (Italy). Devices were kept unbiased during irradiation, like in all irradiations performed within this work. The temperature during irradiation was measured to be 25°C. To ensure a uniform irradiation of the whole area covered by the devices, these were moved along a serpentine path in a plane perpendicular to the beam, by means of a remotely controlled translation stage. The electron fluence was measured by means of a toroidal coil coaxial with the beam, allowing the electric charge of the individual beam to be monitored.

3.2.4 Karlsruhe (26 MeV protons)

Irradiations with 26 MeV protons were performed with the Kompakt-Zyklotron (KAZ) in Karlsruhe (Germany), which accelerates protons up to an adjustable energy between 18 MeV and 40 MeV. The maximum available beam current is around 100 μA. The advantage of the KAZ is the H$^-$-source. The H$^-$ ions are accelerated inside of the KAZ and a magnetic field bends them to a circular track. When the H$^-$ ions achieved the required energy, they are shot through a stripping foil which removes the electrons. Since the H$^+$ ions circular track in the magnetic field is of the opposite direction to the H$^-$ ions, the same magnetic field can be used to move the H$^+$ ions out of the KAZ to the beam lines in which the H$^+$ ions are focussed and transported to the target. The current produced by the electrons collected in the stripping foil is proportional to the H$^+$ fluence. This enables a measurement of the beam current during the irradiation. After irradiation the fluence is checked by activation of Ni-foils placed behind the irradiated structures. Natural Ni has a fraction of 63 % of the $^{58}_{28}$Ni isotope. The protons with an energy of 26 MeV activate the $^{58}_{28}$Ni isotope via a (p,2n) reaction.

$$p +^{58}_{28} Ni \;\rightarrow\; ^{57}_{29}Cu + 2n \tag{3.1}$$

The following β^+ decay of the produced $^{57}_{29}$Cu($\tau_{1/2}$= 199ms) gives the $^{57}_{28}$Ni isotope with a half life of 35.6 h.

$$^{57}_{29}Cu \;\rightarrow\; ^{57}_{28}Ni + \beta^+ + \nu_e \qquad (3.2)$$

This isotope decays via electron capture and shows emission of the characteristic γ at 1377.6 keV which is measured with a germanium detector.

3.2.5 CERN (23 GeV protons)

The irradiation with high energy protons was done with the $24GeV/c$ proton beam of the proton synchrotron PS at CERN. Depending on the number of spills and the beam focussing fluences up to $1 \cdot 10^{14} h^{-1} cm^{-2}$ can be reached. The detectors are put into 5x5 cm^2 cardboards and then transported by a shuttle into the beam. The temperature at the point, where the irradiation takes place is about 27°C. Depending on the activation after the irradiation, the diodes have to rest up to one hour in order to wait for their activity to decrease to a level where the save handling is possible. A freezer is available at the irradiation facility to store the diodes immediately after the irradiation at a temperature of about -20°C. It is also possible to anneal the diodes at 80°C and to measure C/V- and I/V-curves directly at CERN.

The fluences were measured using aluminum foils which were irradiated together with the diodes. In the activated aluminium foils ($^{27}Al(p,3pn)^{24}Na$) the gamma emission (1.37 MeV and 2.75 MeV) of ^{24}Na which has a half-life of about 15 hours is measured. For long irradiations the aluminum sheets had to be changed during the measurement. The determination of the fluence via this method has an error of about 7%. A second possibility for dosimetry is to measure the gamma emission from the ^{22}Na-isotope (1.27 MeV) which is also produced via the reaction $^{27}Al(p,3p3n)^{22}Na$. This isotope has a half-life of 12.6 years.

3.2.6 Ljubljana (reactor neutrons)

For neutron irradiation the TRIGA nuclear reactor of the Josef Stefan Institute in Ljubljana (Slovenia) was used. The neutron energy spectrum extends up to 10 MeV. The operating power of the reactor can be varied between a few Watts and 250 kW within an hour, i.e. a wide range of fluences can be covered. Even high fluences can be reached within a short irradiation time. The neutron flux scales linearly with the power. The scaling factor is about $7.5 \cdot 10^9/cm^2 s/kW$. For the irradiation the samples are stored in irradiation capsules and put from the top into the reactor. Depending on the radioactivity a cooling down time up to one hour is necessary, before the samples are stored at -20°C [Kra01].

3.3 C/V- and I/V-measurements

The macroscopic parameters of a diode, the depletion voltage U_{dep} and the reverse current I_{dep} at the depletion voltage, are of main interest and therefore measured as capacitance-voltage (C/V) and current-voltage characteristics (I/V). The depletion voltage of the diode is extracted by fitting two lines to the measured C/V-curve

plotted in a log-log scale. One line is fitted to the slope of the curve, where the measured capacitance is decreasing, the other line is a line put on the final horizontal part, with the value of geometrical capacitance of the diode. The intersection point of these two lines gives the depletion voltage U_{dep} in Fig. 3.3.

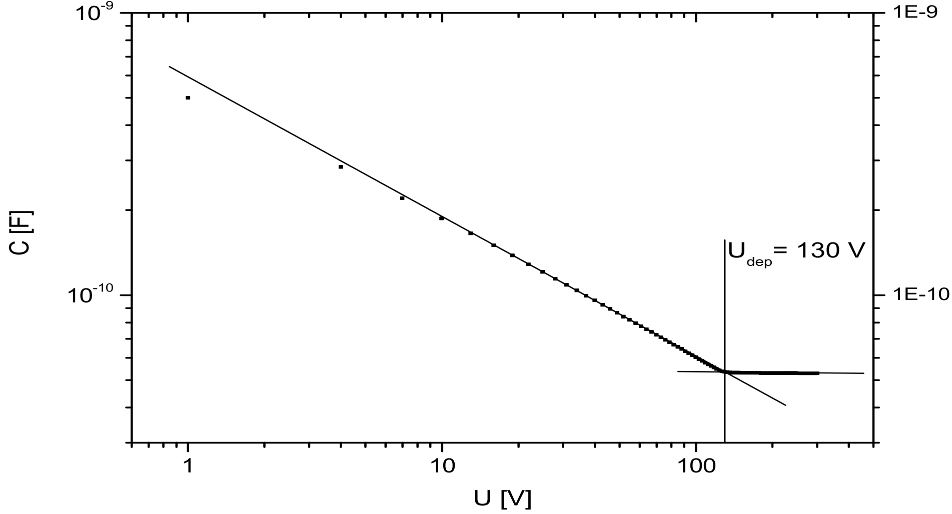

Figure 3.3: *C/V-characteristic of an unirradiated epitaxial-diode with a layer-thickness of 50 μm and a resistivity of 50 Ωcm. The C/V-curves are fit with straight lines to extract the depletion voltage.*

The C/V-measurements were performed with a HP 4284A LCR Meter by measuring the admittance Y of the diodes. A schematic description of the setup can be found in [Fei97, Mol99]. For a circuit with a capacitor and a resistor in parallel the admittance Y is given by

$$Y = \frac{1}{R_P} + j\omega C_p. \tag{3.3}$$

An unirradiated detector can be approximated by the parallel circuit, because the conductivity of the undepleted bulk is very high, while the conductivity of the depleted bulk is very low. Therefore, the measured admittance represents almost only the capacitance. This changes with radiation induced damage of the diodes. With increasing damage the undepleted region becomes intrinsic, i.e. the resistivity becomes large, thus the serial resistance R_S becomes large. As long, as the reverse current is not too high the serial circuit is the appropriate model

$$Z = R_s - j\frac{1}{\omega C_s}. \tag{3.4}$$

It is possible to transform the measured admittance Y into the impedance Z and vice versa, since both circuits represent the same measured data. The transformation of the admittance into the impedance is given by

$$C_s = \frac{1 + \omega^2 R_p^2 C_p^2}{\omega^2 R_p^2 C_p} \quad , \quad R_s = \frac{R_p}{1 + \omega^2 R_p^2 C_p^2}. \tag{3.5}$$

The measurement of the admittance or the impedance is done by adding a small AC voltage with an amplitude of 0.5 V and a frequency ω to the DC voltage of the reverse bias. The frequency can be chosen in a range of frequencies from several Hz to about 1 MHz. For all C/V-measurements performed in this work a frequency of 10 kHz was used.

The I/V-characteristics is measured with a Keithley 6517A Electrometer. Since the value of the measured current strongly depends on the temperature also the temperature during the I/V-measurements is recorded with a Keithley 195 A Multimeter. The measured I/V-curve can be normalized to a reference temperature of $T_R = 20^\circ$ C by multiplying the measured values with the factor F(T) [Sze81]

$$I(T_R) = I(T) \cdot F(T), \qquad F(T) = (\frac{T_R}{T})^2 exp(-\frac{E_g}{2k_B}[\frac{1}{T_R} - \frac{1}{T}]). \tag{3.6}$$

3.4 Deep Level Transient Spectroscopy (DLTS)

The deep level transient spectroscopy (DLTS) is a widely used and powerful tool to determine all parameters related with a defect level, like activation energy, capture cross section, and trap concentration. The DLTS method can also distinguish, whether a defect acts as an electron or hole trap. In addition to the classical C-DLTS (Capacitance-DLTS) method which is introduced in detail in section 3.4.1 also other DLTS methods are possible. All DLTS methods are based on transient measurements caused by a relaxation process. By applying a reverse bias on a p+/n junction or a Schottky diode a space charge region (SCR) is established. The traps inside this SCR are filled with a voltage pulse or via illumination by optical generation of carriers. For the C-DLTS technique, originally proposed by D. V. Lang [Lan74], after the end of the pulse the capacitance transient due to the emission of carriers from the traps is recorded. An exponential time dependence of the capacitance transient is only observed, if the concentration of defects is at least an order of magnitude smaller than the effective doping.

CC-DLTS and I-DLTS

CC-DLTS also known as U-DLTS stands for constant capacitance DLTS, respectively voltage DLTS. During the transient measurement the capacitance of the SCR region is kept constant by adjusting the applied voltage. The advantage of this method is, that the width of the SCR is not changed during the emission process. Therefore the CC-DLTS method is useful for trap concentrations at the limit of the C-DLTS method, but for small trap concentrations it is not as sensitive as the C-DLTS method.
Another DLTS method is the I-DLTS technique, where the current transient is measured [Li98]. The I-DLTS method is not limited by the effective doping of the sample, as long as it is possible to provide enough free carriers to fill the traps. This can be done via optical injection of carriers by illumination of one of the contacts for example. Instead of the current, also the charge can be monitored.

3.4.1 DLTS principle

The left hand side of Fig. 3.4 shows the principle of the DLTS method for an electron trap in the upper half of the bandgap of an n-type diode [Mol99]. In the first stage [1] the diode is reversed biased with a voltage smaller than the depletion voltage, therefore the diode is just partially depleted, and the traps inside the depleted region are not occupied with electrons. A positive space charge has built up inside the depleted region because of the doping of the diode. In stage [2] the bias voltage is reduced towards a smaller voltage to sweep electrons into the space charge region. The defect states are now below the Fermi level and filled with electrons. Right after the end of the pulse the electron traps are filled and the positive space charge is partially compensated by the trapped electrons, thus the capacitance of the junction is reduced. In stage [3] the electrons are emitted into the conduction band if the thermal energy present is sufficient, i.e the junction relaxes back into the normal reverse bias condition. The emission of carries is monitored as a capacitance transient shown in the lower part of the left hand side of Fig. 3.4.

The right hand side of Fig. 3.4 shows the DLTS principle for a hole trap. Applying a forward bias sweeps both types of carriers into the space charge region. To measure the emission of holes from a hole trap by forward biasing the capture coefficient of the defect for holes has to be much higher than the one for electrons $c_p >> c_n$. If both kind of carriers are injected into the space charge region the occupation of traps with holes is given by the ratio of the electron and hole capture coefficients $p_t = (1 + \frac{c_n}{c_p})^{-1}$. After the filling of the traps with holes the space charge region is even more positively charged, and hence a higher junction capacitance is measured. After the end of the pulse and reestablished V_R the holes are emitted and the junction capacitance returns to its initial value C_R.

3.4.2 Classical DLTS method

The classical DLTS system was invented by Lang in 1974 [Lan74]. For the analysis of the transients based on the classical DLTS system the so-called double boxcar method was used. The basic assumption of all DLTS methods is, that the emission transient has an exponential behavior which is only due to one time constant τ_e:

$$C(t) = \Delta C_0 \cdot exp(-\frac{t + t_0}{\tau_e}) + C_R, \tag{3.7}$$

where ΔC_0 is the amplitude of the transient, t_0 is the bridge recovery time and C_R is the junction capacitance under reverse bias. The capacitance transient is also shown in Fig. 3.5, where $t = 0$ and $t = T_W$ represent the begin and the end of the so called time window where the capacitance is measured.

In Fig. 3.6 the principle of the double boxcar method is shown. The distinct temperature dependence of the capacitance transients is pointed out. The difference in capacitance between the two points in time (t_1 and t_2) $\Delta C = C(t_1) - C(t_2)$ for each transient is plotted versus the temperature in the right hand side of Fig. 3.5. This difference ΔC is at maximum, if the optimal temperature T_{max} for the time constant τ_e of a defect level is reached for a fixed time window. With the temperature

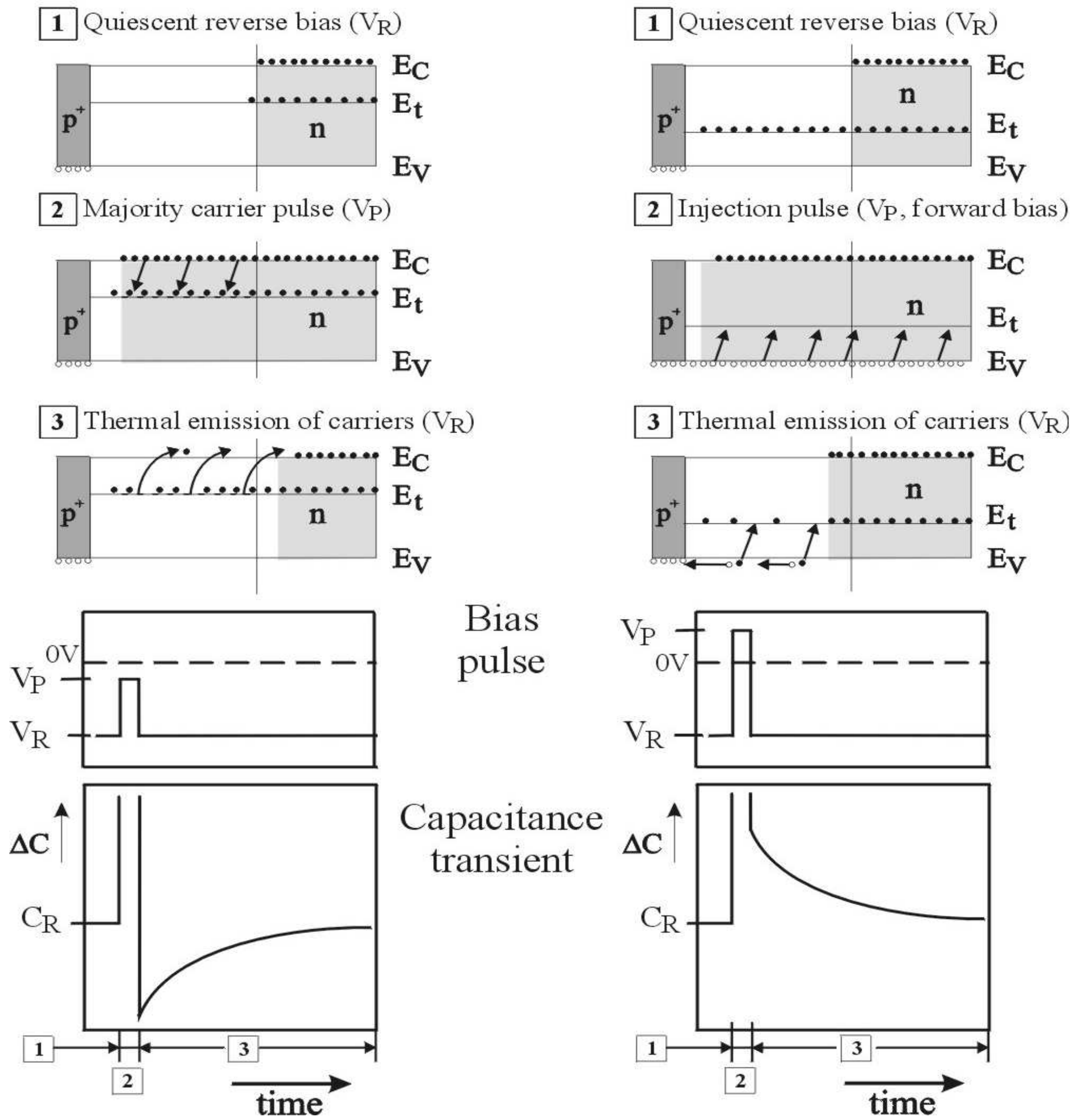

Figure 3.4: *DLTS principle of operation in case of majority carrier injection (left hand side) and high injection by a forward pulse (n≈p) (right hand side) for an n-type diode (taken from [Mol99]).*

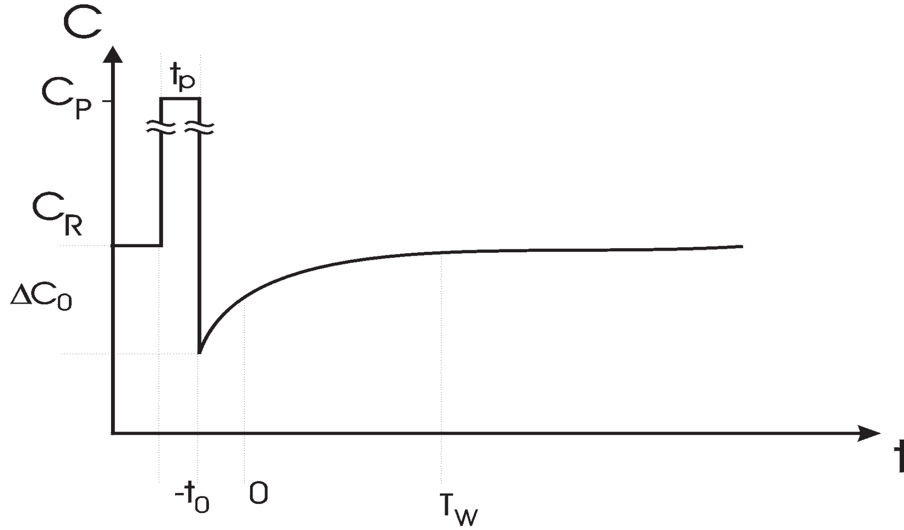

Figure 3.5: *Emission transient after a pulse of majority carriers.*

T_{max} the emission time constant τ_e for the defect level can be calculated by

$$\tau_e(T_{max}) = \frac{t_1 - t_2}{ln(\frac{t_1}{t_2})}. \tag{3.8}$$

By changing the time windows T_W the maximum of ΔC will appear at different temperatures. Therefore, the measurement is repeated for different time windows. With the data pairs (τ_e, T_{max}) an Arrhenius plot can be extracted (see later on the right hand side of Fig. 3.8).

3.5 DLTFS method

3.5.1 Principle

The double boxcar DLTS method (or classical DLTS) based on only two values of the whole transient, while in this work the transients, recorded with a transient recorder, have been analyzed with a computer program developed by Phystech [PHYS], which is using the information of the whole transient. The program is based on the so-called DLTFS method which stands for Deep Level Transient Fourier Spectroscopy [Wei91].

For this method the transient is digitized into N data points which are taken by a transient recorder. Using the Discrete Fourier Transformation (DFT) the discrete Fourier coefficients a_n^D and b_n^D of the transients are calculated. The emission of carriers will show an exponential behavior. This exponential time law is transformed into a Fourier series and the calculation of continuous coefficients a_n and b_n is done. The comparison of the continuous and the discrete coefficients the parameters gives the possibility of the determination of the emission. The calculation of the Fourier coefficients can be regarded as a weighting of the transients with a correlator function. More about the Fourier transformation and correlator functions can be found in appendix B.

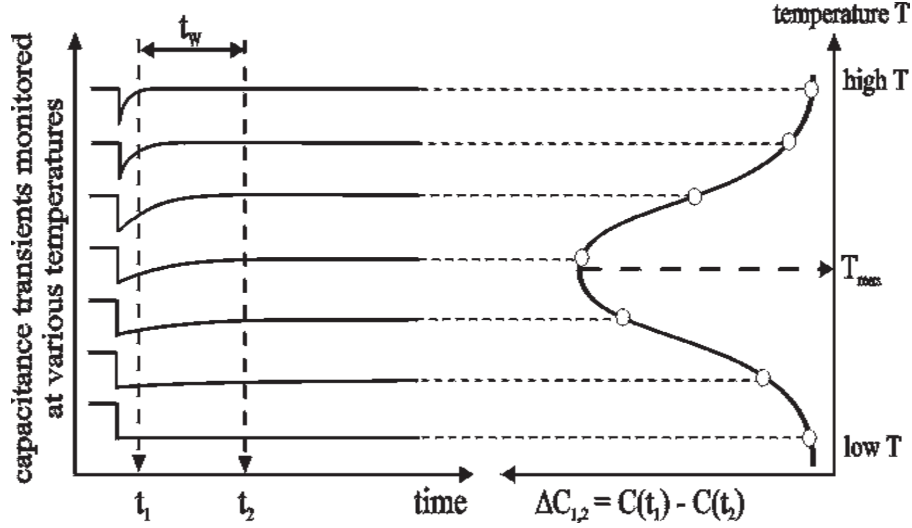

Figure 3.6: *The left-hand side shows capacitance transients at various temperatures, while the right-hand side shows the corresponding DLTS signal resulting from the use of the double boxcar method to display the difference in capacitance at t_1 and t_2 as a function of temperature (after [Lan74]).*

The N data points of the transient which are taken within the time window T_W are taken into account for the evaluation. After taking the data the transient is weighted by folding the measured data with a set of correlator functions. In Fig. 3.7 these correlator functions are shown.

One example is the so-called b_1 coefficient:

$$b_1 = \frac{2\Delta C_0}{T_W} \int_0^{T_W} exp(-\frac{t+t_0}{\tau_e}) sin(\frac{2\pi}{T_W} t) dt. \tag{3.9}$$

The weighted transients show again a temperature dependence like it was shown for the capacitance amplitude in the double boxcar method. A set of correlator functions shown in Fig. 3.7 are used. Their temperature dependence is exemplarily shown for some of them on the left hand side of Fig. 3.8.

By determining the peak maximum of the coefficient the time constant τ_e can be evaluated. With a variation of the ratio τ_e/T_W for the coefficients the amplitude of the coefficient and the emission time constant are calculated numerically. This results in a data pair $(\tau_e(T_{max}), T_{max})$ for each coefficient. By

$$1 = e_n \tau_e \tag{3.10}$$

the correlation of the emission time constant τ_e and the emission rate of a defect level e_n, which was defined in section 2.4.4, is given. With the time constant τ_e equation 2.34 can be transformed into

$$ln(\tau_e c_{n,p} N_{C,V} X_{n,p}) = \frac{\Delta H}{k_B T}. \tag{3.11}$$

The definition of the capture cross section lead to the Arrhenius relation

$$ln(\tau_e v_{th,e,h} N_{C,V}) = -ln(\sigma_{n,p}) + \frac{\Delta H'}{k_B T}. \tag{3.12}$$

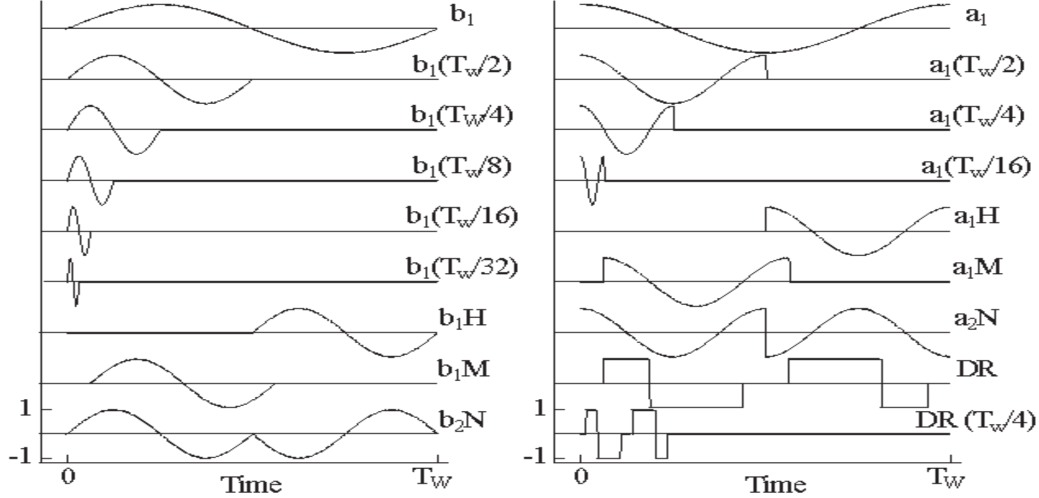

Figure 3.7: *Different correlator functions (taken from [Mol99]).*

Since no temperature dependence of the capture cross section is taken into account, the activation energy is called by $\Delta H'$, instead of ΔH, and the unknown entropy factor is neglected ($X_{n,p} = 1$). Because of the temperature dependence of $v_{th,n,p}$ and $N_{C,V}$ the product $v_{th,n,p}N_{C,V}$ is proportional to T^2. This temperature dependence is often regarded as T^2-correction if it is not neglected.

The slope of a linear fit of the Arrhenius data gives the activation energy while the capture cross section can be extracted from its extrapolation towards 1/T = 0. At this intersection point with the y-axis the capture cross section can be calculated using Eq. 3.12. In this work the measurements were performed using three time windows with the length 20 ms, 200 ms and 2s in order to get a higher precision of both, the activation energy and the capture cross section.

3.5.2 Fourier transformation

Each periodical signal $f(t)$ with a period $\omega = \frac{2\pi}{T_W}$ can be written as an infinite sum of harmonic functions:

$$f(t) = \frac{a_0}{2} + \sum_{n=1}^{\infty} a_n cos(n\omega t) + \sum_{n=1}^{\infty} b_n sin(n\omega t) \tag{3.13}$$

with the so-called Fourier coefficients a_n and b_n

$$a_n = \frac{2}{T_W} \int_0^{T_W} f(t) cos(n\omega t) dt \tag{3.14}$$

$$b_n = \frac{2}{T_W} \int_0^{T_W} f(t) sin(n\omega t) dt. \tag{3.15}$$

Since the time t=0 is set to the start of the recording of the transient the calculation of the Fourier coefficients for the exponential time law for the emission defined in equation 3.7 results in:

$$a_0 = \frac{2\Delta C_0}{T_W} exp(-t_0/\tau_e)(1 - exp(-T_W/\tau_e))\tau_e + 2C_R \tag{3.16}$$

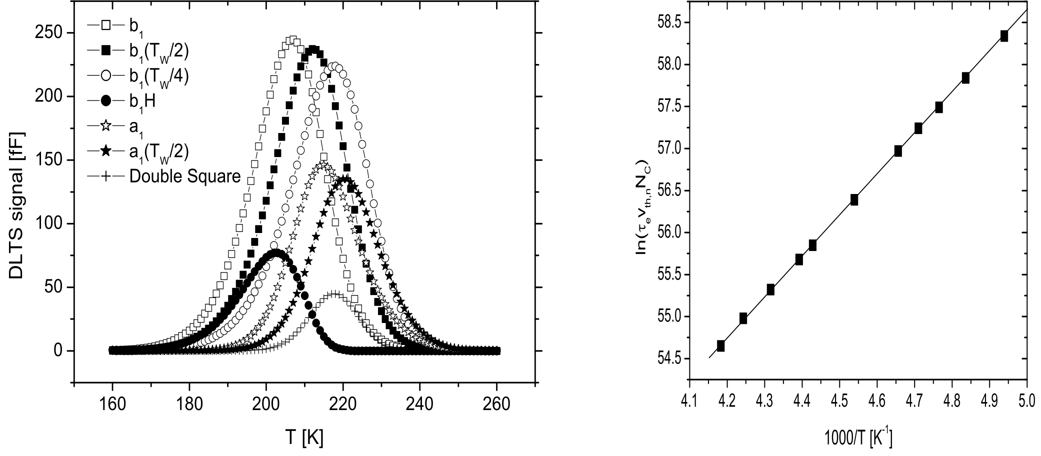

Figure 3.8: *The left hand side of the figure shows the temperature dependence of some of the correlator functions for a simulated defect level with* $\Delta H' = 0.420\ eV$ *and* $\sigma_n = 1.3 \cdot 10^{-15}\ cm^2$. *In the right hand side an Arrhenius plot constructed with the values extracted from the maxima of the correlator functions is shown.*

$$a_n = \frac{2\Delta C_0}{T_W} exp(-t_0/\tau_e)(1 - exp(-T_W/\tau_e)) \frac{1/\tau_e}{1/\tau_e^2 + n^2\omega_0^2} \tag{3.17}$$

$$b_n = \frac{2\Delta C_0}{T_W} exp(-t_0/\tau_e)(1 - exp(-T_W/\tau_e)) \frac{n\omega_0}{1/\tau_e^2 + n^2\omega_0^2} \tag{3.18}$$

The emission time constant τ_e can be calculated from the Fourier coefficients:

$$\tau_e(a_n, a_k) = \frac{1}{\omega_0}\sqrt{\frac{a_n - a_k}{k^2 a_k - n^2 a_n}} \tag{3.19}$$

$$\tau_e(b_n, b_k) = \frac{1}{\omega_0}\sqrt{\frac{k b_n - n b_k}{k^2 n b_k - n^2 k b_n}} \tag{3.20}$$

$$\tau_e(a_n, b_n) = \frac{1}{n\omega_0}\frac{b_n}{a_n}. \tag{3.21}$$

Only the ratio of the coefficients is necessary for calculation of the emission time constants, neither the offset C_R nor the amplitude are contributing to the result. Therefore, a temperature dependence of the amplitude or a drift of the reverse capacitance will not influence the evaluation. If the time constant τ_e is known, also the amplitude can be directly calculated from the coefficients

$$\Delta C_0 = b_n \frac{T_W}{2} \frac{exp(t_0/\tau_e)}{1 - exp(-T_W/\tau_e)} \frac{1/\tau_e^2 + n^2\omega_0^2}{n\omega_0}. \tag{3.22}$$

With the known time constant and the temperature each transient contributes to an Arrhenius plot. With this method also the quality of the transients can be evaluated. For an exponential transient the following equations hold for the coefficients:

$$a_2 < a_1 < 4a_2 \tag{3.23}$$

$$b_2/2 < b_1 < 2b_2 \tag{3.24}$$

$$\frac{b_1 a_2}{a_1 b_2} = \frac{1}{2} \tag{3.25}$$

If the transients do not fulfill these equations they are rejected. A low quality factor of the transients might have its reason in more than one emission time constant contributing to the transient. This can happen when more then one level contributes to a DLTS peak. For most of the evaluations done in this work the maxima search method has been used.

3.5.3 Defect concentration

The direct evaluation of the trap concentration from the capacitance transients is influenced by the so-called transition region at the edge of the depleted zone of thickness λ which has to be taken into account. In case of majority carrier traps this transition or λ region influences the evaluation of the concentration. An n-type semiconductor with a shallow doping N_D and a trap concentration N_t of an acceptor level with the energy E_t in the upper half of the bandgap is taken as an example. In Fig. 3.9 the band diagram of an abrupt junction of a p+/n diode under reverse bias directly after the end of a majority carrier filling pulse is shown. The system is not in an equilibrium condition.

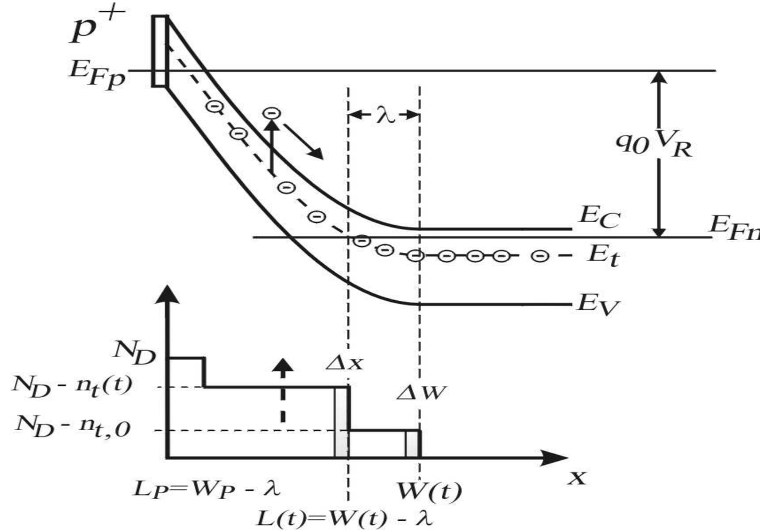

Figure 3.9: Band bending diagram of a p$^+$/n junction under reverse bias (taken from [Mol99]).

The reverse bias causes an energy difference $q_0 V_R$ between the quasi Fermi level at the p$^+$-side and the n-side. And as shown in the lower part of Fig. 3.9 the SCR is divided into two parts. At the outer edge of the region there is a transition between the neutral bulk and the central part of the SCR which is depleted of free carriers. For a defect with an energy level at E_t this gives rise to the transition region with a thickness λ, defined by the crossing point of the trap level and the quasi-Fermi level E_{Fn}. The quasi-Fermi level is assumed to be constant throughout the transition

region and equal to the Fermi level within the neutral bulk. With the assumption $N_t \ll N_D$ and with the help of the Poisson equation it can be shown that

$$\lambda = \sqrt{\frac{2\epsilon\epsilon_0(E_F - E_t)}{q_0^2 N_D}}. \tag{3.26}$$

The filling pulse leads to an occupation with electrons of all defects in the region $x > L_P = W_P - \lambda$. After the end of the filling pulse the electrons in the region $L_P < x < L_t = W_t - \lambda$ will be emitted. The corresponding change in the capacitance signal can be calculated (for details see [Mol99]). These calculations show that the amplitude of the capacitance transient ΔC_0 is proportional to the defect concentration N_t:

$$N_t = -2N_D \frac{\Delta C_0}{C_R} \frac{W_R^2}{L_R^2 - L_P^2} \tag{3.27}$$

From an experimental point of view it is convenient to express the length of the different regions by their corresponding capacitance values

$$N_t = -2N_D \frac{\Delta C_0}{C_R} \left[1 - \left(\frac{C_R}{C_P}\right)^2 - \frac{2\lambda C_R}{\epsilon\epsilon_0 A}\left(1 - \frac{C_P}{C_R}\right)\right]^{-1}. \tag{3.28}$$

This is called the λ-correction, which is done automatically by the evaluation software when calculating the trap concentrations. The position of the trap energy in the bandgap is not known during the measurement, therefore it is calculated assuming a fixed capture cross section for all traps at the corresponding temperature. This can lead to an evaluation error of up to 10 %. To calculate the exact trap concentration, the evaluation has to be repeated with the correct activation energy of the trap. However, quite often the transition region is neglected. In that case the trap concentration can be approximated by

$$N_t \approx 2N_D \frac{|\Delta C_0|}{C_R}. \tag{3.29}$$

3.6 Capture measurements

When measuring the capture time constant it is possible to separate the capture cross section and the entropy factor from equation 3.11. By varying the width of the filling pulse t_p the capture constant can be measured, because the amplitude of the ΔC-transient depends on the width of the filling pulse. If the capture dominates the emission and the trap concentration is small compared to the doping concentration, the concentration of filled traps is given by [Wei91]

$$n_t(t_p) = N_t(1 - exp(-\frac{t_p}{\tau_c})). \tag{3.30}$$

Via the relation $c_n n = 1/\tau_c$ the information about the capture time constant τ_c can be used to calculate the capture coefficient. Comparing this result with the data extracted from the Arrhenius plot (Eq. 3.12 where $c_n = v_{th,n}\sigma_n$) the entropy factor X can be calculated. Capture measurements at different temperatures give rise to the temperature dependence of the capture cross section. This temperature dependence and the calculated entropy factor lead to the enthalpy ΔH of the defect level (see Eq. 3.11). However, the enthalpy and the entropy factor are both temperature-dependant.

3.7 Refolding method

Sometimes a peak in a temperature scan can be caused by two or more defect levels with similar defect parameters. In such cases the exponential quality of the recorded transients is very bad, which is a good indication for a contribution of more than one emission time constant to the measured transients.

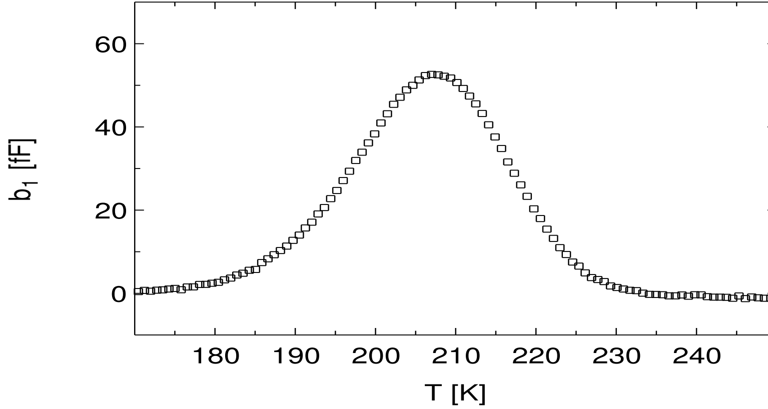

Figure 3.10: *DLTS spectrum of two levels with similar properties. One Level is the* $V_2^{(-/0)}$ *and the second is the* $X^{(-/0)}$.

Fig. 3.10 shows a DLTS spectrum with two defects with similar properties. To extract the defect parameters a high resolution DLTFS measurement (HRDLTS) is needed. This measurement will be called refolding method in the following.

The refolding method needs transients which are measured and weighted with correlator functions at a constant temperature. For this technique, which is called frequency or period scan, a variation of the time window T_W is essential. As an example the equation 3.18 for the coefficients can be rewritten as

$$b_n = 2\Delta C exp(-\frac{T_W}{\tau}\frac{t_0}{T_W})(1 - exp(-\frac{T_W}{\tau}))\frac{2\pi n}{\frac{T_W^2}{\tau^2} + 4n^2\pi^2}. \tag{3.31}$$

With a constant ratio t_0/T_W during the measurement it is possible to calculate the normalized coefficients $b_n(\tau/T_W)$ depending only on the ratio τ/T_W.

The measurement of the frequency scan lead to the discrete coefficients $b_n^d(T_W)$ depending on the time window T_W. For a fixed ratio t_0/T_W the factors f_A and f_τ to transform the coefficient from $b_n(T_W)$ into $b_n(\tau)$ can be calculated numerically by the continuous coefficients 3.31 for the peak maximum of the frequency scan [Sta04].

$$b_n^d(T_W) \rightarrow b_n^d \cdot f_A \cdot (T_W \cdot f_\tau) \rightarrow b_n^d(\tau) \tag{3.32}$$

A minimum time for the capacitance bridge to settle is needed, therefore in case of small time windows it is not possible to keep the ratio t_0/T_W constant. In such a case the factors f_A and f_τ have to be calculated numerically for each T_W. Since

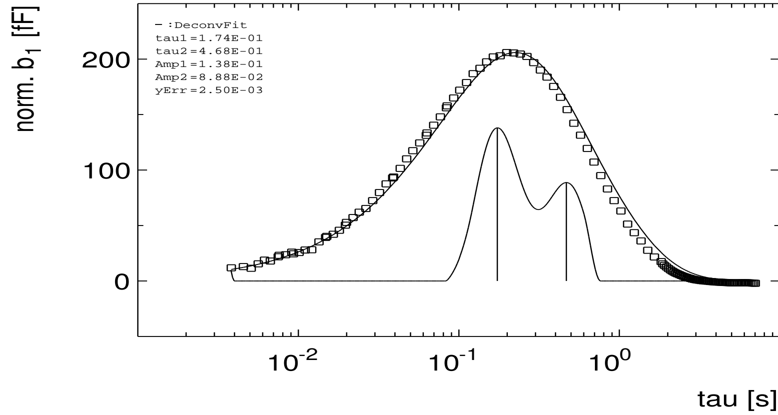

Figure 3.11: *Refolding of the example given in Fig. 3.10. The squares represent the transformed measured data points. The solid line represents the refolded function of the two levels, where the maxima are indicated by vertical lines. The line fitting the transformed data points represents the expected data using the two levels. If this line matches the measured curve, the evaluated levels describe the data.*

the amplitude factor f_A also depends on the time window, the transformation from $b_n^d(T_W)$ to $b_n^d(\tau)$ can lead to a change of the values on the y-axis. Mathematically the transformed measured coefficient functions $b_n^m(\tau)$ are the result of the folding of two functions g(t)=h(t)*f(t). For more information see appendix B. The continuous coefficients $b_n(\tau)$ are the folding function $h(x)$ or in the discrete case h_k. The function $f(t)$, or here $f(\tau)$ is the function of the levels. On the other hand the continuous case $f(\tau)$ would be a sum of Dirac δ-distributions, with a Dirac δ-distribution for each level. To determine the function $f(\tau)$ the transformed measured coefficient function $a_n^m(\tau)$ is refolded with the folding function in this case is the continuous coefficient $b_n(\tau)$. The refolding is done by normalizing the amplitude of the coefficient function and using $x = log(\tau)$ as x-axis.

The continuous function $b_1(\tau)$ has to be put into the discrete form $b_{1,k}^d$ with the number of orders N. In the discrete case the resulting function of the refolding $f(\tau)$ will not be a sum of Dirac δ-distribution, it will be sum of Gauss-distributions. The width of the distribution depends on the number of orders N. The peak width of the level function with the higher order is much smaller. The highest possible number of orders N is limited by the signal-to-noise ratio of the measurement. The normalized b_1 coefficient of the example from Fig. 3.10 is shown as an example in Fig. 3.11.

For a measurement the number of levels contributing to a peak in the DLTS-spectrum should not be more than three, sometimes it is not possible to separate even two levels. The maximum number of levels which can be separated with this method depends also on the difference of their time constants and the difference of their concentrations. The difference in the time constants should be at least a factor of two, and the difference in concentrations should be a maximum factor of ten. The concentration and the activation energy can be evaluated most of the time with an

error less than 15 %, but the error of the capture cross section can be more than an order of magnitude.

3.8 Thermally Stimulated Current (TSC)

The DLTS method is limited to low defect-concentration where $N_t << N_D$. The TSC method is not limited by this requirement and investigation of samples with higher defect-concentrations can be done. Therefore it is a very powerful tool to investigate defects in semiconductors. The TSC method was originally used for investigations on insulators and semiinsulators, but in the late 60's the method has been extended also for semiconductor diodes [Wei68]. In this section a short description of the TSC method will be presented.

3.8.1 Principle of operation

A schematic principle of the TSC method is presented in Fig. 3.12 for an n-type diode cooled down under reverse bias [Fei97]. The measuring procedure can be divided into three steps.

a) Cooling:
The samples are cooled down to low temperatures, where the traps will be filled. The cooling can be done under zero bias or with a reverse bias applied. If the sample is cooled under reverse bias the traps will not be filled with carriers during the cooling. In this case the generation current during the cooling due to the steady state generation current can be monitored. If the cooling is done under zero bias the traps will be filled with majority carriers, if the amount of available carriers is larger than the total concentration of traps.

b) Filling
At the wanted low temperature the filling step is performed. Therefore a forward bias can be applied, or the samples can be illuminated with light on one of the contacts of the diode. If using forward bias to fill the traps, they will be filled with electrons and holes, and the occupation of each trap depends on its individual capture cross sections for electrons and holes at the filling temperature (see section 2.4.4). If using an optical injection the kind of filling depends on the wavelength of the light. If the penetration depth of the laser light is large enough to penetrate through the whole sample, the traps will be filled with both types of carriers. With a penetration depth of only a few microns electrons or holes depending on the side from where the illumination is performed will travel through the depleted volume and fill the traps. If the illumination is done on the n^+-side of the diodes their fully depletion is necessary, such that the holes are caught by the electric field.

c) Recording
After the end of the filling pulse a reverse bias is applied to the diode and a delay time is used to wait for the diode to relax back to a steady state. Afterwards the heating is performed with a constant heating rate β under reverse bias and at spe-

a) Cooling

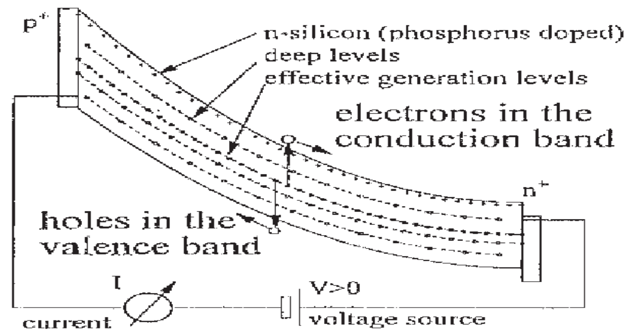

b) Injection

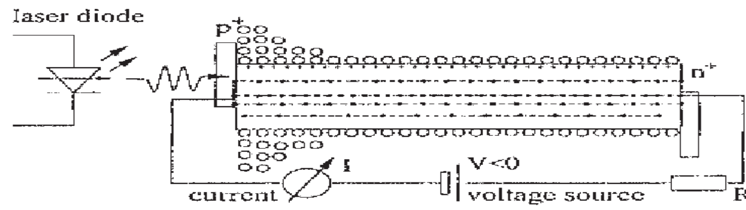

c) Recording

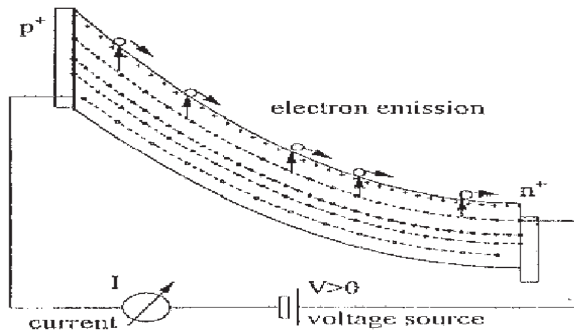

Figure 3.12: *TSC principle: (a) Cooling down under reverse bias, (b) Injection of free carriers at low temperatures and (c) recording of the TSC spectrum (taken from [Fei97]).*

cific temperatures the trapped charges are released, which will cause peaks in the current spectra.

3.8.2 Determination of defect parameters

To determine the defect parameters from the TSC spectra the so-called "initial rise method" was used in this work [Gar48]. In [Mol99] other methods, like the "delayed heating method" or the method of variable heating rate are described.

In case of only one trap and a totaly depleted diode the TSC current is given as a function of temperature T by

$$I_{TSC}(T) = \frac{A \cdot d}{2} \cdot q_0 \cdot e_n(T) \cdot N_t \cdot exp(-\int_{T_0}^{T} \frac{1}{\beta} e_n(T')dT'), \tag{3.33}$$

with A being the area and d the thickness of the diode. The derivation of this equation is also given in [Mol99]. For the "initial rise method" it is of basic importance that with increasing the temperature the traps start to release the charge. With an activation energy E_a large compared to $k_B T$, the integral in the equation 3.33 can be neglected and the increasing part of the TSC peak can be described by

$$I_{TSC}(T) = \frac{A \cdot d}{2} \cdot q_0 \cdot e_n(T) \cdot N_t \approx k \cdot exp(-E_a/kT) \tag{3.34}$$

The emission rate e_n, defined in section 2.4.4, causes the exponential term. It is possible to get an Arrhenius plot by representing $log(I_{TSC})$ versus $f(1/T)$ to evaluate the activation energy from its slope. In Fig. 3.13 a typical example of a TSC spectrum is shown.

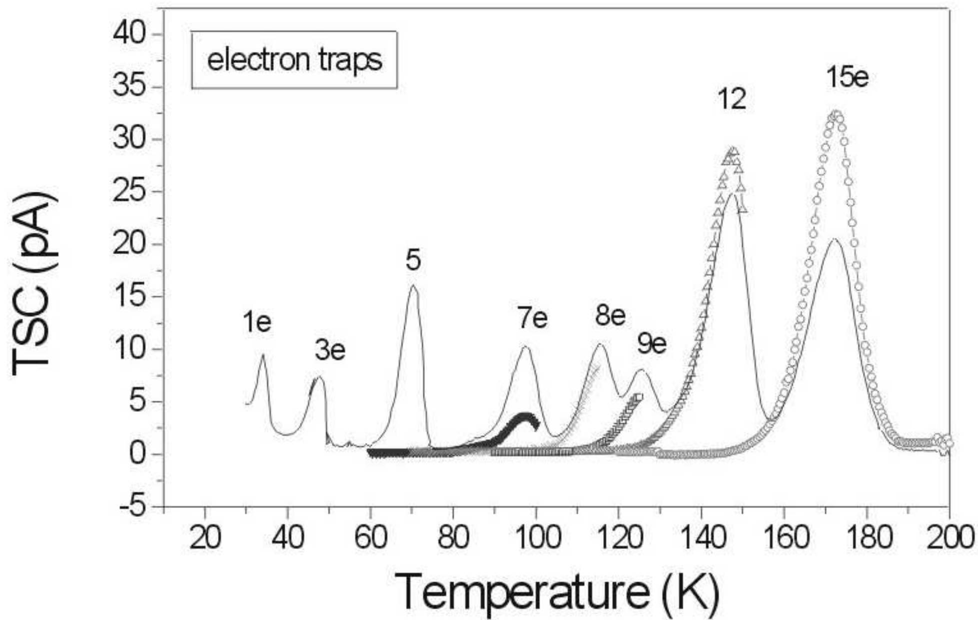

Figure 3.13: *TSC spectrum of a diode after proton irradiation [Pin06c].*

In order to keep the approximation (see Eq. 3.34) valid it is necessary that the measured values which are taken into account for the evaluation start from the beginning of the TSC-peak and should not go further than half of the peak maximum of the increasing part of the current. In case of overlapping peaks like 8e and 9e of Fig. 3.13 it is useful to apply a "thermal cleaning" procedure to correct the estimation of their activation energies. For this procedure the sample is first heated up to a temperature a few degrees higher than the 8e-peak stands for, and then cool back down to this point in order to restart the measurement for the 9e-level. With the knowledge of the activation energy of the 9e-level, it is possible to correct the increasing part of the 8e-peak.

For the evaluation of the defect concentration the TSC equation 3.33 has to be used. This equation considers all possible cases of the trap-evaluation for a diode

with grounded guard ring. The full depletion of the diode is not necessary.

$$I_{TSC} = q_0 A \cdot x(T) \cdot \Gamma(T)/2 \tag{3.35}$$

with the width of the depleted zone

$$x(T) = \sqrt{\frac{2\epsilon_0\epsilon(V + V_{bi}(T))}{q|C(T)|}} \tag{3.36}$$

$$C(T) = N_D - \sum_i n_t^i(T) + \sum_j p_t^j(T) \tag{3.37}$$

$$\Gamma(T) = \sum_i e_n^i(T) n_t^i(T) + \sum_j e_p^j(T) p_t^j(T) \tag{3.38}$$

with n_t^i and p_t^j the density of filled electron (hole) traps

$$n_t^i = N^i exp(-\frac{1}{\beta}\int_{T_0}^{T} e_n^i(T)dT) \tag{3.39}$$

$$p_t^j = P^j exp(-\frac{1}{\beta}\int_{T_0}^{T} e_p^j(T)dT), \tag{3.40}$$

with N^i and P^j as the concentrations of electron and hole traps. These concentrations have to be calculated numerically, by fitting the measured spectra with a set of defect parameters. $|C(T)|$ in equation 3.36 indicates that also the case of type inversion, where the number of acceptor-like traps is larger than the initial doping N_D, is considered. In case of a fully depleted sample $x(T)$ can be set to the thickness of the diode d and the evaluation of the defect concentration is straightforward. When two types of defects an electron and a hole trap have similar defect parameters the calculation of their concentrations is not possible any more. An evaluation is also difficult for complex defect spectra with very deep trapping levels which cannot be detected due to the contribution of reverse current in that temperature range.

To determine the concentration of traps a new method has been developed which will be described in the following [Pin00] [Pin02].

To evaluate the exact trap concentration it is needed that the diodes have different front and rear electrode areas. All p+/n/n+ structures used in this work have a smaller front than rear electrode. With a grounded guard ring the area of the front electrode can be exactly determined. Contribution from surface currents due to the cut edges are avoided in such case. It can be distinguished between three cases:

$$I_{TSC}(T) = q_0 A_f \cdot x(T) \cdot \Gamma(T)/2 \qquad if \quad C(T) \geq 0 \; and \; x_n(T) < d \tag{3.41}$$

$$I_{TSC}(T) = q_0 F A_f \cdot x(T) \cdot \Gamma(T)/2 \qquad if \quad C(T) < 0 \; and \; x_n(T) < d \tag{3.42}$$

$$I_{TSC}(T) = q A_f d \cdot \Gamma(T)/2 \qquad if \quad x_n(T) \geq d \tag{3.43}$$

$$with \qquad C(T) = N_D + M - \sum_i n_t^i(T) + \sum_j p_t^i(T) \tag{3.44}$$

where A_f is the area of the front electrode and A_r is the area of the rear electrode; $F = A_r/A_f$; M is the concentration of very deep traps which remain charged during

the TSC measurement. M is determined by fitting the TSC spectra, and can either be positive or negative.

These three equations cover all possible cases. The first equation 3.41 describes a non inverted partially depleted detector. The second equation 3.42 is used in case of a partially depleted type inverted detector, and the third equation 3.43 describes a fully depleted detector. In this case it does not matter, if the sample is type inverted or not, because of the grounded guard ring, which assures the same active volume of the sample. In case of change of the sign of the space charge region of a partially depleted detector during the temperature scan, a discontinuity in the TSC spectra can be observed, because the electrode area is changed, due to the different size of the front and rear electrode. A discontinuity in the spectra also occurs, if the fully depleted diode becomes partially depleted. For an accurate evaluation the TSC scan should be measured with different reverse bias, to see the depletion behavior of the diode.

3.9 The DLTS and TSC set-up

3.9.1 The cryostat system

A closed cycle two-stage helium refrigerator from CTI-Cryogenics (Model 22C, operated at 50 Hz) was used for the DLTS and TSC measurements in a temperature range between 20 K and 300 K. A detailed description of the set-up can be found in [Mol99]. Compared with that set-up [Mol99] the horizontal holder is exchanged by a vertical holder, which allows optical injections on both sides of the sample without dismounting and gluing the diodes. A picture of the vertical holder inside the cryostat is shown in Fig. 3.14.

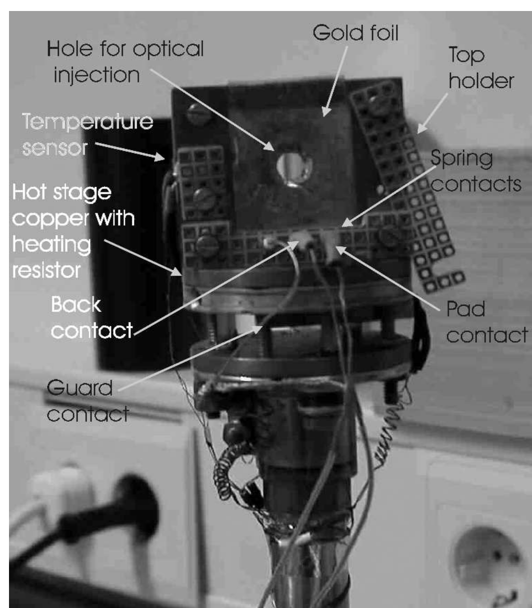

Figure 3.14: *Photo of the hot stage of the cold station inside the cryostat. (taken from [Sta04])*

The samples are glued with conductive silver glue on an Al_2O_3 ceramic with a 3 mm hole in the middle for optical injection from the rear side. The contacts on the ceramic are made via thin gold layers. The ceramics are then mounted on a copper block on top of the cold stage. The connection to the measuring system is done via contact pins which are pressed with a spring on the gold layers. The temperature sensor is mounted directly beside the ceramic for an accurate temperature measurement. The optical injection can be done from the outside through the windows. For this purpose the holder has a 4 mm hole in the middle to let the light pass. The lasers are mounted on x-y tables for adjusting the optical injection.

3.9.2 The electrical set-up

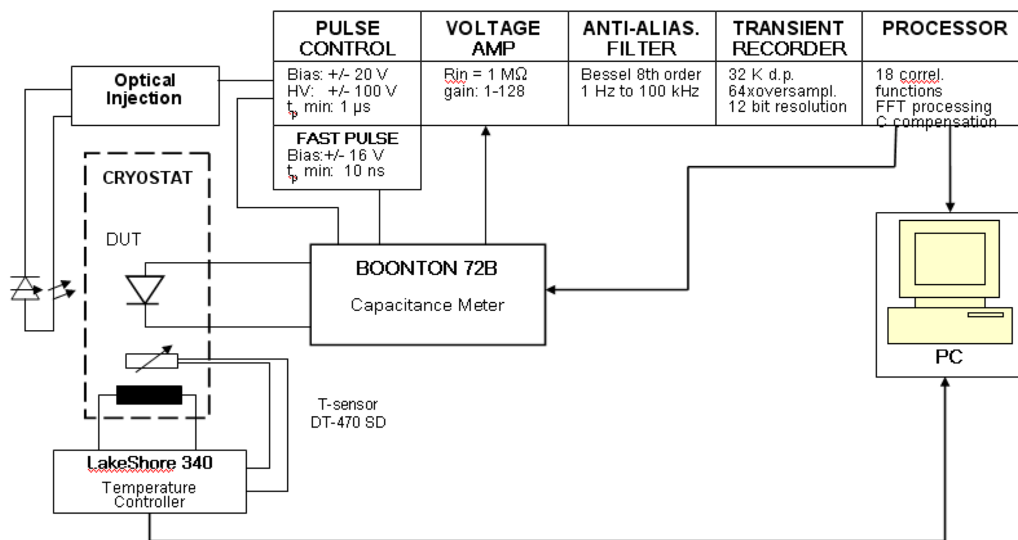

Figure 3.15: *Electrical setup for DLTS measurements (modified after [Sta04]).*

In Fig. 3.15 the schematic view of the electrical set-up of the DLTS system is shown. A Cryogenic compressor 8200 is used for the cooling, while the temperature is controlled by a Lakeshore 340 temperature controller, which is connected to a temperature sensor DT-470 and to two heating resistors with a maximum heating power of 30 Watts. Cooling down the samples to a temperature of 30 K takes about 90 minutes. The measuring system consists out of a capacitance meter, a Boonton bridge 72B working with a 100 mV - 1 MHz signal and a data acquisition system. A PC with a Windows based software is used to store and analyze the data and to perform simulations. This equipment was delivered by the company Phystech at Moosburg [PHYS]. The maximum reverse bias output of the normal hardware is 20 V but it can be increased up to 100 V by an additional amplifier.

The shortest possible filling pulse width that can be generated by the DLTS hardware is $1\,\mu s$. To generate pulses down to $10\,ns$ a fast pulse generator HP 8110A is included in the system. But the fast pulse generator and the high voltage option cannot be used in parallel.

The analogue voltage output of the capacitance meter is connected via a variable gain amplifier to an anti-aliasing filter. Finally the signal is digitized (12 bit ADC) by a transient recorder and stored in a computer system. More information about the hardware and the software can be found in [Wei91].

Chapter 4

Microscopic Investigations - Particle Dependence of Radiation Induced Defects

Only point defects can be observed after ^{60}Co-γ irradiation, while after hadron or electron irradiation also cluster related defects are induced. Irradiation with different particles and energies lead to different introduction rates of defects. Clusters are not stable at room temperature. Therefore, it is difficult to exactly compare irradiations with different particles. Already during the irradiation the annealing of the clusters starts. While the duration of the irradiation is different for different particles also the status of annealing of clusters will already be different at the end of the irradiation. After irradiation the samples have to be kept cold to avoid further annealing effects. Most often also this is not possible, because some time is needed until the activity of the samples has decreased to a level that a handling of them can be done safely.

Annealing can also affect other defects like the carbon interstitial defect (C_i). It's annealing influences the concentration of other detectable defects directly, which will be explained later in this chapter and shown in detail in chapter 6. These effects have to be taken into account when comparing the formation of defects by irradiation.

To exclude problems caused by different material properties, e.g. different P-doping or oxygen concentration, six detectors made of the same material, namely epi-50 diodes of 50 μm active thickness and a resistivity of 50 Ωcm were irradiated with ^{60}Co-γ's, 6 MeV electrons, 900 MeV electrons, 26 MeV protons, 23 GeV protons and reactor neutrons at facilities specified in section 3.2. In same cases the typical error of the fluence determination has been given in that section. In other cases such values were not given by the facilities and therefore estimated to be of about 10%.

In this chapter DLTS measurements of these six detectors after irradiation with fluences in the range of $5.5 \cdot 10^{11}$ - $2.9 \cdot 10^{12}$cm^{-2} equivalent to 1 MeV neutron fluences are presented. Temperatures given for the position of defect associated peaks imply DLTS-spectra (sometimes also called tempscans) taken with a time window of T$_W$= 200 ms. First an overview of the results after different irradiation will be given and afterwards these results and the mechanisms responsible for their formation will be discussed. The reproducibility of the results have shown that the error of the concentration measurement is about 10%. The parameters of the defects

detected in this and the following chapters are summarized in appendix D.

4.1 ^{60}Co-γ irradiation

For the investigation after ^{60}Co-γ-irradiation an epi-50-diode which was irradiated with a dose of 200 kGy was chosen. In Fig. 4.1 the DLTS-spectra after electron

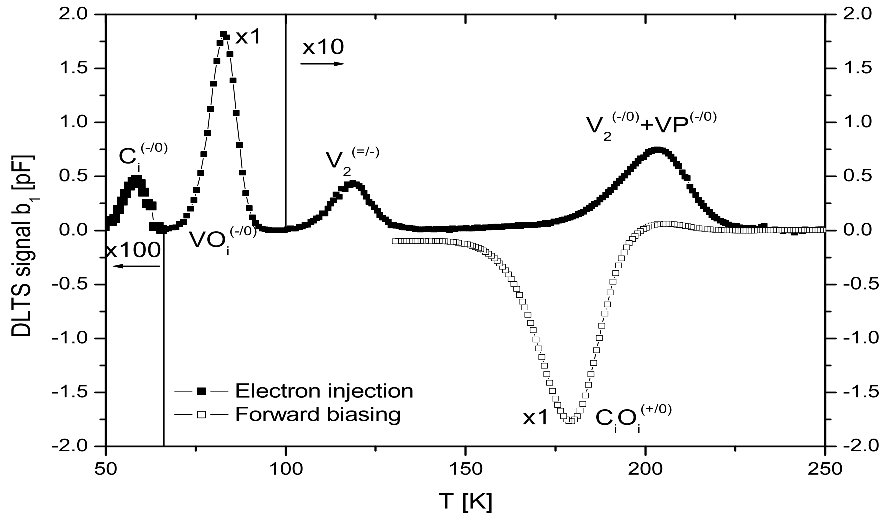

Figure 4.1: *DLTS spectra after electron injection (filled squares) and forward biasing (open squares) of an epi-50-diode irradiated with a fluence of* $\Phi_{eq} = 1.9 \cdot 10^{12}$ cm^{-2} *(^{60}Co-γ-dose of 200 kGy). Measurement:* $U_R = -20$ V, $U_{P,e} = -0.1$ V, $U_{P,f} = 3$ V, $t_P = 100$ ms, $T_W = 200$ ms.

injection and forward biasing are shown. While the spectrum for forward biasing is shown as measured the spectrum after electron injection is scaled by a factor of ten for a better visibility in the temperature range higher than 100 K and by a factor of 100 below 65 K.

Five major peaks are visible in the spectra after ^{60}Co-γ-irradiation, shown in Fig. 4.1. The main trap detected after electron injection is attributed to the $VO_i^{(-/0)}$-defect, also known as the A-center. This defect is the dominant vacancy related defect. The signal from the VO_i is overlapped by the $C_iC_s{}^{(-/0)}$-defect. But its concentration is to small to be measurable (less than 5 % of the whole signal at 84 K).

Nevertheless a small contribution can be expected because the peak associated with the C_i-defect is visible in the spectrum at 58 K. This defect is formed via the *Watkins Replacement Mechanism* by an interstitial silicon atom replacing a substitutional carbon atom at its lattice side (I + C_s → Si + C_i). Most of these carbon-interstitials as well as most of the vacancies are trapped by oxygen interstitials (O_i) forming the $VO_i^{(-/0)}$-defect and the $C_iO_i{}^{(+/0)}$-defect which is associated with the hole-peak at 179 K. It has to be mentioned that the superposition of the $VO_i^{(-/0)}$-and the C_iC_s-defect cannot be resolved by high resolution DLTS technique, since both activation energies and capture cross sections are nearly identical. A known bi-stability of the C_iC_s-defect can in principle be used to separate them within a

capture measurements. This is limited to a minimum concentration of about 5% of the total concentration of the superposition. Hence the C_iC_s-concentration is smaller then 5% of the concentration attributed to the peak at 84 K.

At temperatures higher then 100 K two peaks are shown in Fig. 4.1 after electron injection. These peaks are attributed to the two charged states of the divacancy (V_2) at 118 K ($V_2^{(=/-)}$) and at 204 K ($V_2^{(-/0)}$) which are both well known. Due to the high phosphorus concentration of the epi-50 samples an additional defect containing vacancies becomes detectable. The vacancies and the phosphorus atoms can form the VP-defect which is also known as the E-center. The peak caused by the singly charged divacancy-defect is overlapped by the VP-defect. The E-center also causes the difference in the peak-hight compared with that of the $V_2^{(=/-)}$-defect, because a 1:1 ratio of these two charged states of the divacancy is expected after ^{60}Co-γ-irradiation.

An also expected peak associated with the hole-trap of the carbon interstitial the $C_i{}^{(+/0)}$-defect is not detectable after forward injection. This state of the C_i-defect can not be seen after any of the irradiation experiments presented in this chapter. This effect is first related to the very small concentration of the C_i-defect and second to the much smaller capture rate of the $C_i^{(+/0)}$ for holes compared with the capture rate of the $C_i^{(-/0)}$ for electrons.

Defect	$VO_i^{(-/0)}$+$C_iC_s{}^{(-/0)}$	$C_i{}^{(-/0)}$	$V_2{}^{(=/-)}$	$V_2{}^{(-/0)}$+VP	VP	$C_iO_i{}^{(+/0)}$
IR [1/cm]	6.4	0.02	0.14	0.25	0.11	5.3

Table 4.1: Introduction rates (IR) after ^{60}Co-γ irradiation.

An introduction rate (IR) is introduced to get comparable information about the relation between the defect-concentration and the achieved dose (or fluence). The IR is defined by the ratio of the defect-concentration and the equivalent fluence Φ_{eq}.

For the calculation of Φ_{eq} the dose of the ^{60}Co-γ-irradiation is normalized to an irradiation with 1 MeV neutrons, which can be done with respect to NIEL (see section 2.2). These introduction rates for the detectable defects after ^{60}Co-γ-irradiation are given in Tab. 4.1.

Vacancies and interstitials are always generated in parallel. Therefore a 1:1 ratio of vacancies and interstitials trapped in defects can be expected. A presentation and discussion of these ratios after different irradiation is given at the end of this chapter.

4.2 6 MeV electron irradiation

In this section the damage caused by 6 MeV electrons is presented. An electron fluence of about $\Phi_{eq} = 2.9 \cdot 10^{12}$ cm^{-2} has been achieved. Because of the short time period between irradiation and DLTS measurement it can be expected that annealing effects have not taken place and the investigated sample can be called *as irradiated*.

The spectra after electron injection and forward biasing are shown in Fig. 4.2. Although the introduction rate of the C_i-defect is about double of that after ^{60}Co-

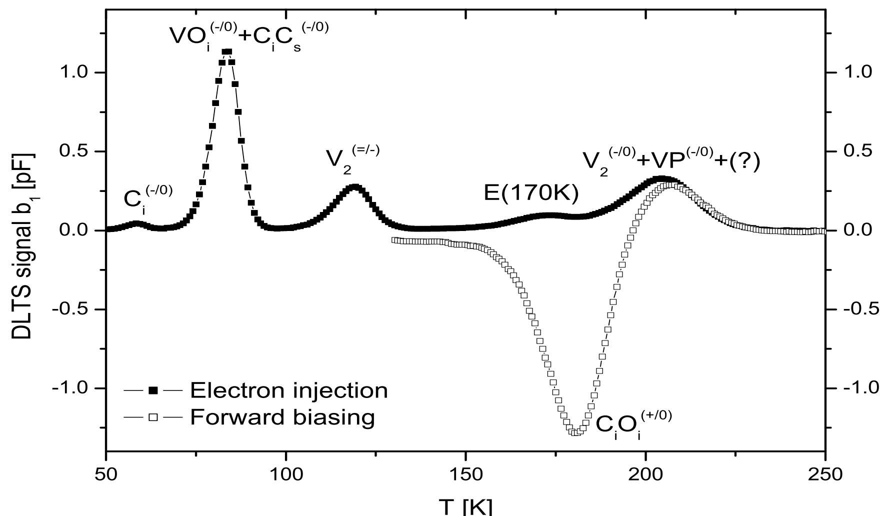

Figure 4.2: *DLTS spectra after electron injection (filled squares) and forward biasing (open squares) of a epi-50-diode irradiated with a fluence of* $\Phi_{eq} = 2.9 \cdot 10^{12}\ cm^{-2}$ *(6 MeV electrons). Measurement:* $U_R = -20\ V$, $U_{P,e} = -0.1\ V$, $U_{P,f} = 3\ V$, $t_P = 100\ ms$, $T_W = 200\ ms$.

γ-irradiation it is still quite small. The formation of this defect is similar to the process after ^{60}Co-γ-irradiation.

The C_i is mainly captured by neighboring O_i forming the C_iO_i-defect while the C_iC_s-defect is not detectable. Therefore at least a minimum of about 95 % of the introduction rate of the superposition of the $VO_i^{(-/0)}$- and the $C_iC_s{}^{(-/0)}$-defect at 84 K can be attributed to the $VO_i^{(-/0)}$-defect.

The ratio of the VO_i- and V_2-concentration is much smaller than after ^{60}Co-γ-irradiation. This is an indication for a direct generation of V_2. In parallel the observation of a much smaller introduction rate of the main interstitial related defect, the C_iO_i-defect also supports this assumption. The direct formation of the V_2-defect is a good evidence to suggest that also di-interstials (I_2) should have been formed. The I_2 can form the I_2O complex which can be measured with infrared absorbtion measurements (IR) [Mur07, Dav06]. By contrast this defect can not be measured with DLTS.

From the results of the experiments after ^{60}Co-γ-irradiation one can estimate a ratio for single-vacancies (SV-ratio) forming the VO_i-defect or the VP-defect in epi-50-diodes. If one assume that the probability for single vacancies to form the VO_i-defect or the VP-defect is in principle the same after different irradiations of the same material one can roughly estimate the introduction rates of the VP-defect not only after irradiation with 6 MeV electrons but also after 900 MeV electrons, 26 MeV protons, 23 GeV protons or reactor neutrons from the SV-ratio. This estimation leads to a VP concentration of about 2% of the VO_i-concentration after 6 MeV electron irradiation. This value is also a good estimation for the investigations after other particle irradiations to come later in this chapter.

The divacancies have been generated mainly direct by 6 MeV electron irradiation.

An overview of all introduction rates after 6 MeV electron irradiation is given in Tab. 4.2.

Defect	$VO_i^{(-/0)}$+$C_iC_s{}^{(-/0)}$	$C_i{}^{(-/0)}$	$V_2{}^{(=/-)}$	$V_2{}^{(-/0)}$+VP+(?)	E(170K)	$C_iO_i{}^{(+/0)}$
IR [1/cm]	2.06	0.084	0.49	0.65	0.16	2.17

Table 4.2: Introduction rates (IR) after 6 MeV electron irradiation.

The differences extracted from peaks attributed to the $V_2{}^{(-/0)}$ and the $V_2{}^{(=/-)}$ can not only be explained by the VP-defect. It is more likely due to a small clustering effect for which the reduction of the DLTS-signal of the $V_2{}^{(=/-)}$ compared with the one of the $V_2{}^{(-/0)}$ is a typical observation. This cluster effect will be discussed later.

A second observation directly made from the spectrum is the presence of a defect labeled E(170K) which is often also attributed to clusters.

4.3 900 MeV electron irradiation

In Fig. 4.3 the DLTS-spectra after electron injection and forward biasing of an epi-50-diode irradiated with 900 MeV electrons with a fluence of $\Phi_{eq} = 1.9 \cdot 10^{12}$ cm^{-2} are shown. The diode was stored in a freezer at a temperature of -28°C for about one year before taking the DLTS spectra. This can be a reason for a reduction of

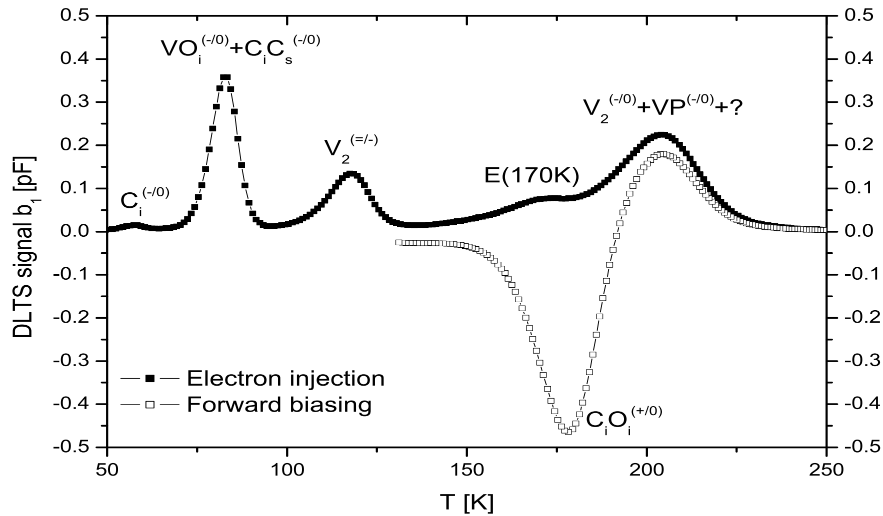

Figure 4.3: *DLTS spectra after electron injection (filled squares) and forward biasing(open squares) of an epi-50-diode irradiated with a fluence of* $\Phi_{eq} = 1.9 \cdot 10^{12}$ cm^{-2} *(900 MeV electrons). Measurement:* $U_R = -20\ V$, $U_{P,e} = -0.1\ V$, $U_{P,f} = 3\ V$, $t_P = 100\ ms$, $T_W = 200\ ms$.

the C_i-defect by a factor of 2 compared with the epi-50-diode irradiated with 6 MeV electrons. Most of the interstitial carbon is captured by O_i forming the only visible hole-trap, the C_iO_i-defect.

The dominant vacancy related defect is the VO_i-defect which causes more than 95 % of the peak at 84 K because the C_iC_s-defect is not detectable.

The peak at 204 K is mainly caused by the singly charged divacancy and a small contribution of the VP-defect as mentioned above. The broadening of this peak is caused by the clustering effect.

The introduction rate of the doubly charged divacancy is only about two third of the one for the singly charged divacancy. The suppression of the peak associated with the ${V_2}^{(=/-)}$-defect is also a well known clustering effect. The stronger suppression compared with the 6 MeV irradiation coincides with a higher introduction rate of the E(170K)-defect.

Single vacancies and interstials are mobile at room temperature, therefore point defects are distributed homogeneously inside the bulk of the diodes. In case of irradiation with high energy particles high energy PKA's are generated. These PKA's lead to a defect cascade and at their end disordered regions are created. The density of defects is very high inside of these disordered regions, even localized amorphous zones might be produced. Most of the generated divacancies are located in these highly damaged regions. Thus the creation of V_2-centers occurs in those lattice regions where a large strain due to the high damage density can be found. As a result of the relative strength of this strain, the amplitude of the peak caused by ${V_2}^{(=/-)}$ decreases [Sve91]. The lattice strain in the disordered regions prevents to a large extent the reorientation of the divacancies and therefore, it is difficult to fill the defect with two electrons. An increase in the rate of elastic energy deposition is supporting this effect [Jag93].

In addition also the ${V_2}^{(-/0)}$-peak is affected by the lattice strain. The increase in peak width compared with the width after γ-irradiation occurs simultaneously with the relative decrease in the amplitude of $V_2^{(=/-)}$. This is interpreted as a broadening of the well defined energy position associated with the isolated V_2-centers. In contrast to the peak caused by the doubly charged divacancy, the peak height of the singly charged divacancy is independent of the rate of elastic energy deposition [Sve97].

It is even suggested that the peak at 204 K is due to an exponential density distribution of energy states caused by lattice deformations [Kuh01]. The additional levels contributing to the ${V_2}^{(-/0)}$-peak are therefore labeled with a question mark.

The introduction rates of all defects detectable by the DLTS-method after 900 MeV electron irradiation are given in Tab. 4.3.

Defect	$VO_i^{(-/0)}+C_iC_s{}^{(-/0)}$	${C_i}^{(-/0)}$	${V_2}^{(=/-)}$	${V_2}^{(-/0)}+VP+?$	E(170K)	$C_iO_i{}^{(+/0)}$
IR [1/cm]	1.11	0.04	0.40	0.65	0.20	1.4

Table 4.3: Introduction rates (IR) after 900 MeV electron irradiation.

4.4 26 MeV proton irradiation

In this experiment an epi-50-diode has been irradiated with 26 MeV protons with a fluence of $\Phi_{eq} = 8.1 \cdot 10^{11}$ cm^{-1}. Afterwards the sample has been stored at -28°C. A small C_i introduction rate can be extracted from the DLTS spectra shown in Fig. 4.4. Nevertheless most of the generated C_i's are trapped by O_i's in order to form the C_iO_i-defect. By contrast the C_iC_s-defect is not detectable. Therefore almost all measured interstitials are related to the C_iO_i-defect, which is also the only hole trap visible in the DLTS-spectra in Fig. 4.4.

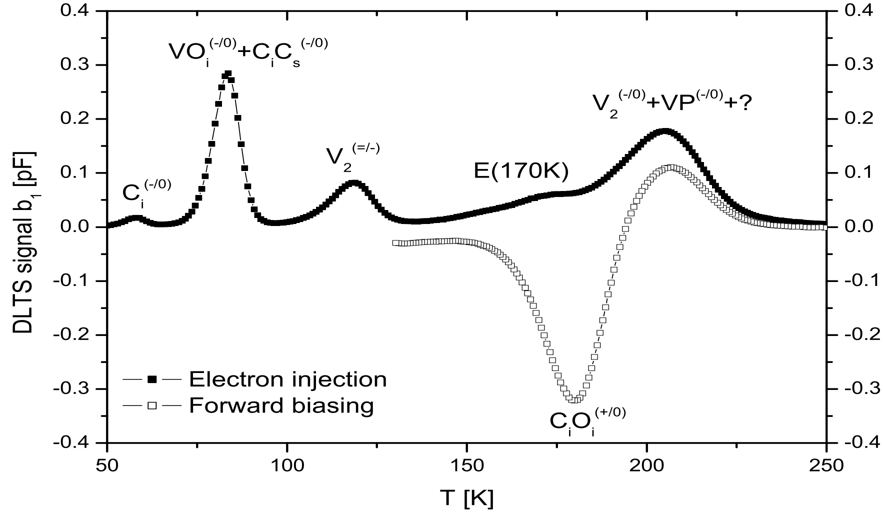

Figure 4.4: *DLTS spectra after electron injection (filled squares) and forward biasing (open squares) of an epi-50-diode irradiated with a fluence of* $\Phi_{eq} = 8.1 \cdot 10^{11} cm^{-2}$ *(26 MeV protons). Measurement:* $U_R = -20\ V$, $U_{P,e} = -0.1\ V$, $U_{P,f} = 3\ V$, $t_P = 100\ ms$, $T_W = 200\ ms$.

The VO_i-defect is the main vacancy related defect whose introduction rate is about 85 % of the one extracted for the C_iO_i-defect. Although the VO_i-defect is the vacancy related defect with the highest introduction rate more vacancies are forming the V_2-defect correlated with the peak at 204 K in the DLTS-spectra.

The overlap from the VP-defect is only about 2 % calculated with the SV-ratio introduced in section 4.1.

The introduction rate for the $V_2{}^{(=/-)}$-defect is about 45 % of the introduction rate of the $V_2{}^{(-/0)}$-defect. This is a substantial argument for the explanation of a larger clustering effect compared to the irradiations described above.

A second observation which is made in case of the clustering effect of the divacancy is the observability of the E(170K)-defect, which can be separated from the divacancy related peak and is often labeled as the shoulder peak of the divacancy.

Defect	$VO_i^{(-/0)}+C_iC_s{}^{(-/0)}$	$C_i{}^{(-/0)}$	$V_2{}^{(=/-)}$	$V_2{}^{(-/0)}+VP+?$	E(170K)	$C_iO_i{}^{(+/0)}$
IR [1/cm]	1.59	0.09	0.45	1.00	0.31	1.81

Table 4.4: Introduction rates (IR) after 26 MeV proton irradiation.

All corresponding introduction rates extracted from the DLTS-spectra in Fig. 4.4 are summarized in Tab. 4.4.

4.5 23 GeV proton irradiation

Also with high energy protons an epi-50-diode was irradiated. The fluence of 23 GeV protons is about $\Phi_{eq} = 8.2 \cdot 10^{11}$ cm^{-2}. It was possible to store the sample after a delay time of about 30 minutes at room temperature in a freezer at about -20°C. Therefore it should have been possible to prevent the sample from annealing.

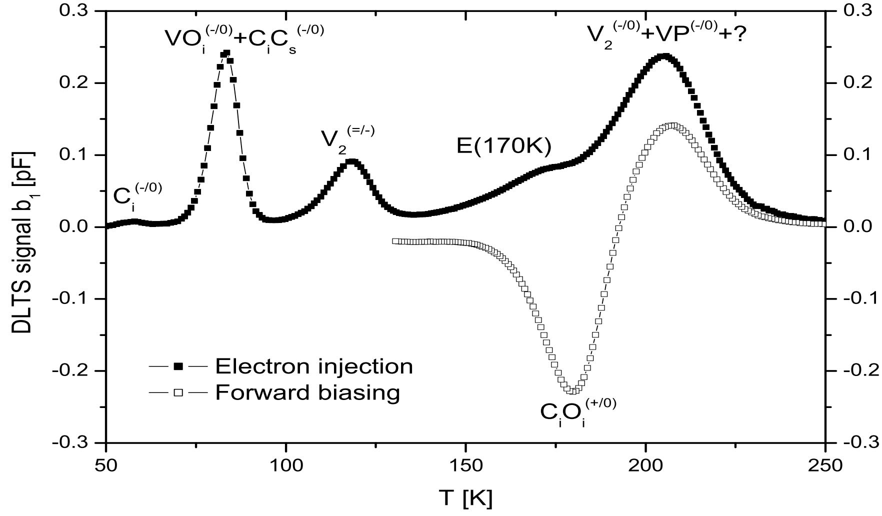

Figure 4.5: *DLTS spectra after electron injection (filled squares) and forward biasing (open squares) of an epi-50-diode irradiated with a fluence of* $\Phi_{eq} = 8.2 \cdot 10^{11}\ cm^{-2}$ *(23 GeV protons). Measurement:* $U_R = -20\ V$, $U_{P,e} = -0.1\ V$, $U_{P,f} = 3\ V$, $t_P = 100\ ms$, $T_W = 200\ ms$.

The DLTS-spectra of this epi-50-diode after electron injection and forward biasing are shown in Fig. 4.5. The dominant and only hole trap visible after forward biasing is the C_iO_i-defect.

With almost the same introduction rate the VO_i-defect is the main vacancy related defect. An overlap with the C_iC_s-defect was not detectable, therefore the peak seen in the DLTS-spectrum for electron injection in Fig. 4.5 is only due to electron emission from the $VO_i^{(-/0)}$-defect and only a small contribution (below 5%) from the $C_iC_s{}^{(-/0)}$-defect could be possible.

A similar introduction rate as for the VO_i-defect is detectable for the divacancy related peak at 204 K. As already mentioned earlier in this chapter about 2 % of the introduction rate of the VO_i-defect can be estimated for the VP-defect whose DLTS signal is overlapping the signal from the $V_2^{(-/0)}$-defect.

The ratio between the introduction rates extracted from the singly charged and the doubly charged divacancy peaks is about 3:1. This is a higher ratio than measured in the experiments shown before and well known as the suppression of the V_2-defect associated with the cluster effect.

Also the higher introduction rate of the E(170K)-defect can be related to the stronger cluster effect after 23 GeV proton irradiation.

Defect	$VO_i^{(-/0)}$+$C_iC_s{}^{(-/0)}$	$C_i{}^{(-/0)}$	$V_2{}^{(=/-)}$	$V_2{}^{(-/0)}$+VP+?	E(170K)	$C_iO_i{}^{(+/0)}$
IR [1/cm]	1.53	0.05	0.55	1.50	0.45	1.48

Table 4.5: Introduction rates (IR) after 23 GeV proton irradiation.

All introduction rates taken from the DLTS-spectra are shown in Tab. 4.5.

4.6 Reactor neutron irradiation

In this section the results taken from the DLTS-spectra of an epi-50-diode irradiated with reactor neutrons are presented. The fluence is of about $\Phi_{eq} = 5.5 \cdot 10^{11}$ cm^{-2}. In Fig. 4.6 the DLTS-spectra for electron- and hole-emission are shown.

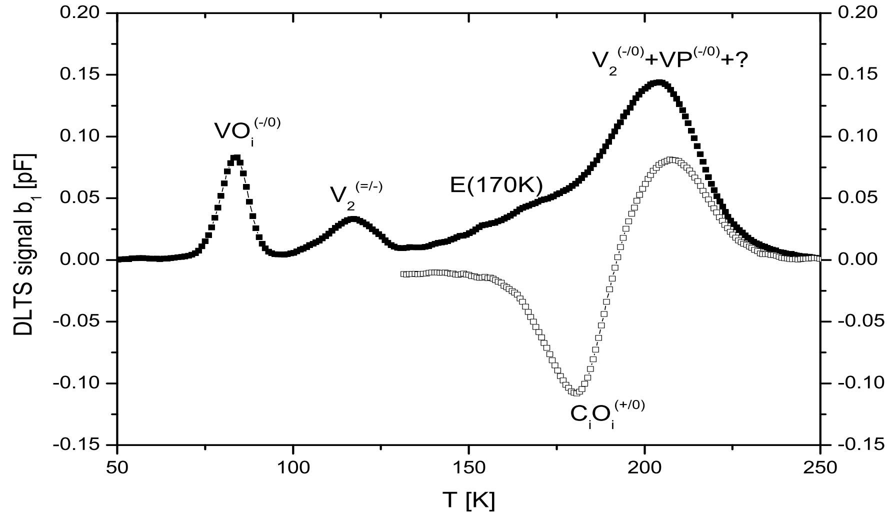

Figure 4.6: *DLTS spectra after electron injection (filled squares) and forward biasing (open squares) of an epi-50-diode irradiated with a fluence of* $\Phi_{eq} = 5.5 \cdot 10^{11}$ cm^{-2} *(reactor neutrons). Measurement:* $U_R = -20$ V, $U_{P,e} = -0.1$ V, $U_{P,f} = 3$ V, $t_P = 100$ ms, $T_W = 200$ ms.

After neutron irradiation the main damage is expected to be due to the clustering effect. If more vacancies and maybe interstitials are trapped in the clustered regions less can be detected in the introduction rates of the corresponding point defects. Compared to the damage mechanism of irradiations with charged particles the irradiation with neutrons is different. While for charged particles coulomb and nuclear interaction dominate the damage mechanism for neutron irradiation it is dominated only by nuclear interaction. Coulomb interaction can also cause small energy transfers to the silicon lattice which can end in the production of point defects. This is not possible for nuclear interaction. Therefore after neutron irradiation single vacancies and single interstitials have to escape from the clustered regions in order to form point defects.

The two cluster related defects, the divacancy and the E(170K)-defect show very similar introduction rates compared to the ones after irradiation with 23 GeV protons. This is an expected result because in both cases the generation of the defects in cluster regions are dominated by nuclear interaction.

The ${V_2}^{(=/-)}$ is even more suppressed compared to the ${V_2}^{(-/0)}$ than it has been observed after 23 GeV proton irradiation. This effect can be explained by the higher density of defects in clustered regions and therefore by stronger corresponding clustering effects.

Due to the much smaller coulomb interaction possible after neutron irradiation (only secondary processes are possible) the generation of point defects like the VO_i-

and the C_iO_i-defect is reduced by about one third compared to the results after irradiation with 23 GeV protons.

Defect	$VO_i^{(-/0)}+C_iC_s{}^{(-/0)}$	$C_i{}^{(-/0)}$	$V_2{}^{(=/-)}$	$V_2{}^{(-/0)}+VP$	E(170K)	$C_iO_i{}^{(+/0)}$
IR [1/cm]	0.86		0.31	1.37	0.45	1.02

Table 4.6: Introduction rates (IR) after reactor neutron irradiation.

Unfortunately the time between irradiation and measurement was quite long. Although the sample was stored at about -28°C the C_i-defect is not detectable anymore. It is already annealed out. But due to its small introduction rate expected from the measurements after all other irradiations this annealing should not have a strong influence on the measured carbon related introduction rates.

The only detectable hole trap after forward injection is the C_iO_i-defect. This defect is also the only detectable interstitial related defect because a contribution of the C_iC_s-defect to the peak at 84 K is not seen. In Tab. 4.6 an overview of the measured introduction rates after neutron irradiation is given.

4.7 Comparison

It is very instructive to compare the introduction rates of specific defects with each other to understand the differences between the damage mechanisms after irradiation with different kind of particles. Beside this understanding a basic problem in comparing different particle irradiations is the knowledge of a scaling factor between the particle-fluences. In this work the NIEL scaling hypothesis and the hardness factors given in Tab. 2.1 are used.

Another scaling method based on the use of hardness factors extracted from a comparison of the current related damage constant α [Mol99] is unfortunately misleading because it takes only those defects into account which are related to current generating defect centers. Therefore the fluence calculation via the α-value is only reliable in case of irradiations where cluster related defects are dominant. This is for example the case after neutron or high energy proton irradiation. If the ratio of defect-centers responsible for the generation of current and other defects is changing due to different recoil energy of the PKA's this method would dramatically underestimate the damage effects caused by low energy particles. Because in such cases the damage is more dominated by shallower point defects, like the VO_i, which are not responsible for generation of current.

4.7.1 The A-center (VO_i)

The main vacancy related damage after ^{60}Co-γ-irradiation detectable with the DLTS-method is caused by the $VO_i^{(-/0)}$-defect also known as the A-center. In Fig. 4.7 an overview of the introduction rates of the $VO_i^{(-/0)}$-defect after all six different irradiations is given. Although the peak at 84 K is caused by an overlap of the $VO_i^{(-/0)}$- and the $C_iC_s{}^{(-/0)}$-defect almost 100 % of the measured defect concentration can be attributed to the $VO_i^{(-/0)}$-defect. In case of ^{60}Co-γ-irradiation the energy of the primarily produced electrons (1 MeV) is sufficient to create vacancies and interstitials.

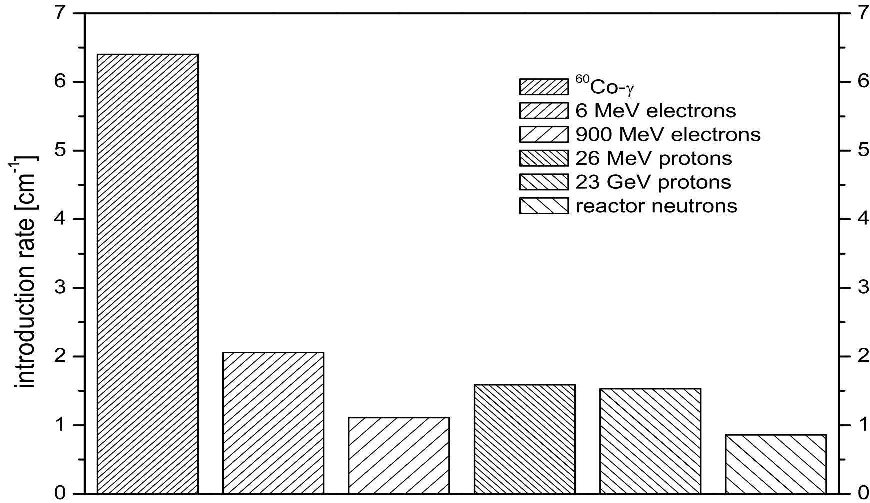

Figure 4.7: *Introduction rates of the $VO_i^{(-/0)}$ ($+C_iC_s^{(-/0)}$)-defect after irradiation with different kind of particles.*

In case of the used epi-50-diodes the oxygen concentration is high enough for a very high probability of a combination of an oxygen interstitial with a single vacancy forming the VO_i-defect. Because of its much smaller concentration pairing of a single vacancy with a phosphorus atom or even with a second radiation induced vacancy is much more unlikely.

Due to the high oxygen concentration and the low fluence also higher order complexes like the V_2O-defect are suppressed. With increasing energy of the impinging particle the introduction rate of the single vacancy related $VO_i^{(-/0)}$-defect is decreasing dramatically.

When irradiating with 6 MeV electrons the energy of the PKA becomes high enough to knock out secondary atoms quite often. But this effect does not introduce more single vacancies because it is very likely that the second vacancy is produced close to the first one. Therefore divacancies are directly generated [Cor65]. Their behavior is different from that of the single vacancies because they are not mobile at room temperature. This effect becomes even more dominant when irradiating with even higher energy particles. It results in a decrease of the VO_i-introduction rate.

In case of irradiation with 900 MeV electrons a limited knowledge of the corresponding hardness-factor for the fluence-calculation could be the reason for the quite small introduction rate compared with those after irradiation with 26 MeV protons, 23 GeV protons and reactor neutrons.

4.7.2 The divacancy (V_2)

As mentioned before, the main damage measurable after ^{60}Co-γ-irradiation is due to introduced point defects. These point defects have their origin in primarily generated interstitials and vacancies. Single vacancies and interstials are mobile at room temperature, therefore defects formed by them are distributed homogeneously inside the bulk of the diodes.

In case of irradiation with high energy particles high energy PKA's are generated.

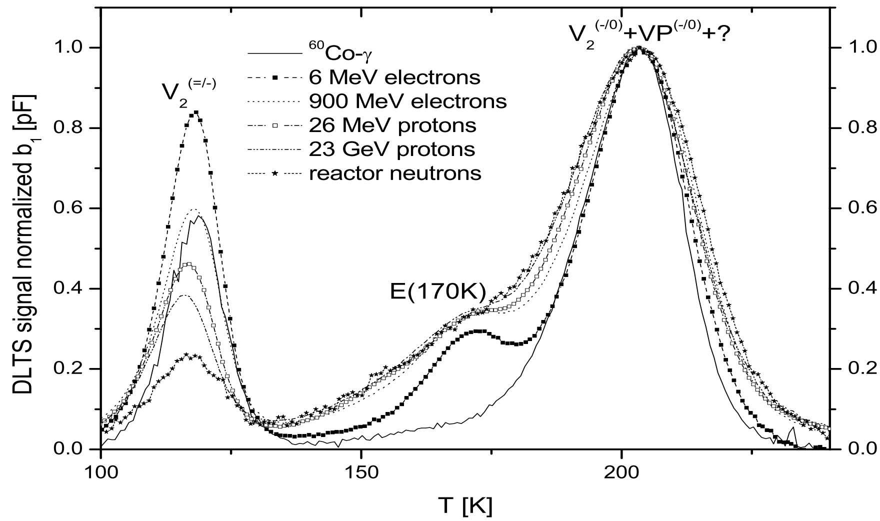

Figure 4.8: *DLTS spectra of all six irradiated samples. Amplitudes are scaled to the maximum of the $V_2{}^{(-/0)}+VP+?$-peak.*

They cause a larger introduction of directly generated divacancies and clustered regions. Two effects already described in section 4.3 are caused by these clustered regions. One is the suppression of the DLTS signal from the $V_2^{(=/-)}$-defect and the second is the broadening of the $V_2^{(-/0)}$-peak. Both effects can be observed in detail

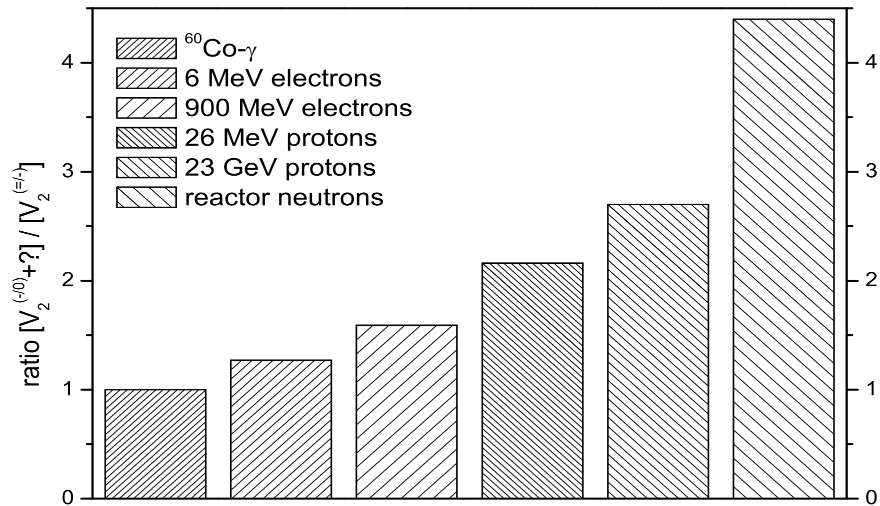

Figure 4.9: *Ratio of the introduction rates of the singly charged and the douply charged divacancy-defect.*

by comparing the DLTS measurements after different irradiations.

In Fig. 4.8 the decreasing amplitude of the $V_2{}^{(=/-)}$-peak and the increasing width of the $V_2{}^{(-/0)}$-?-peak depending on the growing energy of the impinging particles can be observed. It has to be taken into account, that the difference of the peak hight of both divacancy-related peaks in case of ^{60}Co-γ-irradiation is caused by the VP-defect. In this case the VP-defect is represented by about 40 % of the total

peak-height of the $V_2{}^{(-/0)}+VP$-peak while in case of all other irradiations only 1-3 % are caused by the VP-defect (see SV-ratio introduced in section 4.2. It has to be mentioned that the VP-defect also introduces a broadening of the $V_2{}^{(-/0)}$-peak after ^{60}Co-γ-irradiation.

The broadening already after irradiation with 6 MeV electrons is caused by the clustering effect. The same effect causes the decrease of the peak-height associated with the doubly charged state of the divacancy. In Fig. 4.9 the effect is shown by comparing the introduction rates of both divacancy related defects. While after ^{60}Co-γ-irradiation the ratio $([V_2^{(-/0)}]/[V_2^{=/-}])$ is 1:1 it becomes more than 4:1 after neutron irradiation.

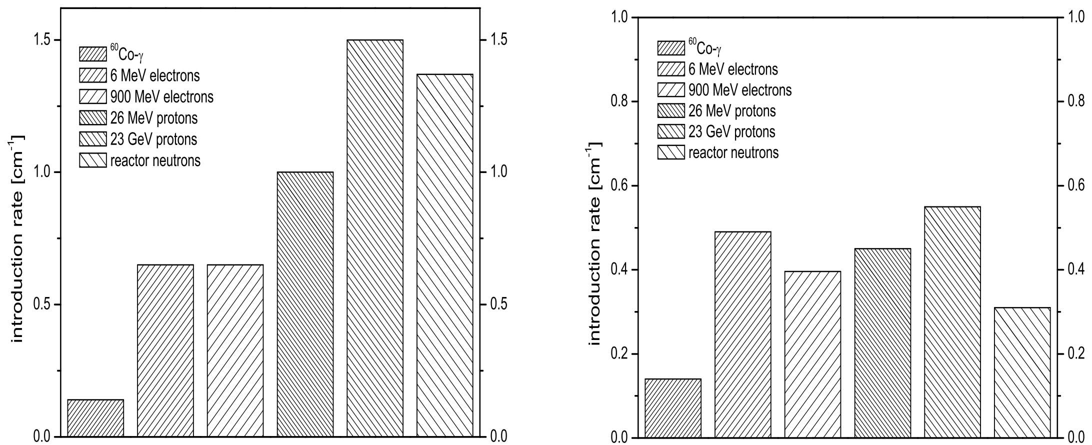

Figure 4.10: *Introduction rates of the $V_2{}^{(-/0)}$+?-defect (left hand side) and the $V_2{}^{(=/-)}$-defect (right hand side) after irradiation with different kind of particles.*

The introduction rates of the singly and the doubly charged states of the divacancy are shown in Fig. 4.10. The introduction rates of the singly charged divacancy increase with particle energy. Compared to the introduction rate after ^{60}Co-γ-irradiation the introduction rates after electron and proton irradiation grow systematically. The main raison for this behavior is the clustering effect. One part of the cluster effect is the larger introduction of divacancies.

After neutron irradiation a small decrease of the introduction rate of the $V_2^{(-/0)}$ is visible. Although the damage mechanism after proton and neutron irradiation is a bit different the main part can be regarded as the nuclear interaction part. In case of irradiation with charged particles coulomb-interaction and nuclear-interaction causes the production of vacancies and interstitials, after neutron irradiation only nuclear-interaction can be observed. But in case of 23 GeV protons the energy is so high that the main damage is also caused by nuclear interaction. Therefore similar introduction rates after neutron and 23 GeV proton irradiation can be observed. The slightly smaller value after neutron irradiation can also be explained be the relatively long storage time of the sample and therefore a first annealing of the cluster.

The right hand side of Fig. 4.10 shows the introduction rates of the $V_2^{(=/-)}$-defect. Here two effects can be seen. One is the higher generation of divacancies and the second part is the cluster related filling effect which can be detected as the reduction

of the peak-height and of course of the corresponding introduction rate. In case of neutron the decrease of the introduction rate is due to the strongest cluster effects which are even stronger than after irradiation with 23 GeV protons.

The growing introduction of divacancies and the growing clustering effect compensate each other and therefore an almost constant introduction of the $V_2^{(=/-)}$-defect can be observed.

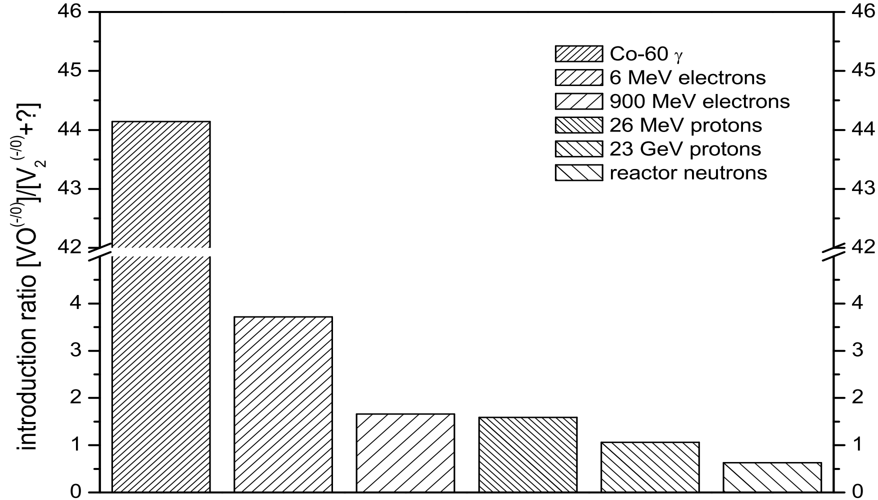

Figure 4.11: *Ratio of the introduction rates of the $VO_i^{(-/0)}$- and the $V_2{}^{(-/0)}+?$-defect.*

A comparison of the introduction rates of the $V_2^{(-/0)}$ and the introduction rates of the VO_i-defect is given in form of ratios in Fig. 4.11.

While the ratio is about 44:1 after ^{60}Co-γ-irradiation it decreases to about 1:1 for neutrons and high energy protons. This reveals that a high number of vacancies is generated by neutrons and high energy protons in a small crystal region. Only in case of vacancies produced close to each other within the PKA cascade they can form divacancies or even higher order vacancy defects. Only a small number of vacancies can be produced by the gamma induced compton electrons. Therefore it is rather unlikely that divacancies are formed and most of the vacancies which do not recombine with interstitials migrate through the lattice until they are captured by an oxygen atom. The ratio extracted by this way is therefore a dimension for a divacancy density in clustered regions.

It is possible to separate one level of the cluster related defects labeled as E(170K) by normal DLTS measurements from the peak caused by the singly charged state of the divacancy. This defect will be discussed in the next section. Because it is suggested that the peak at 204 K is due to an exponential density distribution of energy states due to lattice deformations [Kuh01], the additional levels contributing to the $V_2{}^{(-/0)}$-peak are labeled with a question mark.

4.7.3 The E(170K)-defect

Although the E(170K)-defect sometimes is associated to cluster nothing is known about its structure. Speculations are going into both directions, towards vacancy

related defects as well as towards interstitial related defects. Unfortunately vacancies and interstitials can also form electrical inactive defects, therefore it is not possible to decide wether the E(170K)-peak is associated with vacancies or with interstitials.

But some other observations done within this experiment can be given. An overview of the introduction rates of the E(170K)-defect is given in Fig. 4.12.

After ^{60}Co-γ-irradiation the E(170K)-defect is not measurable, while after 6 MeV electron-irradiation this defect is already seen.

In Fig. 4.8 the DLTS spectra are scaled to the maximum of the $V_2{}^{(-/0)}$+?-peak. A closer look suggests that this is equivalent to scaling the spectra to the E(170K)-peak in case of 900 MeV electron, 26 MeV and 23 GeV proton and reactor neutron irradiation. It results in almost equal defect-ratios after all particle irradiations except 6 MeV electrons. The ratios are given in Tab. 4.7.

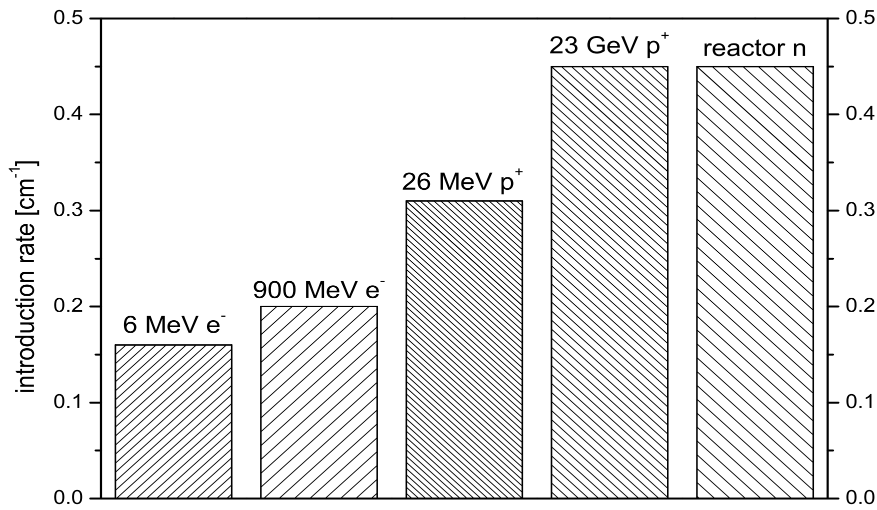

Figure 4.12: *Introduction rates of the E(170K)-defect after irradiation with different kind of particles.*

irradiation	^{60}Co-γ	6 MeV e$^-$	900 MeV e$^-$	26 MeV p$^+$	23 GeV p$^+$	n
[E(170K)]/[$V_2{}^{(-/0)}$+?]		0.24	0.30	0.31	0.30	0.33

Table 4.7: Ratio of introduction rates for the E(170K)-defect and the $V_2{}^{(-/0)}$+?-defect.

Beside the low energy electron irradiation it seems that the given introduction ratio is independent of the kind of particles used for irradiation.

In case of irradiation with 6 MeV electrons the energy of the PKA's are just at the edge of cluster generation and therefore the E(170K)-peak is less pronounced and after ^{60}Co-γ-irradiation not detectable because the energy of the PKA's is too small for cluster generation. In all other cases the generation of the E(170K)-defect corresponds with the generation of the $V_2{}^{(-/0)}$+?-defect very well. Which leads to the suggestion that the generation of the E(170K)-defect is an essential part of the cluster effect. Under this assumption the observation of increasing introduction rates with increasing energy of PKA's can be directly explained with the higher probability of cluster creation.

4.7.4 The C_i-defect

The main trap for primarily generated interstitials are substitutional carbon atoms (C_s). A reaction is possible via the *Watkins replacement mechanism* (I + $C_s \rightarrow$ Si + C_i). Therefore the carbon concentration of the samples is an important factor for the generation of C_i. The mobility of the C_is is much smaller than the one of the interstitials but still high enough to become trapped at O_i forming the C_iO_i-defect if the oxygen content of the sample is sufficiently high. In case of the investigated epi-50-diodes exactly this has happen. Therefore only small amounts of C_is are not being trapped by O_is and no systematic can be found for their introduction rates.

4.7.5 The C_iO_i-defect

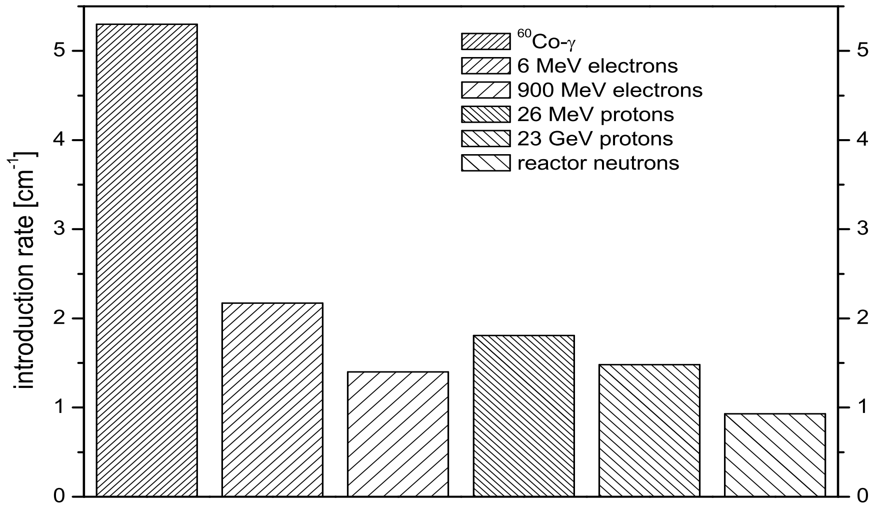

Figure 4.13: *Introduction rates of the $C_iO_i^{(+/0)}$-defect after irradiation with different kind of particles.*

As indicated in the last section the C_iO_i-defect is the main interstitial related defect measurable with the DLTS-method if the oxygen concentration is high enough to capture almost all of the secondarily generated carbon interstitials. In case of these epi-50-diodes this seems to be the best explanation for the introduction of the C_iO_i-defect and the absence of almost all other measurable interstitial related defects.

The introduction rates of the C_iO_i-defect are given in Fig. 4.13. The high value after ^{60}Co-γ-irradiation corresponds with the high probability of creating single vacancies and interstitials mainly. The interstitials become transformed into C_is which are trapped by oxygen atoms.

After 6 MeV electron irradiation vacancies are more often created in form of divacancies or higher order vacancies. It seems that interstitials behave in a similar way. Otherwise it should be possible for them to migrate through the bulk and create defects like the C_iO_i-defect. In such a case the introduction of the C_iO_i-defect would be much higher than the one related to the VO_i-defect. But this behavior is not seen. Only the introduction of higher order interstitials can explain the massive

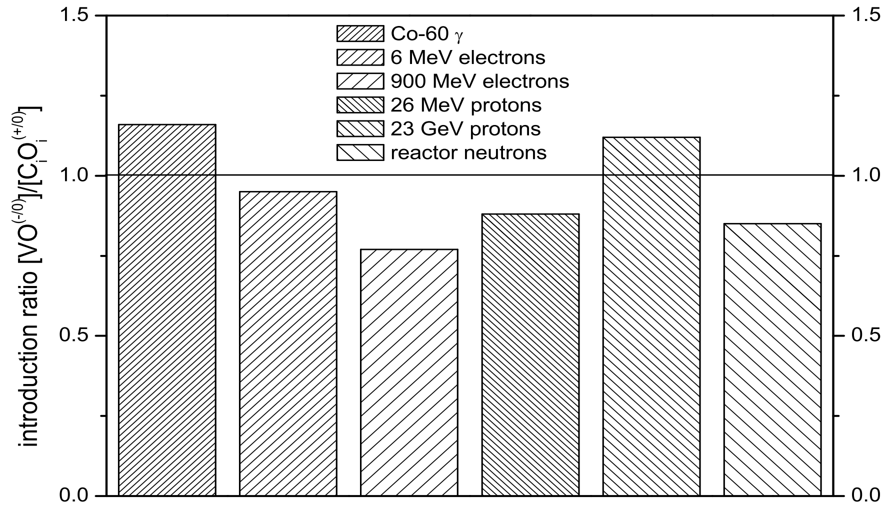

Figure 4.14: *Ratio of the introduction rates of the* $VO_i^{(-/0)}$*- and the* $C_iO_i{}^{(+/0)}$*-defect.*

drop in the introduction rate of the C_iO_i-defect compared to what was measured after ^{60}Co-γ-irradiation.

The decrease of the introduction rates after irradiation resulting in PKA's with even higher energy corresponds with the smaller probability of single vacancy and interstitial creation. This picture is supported by the introduction ratio of the C_iO_i-defect, representing the single interstitials, and the VO_i-defect, representing the single vacancies, given in Fig. 4.14. Ratios close to 1 stand for almost equal introduction rates of both defects.

4.7.6 The VP-defect

The main defects primarily generated by irradiation with ^{60}Co-γ are single vacancies and interstitials. Due to the high oxygen content of the samples, the vacancies can on the one hand side form the $VO_i^{(-/0)}$-defect and due to the high doping of the epitaxial layer another vacancy related defect the vacancy-phosphorus (VP) center.

It has almost identical electrical properties compared with the singly charged divancancy and is therefore overlapping its signal. A 1:1 ratio of the singly and doubly charged divacancy can be expected after ^{60}Co-γ irradiation, therefore the introduction rate of VP can be calculated by simple comparison of the concentration related to the $V_2{}^{(-/0)}$+$VP^{(-/0)}$ peak and the $V_2{}^{(=/-)}$ peak like it is seen in Fig. 4.15.

The introduction rate after ^{60}Co-γ-irradiation is in the range of divacancy generation. The value of 0.11 cm^{-1} for the introduction rate of the VP-defect was found.

In case of all other irradiations it becomes very difficult to measure the VP-concentration. Therefore one has to estimate its introduction by comparing with the introduction of the VO_i-defect. This results in introduction rates of about 1-3 % of the measured introduction rate of the VO_i-defect. This small introduction rate is within the statistical measurement error of up to 10% presuming an introduction

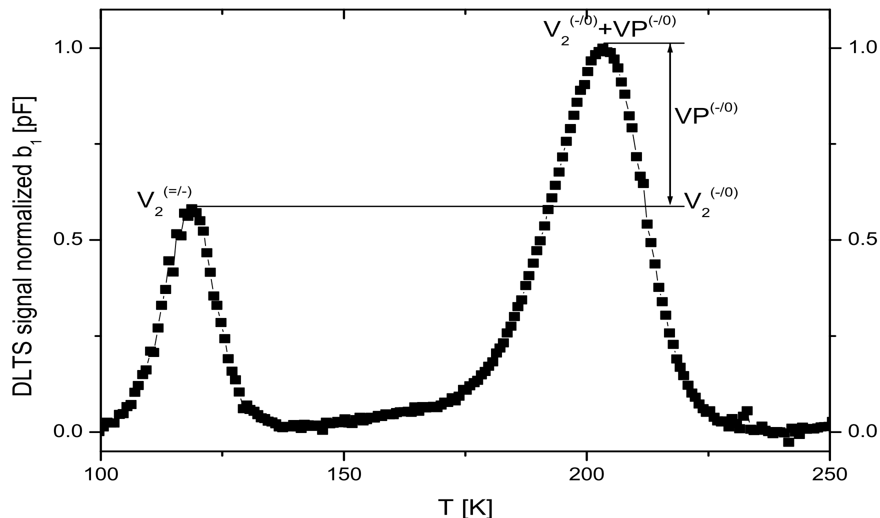

Figure 4.15: *Normalized DLTS spectrum after electron injection. Epi-50-diode irradiated with ^{60}Co-γ's as shown in section 4.1*

rate of the VO_i-defect comparable with that one of the $V_2{}^{(=/-)}$+?-defect.

4.8 Main results for epi-50-diodes

In epi-50-diodes it is possible to identify different kind of defects by DLTS. Besides the main vacancy and interstitial related defects the VO_i- and the C_iO_i-defect the two negative charged states of the divacancy ($V_2{}^{(-/0)}$ and $V_2{}^{(=/-)}$), the $VP^{(-/0)}$-, the carbon interstitial ($C_i{}^{(-/0)}$)- and the E(170K)-defect. The also expected peaks related to the $C_i{}^{(+/0)}$ and the IO_2 are not detectable under the chosen experimental conditions.

The oxygen concentration of the samples is high enough to suppress the formation of C_iC_s and is also high enough to transform almost all C_i's into C_iO_i. This observation is true for all six kind of irradiations.

After ^{60}Co-γ irradiation only point defects are measurable while after all other irradiations characteristic defects for cluster generation are observable. These effects are the suppression of the doubly charged divacancy, the presence of the E(170K)-defect, the broadening of the peak associated with the singly charged divacancy and the decrease of the ratio of the VO_i-defect and the V_2-defect. These effects become more and more significant with increasing energy of the PKA's.

Another main result is the increasing ratio of vacancy related defects and interstitial related defects given in Tab. 4.8.

irradiation	^{60}Co-γ	6 MeV e$^-$	900 MeV e$^-$	26 MeV p$^+$	23 GeV p$^+$	n
$[VO_i]+2\cdot[V_2]+[VP]/$ $[C_iO_i]+[C_i]$	1.28	1.49	1.67	1.89	3.00	3.53

Table 4.8: Ratio of introduction rates of vacancy and interstitial related defects.

These ratios indicate the increasing presence of other interstitial related defects,

like the I_2O or maybe the I_2 [Mur07]. These defects are not electrically active but measurable with IR-absorbtion.

Chapter 5

Microscopic Investigations - Material Dependence of Radiation Induced Defects

In chapter 3 the differences in the defect spectra after irradiation with different particles were shown. In this chapter the focus will be on the material dependence of the detectable defects. Therefore, DLTS studies on different kind of materials irradiated with ^{60}Co-γ, 900 MeV electrons, 26 MeV protons, 23 GeV protons and reactor neutrons will be presented.

5.1 ^{60}Co-γ irradiation

After ^{60}Co-γ-irradiation only point defects are created. This provides an opportunity to investigate the isolated point defects without having to face the problems caused by the cluster effect.

Three different kind of epitaxial silicon, with and without additional oxygen enrichment (epi-72-DO and epi-72-St) and higher doping (epi-50) had been investigated. For an extended comparison also thinned magnetic Czochralski silicon (MCz-100) and thinned float zone silicon (FZ-50) were included.

The DLTS spectra shown in this section were taken about 3 weeks after irradiation. During this time the samples were stored at room-temperature which causes a first annealing. This can influence the concentration of the C_i defect which already starts to anneal out at room temperature. In addition this effect causes an increase of the C_iO_i-concentration due to the capture of mobile C_i's at O_i-sites. Another possible, but here not detected, reaction-channel for C_i is the capture by a C_s which lead to a formation of C_iC_s. The absence of the C_iC_s can be explained by the high oxygen concentration in all five materials which favors the formation of C_iO_i.

In Fig. 5.1 the DLTS-spectra of the three epi materials are shown. The first figure denoted as a) shows the spectra of the epi-50 sample which have already been presented in section 4.1. The figures b) and c) represent the epi-72-St and the epi-72-DO samples accordingly. The main electron trap in all three epi-diodes is the VO_i-defect, detectable at about 84 K. With a similar peak-height the C_iO_i is the main hole-trap in all epi-diodes. It has to be mentioned that the spectra showing

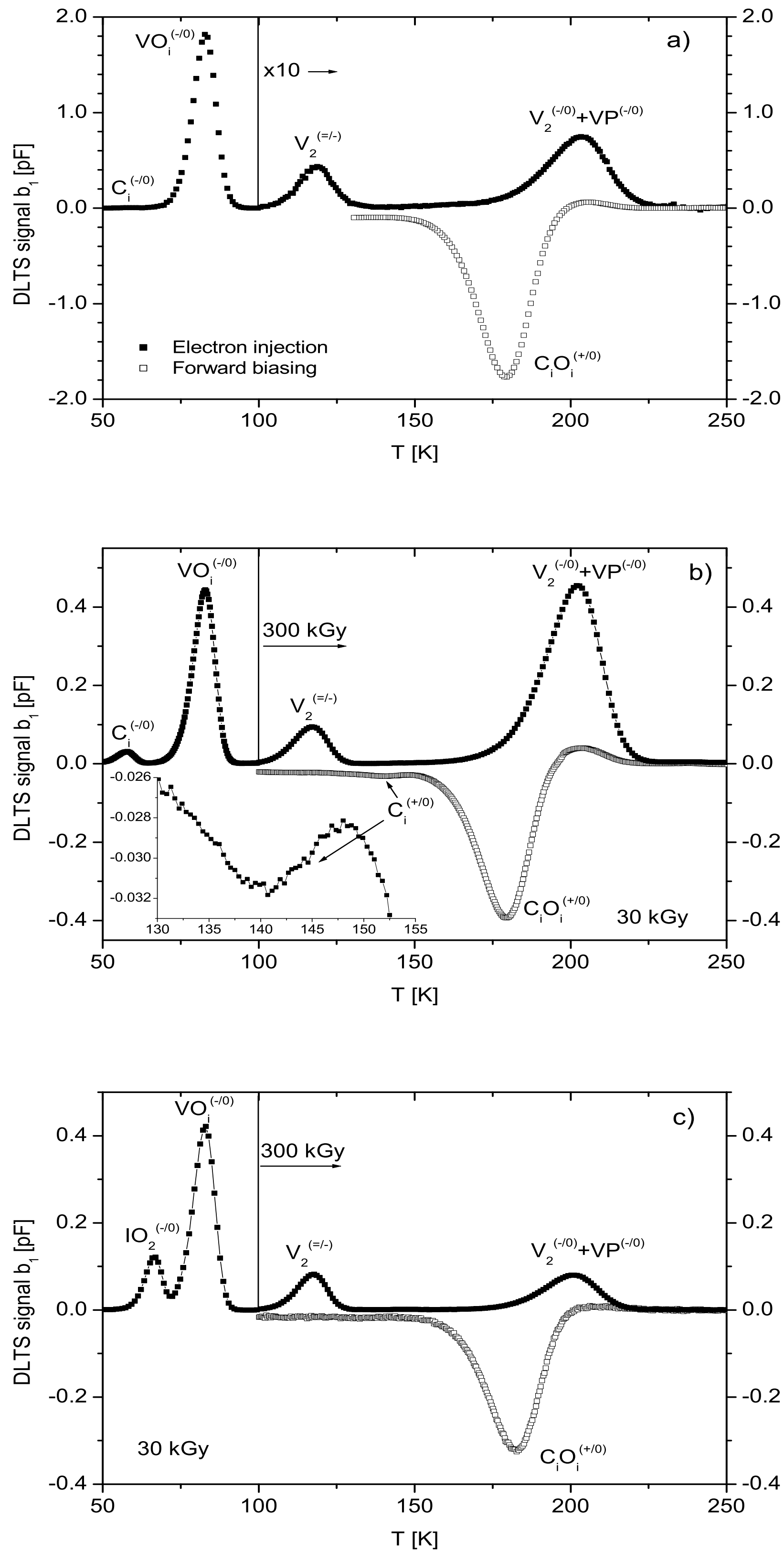

Figure 5.1: *DLTS spectra after electron injection (filled squares) and forward biasing (open squares) of an epi-50-diode (a) irradiated with a* ^{60}*Co-*γ*-dose of 200 kGy (fluence of* $\Phi_{eq} = 18.6 \cdot 10^{11}\ cm^{-2}$*), an epi-72-St- (b) and an epi-72-DO-diode (c) (*^{60}*Co-*γ*-doses of 30 kGy (fluence of* $\Phi_{eq} = 2.8 \cdot 10^{11}\ cm^{-2}$*)) and 300 kGy (*$\Phi_{eq} = 2.8 \cdot 10^{12}\ cm^{-2}$*) for electron traps at temperatures above 100 K. Measurement:* $U_R = -20\ V$, $U_{P,e} = -0.1\ V$, $U_{P,f} = 3\ V$, $t_P = 100\ ms$, $T_W = 200\ ms$.

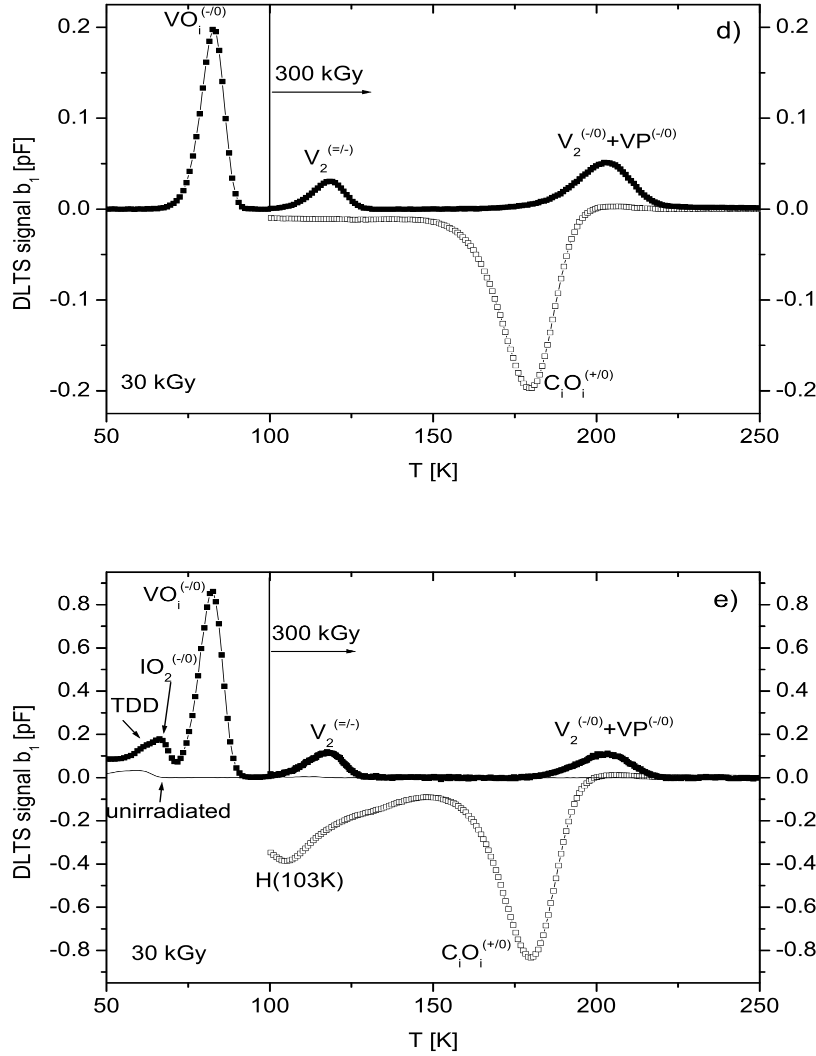

Figure 5.2: *DLTS spectra after electron injection (filled squares) and forward biasing (open squares) of a FZ-50- (d) and a MCz-100-diode irradiated with a fluence of* $\Phi_{eq} = 2.78 \cdot 10^{11}\ cm^{-2}$ *(* ^{60}Co*-*γ*-dose of 30 kGy) and* $\Phi_{eq} = 2.78 \cdot 10^{12}\ cm^{-2}$ *(* ^{60}Co*-*γ*-dose of 300 kGy) for electron traps at temperatures above 100 K. Measurement:* $U_R = -20\ V$, $U_{P,e} = -0.1\ V$, $U_{P,f} = 3\ V$, $t_P = 100\ ms$, $T_W = 200\ ms$.

the other vacancy related defects represent a ten time higher dose (epi-72-St and epi-72-DO) or rather a scaling factor of 10 (epi-50). Therefore the VO_i-defect is also the main vacancy related defect after ^{60}Co-γ irradiation. This finding is in good agreement with the well known observation that this kind of irradiation mainly leads to a creation of single vacancies and interstitials. Most of the single vacancies are captured by O_i's forming the VO_i-defect.

Differences between the materials can be found for those vacancies not being trapped by O_i's. One defect which can be formed by vacancies is the divacancy (V_2). This defect can either be formed directly or by pairing of single vacancies. Most likely most of the V_2's are formed directly because the maximal energy transfer of the primarily generated Compton electrons is higher than the threshold energy for direct V_2 generation. This assumption is also promoted by the much higher

concentration of the other possible reaction-partners for the single vacancy compared to the concentration of single vacancies as another reactant. The V_2 can be seen in the DLTS-spectra in two charge stages (the $V_2^{(-/0)}$ at 204 K and the $V_2^{(=/-)}$ at 118 K).

Their differences in peak-height are caused by another possible reaction product of the single vacancy the VP-defect. The VP-signal is overlapping the $V_2^{(-/0)}$-signal. The differences in VP related DLTS-signal can be explained by two reasons. The high doping of the epi-50 diodes is the main reason for the visibility of the VP-defect. Although the doping of the epi-72-St-diode is much less than the one of the epi-50-diode the signal from the VP-defect is larger. This can be explained by the smaller oxygen concentration of the investigated volume. With less oxygen content the probability for vacancies to become trapped alternatively by phosphorus-atoms increases. In case of the epi-72-DO-diode the VP-defect can not be detected anymore, because the oxygen content is so high that the formation of the VP-defect is much more suppressed than in case of the epi-72-St-sample.

Beside these distinctions another big difference regarding the three epi-materials can be detected with respect to the interstitial related defects. In the epi-50-diode the C_i-defect is represented by a small peak of its acceptor state at 58 K. In the epi-72-St-diode this peak is larger which can be explained by the smaller oxygen content and correspondingly the smaller formation probability of the C_iO_i-defect. Also the donor state of the C_i has been detected. The spectra of the epi-72-DO shows a big difference to the other two.

The absence of the C_i can easily be explained by the much higher oxygen concentration but a second observed effect is different. Another peak at 67 K can be associated with the IO_2-defect. This defect was discovered by DLTS measurements of Cz material [Lin01a] and also investigated in Cz material by [Sta04]. Regarding this defect interstitials are trapped by oxygen dimers before being transformed into C_i. The observation of the IO_2-defect indicates that a high oxygen content coincides with a high oxygen dimer concentration.

For a comparison with other silicon materials a FZ-50- and a MCZ-100-diode have been irradiated additionally. The corresponding DLTS-spectra are shown in Fig. 5.2 and labeled d) and e) accordingly.

The spectra of the MCz-100-diode are comparable with the ones presented for the epi-72-DO sample. The suppression of the VP-defect can be observed as well as the presence of the IO_2-defect. The presence of the IO_2 is expected because of the comparable oxygen- (O_i) and oxygen dimer concentration (O_{2i}) of the MCz-100 and the epi-72-DO sample. The signal from the IO_2 is overlapped by the signal of a defect already observable before irradiation. This defect is identified as a TDD. The VO_i- and the C_iO_i-defect can be observed as expected. A second hole peak labeled H(103K) has been observed in the DLTS-spectra of the MCz-100 sample. This, already before irradiation, detected defect is not known and most likely introduced during the thinning process of the material.

The FZ-50 diode has a relatively low oxygen content and a high doping, which is in between of the doping of the epi-72 and the epi-50 samples. Both effects lead to the presence of the VP-defect in the DLTS-spectra. Regarding this observation the FZ-50 sample is comparable to the epi-50 and the epi-72-St samples. On the other hand the oxygen concentration seems to be high enough to trap all C_i's forming the

C_iO_i. But [O$_i$] and the corresponding [O_{2i}] is too small to form the IO_2-defect. The spectra of the FZ-50 diode look more like the ones from DOFZ material investigated for example in [Sta04] than the ones from standard FZ investigated in the same work.

The concentrations of the defects have been extracted from the DLTS-spectra and introduction rates (IR) have been calculated for the five used materials. The values are given in Tab. 5.1 and they have been illustrated in Fig. 5.3.

Defect/Sample	epi 50μm [cm^{-1}]	epi 72μm [cm^{-1}]	epi 72μm DO [cm^{-1}]	FZ 50μm [cm^{-1}]	MCZ 100μm [cm^{-1}]
$C_i^{(-/0)}$	0.02	0.46			
$IO_2^{(-/0)}$			1.79		1.05
$VO_i^{(-/0)}$	6.40	6.43	5.85	7.11	6.20
$V_2^{(=/-)}$	0.14	0.14	0.12	0.14	0.14
$V_2^{(-/0)}$+VP	0.25	0.73	0.12	0.23	0.14
$C_iO_i^{(+/0)}$	5.30	5.32	4.35	7.28	4.63

Table 5.1: Introduction rates (IR) after ^{60}Co-γ-irradiation.

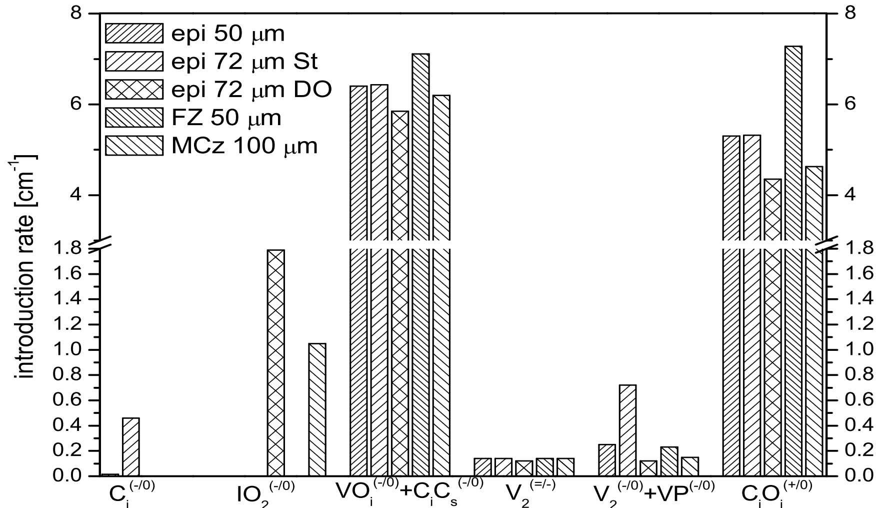

Figure 5.3: *Introduction rates of different defects after ^{60}Co-γ-irradiation with fluences mentioned above for all samples.*

The highest IR is found for the VO_i-defect in all five materials. The samples with the highest oxygen content, the epi-72-DO and the MCz-100, show a slightly smaller introduction than the two epi-diodes with lower oxygen content (epi-50 and epi-72-St). This might be caused by a small introduction of C_iC_s, but whose DLTS-signal is too small (less than 5%) to be separated from the VO_i-signal. The fifth sample the FZ-50 has a higher IR for the VO_i compared with all other materials. The introduction rate of the divacancy V_2 is comparable in all five materials while the one of the VP-defect, which is represented by the difference of the IR of the sum $V_2^{(-/0)}$+VP and the $V_2^{(=/-)}$, is different.

Beside the MCz-diode all others have a comparable high doping, therefore the oxygen concentration has to be regarded as the important factor regarding the VP

introduction. This is in good agreement with the oxygen concentration taken from the SIMS measurements (see Fig. 3.2).

A comparison of the VO_i- and the V_2-defect is given in Tab. 5.2. The differences correspond quite well with the different introduction rates of the VO_i-defect.

	epi-50	epi-72-St	epi-72-DO	FZ-50	MCz-100
$[VO_i]/[V_2]$	44	45	49	51	44

Table 5.2: Ratio of the VO_i-defect and the divacancy.

The primarily generated interstitials can be detected in three different defects. In samples with the highest oxygen content the highly mobile interstitials can be trapped by O_{2i} forming the IO_2-defect or be transformed into C_i at C_s-sites. But due to the high amount of O_i's these C_i's are captured by O_i's forming the C_iO_i. In epi-72-DO the IR of the IO_2 is higher than in the MCz-100-sample, which is in good agreement with the higher oxygen-dimer concentration of the epi-72-DO-sample.

In all other cases the amount of dimers is too small to trap the interstitials, therefore all interstitials are transformed into C_i's, which are than trapped by O_i or being still detectable as C_i.

This measurable amount of C_i depends strongly on the annealing history of the diode. Assuming that the introduction of C_i related defects and the IO_2-defect reflects the primary generation of interstitials, the sum of introduction rates IR(C_i)+IR(C_iO_i)+IR(C_iC_s)+IR(IO_2) is expected to be equal to the total introduction of interstitials IR(I). This sum should be equal to the total number of generated vacancies IR(V) disregarding higher order defects. The ratios of these sums are given in Tab. 5.3.

	epi-50	epi-72-St	epi-72-DO	FZ-50	MCz-100
$[C_iO_i]+[C_i]+[IO_2]/$ $[VO_i]+2\cdot[V_2]+[VP]$	0.78	0.73	1.01	0.97	0.88

Table 5.3: Ratio of the sum of interstitial and vacancy related defects.

The ratios are comparable to what was found by [Sta04] for FZ, Cz and epi diodes. It has to be mentioned, that a small introduction of less than 5 % of C_iC_s compared with VO_i would already have a large impact on the ratio which would be comparable with the difference between the epi-50 and epi-72-St on the one side and the other materials on the other side.

5.2 900 MeV electron irradiation

A set of standard (FZ) and oxygenated (DOFZ) float-zone, Czochralski (Cz) and epitaxial diodes (epi-50) has been irradiated with 900 MeV electrons with fluences of $\Phi_{eq} = 6.4\cdot10^{10}$ cm^{-2} (FZ, DOFZ, Cz) and $\Phi_{eq} = 1.9\cdot10^{11}$ cm^{-2} (epi-50) accordingly. The DOFZ diode has been diffusion oxygenated for about 72 h at 1150°C. After irradiation the samples have been stored at room-temperature for about one day and afterwards in a freezer first at -7° C and later at -28° C. The results, extracted after irradiation, from DLTS measurements are presented in this section.

The DLTS spectra of a FZ diode are given in the upper part of Fig. 5.4. The dominant electron trap is the VO_i-defect, whose peak has a maximum at about 84 K. While this defect represents the main part of generated single vacancies the carbon related defects C_i and C_iO_i represent the introduction of single interstitials. A huge part of the generated C_i is captured by O_i's forming the C_iO_i-defect. But a lot of C_i's remained. The C_iO_i is the main hole trap while the C_i is detected in both, the donor- and acceptor-state. The FZ-sample is the only one showing a very large concentration of the C_i.

In chapter 4 it has been shown that irradiation with 900 MeV electrons introduces clustered regions. As expected, also in the FZ-sample clusters are introduced. At

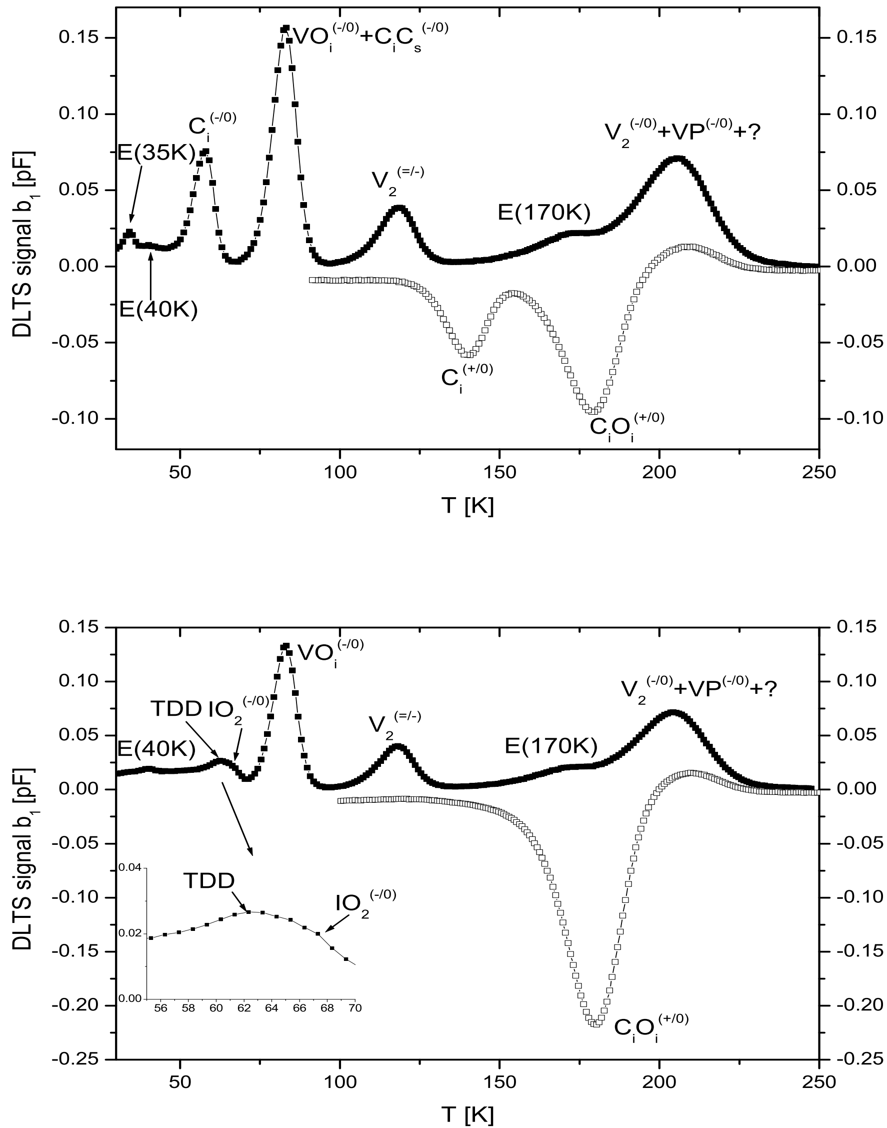

Figure 5.4: *DLTS spectra after electron injection (filled squares) and forward biasing (open squares) of a FZ- (top) and a DOFZ-diode (bottom) irradiated with a fluence of* $\Phi_{eq} = 6.4 \cdot 10^{10}$ cm^{-2} *(900 MeV electrons). Measurement:* $U_R = -20\ V$, $U_{P,e} = -0.1\ V$, $U_{P,f} = 3\ V$, $t_P = 100\ ms$, $T_W = 200\ ms$.

204 K the broadened peak of the $V_2^{(-/0)}$ can be seen while at 118 K a suppression

of the $V_2^{(=/-)}$-peak is visible. Also the cluster related peak at 170 K is observable. The doping of the FZ-diode is too small for a huge introduction of the VP-defect. But of course it should be present and therefore be added to the label of the peak at 204 K. Two other but unknown defects labeled $E(35K)$ and $E(40K)$ can be seen in the DLTS-spectra. More about these defects will be presented in the next chapter.

In the lower part of Fig. 5.4 the DLTS-spectra of a DOFZ diode irradiated with the same fluence than the FZ diode are shown. The same cluster related defects as described in case of the FZ sample have been introduced in the DOFZ sample. The introduction of the VP sample should be present but even smaller as in FZ. It is therefore negligible in consideration of the reached fluence. The VO_i-peak is a bit smaller than in the FZ spectra. The main difference can be observed regarding the interstitial related defects. Due to the much higher oxygen concentration of the DOFZ sample the generated C_i's are totaly trapped by O_i's. As a result the peak-height of the C_iO_i is doubled compared to the FZ sample. Even the concentration of O_2i is high enough to capture primarily generated interstitials before being transformed into C_i. Therefore a small introduction of IO_2 is visible but unfortunately it is to small to become quantifiable. Only a rough estimation can be made. The $E(35K)$-defect is not seen while the $E(40K)$ can be detected as in the FZ diode.

The DLTS-spectra of the epi-50 diode shown in Fig. 5.5 have already been presented in section 4.3.

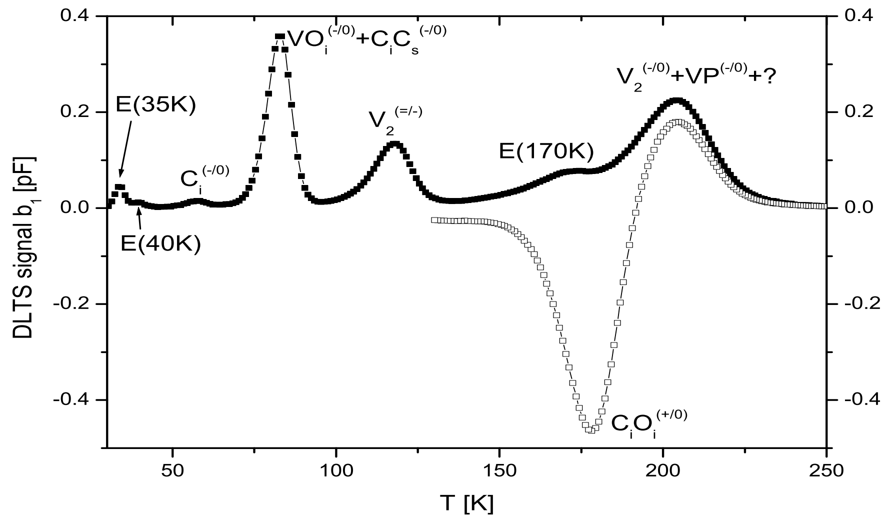

Figure 5.5: *DLTS spectra after electron injection (filled squares) and forward biasing (open squares) of an epi-50-diode irradiated with a fluence of* $\Phi_{eq} = 19.1 \cdot 10^{11}\ cm^{-2}$ *(900 MeV electrons). Measurement:* $U_R = -20\ V$, $U_{P,e} = -0.1\ V$, $U_{P,f} = 3\ V$, $t_P = 100\ ms$, $T_W = 200\ ms$.

Beside the two charge states of the divacancy, which are influenced by cluster, also the other cluster related defect $E(170K)$ is seen. The VO_i-center is the main vacancy related defect. While most of the carbon interstials are captured by oxygen atoms a small concentration remained. The C_iO_i-defect is the one with the highest concentration. The two unknown defects $E(35K)$ and $E(40K)$ detected in FZ material are also visible in epi-50 samples. The DLTS spectra of the Cz-diode are dominated by the appearance of thermal donors introduced during the processing.

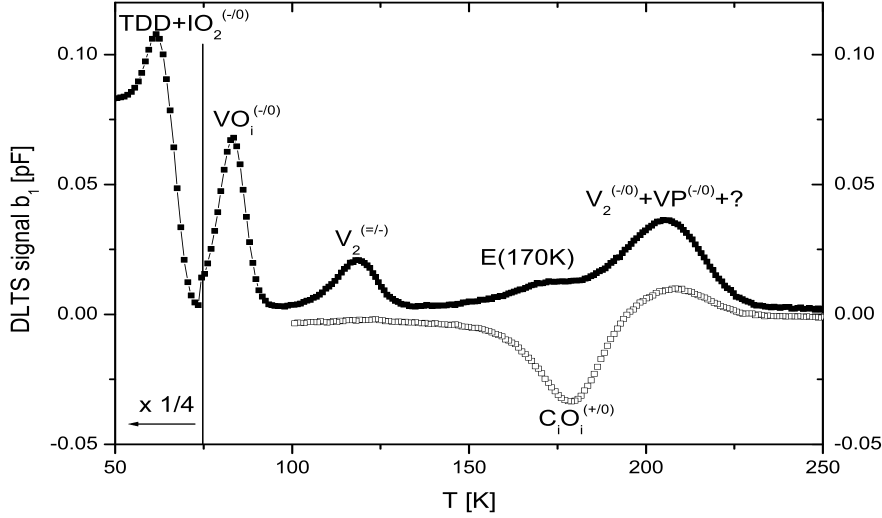

Figure 5.6: *DLTS spectra after electron (filled squares) and forward (open squares) injection of a Cz-diode irradiated with a fluence of* $\Phi_{eq} = 6.4 \cdot 10^{10}$ cm^{-2} *(900 MeV electrons). Measurement:* $U_R = -20$ V, $U_{P,e} = -0.1$ V, $U_{P,f} = 3$ V, $t_P = 100$ ms, $T_W = 200$ ms.

After the irradiation the thermal donors are overlapped by the IO_2-defect. Both peaks are orders of magnitude larger compared to the DOFZ material. Therefore the spectra visualized in Fig. 5.6 are scaled by a factor of 0.25 in the temperature-range below 73 K. As observed for all other diodes the main vancancy related defect in Cz-material is the VO_i-defect. Due to the large content of oxygen it is not influenced by the C_iC_s-defect at all. The C_i's are all captured by O_i's forming the C_iO_i-defect. It is remarkable that the corresponding peak is quite small. But it can easily be explained by the huge concentration of the IO_2-defect which is about three times higher than the C_iO_i-concentration. The interstitials available for further reactions

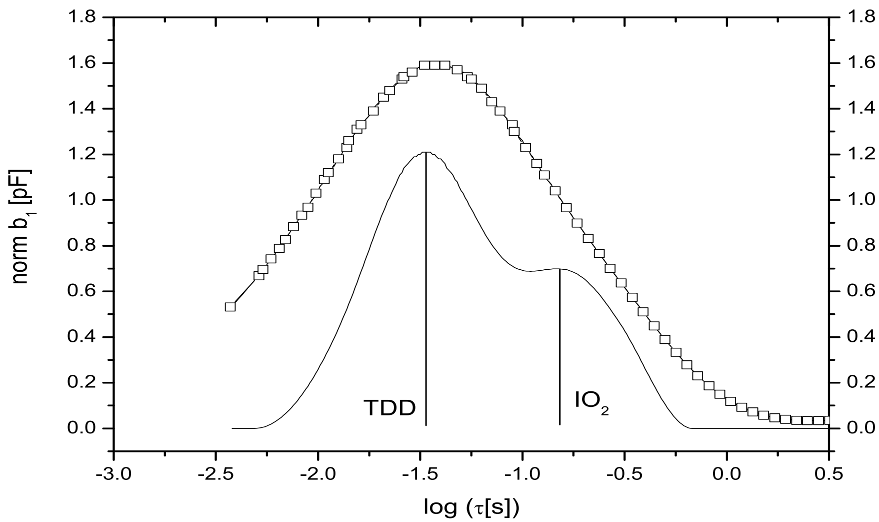

Figure 5.7: *Isothermal spectra of a Cz-diode irradiated with a fluence of* $\Phi_{eq} = 6.4 \cdot 10^{10}$ cm^{-2} *(900 MeV electrons) at 64 K to separate* IO_2 *and TDD. Measurement:* $U_R = -20$ V, $U_{P,e} = -0.1$ V, $t_P = 100$ ms.

after the irradiation are rather captured by oxygen dimers than reacting with substitutional carbon atoms. High resolution DLTS measurements have been performed to extract the introduction rate of the IO_2-defect.

In Fig. 5.7 a scan performed at 64 K is illustrated. Beside the IO_2-defect an even larger peak can be attributed to the thermal donors. The extracted activation energy and capture cross section is in good agreement with former findings in Cz-material [Sta04]. The divacancy and the $E(170K)$-defect are introduced with comparable concentrations as for the other diodes.

The introduction rates for the C_i-, the IO_2-, the VO_i+C_iC_s-,the V_2-, the $E(170K)$- and the C_iO_i-defect of all four samples are given in Tab. 5.4 and illustrated in Fig. 5.8. The measurable concentration of C_i depends on the O_i-concentration and

Defect/Sample	FZ [cm^{-1}]	DOFZ [cm^{-1}]	Cz [cm^{-1}]	epi 50μm [cm^{-1}]
$C_i^{(-/0)}$	1.06			0.04
$IO_2^{(-/0)}$		≈0.10	1.58	
$VO_i^{(-/0)}$+$C_iC_s{}^{(-/0)}$	1.89	1.53	1.24	1.11
$V_2{}^{(=/-)}$	0.45	0.43	0.36	0.40
$E(170K)$	0.23	0.20	0.20	0.20
$V_2{}^{(-/0)}$+VP	0.79	0.77	0.65	0.65
$C_iO_i^{(+/0)}$	1.04	2.36	0.63	1.40

Table 5.4: Introduction rates (IR) after 900 MeV electron-irradiation.

the annealing history during and after irradiation. For all given introduction rates of carbon related defects it has to be taken into account that they contribute to the primarily introduction of C_i. Therefore, the given introduction rates of the C_i-, the C_iO_i- and also, if given, the C_iC_s-defect strongly depend on the annealing history of the diodes. While the informations about the carbon content of the samples

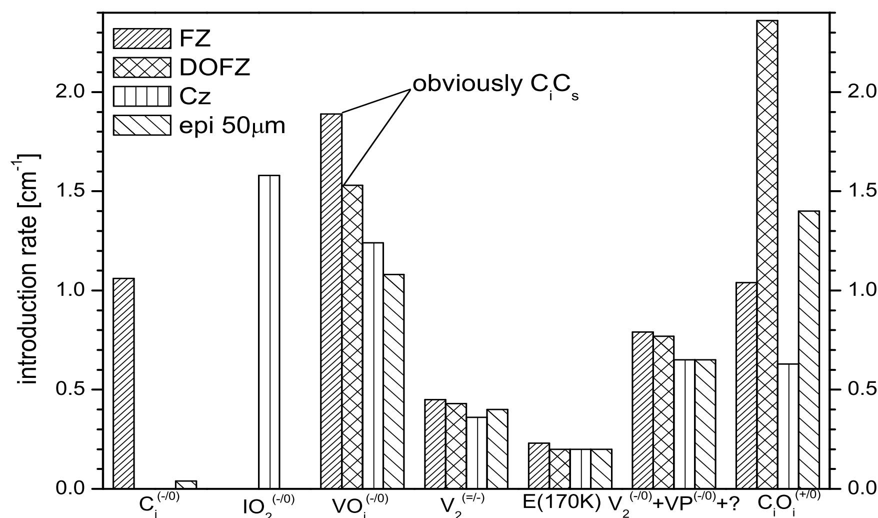

Figure 5.8: *Introduction rates after irradiation with 900 MeV electrons for all samples.*

are limited the oxygen concentration is quite well known. If one assumes the same

carbon content in FZ and DOFZ material and a comparable annealing history the differences in introduction rates related to carbon can mainly be explained by the different oxygen content. While in DOFZ material almost all C_i's are captured in the C_iO_i-defect, in FZ material they are also visible as the $C_i^{(-/0)}$ transition itself. The difference of the sum of these two introduction rates in FZ compared with the one in DOFZ corresponds very well with the differences in the introduction rate of the VO_i-defect. Hence it can be stated, that this difference is most likely due to the C_iC_s-defect introduced the FZ sample. Therefore the VO_i-defect in Tab. 5.4 is labeled as VO_i+C_iC_s. Taking this possible contribution of the C_iC_s-defect in FZ into account a sum of interstitial related defects given in Tab. 5.5 can be introduced for all four materials. It can be seen that the number of interstitials in FZ, DOFZ and Cz material is in the same range while it is in epi-50 much smaller. This suggest an unknown trap for interstitials, which might be electrically inactive, with the largest concentration in epi-50 samples. Another explanation would be a possible disappearance of interstitials at the surface or the substrate of the epi-50 diode. The smaller value for $\sum$ I in epi-50 was also seen after proton irradiation in [Sta04]. The introduction rates for the two charged states of the divacancy as well as the $E(170K)$ is almost constant for all samples. Introduction rates for the $E(35K)$- and the $E(40K)$-defect are not given because they are even more affected by the annealing history. This will be shown in the chapter 6.

	FZ	DOFZ	Cz	epi-50
$\sum$ I [1/cm]	2.46	2.46	2.21	1.40

Table 5.5: Sum of the introduction rates of the interstitial related defects after 900 MeV electron-irradiation.

In order to summarize one can say that the defects related to divacancies and clusters have identical introduction rates for all materials, while the defects affected by the oxygen or the oxygen dimer concentration show large deviations.

5.3 26 MeV proton irradiation

In this section the damage caused by 26 MeV protons in different kind of epitaxial and magnetic Czochralski silicon diodes is described. Three epi-diodes are of the same resistivity but with different thickness. These diodes are labeled epi-25, epi-50 and epi-75. Another two epi diodes with a doping which is three times higher are also investigated. One of them is labeled epi-72-St and the other epi-72-DO. The magnetic Czochralski diode has a thickness of 300 μm and a resistivity of more than 600 Ωcm, it is denoted as MCz. The fluence achieved for the MCz is $4.6 \cdot 10^{11}$cm^{-2} while for the other samples it is $8.1 \cdot 10^{11}$cm^{-2}. All fluences are 1 MeV neutron equivalent values.

The DLTS spectra of an epi-25 diode are shown in Fig. 5.9a. The epi-25 sample has the highest oxygen content in the investigated volume of the high doped epi-samples. Therefore also the highest oxygen dimer concentration is expected in this sample. As a result a peak related to the IO_2-defect is visible in the its DLTS-spectra. By contrast the IO_2 is not visible in the investigated volume of the epi-50 and epi-75 diodes. But the C_i-defect has been detected in those diodes. Their spectra

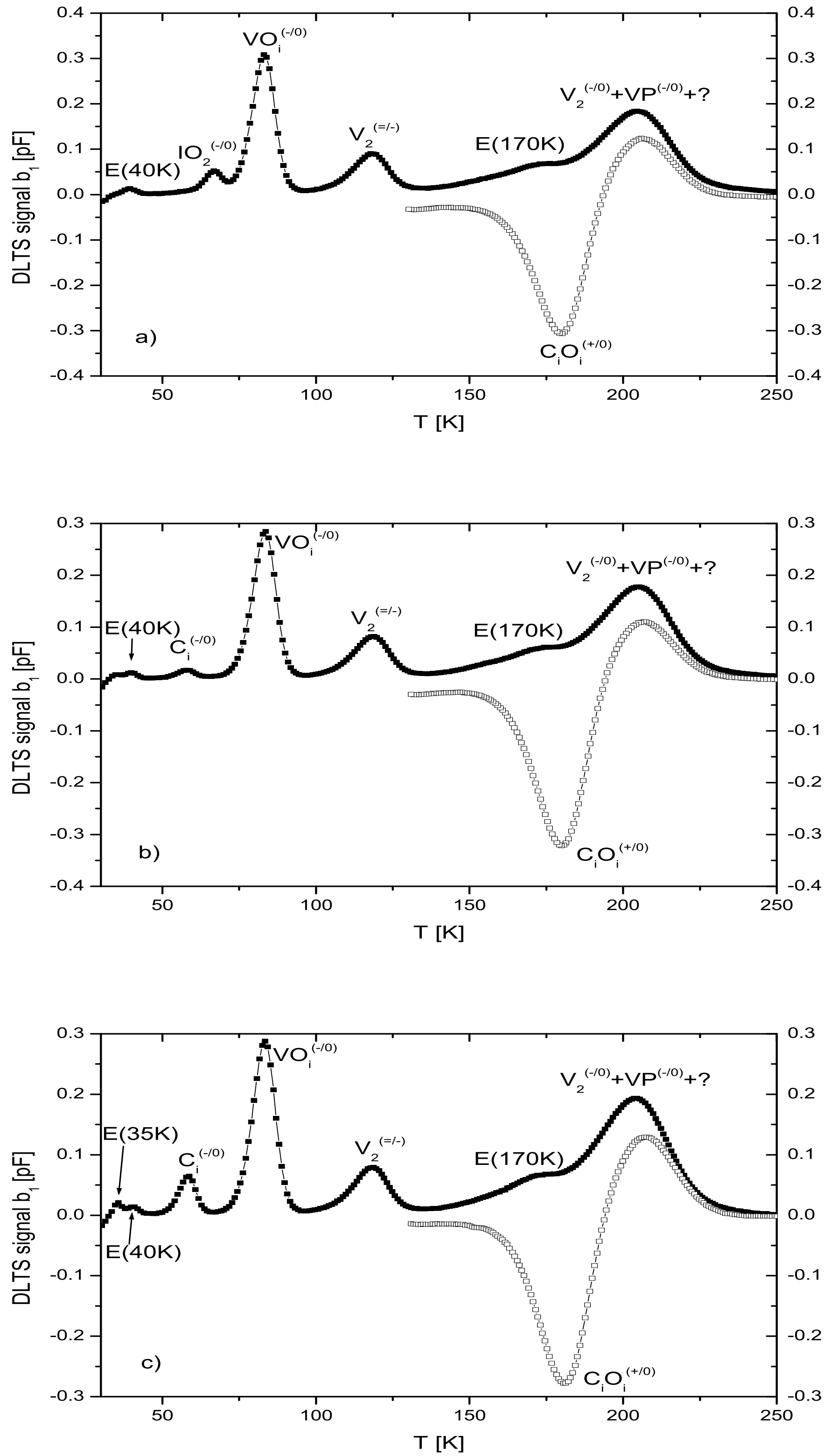

Figure 5.9: *DLTS spectra after electron injection (filled squares) and forward biasing (open squares) of 25 (a), 50 (b) and 75 (c) μm thick epi-diodes irradiated with a fluence of $\Phi_{eq} = 8.1 \cdot 10^{11}\ cm^{-2}$ (26 MeV protons). Measurement: $U_R = -20\ V$, $U_{P,e} = -0.1\ V$, $U_{P,f} = 3\ V$, $t_P = 100\ ms$, $T_W = 200\ ms$.*

are shown in Fig. 5.9 b) and c) accordingly. Due to the comparable annealing history of the epi-50 and epi-75 sample the different peak-heights of the C_i can be explained by the different oxygen profiles of both materials. Therefore more C_i is captured by O_i in the epi-50 than in the epi-75 sample resulting in a smaller C_i-peak in epi-50. And vice versa the C_iO_i-peak, visible after forward biasing, is larger in epi-50 than in epi-75. These are the main differences between these three epi-diodes with the same high doping.

In all three diodes the highest peak visible is the VO_i-peak at 84 K. Due to the high oxygen concentration no overlap by the C_iC_s-defect is detectable.

The concentration of the VP-defect is too small to influence the singly charged divacancy, while the clustered regions cause a broadening of the corresponded peak. The $E(170K)$-defect can also be attributed to the formation of cluster regions. The cluster effect is additionally responsible for the measurable reduction of the $V_2^{(=/-)}$-peak compared to the singly charged one. The unknown defect $E(40K)$ has also been detected in these samples while the $E(35K)$-defect has only been seen in the epi-75-diode.

In the epi-75 sample a quite large concentration of C_i has been found. This finding has been a motivation to perform another experiment in which an epi-72-St sample was investigated in case of a depth profile measurement. This material has a similar oxygen profile than the epi-75 one. In Fig. 5.10 the strong inhomogeneity of the C_i-defect-concentration is presented. The depth profile is plotted together with the oxygen concentration of the same type of samples, measured by SIMS as presented in section 3.1.4. The $[C_i]$ profile has a maximum at a depth were the

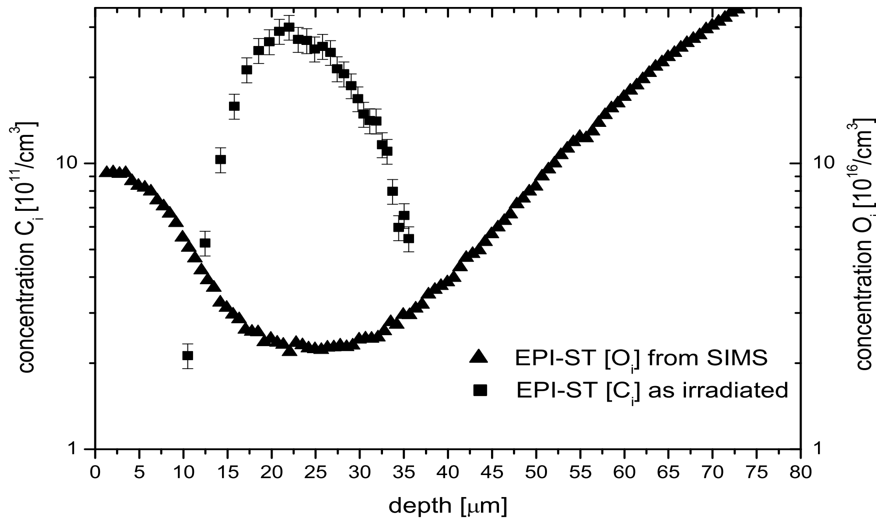

Figure 5.10: *Depth profile of the C_i concentration in an epi-72-St detector irradiated with 26 MeV protons with a fluence of $\Phi_{eq} = 8.1 \cdot 10^{11}$ cm^{-2} and correlated with the oxygen concentration.*

oxygen concentration has its minimum. Towards the regions with higher oxygen concentration the $[C_i]$ drops down rapidly. This rapid decrease is due to the high capture rate of C_i by oxygen atoms forming the C_iO_i complex, when the oxygen concentration is sufficiently large. The competing formation of C_iC_s plays a minor role since the carbon concentration is much smaller than the oxygen concentration.

This behavior is also shown by DLTS spectra for electron emission of this sample under different filling conditions shown in Fig. 5.11.

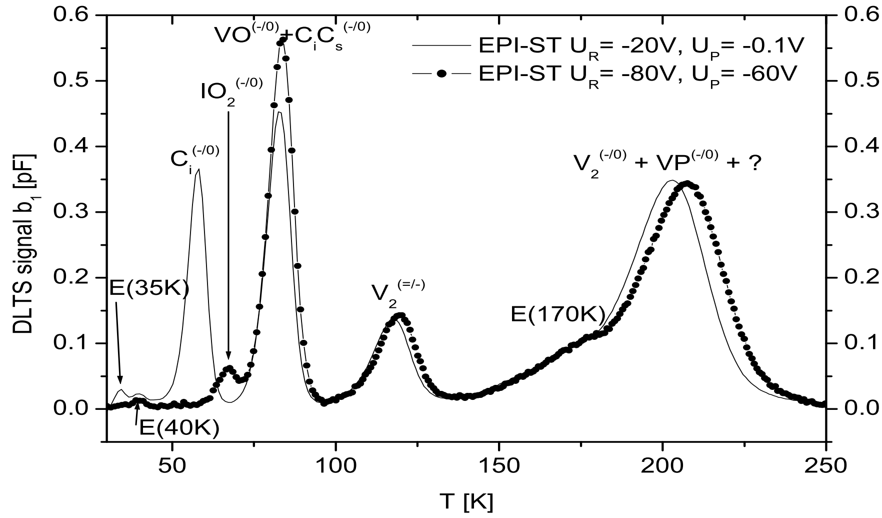

Figure 5.11: *DLTS spectra for epi-72-St irradiated with 26 MeV protons with a fluence of* $\Phi_{eq} = 8.1 \cdot 10^{11} cm^{-2}$*. Comparison of DLTS measurements close to the substrate (*$U_R = -80V$*,* $U_P = -60V$*) and in the region of low oxygen concentration (*U_R*=-20V,* $U_P = -0.1V$*),* t_p*=100ms,* $T_W = 200ms$*.*

The spectra are scaled to the same peak-hight of the $V_2^{(=/-)}$ because for this defect no depth profile is expected. Under usual filling condition used mostly for DLTS measurments in this work (U$_R$ = -20 V, U$_P$ = -0.1 V) the depth from 5 to 33 μm from the top side of the diode can be investigated in this sample. Using these filling conditions the C_i-defect can be observed. In this region the IO_2-concentration is expected to be very small since the oxygen concentration is low. But near the interface of the epi-layer and the Cz substrate the oxygen concentration is much higher (see Fig. 3.2 in section 3.1.4). Therefore it is expected that the oxygen dimer concentration in this region is also much higher compared to the front region and the IO_2 should become visible. In fact, this is demonstrated in Fig. 5.11 for the second spectrum where the filling condition corresponds to a depletion region near to the interface. It is also obvious that in this region with its high oxygen concentration the C_i-defect is not visible anymore due to the formation of the C_iO_i-complex.

In Fig. 5.12 the DLTS spectra of the epi-72-St diode are compared with the ones of the epi-72-DO sample. The DLTS peaks at 204 K and 118 K are attributed to the both negatively charged states of the divacancy ($V_2^{(-/0)}$, $V_2^{(=/-)}$), whereby the strong reduction of the signal from the doubly charged state compared to the one from the singly charged state is the well known effect of hadron induced strain fields in heavily disordered regions, also known as the cluster effect. The slightly larger $V_2{}^{(-/0)}$ in the epi-72-St diode can most likely be attributed to a concentration of the E-center (VP) which is created in the region of the epi-72 sample where the oxygen profile exhibits a broad minimum. One the other hand the peak height of the VO_i-defect in epi-72 material is a bit smaller than in in the epi-72-DO diode which is a further indication, that the single vacancy related defects (VP, VO_i) are influenced by the depth profile of the oxygen content in the epi-72 material. But the

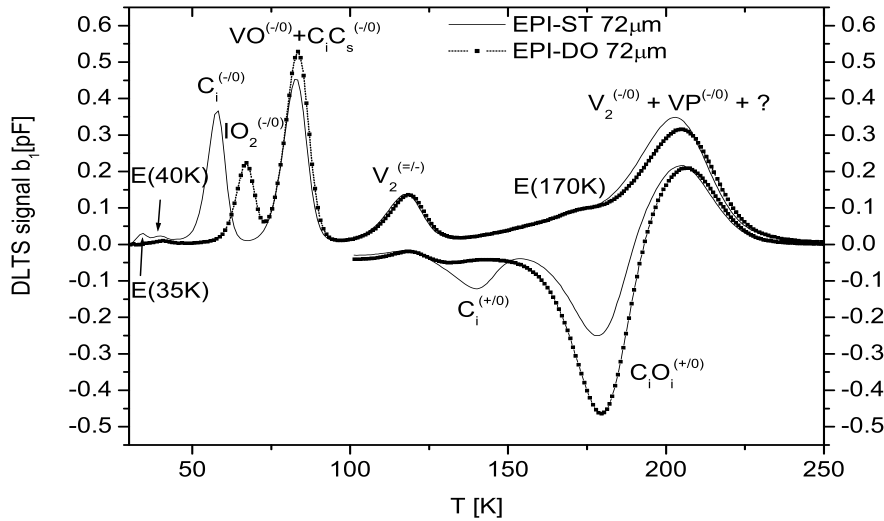

Figure 5.12: *DLTS spectra for epi-72-St and epi-72-DO irradiated with 26 MeV protons with a fluence of* $\Phi_{eq} = 8.1 \cdot 10^{11} cm^{-2}$. $U_R = -20V$, $U_P = -0.1V$,*t_p=100ms*, $T_W = 200ms$.

most obvious difference between both spectra is the fact that the interstitial-dimer-complex (IO_2) is only seen in the epi-72-DO sample while the carbon interstitial (C_i) is only seen in the epi-72-St sample.

In Fig. 5.13 the DLTS spectra of an MCz diode are shown. It can be seen that the specta are very similar to what has been recorded in case of the epi-72-DO sample. Especially a clear IO_2-signal has been seen and no C_i signal. In Fig. 5.13 a

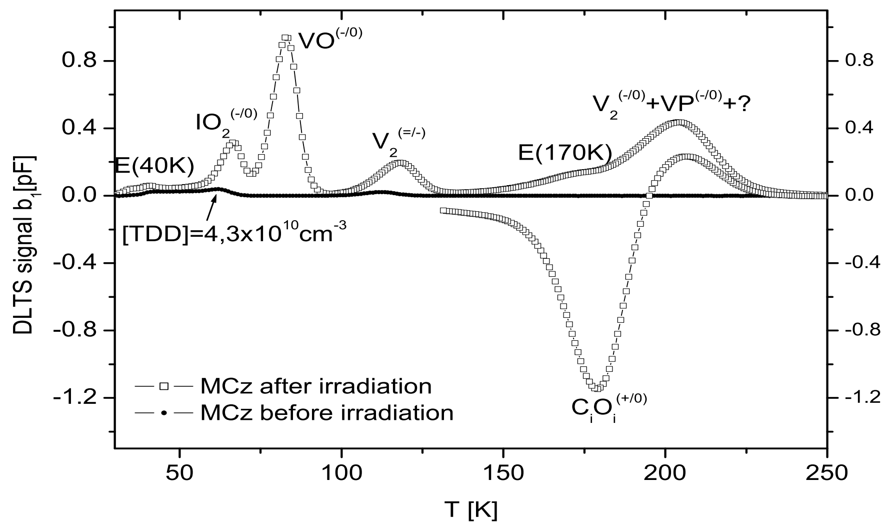

Figure 5.13: *DLTS spectra for MCz material before and after irradiation with 26 MeV protons with a fluence* $\Phi_{eq} = 4.6 \cdot 10^{11} cm^{-2}$. $U_R = -20V$, $U_P = -5V$,*t_p=100ms*, $T_W = 200ms$.

spectrum for electron emission before irradiation is included which shows two small peaks located at about 112 K and 62 K. While the 112 K peak cannot be attributed to any known defect, the signal at 62 K is most likely related to the thermal double donor TDD. This assignment is based on a direct capture measurement resulting

in a very large value of $\sigma_n = 1 \cdot 10^{-12}$ cm^2 which is expected for shallow double donor. The IO_2 depth profiles were as well as the C_i depth profile shown above extracted from transient measurement, recorded at a constant temperature of 67 K (IO_2) and 58 K (C_i) accordingly, varying the reverse bias and the pulse bias and using a time window T$_W$ of 200 ms. In Fig. 5.14 the depth profiles of the IO_2

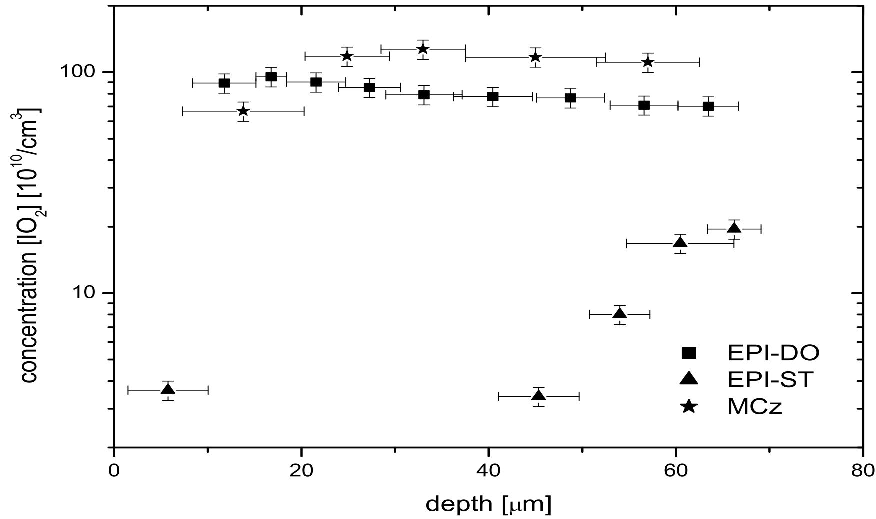

Figure 5.14: *Depth profiles of IO_{2i} defect concentration in epi-72-St, epi-72-DO and MCz devices after irradiation with 26 MeV protons with fluences of $\Phi_{eq} = 8.1 \cdot 10^{11} cm^{-2}$, $\Phi_{eq} = 4.8 \cdot 10^{11} cm^{-2}$ and $\Phi_{eq} = 4.6 \cdot 10^{11} cm^{-2}$ accordingly. All concentrations are scaled to $\Phi_{eq} = 8.1 \cdot 10^{11} cm^{-2}$*

concentration are plotted for the epi-72-St, the epi-72-DO and MCz materials. As expected, the profiles of the MCz and the epi-72-DO material are nearly flat in the measured region with the exception of the first point of the MCz diode near the p$^+$ surface. But the profile of the epi-72-St reflects the inhomogeneity of the oxygen profile as measured by SIMS. This correlation between the respective IO_2 and oxygen concentration has led to the question whether the measured IO_2 concentration can be taken as a relative measure of the O_{2i} concentration itself in this material. If we assume that the formation of the IO_2 is not disturbed by the competing formation of I_2O_2 [Lin01a] the IO_2 concentration should reflect the oxygen dimer content in the material. IR absorbtion measurements by L.I. Murin et al. [Mur98] showed a quadratic dependence of the oxygen dimer concentration on the oxygen content in oxygen rich Czochralski silicon. In Fig. 5.15 the correlation of the IO_2-defect and the oxygen concentration for the epi-72-St, the epi-72-DO and the MCz samples is plotted. In case of the epi-72-St and the MCz sample a quadratic dependence as suggested can be shown. However this quadratic function does not reproduce the value observed for the epi-72-DO, which is only about 50% of the expected concentration. This finding is so far not understood.

The introduction rates for all samples are given in Tab. 5.6 and illustrated in Fig. 5.16.

The epi-25, epi-50, epi-75, epi-72-St and epi-72-DO have all been irradiated with the same fluence and at the same time. Therefore one can assume that a comparison of their introduction rates is not influenced by uncertainties of the absolute

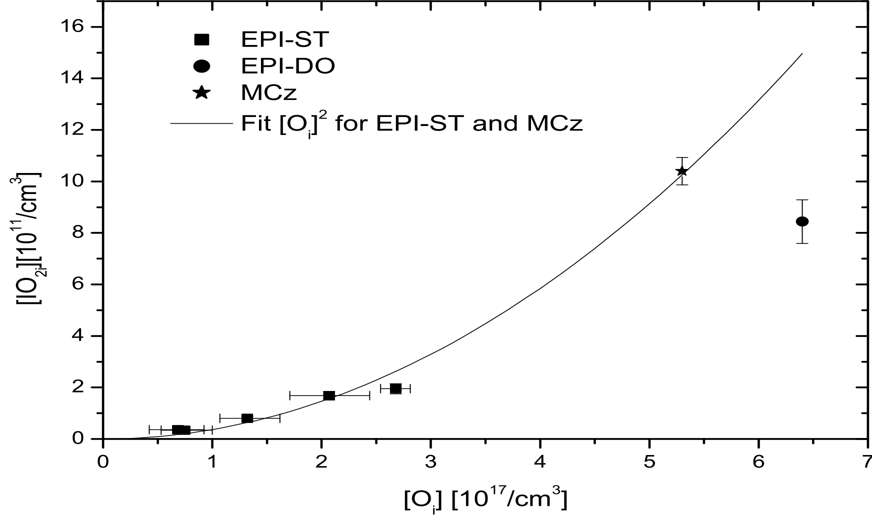

Figure 5.15: *Concentration of the IO_{2i} defect in epi-72-St, epi-72-DO and MCz detectors as function of the oxygen concentration. The solid line represents a fit with a quadratic function.*

Defect/Sample	epi 25μm [cm^{-1}]	epi 50μm [cm^{-1}]	epi 75μm [cm^{-1}]	epi 72μm St [cm^{-1}]	epi 72μm DO [cm^{-1}]	MCz 300μm [cm^{-1}]
$C_i^{(-/0)}$		0.089	0.38	1.33		
$IO_2^{(-/0)}$	0.29				0.90	1.33 (1.02)
$VO_i^{(-/0)}$	1.91	1.88	1.84	1.88	2.31	3.50 (2.69)
$V_2^{(=/-)}$	0.54	0.53	0.50	0.54	0.56	0.69 (0.54)
$E(170K)$	0.38	0.36	0.38	0.33	0.35	0.42 (0.32)
$V_2^{(-/0)}$+VP+?	1.11	1.18	1.20	1.31	1.22	1.43 (1.10)
$C_iO_i^{(+/0)}$	1.89	2.12	1.75	0.98	1.81	1.18 (0.91)

Table 5.6: Introduction rates (IR) after 26 MeV proton-irradiation.

fluence value. The introduction of the VO_i-defect is identical for first four samples. Although the oxygen content for the epi-25 sample is relatively high compared to the other three samples, the introduction rate of the VO_i is in the same range. This finding implies that no generation of the C_iC_s-defect has to be taken into account. Otherwise a higher introduction rate for the epi-50, epi-75 or epi-72-St would have been expected. The introduction of the divacancy is identical in all five samples which can be seen by the similar introduction rates of the $V_2^{(=/-)}$. This also implies that the cluster effect is similar in all epi materials. The slightly higher introduction rate of the singly charged divacancy in case of the epi-72-St can be expected as a small introduction of the VP-defect. The differences in the introduction rates of the C_iO_i-defect coincide with the different channels available for interstitial reactions. These are mainly the C_i- and the IO_2-defect. The different behavior of all six samples in relation to these two defects are widely discussed above. Neither the concentration of the divacancy nor the one of the $E(170K)$-defect is affected by the different oxygen contents. The introduction rate of the VO_i and the sum of interstitials as given in Tab. 5.7 in case of the epi-72-DO sample compared to the other epi samples is about 20% higher. This deviation could be an unknown effect or is

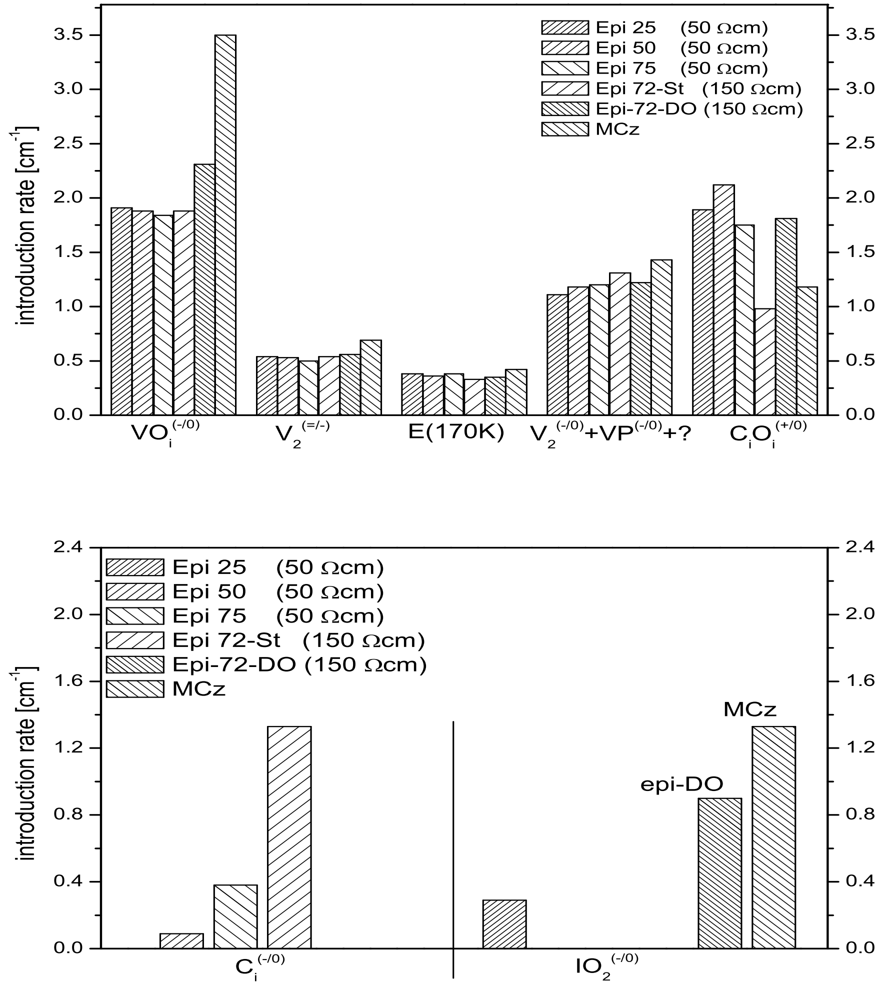

Figure 5.16: *Introduction rates after irradiation with 26 MeV protons for all samples.*

simply related to a relatively high error. The slightly higher introduction rate of the $V_2^{(=/-)}$ in MCz compared to the other samples implies a higher fluence of the sample as measured. From the comparison of the divacancy-introduction the fluence of the MCz seems to be underestimated by about 25% while the typical error of the fluence value is about 10%. If one scales the introduction rates to the typical values of the

	epi-25	epi-50	epi-75	epi-72-St	epi-72-DO	MCz
$\sum$ I [1/cm]	2.18	2.21	2.13	2.31	2.71	2.51 (1.93)

Table 5.7: Sum of the introduction rates of the interstitial related defects after 26 MeV proton-irradiation.

epi samples using the $V_2^{(=/-)}$ as a norm, all values become identical beside the VO_i. It's introduction rate would still be higher than the ones from the epi samples. The scaled values of the MCz are given in a second column of Tab. 5.6 and of Tab. 5.7 in brackets.

5.4 23 GeV proton irradiation

In this section the damage caused by 23 GeV protons is investigated. The irradia-

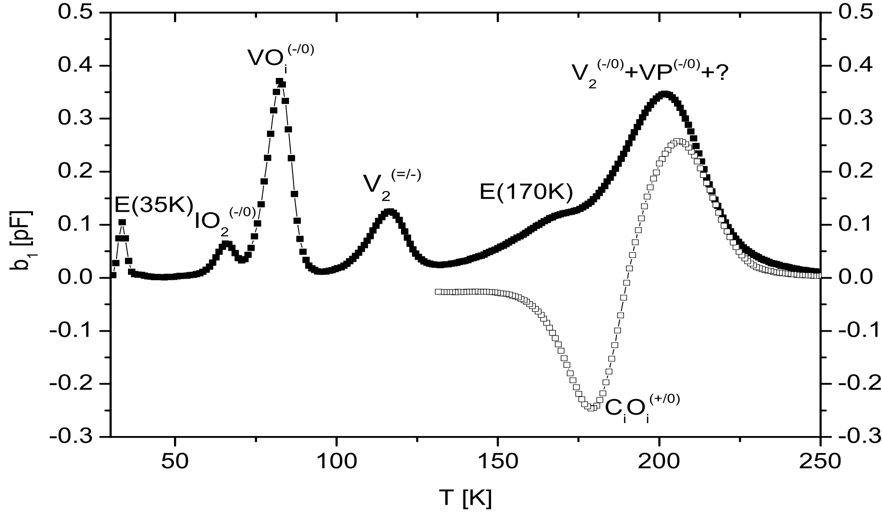

Figure 5.17: *DLTS spectra after electron injection (filled squares) and forward biasing (open squares) of an epi-25-diode irradiated with a fluence of* $\Phi_{eq} = 7.3 \cdot 10^{11}$ cm^{-2} *(23 GeV protons). Measurement:* $U_R = -20$ V, $U_{P,e} = -0.1$ V, $U_{P,f} = 3$ V, $t_P = 100$ ms, $T_W = 200$ ms.

tions were performed at the CERN PS. Unfortunately the availability of this facility was restricted during this work, therefore only epi-diodes with a resistivity of 50 Ωcm had been irradiated. The epi-25 and epi-75 samples achieved a fluence equal to 1 MeV neutrons of $7.3 \cdot 10^{11}$ cm^{-2} while the epi-50 sample were irradiated with a fluence of $8.2 \cdot 10^{11}$ cm^{-2}. It was possible to store the diodes after about 30 minutes at room temperature in a freezer at temperatures below -20°C. Therefore an annealing of the defects can be excluded. A statement which can be proven by the appearance of the $E(35K)$-peak in all three DLTS-spectra. This $E(35K)$-defect is known to anneal out very fast at room temperature. An effect which will be shown in the next chapter.

The DLTS-spectra of an epi-25 diode are shown in Fig. 5.17. Beside the already mentioned peak at 35 K a peak at 67 K is detectable. This peak can be attributed to the IO_2-defect. All three epi-diodes show a typical oxygen profile (see Fig. 3.2 in chapter 3.1.4). In case of the epi-25 diodes the oxygen concentration is the highest of all three. In the last section it was illustrated, that the generation of the IO_2-defect reflects the initial concentration of oxygen dimers. Their concentration is orders of magnitude smaller than the oxygen concentration, therefore the IO_2-defect can in principle only be observed in samples with high oxygen content. Also due to the high oxygen concentration is the absence of the C_iC_s-defect. The peak at 84 K can therefore be attributed to the electron emission from the A-center. The reduction of the doubly charged state of the divacancy can be attributed to clustered regions. The same effect causes the appearance of the $E(170K)$-peak and the broadening of the peak at 204 K. Due to the high oxygen concentration an overlap of a signal from the VP-defect can be neglected. The only hole peak visible after forward injection

is related to the C_iO_i-defect. It is expected that the carbon content of the three

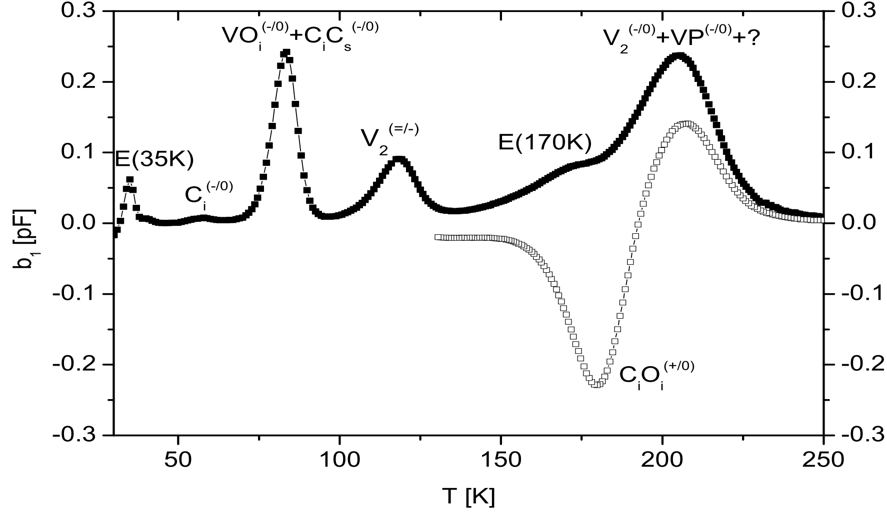

Figure 5.18: *DLTS spectra after electron injection (filled squares) and forward biasing (open squares) of an epi-50-diode irradiated with a fluence of* $\Phi_{eq} = 8.2 \cdot 10^{11}\ cm^{-2}$ *(23 GeV protons). Measurement:* $U_R = -20\ V$, $U_{P,e} = -0.1\ V$, $U_{P,f} = 3\ V$, $t_P = 100\ ms$, $T_W = 200\ ms$.

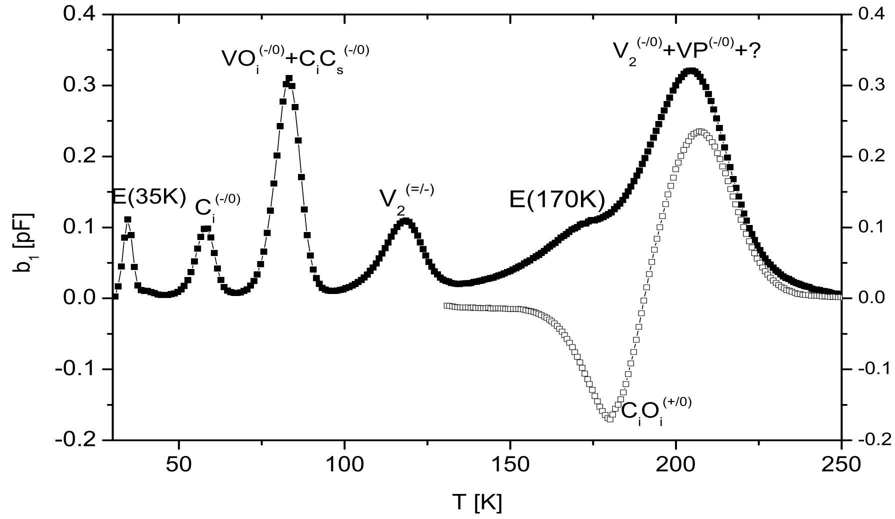

Figure 5.19: *DLTS spectra after electron injection (filled squares) and forward biasing (open squares) of an epi-75-diode irradiated with a fluence of* $\Phi_{eq} = 7.3 \cdot 10^{11}\ cm^{-2}$ *(23 GeV protons). Measurement:* $U_R = -20\ V$, $U_{P,e} = -0.1\ V$, $U_{P,f} = 3\ V$, $t_P = 100\ ms$, $T_W = 200\ ms$.

samples do not differ very much therefore the small peak at 58 K visible in Fig. 5.18 is remarkable. This defect is associated with the C_i-defect. The small peak of the C_i-defect in the epi-50 sample illustrates very well, that the oxygen concentration is high enough to trap the carbon interstitial's almost completely by forming the C_iO_i but not high enough for oxygen dimers to introduce a detectable amount of IO_2 by

irradiation. Therefore no peak at 67 K is visible. The larger C_iO_i peak compared to the epi-25 sample is due to the higher possibility of interstitials to form the C_i instead of the IO_2 and the following capture of these C_i's by oxygen atoms. The difference in the appearance of these three peaks are the main differences between the epi-25 and the epi-50 sample. Regarding other defects the DLTS spectra of both epi-diodes look very similar.

Regarding the divacancy, the E(170)-signal or the $E(35K)$-peak, the spectra of the epi-75 diode look similar to the other epi samples. But due to the smaller oxygen content the C_i-defect becomes more dominant compared to the epi-50 sample. The C_iO_i-signal is reduced accordingly. A small contribution of the C_iC_s to the peak of the A-center can be expected. The DLTS spectra of the epi-75 sample are shown in Fig. 5.19.

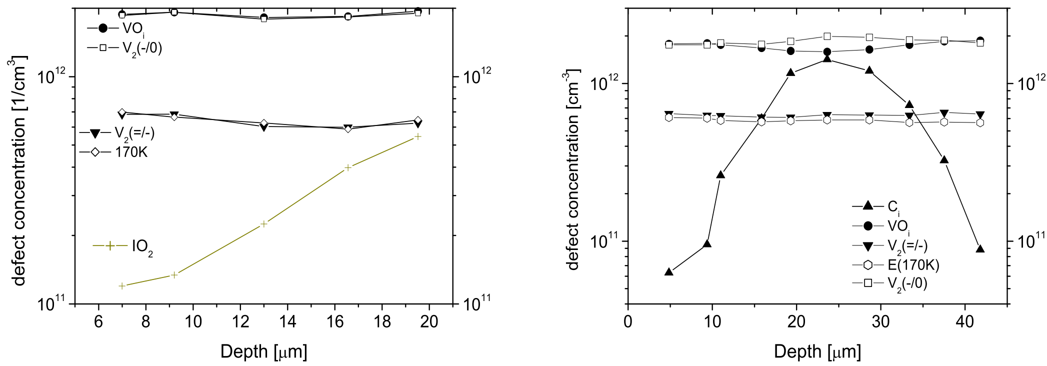

Figure 5.20: *Depth profiles of several defects for an epi-25 sample (left hand side) and an epi-75 sample (right hand side)*

In order to understand the differences regarding mainly the interstitial related defects depth profile measurements are presented in Fig. 5.20 for the epi-25 and the epi-75 samples. In case of the epi-25 sample a clear homogeneity for all investigated defects can be seen except the IO_2-defect. This defect has an increasing concentration with larger depth calculated from the p$^+$-side of the diode. The increase corresponds very well with the oxygen concentration given in Fig. 3.1 in section 3.1.4. On the right-hand side of Fig. 5.20 depth profiles of the defects detected in an epi-75 sample are presented. As expected, strong variances in the C_i-profile are visible with a maximum in the depth where the oxygen profile given in Fig. 3.1 shows a minimum in concentration. In this depth also a drop in the VO_i-concentration is observed. This can only be explained by a smaller amount of created A-centers. Also an increase in the concentration of the singly charged divacancy is detectable which can be due to a stronger formation of E-centers. This increase is correlated with the decrease of the VO_i-concentration.

The introduction rates given in Tab. 5.8 are illustrated in Fig. 5.21 for the three epi samples. The main differences between the three materials are due to those defects which are strongly involved by the oxygen content. There are the big differences in the introduction rates of the C_i-defect between the epi-75 and the epi-50 sample and a total suppression of this defect in epi-25. This effect corresponds with the introduction rates of the C_iO_i-defect, which is bigger in epi-50 than in epi-75. The smaller introduction rate in epi-25 can be explained by the appearance of the IO_2-defect. Therefore it is very impressive that the sum of these three interstitial related

Defect/Sample	epi 25μm [cm^{-1}]	epi 50μm [cm^{-1}]	epi 75μm [cm^{-1}]
$C_i^{(-/0)}$		0.05	0.75
$IO_2^{(-/0)}$	0.42		
$VO_i^{(-/0)}+C_iC_s{}^{(-/0)}$	2.74	2.18	2.35
$V_2{}^{(=/-)}$	0.88	0.78	0.79
$E(170K)$	0.77	0.68	0.73
$V_2{}^{(-/0)}+VP$	2.41	2.1	2.33
$C_iO_i^{(+/0)}$	1.68	1.95	1.13

Table 5.8: Introduction rates (IR) after 23 GeV proton-irradiation.

defects is almost equal in the three epi materials. It is also equal with the results found for FZ and DOFZ material in the former work of J. Stahl [Sta04]. The

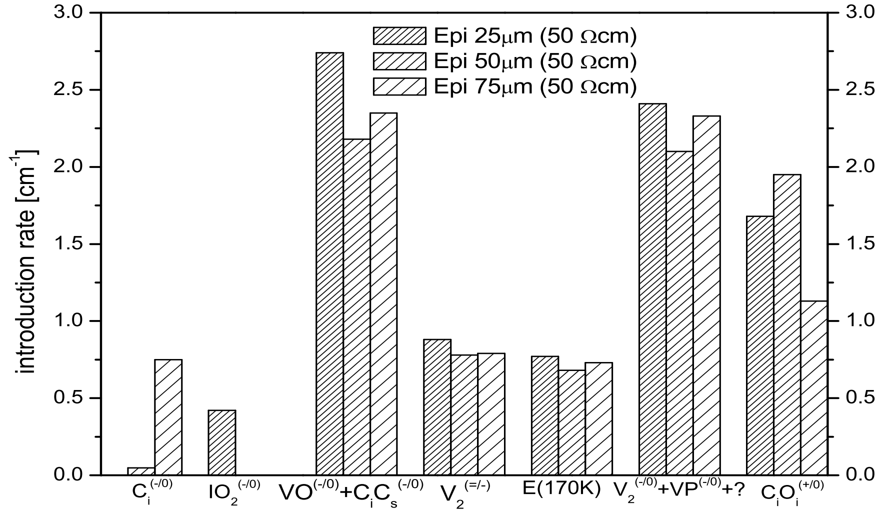

Figure 5.21: *Introduction rates after irradiation with 23 GeV protons for all samples.*

introduction rates of the $V_2{}^{(=/-)}$- and the $E(170K)$-defect are almost identical in all three materials which can be explained with the same cluster effects in the samples. The differences in the introduction rate of the A-center can most likely be attributed to an small formation of the C_iC_s-defect in case of the epi-75 sample and a stronger capture of vacancies by oxygen atoms in epi-25. Nevertheless the differences are so small that they can also be explained by the error of the concentrations. The introduction rates of the VO_i are slightly higher compared to the old measurements of Stahl [Sta04]. The introduction rates of the $V_2^{(-/0)}+VP+?$ are identical and in the same range as it was found in FZ and DOFZ and also Cz material in [Sta04]. Introduction rates presented by [Kuh01] as well as by [Dav06] are smaller than the ones presented here. The ratio $[V_2^{(=/-)}]/[V_2^{(-/0)}+VP+?]$ is similar to the data from [Kuh01], while the ratio is smaller by a factor of almost two in [Dav06]. This smaller ratio can be explained by the very small filling time of 0.1 ms used in [Dav06] which reduces the signal from the $V_2^{(=/-)}$ dramatically compared to the values extracted in this work where a filling time of 100 ms has been used. This is a typical aspect of

the cluster effect. The difference in concentrations compared with [Kuh01] might

	epi-25	epi-50	epi-75
$\sum$ I [1/cm]	2.10	2.00	1.88

Table 5.9: Sum of the introduction rates of the interstitial related defects after 23 GeV proton-irradiation.

be due to differences in the determination of the fluence. The sums of the detected interstitial related defects, namely the C_i, the C_iO_i and the IO_2 are given in Tab 5.9.

5.5 Reactor neutron irradiation

In this section an overview of the damage caused by reactor neutrons is given. Therefore five samples of epi-25, epi-50, epi-72-St, epi-72-DO and MCz material have been irradiated with fluences between $9.0 \cdot 10^{10}$ cm^{-2} and $9.0 \cdot 10^{11}$ cm^{-2}. The fluence values are 1 MeV neutron equivalent. The damage caused by neutrons is strongly influenced by the generation of clustered regions. Therefore the DLTS spectra are dominated by the strong peak at 204 K.

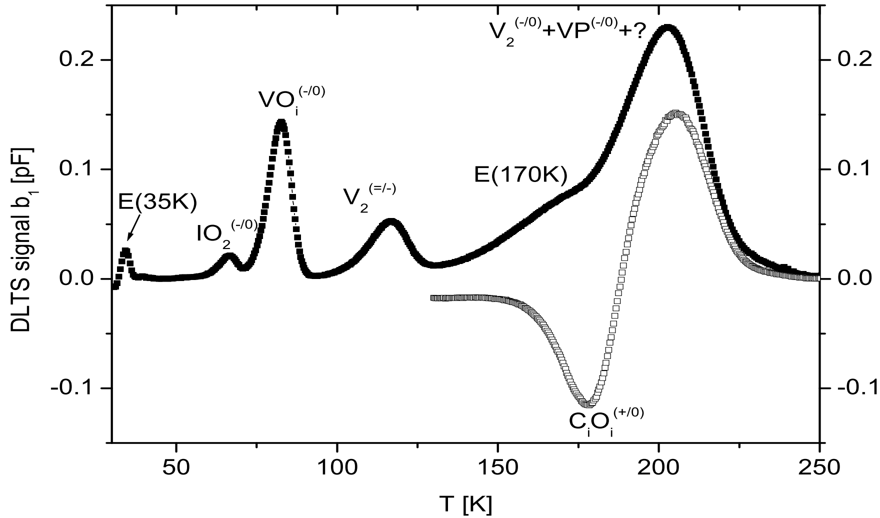

Figure 5.22: *DLTS spectra after electron injection (filled squares) and forward biasing (open squares) of an epi-25-diode irradiated with a fluence of* $\Phi_{eq} = 2.7 \cdot 10^{11}$ cm^{-2} *(reactor neutrons). Measurement:* $U_R = -20$ V, $U_{P,e} = -0.1$ V, $U_{P,f} = 3$ V, $t_P = 100$ ms, $T_W = 200$ ms.

In Fig. 5.22 the DLTS spectra for the epi-25 diode are shown. Beside the dominating peak at 204 K associated with the singly charged divacancy the cluster related peak at 170 K and the strong suppression of the $V_2^{(=/-)}$ can be seen. The small peak related to the VO_i-defect can be explained with the dominating role of the direct nuclear interaction caused by neutron irradiation. The vacancies have to escape from the highly disordered cluster regions in order to become a source for defects related to single vacancies. This is in contrast to irradiation with charged particles

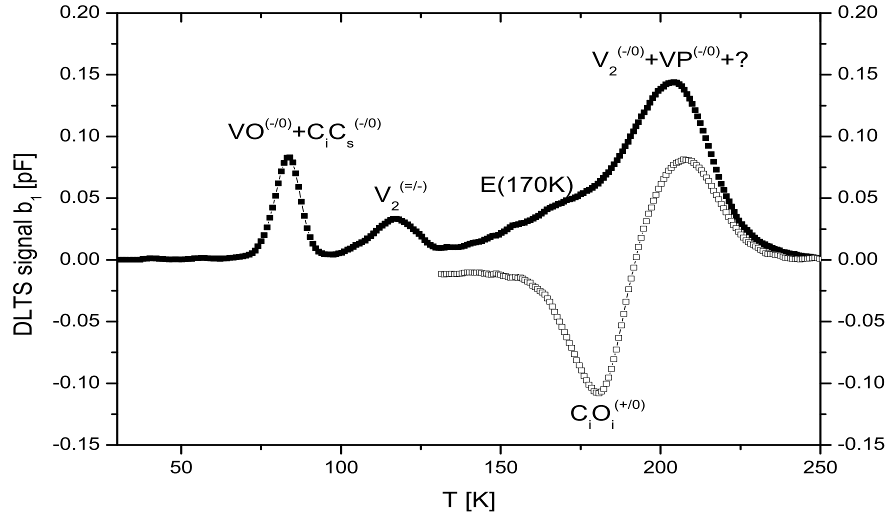

Figure 5.23: *DLTS spectra after electron injection (filled squares) and forward biasing (open squares) of an epi-50-diode irradiated with a fluence of* $\Phi_{eq} = 9.0 \cdot 10^{11}$ cm^{-2} *(reactor neutrons). Measurement:* $U_R = -20$ V, $U_{P,e} = -0.1$ V, $U_{P,f} = 3$ V, $t_P = 100$ ms, $T_W = 200$ ms.

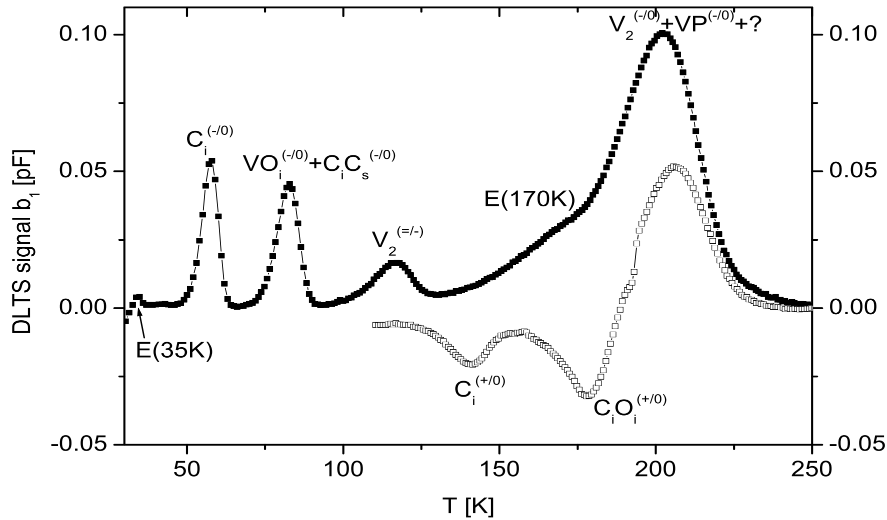

Figure 5.24: *DLTS spectra after electron injection (filled squares) and forward biasing (open squares) of an epi-72-St-diode irradiated with a fluence of* $\Phi_{eq} = 2.7 \cdot 10^{11}$ cm^{-2} *(reactor neutrons). Measurement:* $U_R = -20$ V, $U_{P,e} = -0.1$ V, $U_{P,f} = 3$ V, $t_P = 100$ ms, $T_W = 200$ ms.

where coulomb interaction with small energy transfer is much more likely. Therefore more single vacancies can be generated by charged particles.

The relatively high concentration of oxygen and oxygen dimer in epi-25 material leads to a formation of IO_2-centers in a measurable concentration. The generated C_i's are all captured by oxygen atoms, which results in the C_iO_i-defect. This is the only measurable hole trap after forward biasing in this diode. The small introduction of the $E(35K)$-defect can be regarded as an indication for a short annealing history

of the sample.

In Fig. 5.23 the DLTS spectra for the epi-50 diode are shown. Neither the IO_2-signal nor the C_i-signal can be seen in these spectra. The absence of the first one can easily be explained by the too small source of oxygen dimers in the investigated volume, while the absence of the C_i can only be explained by the long storage time of the sample and a possible annealing out of this defect. This explanation is also supported by the absence of the $E(35K)$-peak which usually anneals out even faster then the C_i-p. The slightly bigger signal from the C_iO_i can be attributed to a lack of other interstitial related defects. Regarding the cluster related defects a similar behavior as observed in the epi-25-sample is detected.

In Fig. 5.24 the DLTS spectra obtained on an epi-72-St-diode are presented. It is very impressive that the signal from the C_i-defect has a bigger amplitude than the one from the A-center. In contrast to the 50 Ωcm epi-samples in 150 Ωcm ones the donor state of the C_i-defect is visible in the spectra. A small contribution from the

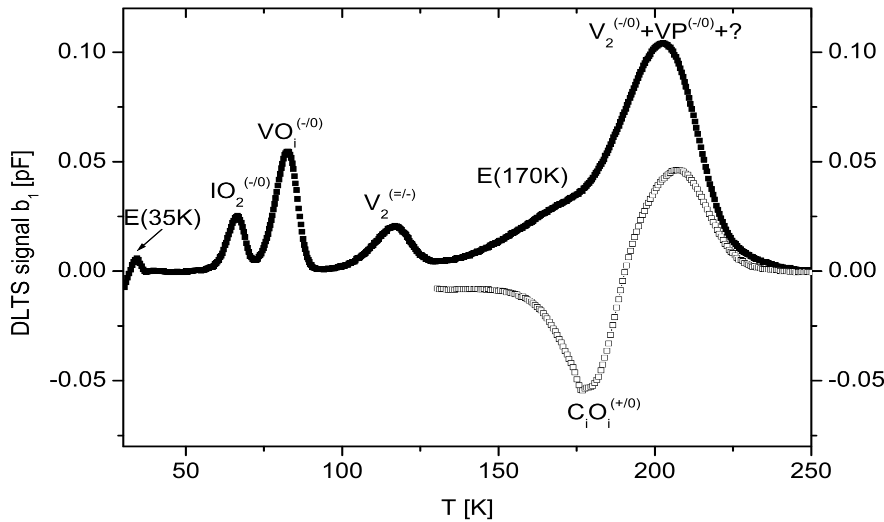

Figure 5.25: *DLTS spectra after electron injection (filled squares) and forward biasing (open squares) of an epi-72-DO-diode irradiated with a fluence of* $\Phi_{eq} = 2.7 \cdot 10^{11}\ cm^{-2}$ *(reactor neutrons). Measurement:* $U_R = -20\ V$, $U_{P,e} = -0.1\ V$, $U_{P,f} = 3\ V$, $t_P = 100\ ms$, $T_W = 200\ ms$.

$E(35K)$-defect can also be seen. Due to the lower oxygen content compared to the other samples less C_i's are captured by O_i's, therefore a large signal from the C_i can be observed while the C_iO_i-defect contributes with a smaller peak to the spectra. The IO_2 is not seen in the epi-72-St-diode. The appearance of the cluster related peaks is similar as in case of the two higher doped epi-samples.

The spectra of the epi-72-DO as shown in Fig. 5.25 reflect the much higher oxygen content compared with the epi-72-St-sample. There is no peak related to the C_i visible in the spectra although the carbon content should be similar. While the C_iO_i-peak is only slightly larger a lot of interstitials are trapped before they become transformed into C_i. This indicates a high content of oxygen dimers in the epi-72-DO-diodes. Regarding the other defects no differences can be seen.

The last spectra presented in this section are from the MCz sample in Fig. 5.26. As already shown in the sections before in the MCz-material a small amount of

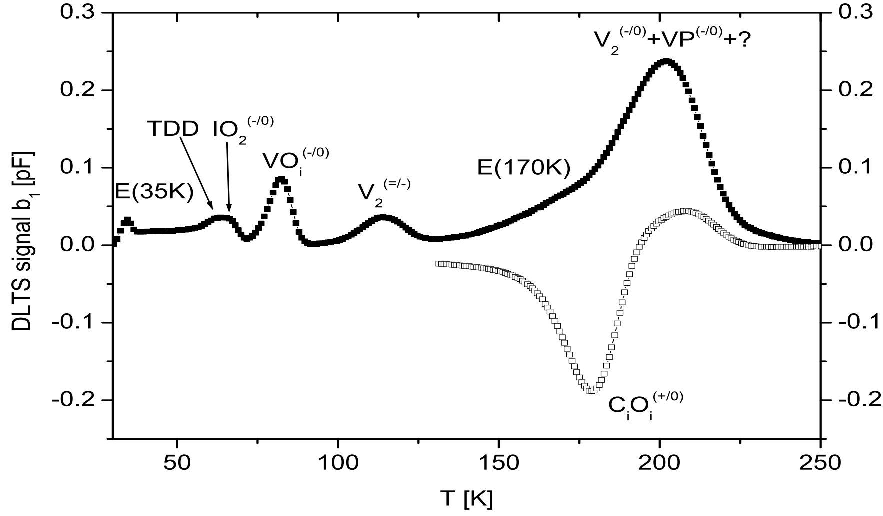

Figure 5.26: *DLTS spectra after electron injection (filled squares) and forward biasing (open squares) of a MCz-diode irradiated with a fluence of* $\Phi_{eq} = 9.0 \cdot 10^{10}\ cm^{-2}$ *(reactor neutrons). Measurement:* $U_R = -20\ V$, $U_{P,e} = -0.1\ V$, $U_{P,f} = 3\ V$, $t_P = 100\ ms$, $T_W = 200\ ms$.

TDD's is already present before irradiation. This concentration is not influenced by the irradiation The relatively low fluence introduces only a small amount of IO_2-defects. Therefore an overlap of its signal with the one from the TDD's is seen. Due to the small signals from these defects a separated evaluation of both concentrations has been difficult. By a simulation of the DLTS-spectrum with the known concentration of the TDD's it has been possible to calculate the concentration of the IO_2-defect. The other peaks in the spectra are due to the signals from the two charged states of the divacancy, the $E(170K)$, the C_iO_i-defect and the A-center. A small peak at 35 K is also detectable.

The introduction rates for the five materials are given in Tab. 5.10 and illustrated in Fig. 5.27.

Defect/Sample	epi 25μm [cm^{-1}]	epi 50μm [cm^{-1}]	epi 72μm [cm^{-1}]	epi 72μm DO [cm^{-1}]	MCZ 300μm [cm^{-1}]
$C_i^{(-/0)}$			0.67		
$IO_2^{(-/0)}$	0.12			0.33	0.21
$VO_i^{(-/0)}+C_iC_s^{(-/0)}$	0.84	0.79	0.56	0.67	0.46
$V_2{}^{(=/-)}$	0.30	0.28	0.23	0.25	0.31
$E(170K)$	0.41	0.41	0.37	0.37	0.33
$V_2{}^{(-/0)}+VP$	1.30	1.25	1.22	1.25	1.24
$C_iO_i^{(+/0)}$	0.70	0.93	0.57	0.65	0.95

Table 5.10: Introduction rates (IR) after reactor neutron-irradiation.

The cluster influenced defects related to the divacancy have similar introduction rates for all five samples. The main differences observed are caused by interstitial related defects. The generation of the C_i-defect is only seen in samples with a relatively low oxygen concentration. In samples with higher oxygen concentration

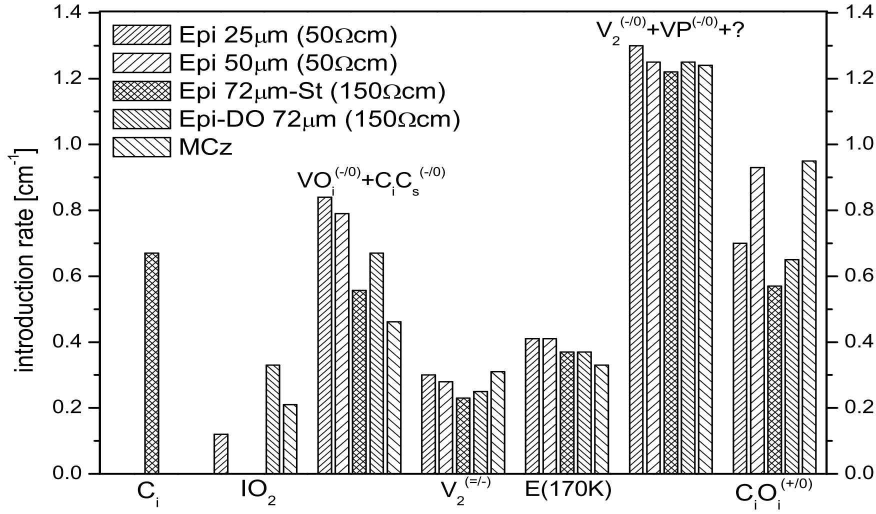

Figure 5.27: *Introduction rates after irradiation with reactor neutrons for all samples.*

the formation of the C_i defect is suppressed in two ways. The first one is due to the higher probability of the C_i to become captured at an O_i-site forming the C_iO_i-defect. The second way starts even before generating the carbon interstitials by capturing the Si_i at an oxygen-dimer-site forming the IO_2-defect. Therefore the sum of interstitials as given in Tab. 5.11 becomes comparable for all materials. The slighly smaller sum for the epi-25 and epi-50 samples might be explained by their smaller thickness which can introduce an additional sink at the surface or the interface to the substrate for interstitials. An explanation for the differences in

	epi-25	epi-50	epi-72	epi-72-DO	MCz
$\sum$ [1/cm]	0.93	0.82	1.24	0.98	1.16

Table 5.11: Sum of the introduction rates of the interstitial related defects after neutron irradiation.

the introduction rates for the peak associated with the A-center is not so easily given. But this finding has already been observed in earlier works [Mol99]. It has to be mentioned that the systematic error in the determined defect introduction rates can easily reach 20% taking into account the error in the fluence measurement, the reproducibility of the defect analysis and the lateral field extension due to the floating guard ring of the diodes.

Chapter 6

Annealing of Radiation Induced Defects

Only a few defects which are observed in DLTS spectra like the single vacancy (V), the silicon interstitial (I), the carbon interstitial (C_i) or the interstitial oxygen dimer (IO_2) are mobile at room temperature. These defects will get trapped at other defects or impurities and form higher order defect complexes which are stable at room temperature. More information about different defects can be achieved performing annealing experiments at different temperatures. A comparison of the annealing behavior of defects with annealing experiments accomplished with other measurement techniques, that give information about the defect structure, are also useful. To accelerate the migration velocity of defects annealing experiments at elevated temperatures can be performed. The higher mobility increases the rate of reactions.

The divacancy is able to migrate starting from temperatures around 250°C, while the VO_i-complex will start to migrate at about 300°C and the dissociation of the C_iC_s can be observed between 200 and 250°C. The probability of reactions is also influenced by the concentration of possible reactants. Therefore the activation energies of annealing reactions strongly depend on the used silicon material and the concentration of its impurities. Some reactions which can occur at higher temperatures around 250°C are listed in Tab. 6.1.

$V_2 + O_i \rightarrow V_2O$	$VO_i + H \rightarrow VOH$	$C_iC_s \rightarrow C_i + C_s$	
$V_2 + O_2 \rightarrow V_2O_2$	$VO_i + O_i \rightarrow VO_2$		$C_i + O_i \rightarrow C_iO_i$
	$VO_i + VO_i \rightarrow V_2O_2$		

Table 6.1: *Possible defect kinetics at higher temperatures.*

It is possible to follow the evolution of the radiation induced defects by annealing studies in a wide temperature range. In this work they are performed in the range between 50°C and 320°C. During the whole experiment the diodes were not removed from the ceramics if possible, because mounting and dismounting can destroy them after a few annealing steps. Former annealing experiments have shown that the ceramic itself does not influence the annealing behavior of the diodes.

6.1 Defects after ^{60}Co-γ irradiation

In order to understand the principle annealing effects in different silicon materials the investigation of point defects is a key technique. The only available irradiation source generating only point defects has been the ^{60}Co-γ-source at BNL. Therefore no problems caused by the generation of clustered regions affect the annealing experiments presented in this section. To investigate the possible annealing reactions different kind of silicon materials have been irradiated and annealed afterwards. DLTS measurements have been obtained on epi-72-St, epi-72-DO, MCz-100 and FZ-50 diodes after each annealing step. The isochronal annealing employed in this section in the range between 120°C and 320°C has been taken 20 min at each annealing temperature. The samples were irradiated in a dose-range from 10 kGy up to 30 kGy.

The annealing of the divacancy studied in several works before (e.g. [Sta04], [Pel01], [Mon02]) has been subject of investigation focusing on the role of the oxygen content of the diodes on the annealing of the divacancies. Therefore three different DOFZ diodes with oxygen concentrations from $6 \cdot 10^{16}$ cm^{-3} up to $12 \cdot 10^{16}$ cm^{-3} were irradiated with a dose of 40 kGy and subsequently annealed up to 50000 minutes at 250°C.

6.1.1 Isochronal annealing of Epi-72-St silicon

An isochronal annealing experiment has been performed on an epi-72-St diode. The sample has been exposed for 20 min to temperatures of 120, 150, 200, 250, 300 and 320°C. After each annealing step DLTS measurements have been performed.

In Fig. 6.1 the evolution of the DLTS spectra for electron injection after irradiation and subsequent annealing steps is shown. Each spectrum resulting from electron injection is separated into two spectra representing the temperature range from 30 K to 100 K and from 100 K to 250 K respectively. In the range from 30 K to 100 K two radiation induced defects can be observed.

One peak can be identified as the negative charge state of the carbon interstitial (C_i). This peak located at about 58 K is already strongly influenced by the lowest used annealing temperatures. Due to its relatively high mobility already at room temperature its trapped either by other C_s's forming the C_iC_s or by O_i's forming the C_iO_i.

The second radiation induced defect is the $VO_i^{(-/0)}$-defect causing the peak at 84 K. This peak is also influenced by the first annealing step. The increase of the peak-height can be explained with the formation of the C_iC_s-defect whose peak overlaps the one of the VO_i-defect.

At higher annealing temperatures also the VO_i+C_iC_s-peak starts to anneal out. The decrease of the peak can be separated into two parts. The first part is attributed to the dissociation of the C_iC_s while the second part at temperatures above 300°C is due to the annealing out of the VO_i itself. This second part of the decay can be correlated with an increase of the defect labeled $E(152K)$, most likely the $VOH^{(-/0)}$-defect (see lower part of Fig. 6.1.

In this figure three radiation induced defects can be observed. It is known from ^{60}Co-γ irradiation that the two negatively charged states of the divacancies can be

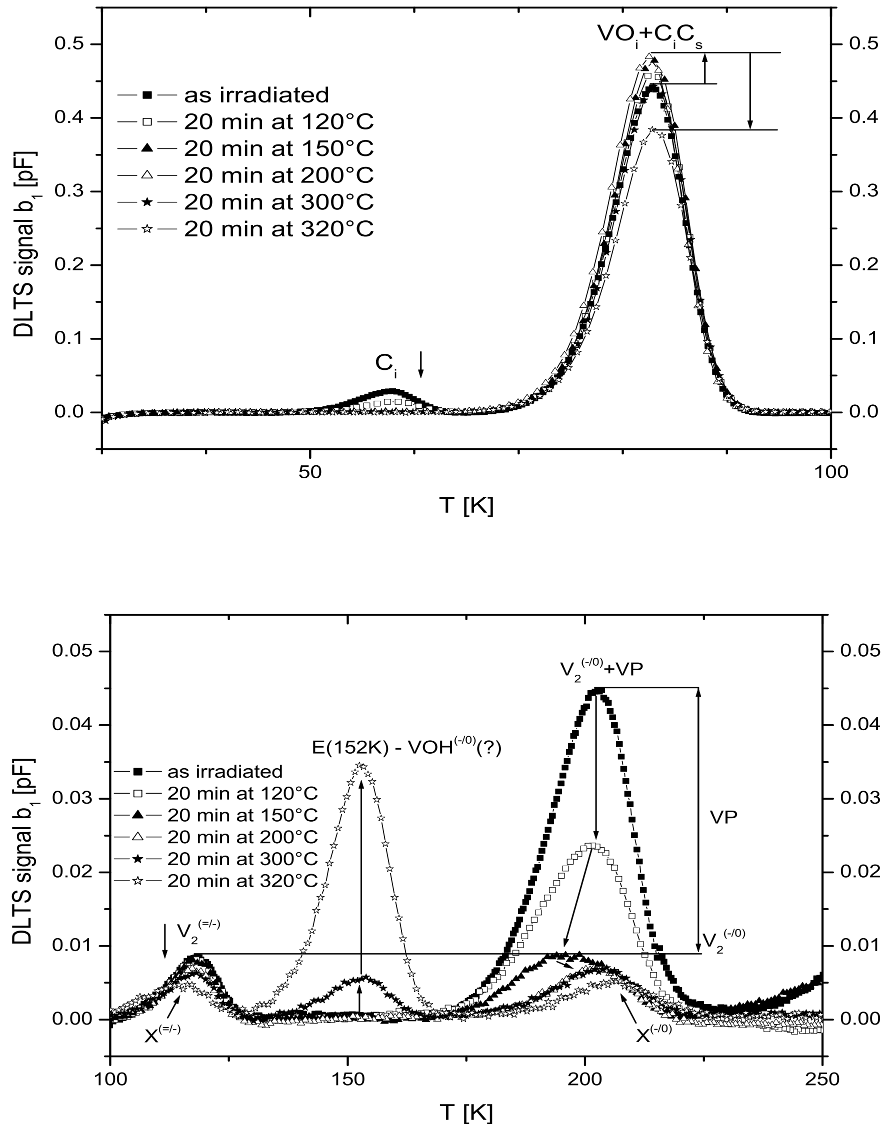

Figure 6.1: *Evolution of DLTS spectra after electron injection of an epi-72-St diode irradiated with a fluence of $\Phi_{eq} = 2.8 \cdot 10^{11}\ cm^{-2}$ (^{60}Co-γ-dose of 30 kGy). Measurement: $U_R = -20\ V$, $U_{P,e} = -1\ V$, $t_P = 100\ ms$, $T_W = 200\ ms$.*

detected with similar peak height in the DLTS-spectra and therefore with similar concentration. The peak observed at 118 K is identified as the one caused by the doubly charged state of the divacancy (${V_2}^{(=/-)}$). The second radiation induced peak at about 204 K is not only caused by the singly charged state of the divacancy (${V_2}^{(-/0)}$) but also by the vacancy-phosphorus (VP) defect. The peak is an overlap of both signals.

The VP defect is known to be the origin of the so called "donor removal". I.e. that those phosphorus atoms which have trapped a vacancy are not electrically active as a donor anymore and therefore the VP is indirectly influencing the effective doping concentration of the diode. The strong decrease of the associated peak can be interpreted as the annealing out of this defect during the first annealing steps. This annealing leads to a release of single vacancies and phosphorus atoms. After

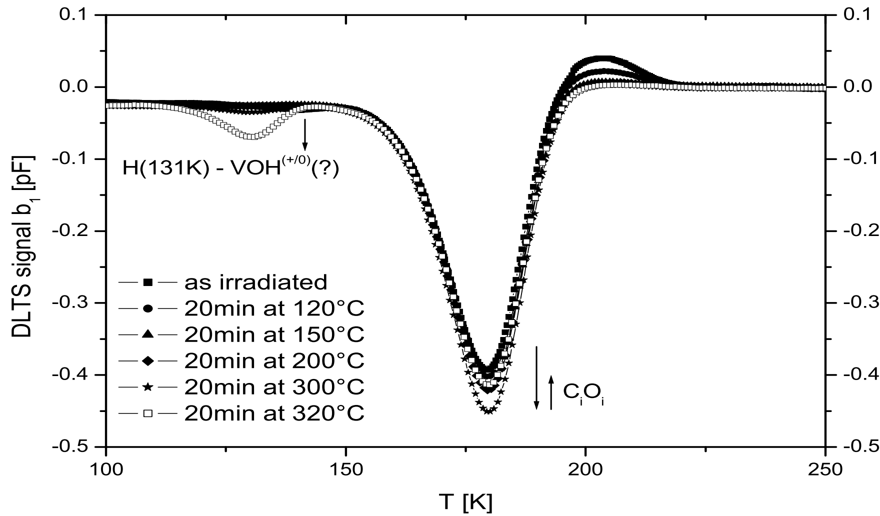

Figure 6.2: *Evolution of DLTS spectra after forward biasing of an epi-72-diode irradiated with a fluence of* $\Phi_{eq} = 2.8 \cdot 10^{11}$ cm^{-2} *(^{60}Co-γ-dose of 30 kGy). Measurement:* $U_R = -20$ V, $U_{P,e} = 3$ V, $t_P = 100$ ms, $T_W = 200$ ms.

the annealing step at 200°C the VP-defect is vanished and the phosphorus atoms can act as donors again.

After the annealing step at 150°C a shift of the peak towards lower temperature can be observed. The relatively broad peak is an indication for a third defect contributing to the peak. After the annealing at 200°C not only the VP-defect but also these unknown third defect is annealed out. Afterwards the peak-height of the $V_2^{(-/0)}$ becomes similar to the one of the $V_2^{(=/-)}$. At even higher temperature a shift of both peaks can be observed. While the $V_2^{(=/-)}$ peak shifts towards lower temperature the $V_2^{(-/0)}$ shifts towards higher temperature. This effect is typically observed for the annealing out of the divacancy in the presence of a relatively high oxygen content [Sta04]. In case of low oxygen concentration it is typically observed that the divacancy dissociate, while in case of high oxygen concentration another annealing reaction with a smaller time-constant is observed. This oxygen related process is the formation of the so called X-defect. Up to now two different interpretations of the nature of this defect are discussed in the scientific community. These two models will be explained later in this chapter. It is also known that the X-defect anneals out at higher temperatures. Which can be followed by the continuing decrease of the shifted peaks in Fig. 6.1 now labeled as $X^{(=/-)}$ and $X^{(-/0)}$.

As already stated above an electron trap becomes visible in the DLTS-spectra at about 152 K at annealing temperatures equal and above 300°C. The increase of this peak coincides with the decay of the VO_i-peak. This peak is most likely caused by the $VOH^{(-/0)}$-defect. The appearance of this defect is well correlated with the increase of a peak caused by a hole trap visible in the DLTS-spectra after forward biasing (see Fig. 6.2). The peak is labeled as H(131K) and most likely associated to the $VOH^{(+/0)}$-defect.

The second peak detectable after forward biasing is associated to the C_iO_i. The peak height increases up to an annealing temperature of 300°C. The main and

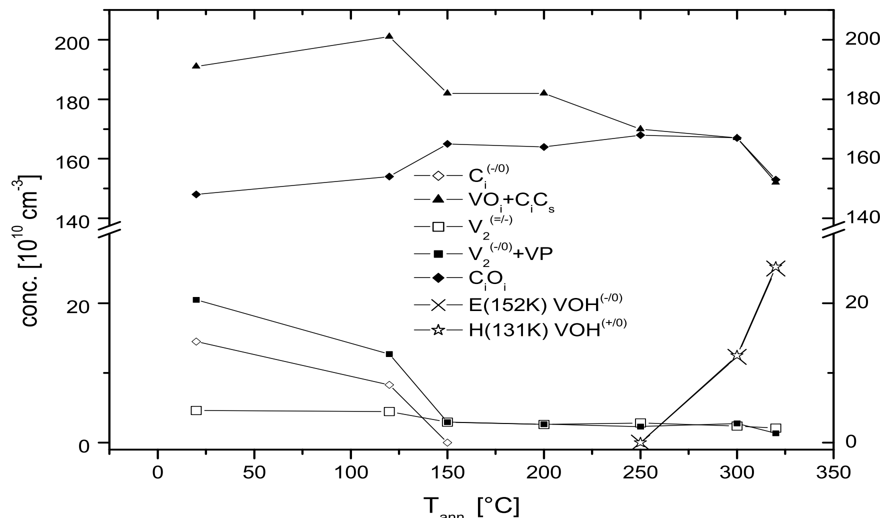

Figure 6.3: *Evolution of the defect concentrations in an epi-72-St diode during an isochronal annealing between 20°C and 320°C for 20min at each annealing step.*

early part can be correlated with the decrease of the C_i-defect. On the other hand the second part of the increase at higher temperatures can be correlated with the annealing out of the C_iC_s, which again is a source of C_i's. At the last annealing step at 320°C a decrease of the C_iO_i-concentration can be observed with a comparable rate as it is observed for the decrease of the VO_i-defect.

The evolution of the concentrations of the detected defects is displayed in Fig. 6.3. The concentration of the two charge stages of the divacancy should have the same concentration during the annealing. Therefore the difference of both can be explained by the VP defect. After the 150°C annealing step the VP is already annealed out and as expected the concentrations of both charged stages of V_2 become equal. At higher annealing temperatures another defect contributing to this concentration has been introduced above. Because the X-defect influences both charged stages of V_2, the measured concentration, representing the overlap of the V_2- and X-defect, stays equal. A separation of both defects as it will be shown in section 6.1.5 for DOFZ diodes has not been performed.

The decrease of the C_i concentration is very well correlated with an increase of the C_iO_i and C_iC_s concentration. The second defect is of course responsible for the increase of the sum of the VO_i and C_iC_s concentration as shown in Fig. 6.3 by the filled circles.

At temperatures of about 250°C the C_iC_s is known to anneal out. It dissociates into C_i and C_s. The C_i can now react with O_i while the reorganization with C_s is not possible at this elevated temperature. This effect is shown in Fig. 6.3.

The C_iO_i decays at temperatures above 300°C. A simple dissociation can not be a reason for this effect, because the C_i-defect would immediately react with the O_i when cooling down the sample and C_iO_i would be reestablished. Therefore two other explanation have to be taken into account. One possibility would be a formation of another new defect. The second possibility would be a dissociation combined with some annihilation of VO_i-centers [Kim76, Mur06]. This mechanism would be supported by the contemporaneous decay of the VO_i as shown in Fig. 6.3.

Nevertheless it has to be noted that the annealing of the VO_i can also be correlated with the increase of the defect labeled $E(152K)$. This defect can be associated with the $VOH^{(-/0)}$-center identified in [Mak03]. Also the donor state $VOH^{(+/0)}$ has been detected in similar concentration. For the evaluation a baseline-shift of the left hand side of Fig. 6.2 has been taken into account. The increase of the VOH is less than the decrease of the VO_i. Therefore it might also be possible that both reactions participate in the evolution of the VO_i, the C_iO_i and the VOH concentrations.

6.1.2 Isochronal annealing of Epi-72-DO silicon

In order to understand differences in the annealing behavior, caused by a much higher oxygen concentration, an epi-72-DO diode has been irradiated with the same dose as reported for the epi-72-St sample. Identical annealing steps have been performed. The evolution of all defect concentrations as function of the annealing temperature is demonstrated in Fig. 6.4.

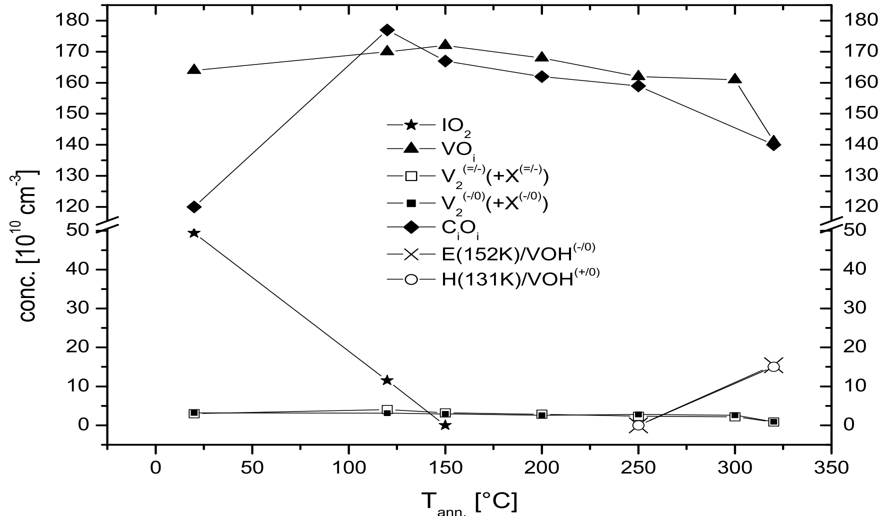

Figure 6.4: *Evolution of the defect concentrations in an epi-72-DO diode during an isochronal annealing between 20°C and 320°C for 20min at each annealing step.*

The DLTS spectra for electron injection were separated into two plots for a better visualization of the corresponding peaks. In Fig. 6.5 both DLTS spectra are shown for the temperature range between 30 K and 100 K and 100 K and 230 K respectively.

The main radiation induced defects are the VO_i- and the IO_2-defect located at temperatures of 84 K and 67 K respectively. The annealing out of the IO_2-defect is mainly observable within in the first annealing step at 120°C. After the second step at 150°C the IO_2 concentration is below the detection limit.

The main peak, which is caused by the VO_i-defect, is not influenced by any heat treatment up to 300°C. The almost constant peak height corresponds quite well with the extracted defect concentration as presented in Fig. 6.4. This observation indicates the absence of the C_iC_s-defect in this material. This is in contrast to the findings in epi-72-St material. At temperatures higher than 300°C the annealing out of the VO_i-defect becomes visible.

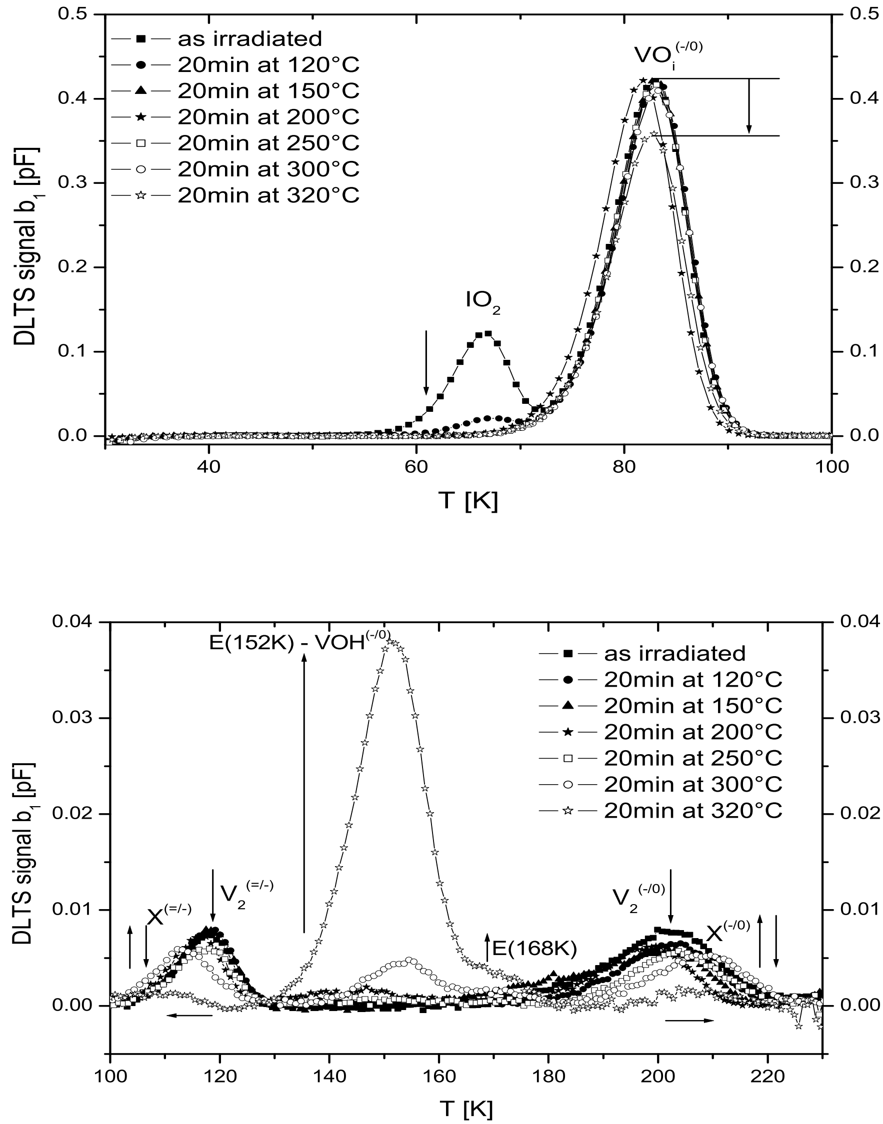

Figure 6.5: *Evolution of DLTS spectra after electron injection of an epi-72-DO-diode irradiated with a fluence of* $\Phi_{eq} = 2.8 \cdot 10^{11}\ cm^{-2}$ *(^{60}Co-γ-dose of 30 kGy). Measurement:* $U_R = -20\ V$, $U_{P,e} = -1\ V$, $t_P = 100\ ms$, $T_W = 200\ ms$.

At the same annealing stage the increase of a peak at 152 K, most likely attributed to the VOH-defect, is observed. The acceptor state of this defect ($VOH^{(-/0)}$) is seen in the lower part of Fig. 6.5. The donor state $VOH^{(+/0)}$ can be seen after forward biasing in Fig. 6.6. Although the VOH-defect already appears at 300°C the main increase of its peaks is observed only after the annealing step at 320°C.

Also the annealing of the two charged stages of the divacancy ($V_2^{(=/-)}$ and $V_2^{(-/0)}$) can be investigated in the lower part of Fig. 6.5. Due to the high oxygen content the formation of the VP-defect is suppressed. Therefore the annealing of the V_2 is not influenced by an overlap of the VP-defect and the $V_2^{(-/0)}$. A remarkable observation is the accelerated shift of both states of the divacancy-related peaks towards lower (${V_2}^{(=/-)}$) and higher (${V_2}^{(-/0)}$) temperatures in the spectra compared to what has been reported for the more oxygen lean material (epi-72-St). This finding can be

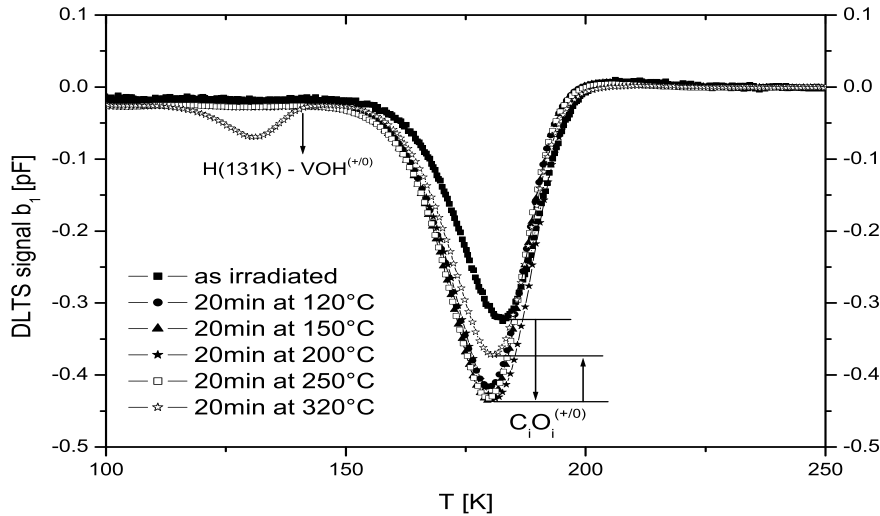

Figure 6.6: *Evolution of DLTS spectra after forward biasing of an epi-72-DO diode irradiated with a fluence of* $\Phi_{eq} = 2.8 \cdot 10^{11}\ cm^{-2}$ *(^{60}Co-γ-dose of 30 kGy). Measurement:* $U_R = -20\ V$, $U_{P,e} = 3\ V$, $t_P = 100\ ms$, $T_W = 200\ ms$.

explained by a more pronounced transformation of the divacnacy into the X-defect. Further, the X-defect is almost annealed out after the annealing step at 320°C. This behavior is also different to that observed for the epi-72-St material. More detailed studies of the annealing of the divacancy and the X-defect will be presented later on in this chapter.

After the last annealing step another defect can be observed in Fig. 6.5 at about 168 K which is labeled $E(168K)$. The origin of this defect is not known.

The most prominent defect after forward biasing is the C_iO_i-defect, visible in Fig. 6.6. The annealing of this defect can be separated into three parts. The first part which corresponds with a huge increase of the C_iO_i can be correlated with the annealing of the IO_2-defect reported above. The released interstitials from the IO_2-defect transfer into interstitial carbon by the already reported *Watkins Replacement Mechanism*. The mobile C_i is afterwards captured by interstitial oxygen atoms forming the C_iO_i-defect. This effect mainly happens within the first annealing step at 120°C. Afterwards the peak-height of the C_iO_i stays quite constant. Only with the last annealing step at 320°C a strong reduction of the defect concentration and the corresponding peak-height is seen. Nevertheless at this point it has to be noted, that the measurements in case of forward biasing after the 300°C annealing step have not been analyzable.

6.1.3 Isochronal annealing of MCz-100 silicon

In this section an isochronal annealing experiment of a MCz-100-diode with a thickness of 100μm is presented. The annealing steps are the same as the one mentioned before with the only exception that the experiment has been stopped already after the annealing step at 300°C. The presentation is done in the same way as in the two previous sections. In Fig. 6.7 the evolution of the main defect concentrations during the annealing experiment is displayed.

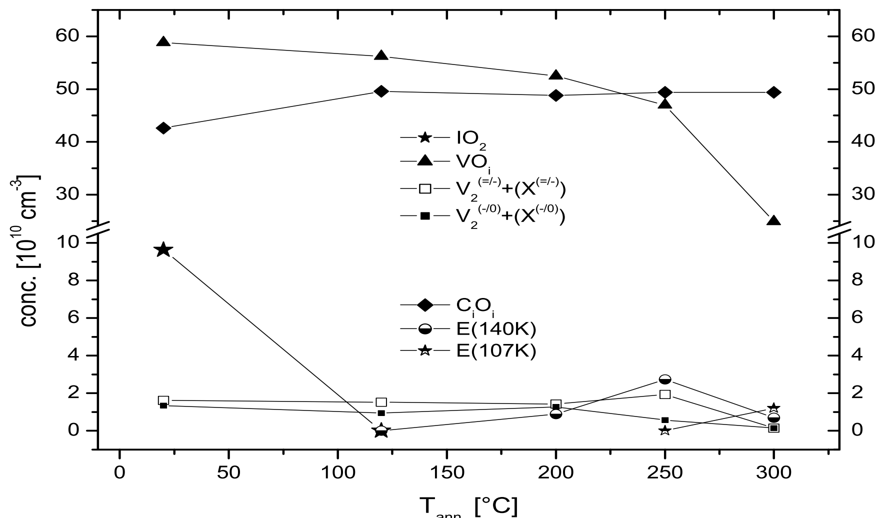

Figure 6.7: *Evolution of the defect concentrations in a MCz-100 diode during an isochronal annealing between 20°C and 300°C for 20min at each annealing step.*

In Fig. 6.8 the DLTS spectra of the main radiation induced electron traps are plotted.

The dominant defect is the VO_i. Its concentration does not change during the first annealing steps. Therefore no formation of the C_iC_s-defect is seen. This finding is in good agreement with the observation reported for the epi-72-DO sample regarding the comparable high oxygen concentration of the MCz-100 diodes. Only the annealing at temperature of and above 250°C leads to a significant decay of the VO_i concentration, which will be demonstrated in Fig. 6.7.

The further radiation induced defect is the IO_2-defect. In can be seen that this defect is slightly overlapped by a second defect the $\mathrm{TDD}^{(+/++)}$. The thermal double donors (TDD's) have already been detected before irradiation. Their concentration was equal to what is measured after the annealing out of the IO_2-defect. Therefore it can be stated that the TDD's are not influenced by irradiation. The IO_2-defect anneals out already after the first annealing step at 120°C.

In the lower part of Fig. 6.8 the other defects which have been detected above 100 K during this annealing experiment are shown. In the DLTS spectrum after irradiation only the two peaks associated with the two acceptor states of the divacancy are detectable. No contribution of the VP-defect is observed.

In chapter 3.4 it has been shown that for the use of the DLTS method the concentration of defects has to be much smaller than the effective doping. Otherwise the capacitance transients needed for this methods do not show an exponential time dependence anymore. Therefore the five times smaller doping of the MCz-100 diodes compared to the epi-72 diodes allows only a smaller introduction of defects and hence a lower dose. This low irradiation dose leads to quite small peaks in the spectra, therefore their evaluation is difficult and the errors in the evaluation of the concentrations are large. But nevertheless the basic annealing trends are visible.

The annealing of the divacancy is only possible to clearly observe in case of the singly charged state. The annealing of the divacancy is strongly enhanced because of the high oxygen concentration of the MCz-100 material compared to the epi-72-

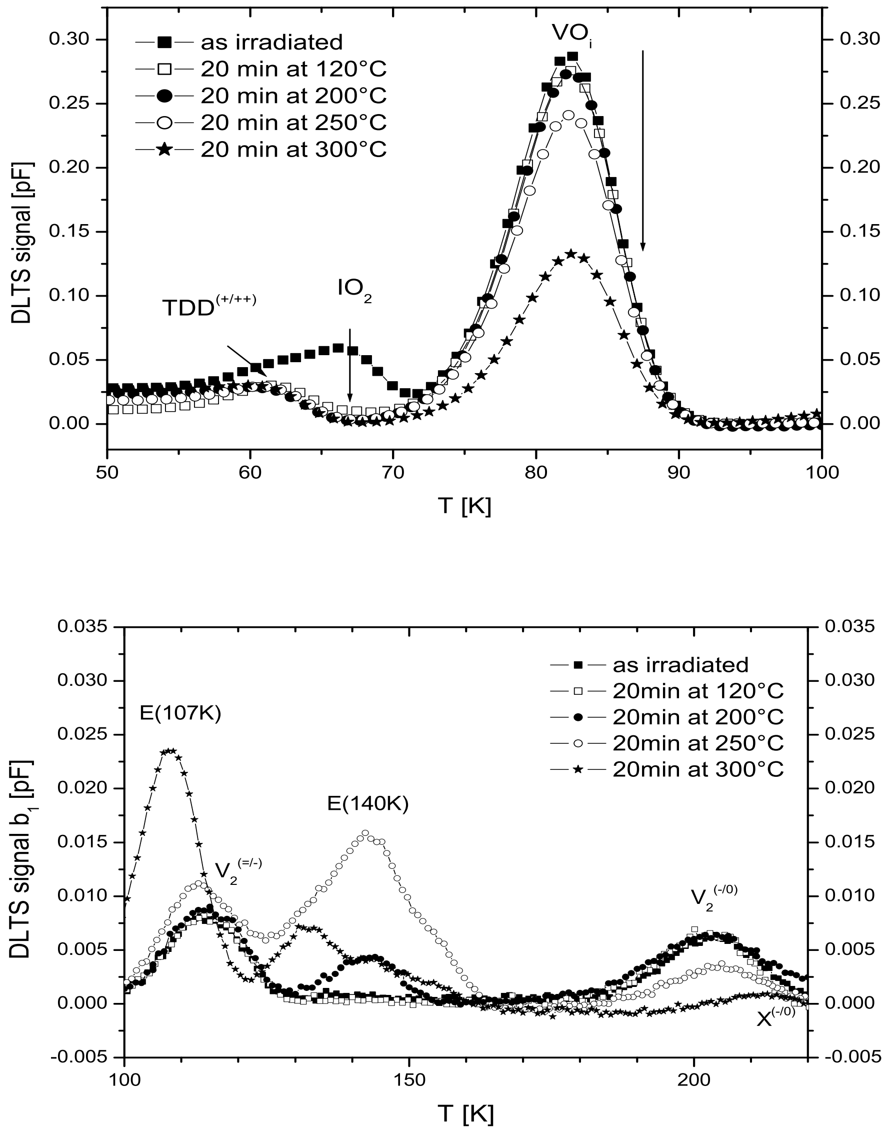

Figure 6.8: *Evolution of DLTS spectra after electron injection of a MCz-100-diode irradiated with a fluence of* $\Phi_{eq} = 0.9 \cdot 10^{11}$ cm^{-2} *(^{60}Co-γ-dose of 10 kGy). Measurement:* $U_R = -20$ V, $U_{P,e} = -1$ V, $t_P = 100$ ms, $T_W = 200$ ms.

St sample. But also the comparison with the epi-72-DO sample indicates a faster annealing of the divacancy in MCz-100 material. The annealing of the V_2 can be observed by the shift of the peak at 204 K towards higher temperature which is an indication for a transformation into the X-defect. The X-defect also seems to anneal out very fast, therefore the peak associated with this defect is almost disappeared after the annealing step at 300°C. Unfortunately this is the only observation which is quite clear regarding the annealing of this MCz-material beside the annealing out of the IO_2.

In the range from 100 K to 150 K in the spectra (see lower part of Fig 6.8) several peaks appear or disappear during the isochronal annealing. Already after the annealing at 200°C an unknown defect labeled $E(140K)$ is formed. This defect seems to be similar to a defect investigated in DOFZ material (see section 6.1.5 and

[Sta04]).

The broadening of the $E(140K)$-peak after the annealing step at 250°C can be explained by the introduction of at least two other peaks, one at about 150 K (possibly the VOH) and a second unknown one at about 130 K. Nevertheless a simulation of the $E(140K)$-peak leads to only small contribution of these two peaks. During the last annealing step the $E(140K)$-defect anneals out by about two third while a new defect at 107 K (labeled $E(107K)$) appears. This peak is overlapping the $V_2^{(=/-)}$-peak and might also be responsible for the increase of the $V_2^{(=/-)}$-peak already after annealing at 250°C. The peak at about 130 K seems to increase at 300°C.

Already at 250°C the VO_i-defect starts to anneal out. At 300°C it is annealed out by almost half of its initial concentration. This can not be associated with any increase of other defects like it is seen in the two epi-diodes. Most likely a formation of electrically inactive defects are responsible for this behavior.

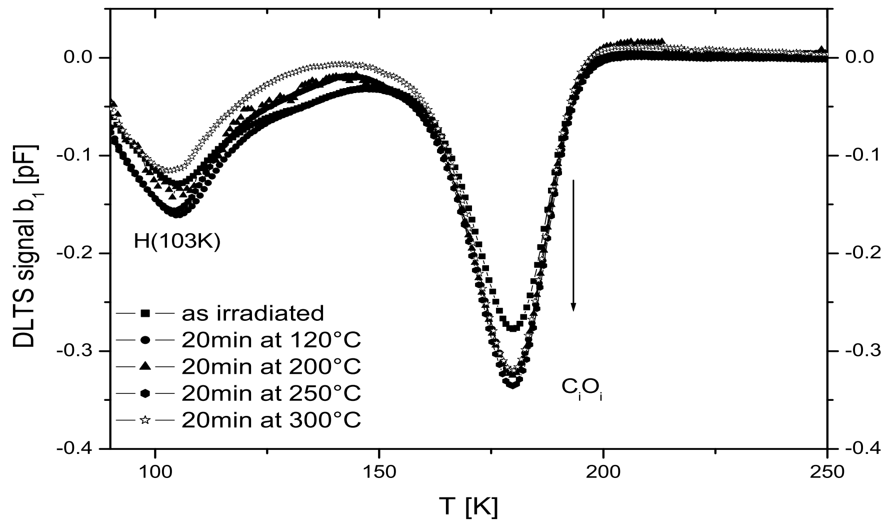

Figure 6.9: *DLTS spectra after forward biasing of a MCz-100-diode irradiated with a fluence of* $\Phi_{eq} = 0.9 \cdot 10^{11}\ cm^{-2}$ *(^{60}Co-γ-dose of 10 kGy). Measurement:* $U_R = -20\ V$, $U_{P,e} = 3\ V$, $t_P = 100\ ms$, $T_W = 200\ ms$.

The defect labeled $H(103K)$ (see Fig. 6.9) cannot be associated with any known defect. The concentration of this defect is not influenced by the annealing process and has also been detected with identical concentration in an unirradiated sample. It can therefore be labeled material- or process-induced. One can speculate about the origin of this effect. Maybe it is caused by the thinning process of the diodes during their production.

The second hole trap visible in that spectra is the C_iO_i-defect. Its peak increases after the first annealing step which can be associated with the annealing out of the IO_2-defect. The change in concentration is almost equal for the decrease of the IO_2-defect as well as for the increase of the C_iO_i-defect. Afterwards this defect stays constant in concentration up to the annealing step at 300°C.

6.1.4 Isochronal annealing of FZ-50 silicon

A fourth material which underwent the same annealing experiment has been the FZ-50 material. This thinned float zone silicon has been irradiated with the same dose as the two epi diodes. The evolution of all detected defect concentrations during this annealing experiment are shown in Fig. 6.10.

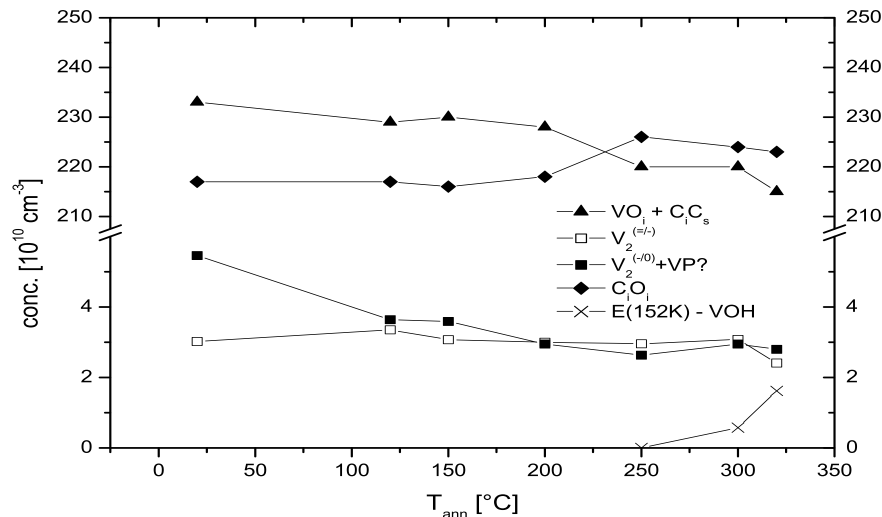

Figure 6.10: *Evolution of the defect concentrations during an isochronal annealing of 20min for each annealing step as indicated in the figure.*

The only defect which is detectable below 100 K in the DLTS-spectra is the VO_i-defect. In Fig. 6.11 its annealing behavior is presented in the upper part of the figure. The concentration of the VO_i-defect stays almost constant up to an annealing temperature of 200°C. At 250°C a decrease of the VO_i concentration can be evaluated from the DLTS measurements. This behavior can be explained with the presence of the C_iC_s-defect from the beginning. This defect is known to anneal out at this temperature [Wat00, Mol99].

A problem for the investigation of defects after ^{60}Co-γ irradiation is the time between irradiation and investigation. The samples have not been cooled during this period therefore some defects like the C_i-defect can start to anneal out. Insofar it is not clear whether the C_i defect would have been detectable in this material directly after irradiation or not. The presence of the C_iC_s-defect implies that the C_i defect had been annealed out during the delay between the irradiation and the DLTS measurement.

The DLTS-spectra after forward biasing are shown in Fig. 6.12. The only hole trap detectable during the annealing experiment is the C_iO_i-defect. Its concentration does mainly increase at 250°C. This finding correlates with the annealing out of the C_iC_s. Before this annealing step no changes of the concentration are observed. This correlates with the absence of the interstitial related defects C_i or IO_2 in the as irradiated sample. Therefore no carbon interstitials are available directly (C_i) or indirectly by annealing of IO_2. Only a slight decrease of the C_iO_i peak can be seen at higher temperatures.

At 320°C a further decrease of the VO_i concentration can be seen, while at the

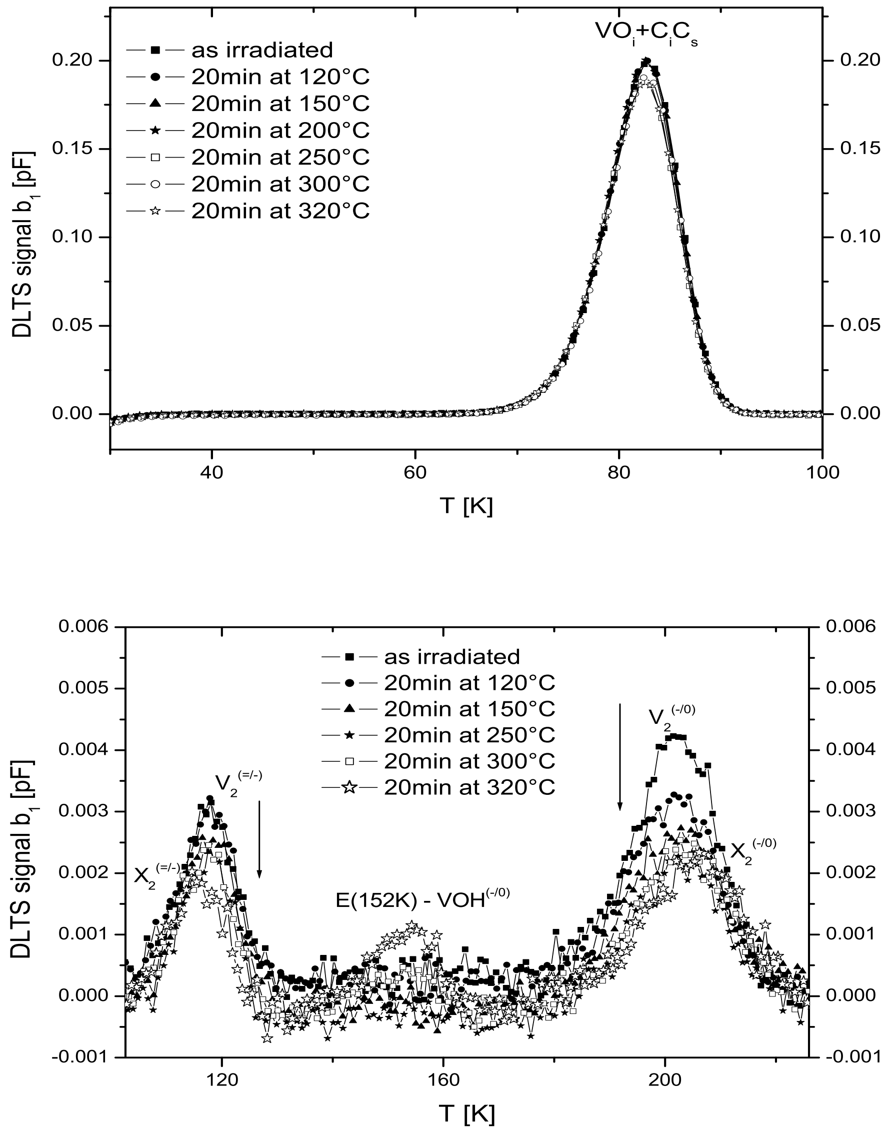

Figure 6.11: *DLTS spectra after electron injection of an FZ-50-diode irradiated with a fluence of* $\Phi_{eq} = 2.8 \cdot 10^{11}\ cm^{-2}$ *(*^{60}*Co-*γ*-dose of 30 kGy). Measurement:* $U_R = -20\ V$, $U_{P,e} = -1\ V$, $t_P = 100\ ms$, $T_W = 200\ ms$.

same time a defect at 152 K appears which is associated with the VOH-defect. This defect is visible in the lower part of Fig. 6.11. Although the spectra are very noisy, which is due to the small signal compared to the background noise, their evaluation has been possible.

The second defect visible in these spectra is the divacancy with its two acceptor states. The peak of the singly charged state is slightly higher than the one of the doubly charged state, which is attributed to a small contribution of the VP-defect. The annealing out of the divacancy is less forced than in epi-72-DO or MCz-100 material. This is an indication for a much lower oxygen content. The shift of the peaks associated to the two charged states of the divacancy at higher annealing temperatures can be explained with a transformation into the X-defect. The formation of the X-defect in this material is an indication for the interpretation

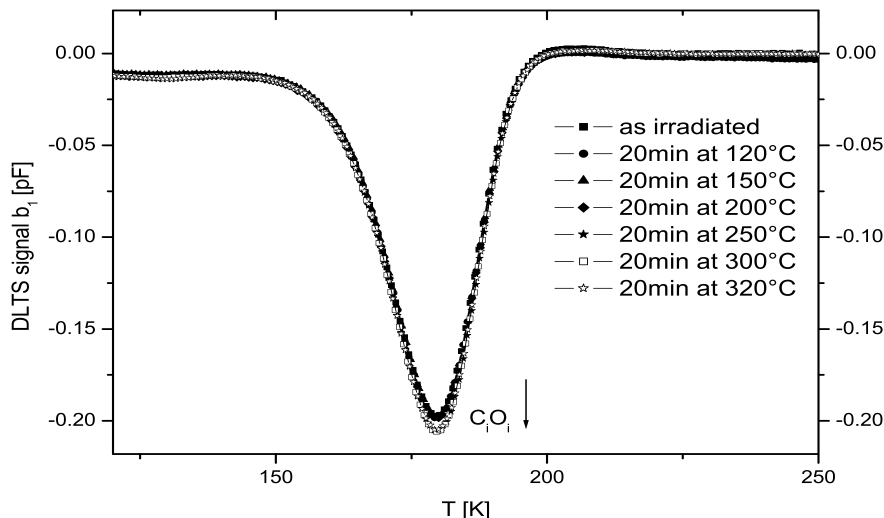

Figure 6.12: *DLTS spectra after forward biasing of an epi-72-diode irradiated with a fluence of* $\Phi_{eq} = 2.8 \cdot 10^{11}\ cm^{-2}$ *(^{60}Co-γ-dose of 30 kGy). Measurement:* $U_R = -20\ V$, $U_{P,h} = 3\ V$, $t_P = 100\ ms$, $T_W = 200\ ms$.

that this material is most likely a DOFZ material than a standard FZ material, since no transformation of the V_2-defect into the X-defect was found in standard FZ material with low oxygen content ([O] $\approx 10^{16}$cm^{-3}) [Sta04].

6.1.5 Isothermal annealing of the divacancy-defect

Several studies have been performed in order to get an insight into the mechanisms responsible for the annealing of the divacancy. At elevated temperatures a typical shift of the $V^{(-/0)}$-peak towards higher temperature and a shift of the $V^{(=/-)}$-peak towards lower temperature in the DLTS spectra is observed. This effect is associated with the formation of the so-called X-defect with its single and double negatively charged states. The shift is within a few Kelvin. A separation of the defects can be performed with the *High Resolution DLTS*.

In case of low oxygen concentration this effect is strongly suppressed [Sta04].

Up to now it is not decided whether the X-defect can be associated to a model introduced by Monakov et al. [Mon02], where the X-defect is identified with the V_2O-defect generated by a capture of the mobile divacancy by an oxygen atom or by a model introduced by Pintilie and Stahl [Sta04], where the X-defect is identified as the V_2O_2-defect, generated via the capture of the divacancy by an oxygen dimer. Both models display the main channel for the generation of the X-defect at doses in the range of less than hundred kGy.

In this work DOFZ diodes with different oxygen content have been investigated in order to understand the influence of the oxygen content on the transformation of the divacancy into the X-defect and its following annealing out. Therefore three different DOFZ diodes labeled cb-, cc- and cd-diodes have been irradiated with a dose of 40 kGy from the ^{60}Co-γ-source. All diodes have been annealed at 250°C and DLTS measurements have been performed at several annealing steps. These isothermal annealing experiments have been pursued up to an annealing time of 840

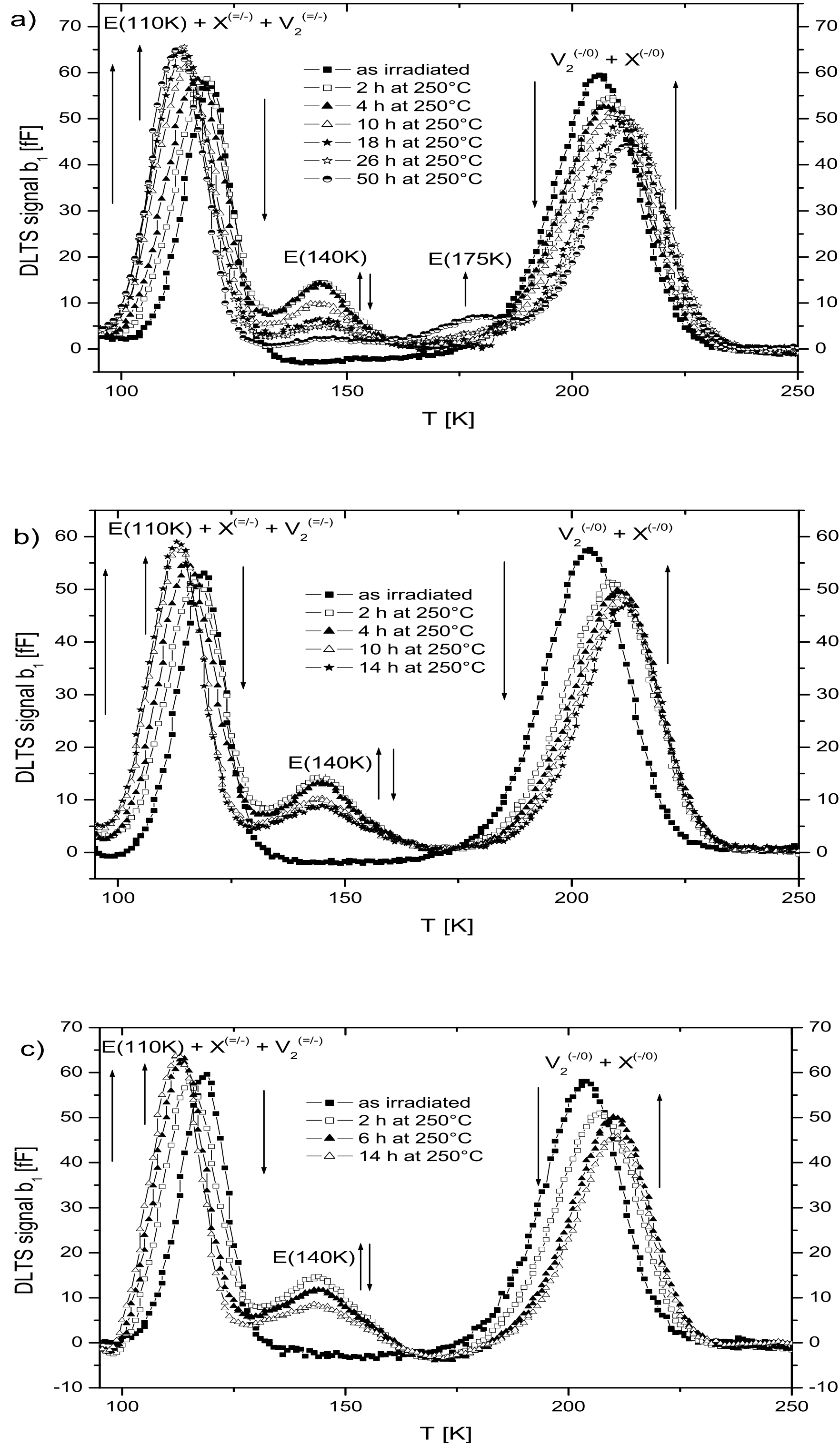

Figure 6.13: *DLTS spectra illustrating the annealing out of the divacancy and the generation of the X-defect after electron injection in a cb- (a), a cc- (b) and a cd- (c) DOFZ-diode irradiated with a fluence of* $\Phi_{eq} = 3.7 \cdot 10^{11}\ cm^{-2}$ *(^{60}Co-γ-dose of 40 kGy). Measurement:* $U_R = -20\ V$, $U_P = -0.1\ V$, $t_P = 100\ ms$, $T_W = 200\ ms$, $T_{ann} = 250°C$.

hours. A separation into two annealing parts, one of the divacancy and a one of the X-defect has been done.

In Fig. 6.13.a the evolution of the DLTS spectra for a cb diode up to an annealing time of 50 h at 250°C is shown. To separate the divacancy and the X-defect HRDLTS measurements have been performed in the range between 106 K and 120 K in order to separate the two doubly charged defects and between 200 K and 215 K to separate the singly charged divacancy and X-defect. Both measurements were performed in steps of 1 K. The same measurement parameters were chosen for the cc and the cd diodes.

The separation of the two doubly charged defects is only possible when introducing a third defect-level. The same defect was found by Stahl [Sta04] while it was not detected by Monakhov [Mon02] nor within any other annealing experiment in this work. This defect, $E(110K)$, is also labeled as the Q-defect (see [Sta04]). It seems to be a defect whose origin is not known and which is typical for the DOFZ material used in this experiment. The formation of the Q-level seems to be independent of the oxygen content of the diodes.

Another defect detectable in all three DOFZ diodes is the E(140K). Its formation is also independent of the oxygen content. It is formed within the first 2 hours of annealing in all three diodes and afterwards it anneals out. After about 100 hours it is vanished.

During the long term annealing a defect labeled $E(175K)$ becomes detectable. The formation of this defect is strongly suppressed by a higher oxygen content. It was associated with the VOH defect in former works [Sta04]. But as it is not known why the formation of the VOH defect should be suppressed by oxygen an identification of this defect with the VOH defect is unlikely.

The much faster annealing out of the divacancies in the cc and the cd-diodes is illustrated in the corresponding DLTS-spectra of both samples in Fig. 6.13.b and Fig. 6.13.c.

The evolution of the divacancy concentration during the annealing at 250°C can be described by exponential functions

$$N_t = N_0 \cdot exp\left(-\frac{t-t_0}{\tau}\right). \tag{6.1}$$

The resulting time-constants are shown in Tab. 6.2.

sample	$\tau_{250°C}$
cb	460 min ± 20 min
cc	210 min ± 10 min
cd	170 min ± 10 min

Table 6.2: *Time constants for the annealing of* V_2

The corresponding evolution of the concentration of the divacancy (average of $[V_2^{(-/0)}]$ and $[V_2^{(=/-)}]$) in all three materials shown in Fig. 6.14 lead to the three time constants, given above, for the exponential behavior of their annealing, depending on the oxygen content of the samples.

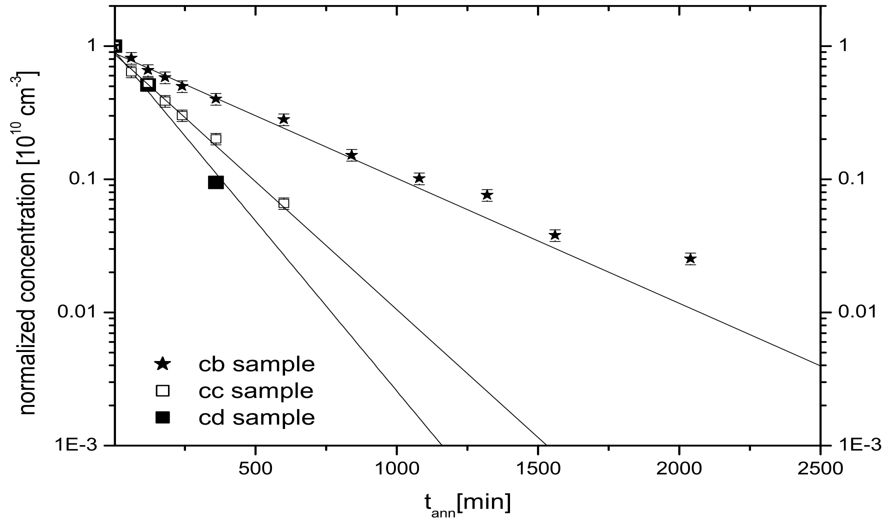

Figure 6.14: *Divacancy concentration of all three DOFZ materials during isothermal annealing at 250°C.*

In contrast to the annealing of the V_2 the annealing of the X-defect is dominated by at least two components. First the formation of the X-defect and second the annealing of it. But the second component already starts with the first generated X-defect. Such a process can mathematically be described by

$$N_X(t) = N_{VV}(t=0)\frac{\frac{1}{\tau_1}}{\frac{1}{\tau_2}-\frac{1}{\tau_1}}\left(exp\left(-\frac{t}{\tau_1}\right) - exp\left(-\frac{t}{\tau_2}\right)\right). \qquad (6.2)$$

With this equation the evolution of the X-defect concentration can be fitted which results in six time-constants, two for each material, as it is shown in Fig. 6.15.a).

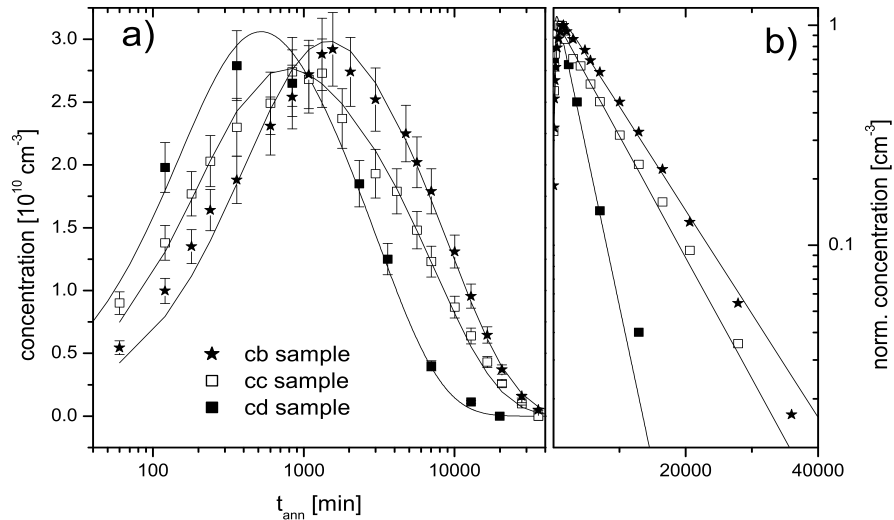

Figure 6.15: *X-center concentration of all three DOFZ materials during isothermal annealing at 250°C.*

In the second part of the figure, labeled b), the exponential decrease of the normalized X-concentration is demonstrated.

The resulting time-constants for the processes are given in Tab. 6.3.

sample	formation of X ($\tau_{250°C}$)	annealing of X ($\tau_{250°C}$)
cb	462 min ± 20 min	9220 min ± 50 min
cc	215 min ± 10 min	7380 min ± 40 min
cd	170 min ± 10 min	2980 min ± 20 min

Table 6.3: *Time constants for the formation and the annealing of the X-defect.*

An alternative to describe the evolution of the X-concentration is based on the reaction kinetics as introduced in section 2.5.1. Therefore the basic model of X-defect being the V_2O [Mon02] is used to analyze the evolution of the X-concentration. The main reactions at 250°C are $V_2 + O_i \rightarrow V_2$O and the dissociation of V_2O into VO_i and V. The corresponding coupled differential equations can be derived by applying the theory for diffusion limited reactions developed by Waite [Wai57]. The corresponding rate equation is:

$$\frac{d[V_2O]}{dt} = -C_{V2O}^{Diss}[V_2O] + \left([VV] - \frac{d[VV]}{dt}\right) \tag{6.3}$$

The first part is the dissociation of the V_2O and the second part its formation. The separated dissociation can be described by:

$$\frac{d[V_2O]}{dt} = [V_2O] \cdot e^{-kt} \tag{6.4}$$

For the rate constant k an Arrhenius behavior is expected:

$$k(T) = k_0 \cdot exp\left(\frac{-E_a}{k_B T}\right) \tag{6.5}$$

With an activation energy $E_a = 2.02 \pm 0.12$ eV and a pre-factor $k_0 = 2 \cdot 10^{13} s^{-1}$, with about one order of magnitude in uncertainty [Mik07].

The second part, which represents the increase of V_2O can be written as:

$$\frac{dV_2O}{dt} = [V_2]_{t=0} - [V_2]_{t=0} \cdot exp\left(-4\pi R \cdot (D_{V_2}(T) + D_{O_i}(T)) \cdot [O_i] \cdot t_a\right) \tag{6.6}$$

The diffusivity of V_2 (D_{V_2}) and O_i (D_{O_i}) follows Arrhenius behavior with activation energies E_a of 1.30 eV [Mik05] and 2.54 eV respectively [Abe98]. The radius R is of 5 Å, $[O_i]$ is the oxygen content given by the SIMS measurements shown in section 3.1.4 and t_a is the annealing time.

Fitting the values for the X-defect with these coupled functions a good fit is only possible for oxygen concentrations being 10 - 30 % higher than extracted from the SIMS measurements. The time-constants are similar to what has been extracted for the mathematical model above. The values are given in Tab. 6.4.

Although the time-constants for the decrease of the X- or V_2O-defect are within the error margins given by [Mik07] a strong dependence on the oxygen content can be seen. This finding suggests that the model for the decrease of the X-defect might

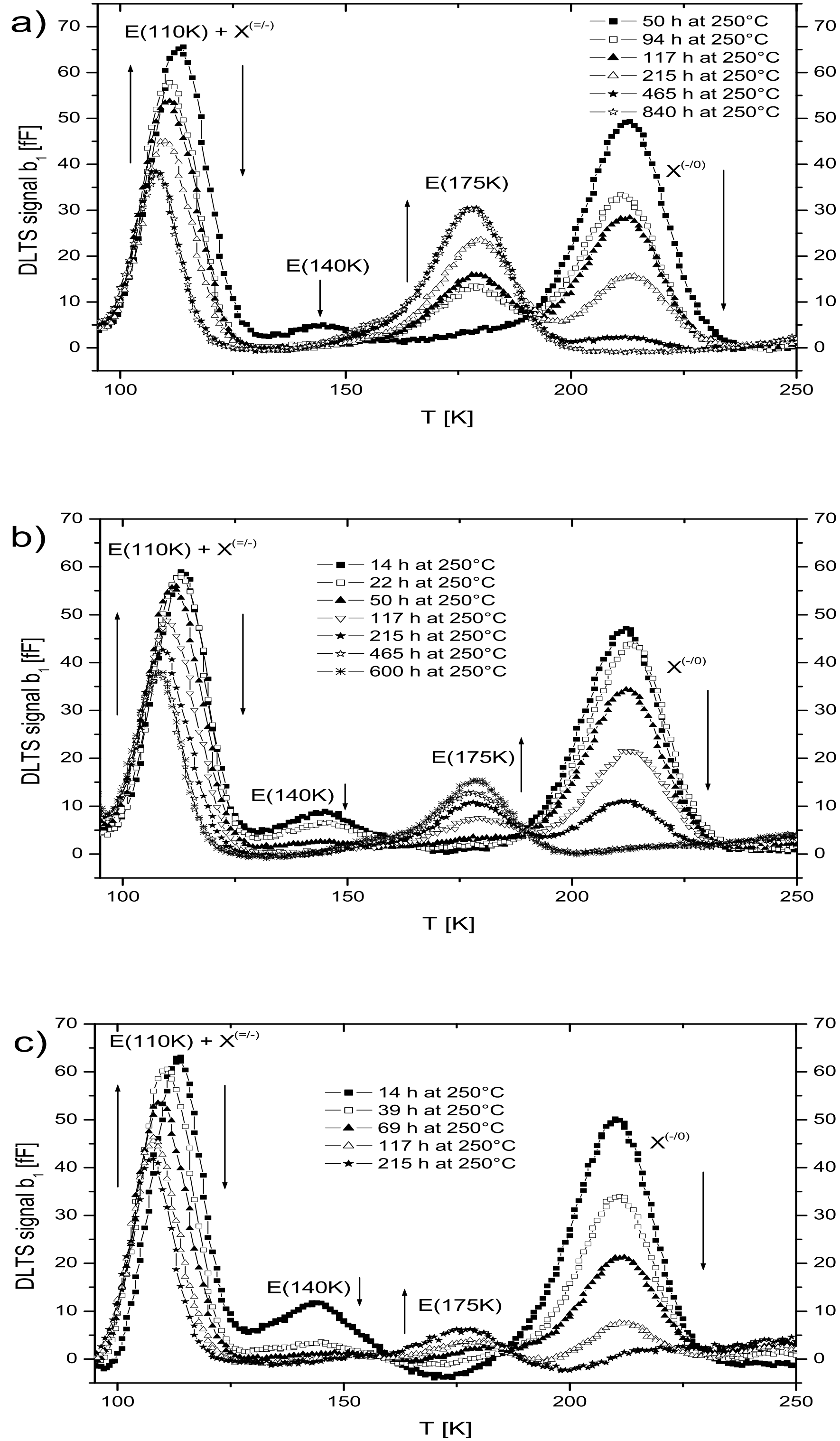

Figure 6.16: *DLTS spectra illustrating the annealing out X-defect after electron injection in a cb- (a), a cc- (b) and a cd- (c) DOFZ-diode irradiated with a fluence of* $\Phi_{eq} = 3.7 \cdot 10^{11}\ cm^{-2}$ *(^{60}Co-γ-dose of 40 kGy). Measurement:* $U_R = -20\ V$, $U_P = -0.1\ V$, $t_P = 100\ ms$, $T_W = 200\ ms$, $T_{ann} = 250°C$.

sample	formation of V_2O ($\tau_{250°C}$)	annealing of V_2O ($\tau_{250°C}$)
cb	462 min	9840 min
cc	215 min	7758 min
cd	170 min	2972 min

Table 6.4: *Time constants for the formation and the annealing of the X-defect (V_2O)*

be more complicated than a simple dissociation. Indeed a dissociation of V_2O into VO_i and V would lead to a capture process (V + $O_i \rightarrow VO_i$). Unfortunately it was not possible to observe the VO_i concentration during this experiment. But also other reactions are oxygen dependent like the reaction (V_2O + $O_i \rightarrow V_2O_2$), as reported in [Lee76].

It has to be noticed that the data can also be fitted with functions assuming X-defect to be V_2O_2. This model needs similar time-constants but smaller oxygen concentrations than reported from SIMS. Therefore no clear answer can be given from these DLTS measurements whether the X-defect can be identified with V_2O or with V_2O_2.

In Fig. 6.16 the DLTS spectra showing the annealing of the X-defect (average of $[X^{(-/0)}]$ and $[X^{(=/-)}]$) are presented for all three DOFZ samples.

Beside the defects observed above two other defects have been detected at 143 K with an energy level of E_C - 320 meV and at 175 K with an energy level of E_C - 360 meV. The first level increases in concentration during the first annealing step and afterwards decreases with an independent time constant for all three DOFZ materials of 1100 ± 100 min. The second level is formed during the annealing of the X-defect and is strongly suppressed by higher oxygen contents. Its increase stops after the annealing out of the X-defect but a correlation with the X-defect would only be speculative. An identification of this defect has not been possible. The Q-defect has been detected with an energy level of E_C - 235 meV.

A second experiment has been performed to get an inside into the annealing of the divacancy by using the TSC-method for higher irradiated samples. In Fig. 6.17 the evolution of the TSC spectra during an isothermal annealing at 300°C for two epi-50 samples irradiated with doses of 3.15 MGy and 5.20 MGy are presented.

While after irradiation with low doses, as shown in the DLTS-experiment above, the concentration of the X-center never reaches the initial concentration of the divacancy in these cases the concentration of the X-centers reaches three respectively five times the initial V_2-concentration. In order to explain such high concentrations more reaction channels have to be taken into account.

The diffusion and dissociation reactions given in Tab. 6.5 have been included in the numerical simulations

With the parameters like diffusion and dissociation constants which can be found in [Pin06b] the simulation results in different evolutions of the concentration depending on the oxygen concentration of the material.

This more complex model than the one used for the simulation of the DLTS results shows that at elevated temperature (300°C) both complexes the V_2O as well as the V_2O_2 can be formed. But with VO_i being the main source for vacancies the simulations show that the V_2O_2 can be produced in similar concentration as measured

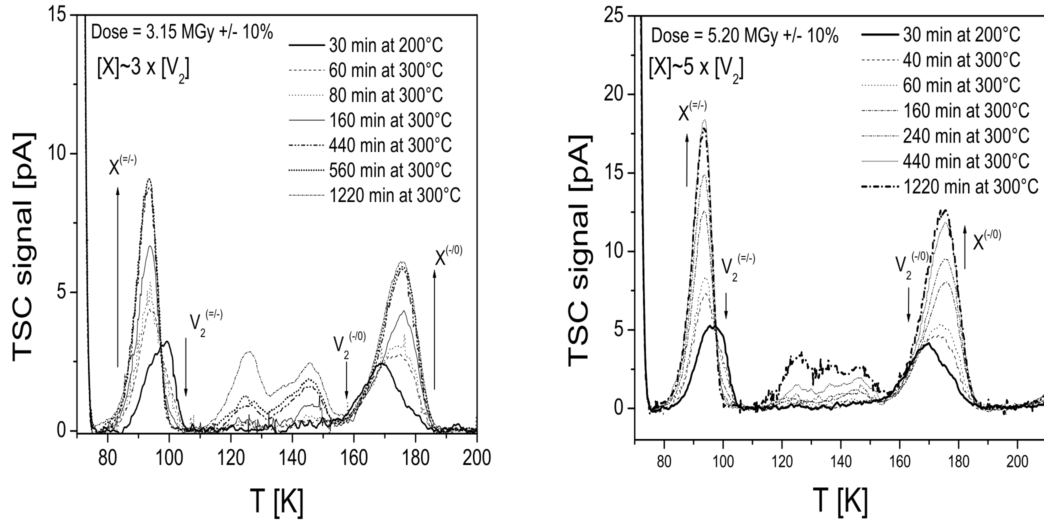

Figure 6.17: *TSC spectra illustrating an isothermal annealing at 300° C of the divacancy for two epi-50 samples irradiated with 3.15 MGy and 5.20 MGy.*

diffusion reactions	dissociation reactions
V + $O_i \rightarrow VO_i$	$VO_i \rightarrow$ V + O_i
V + $VO_i \rightarrow V_2$O	V_2O $\rightarrow$ V + VO_i
V + V $\rightarrow V_2$	$V_2 \rightarrow$ V + V
$V_2 + O_i \rightarrow V_2$O	
$V_2 + O_2 \rightarrow V_2O_2$	$V_2O_2 \rightarrow VO_i + VO_i$
V + $O_2 \rightarrow VO_2$	
$VO_i + O_i \rightarrow VO_2$	
V + $VO_2 \rightarrow V_2O_2$	
$VO_i + VO_i \rightarrow V_2O_2$	

Table 6.5: *Diffusion and dissociation reactions involved in the simulation of TSC results upon X-annealing.*

by TSC while the concentration of the V_2O can not reach this concentration.

Summing-up one can say, that the investigation of the annealing of the divacancy at 250°C can not be terminatory associated with either the formation of the V_2O or the V_2O_2. Both models are able to explain the findings in the the chosen low dose range.

In the higher dose range used for the TSC experiment it is more likely that the annealing of the V_2 is associated with the V_2O_2 than with the V_2O. Nevertheless at 300°C also other reactions become important like the annealing of the VO_i which therefore has been included in the simulations. But for the used epi-50 material it is not known whether other sources for vacancies (e.g. from the Cz-substrate) become important or not. Therefore it is hard to decide whether the X-defect can be associated with the V_2O or the V_2O_2.

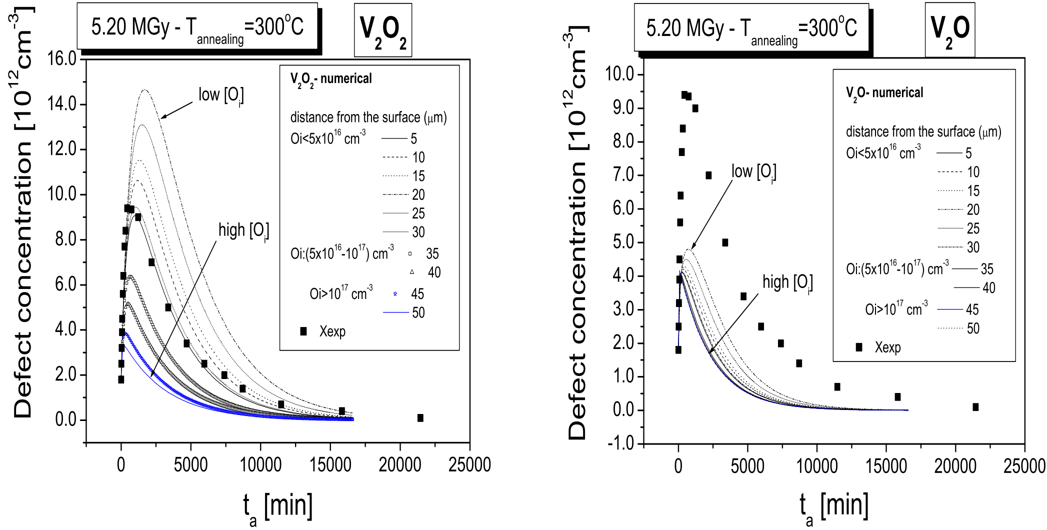

Figure 6.18: *Evolution of the X-defect concentration during an isothermal annealing at 300°C for an epi-50 diode. Fits for different oxygen contents representing the inhomogeneity of [O_i] are included for both models, X assumed to be V_2O_2 (left side) or V_2O (right side).*

6.2 Defects after 900 MeV electron irradiation

Diodes from different materials (FZ, DOFZ, Cz and epi-50) have been irradiated with 900 MeV electrons at the synchrotron light facility Elettra. The reached 1 MeV neutron equivalent fluences are $6.4 \cdot 10^{10}$ cm^{-2} for FZ, DOFZ and Cz diodes and $19.1 \cdot 10^{11}$ cm^{-2} for epi-50 diodes. The annealing has been performed at 80°C up to 111 days. At different annealing stages DLTS spectra were taken.

6.2.1 Isothermal annealing of FZ silicon

In this section the results of the isothermal annealing experiment of the FZ diode are presented. The main damage caused by 900 MeV electrons was described in section 5.2.

In Fig. 6.19 the DLTS spectra after some significant annealing steps are plotted. The defect which anneals out first in time due to the heat treatment is the one labeled $E(35K)$. Already after a few minutes of thermal treatment its peak completely vanishes. At the same time a new peak at 40 K appears. Both peaks are not known. The concentration of the defect $E(40K)$ increases during the first annealing steps and stays constant later on. The much stronger peak at 58 K is typically associated with the acceptor state of the C_i-defect. Also its donor state $C_i^{(+/0)}$ is visible after forward injection. Both peaks are annealing out simultaneously. After 630 min at 80°C the C_i-defect is annealed out. After the same annealing step the increase of the concentration of the C_iO_i and the strong increase of the peak at 84 K stops. This can be explained by a formation of C_iO_i and also C_iC_s which contributes beside the VO_i to the peak at 84 K.

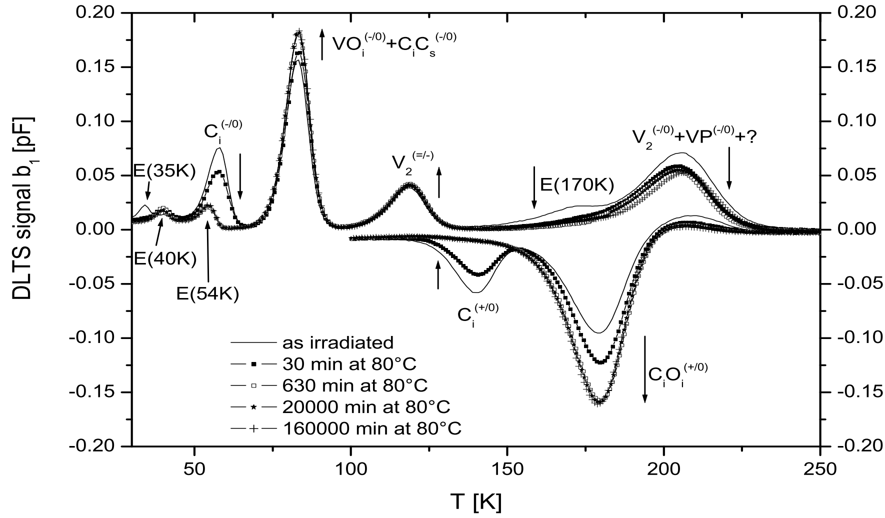

Figure 6.19: *DLTS spectra after electron injection (upside) and forward biasing (downside) of an FZ-diode irradiated with a fluence of* $\Phi_{eq} = 6.4 \cdot 10^{10}\ cm^{-2}$ *(900 MeV electrons). Measurement:* $U_R = -20\ V$, $U_{P,e} = -0.1\ V$, $U_{P,f} = 3\ V$, $t_P = 100\ ms$, $T_W = 200\ ms$.

The evolution of all concentrations during the isothermal annealing is shown in Fig. 6.20. The peak at 84 K is mainly associated with the VO_i-defect. But, as

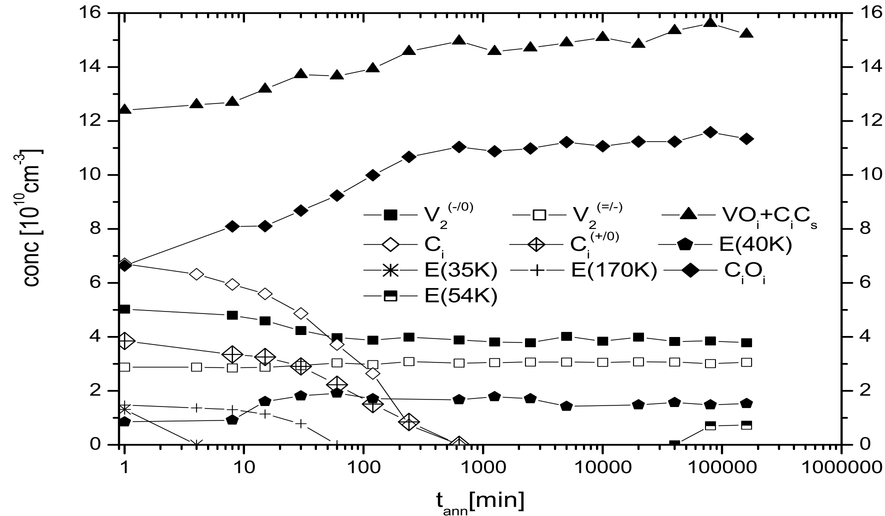

Figure 6.20: *Annealing behavior of different defects in an FZ sample detected after irradiation with 900 MeV electrons with a fluence of* $\Phi_{eq} = 6.4 \cdot 10^{10}\ cm^{-2}$. $T_a = 80°C$.

presented in section 5.2, about 25 % of this initial concentration can be attributed to the overlapping C_iC_s-defect. The concentration of this peak is increasing during annealing up to the time where the C_i-defect is annealed out. The same behavior can be observed for the hole-trap the C_iO_i. Two main channels are available for the annealing of the C_i-defect. While about two third of the C_is are transferred into C_iO_i only one third is transferred into C_iC_s. This ratio of about 2:1 is in good agreement with the initial ratio after irradiation. This result is not surprising because neither

the concentration of oxygen nor the carbon content is changing during irradiation or annealing. The time constant for the annealing of the C_i defect is of about 100 min which is similar to the ones found for the increase of the C_iO_i and the C_iC_s. The same annealing behavior can be found for the donor state of the C_i ($C_i^{(+/0)}$). A smaller concentration of this hole-trap compared with the $C_i^{(-/0)}$-transition can be explained by the similar capture cross sections for holes and electrons of the $C_i^{(+/0)}$ (see [Mol99]). Because of this similarity the defect cannot be fully filled with holes in case of high injection (n = p).

After the annealing out of the C_i another defect labeled $E(54K)$ becomes visible. An identification of this defect is not known up to now.

At about 118 K the doubly charged state of the divacancy is detectable. A small increase of its concentration can be observed during the annealing. This behavior can be explained by the relaxation of the disordered regions. This cluster effect is known to be observable by a suppression of the signal from the doubly charged compared to the signal from the singly charged divacancy.

The annealing of the singly charged divacancy can be separated into two parts. In the first part up to an annealing time of $t_a = 60$ min a fast reduction of the defect concentration is observed. This first part of the annealing proceeds with a similar time constant than the annealing of the $E(170K)$-defect. Unfortunately the origin of the $E(170K)$-defect is not known. From the short term annealing up to 30 min at 80°C visible in Fig. 6.19 it can be suggested that the annealing of the singly charged divacancy is also caused by a second overlapping peak at temperatures a bit bit higher than 204 K. This annealing of two defects overlapped with the divacancy was also reported by [Kuh01] after neutron irradiation.

Afterwards a small but continuous decrease of the $V_2^{(-/0)}$ is seen.

6.2.2 Isothermal annealing of DOFZ silicon

In parallel to the standard FZ diode presented in the last section a DOFZ diode was irradiated with the same fluence. The same annealing procedure has been done with this sample as with the FZ one. A small concentration of thermal donors has been detected already before irradiation. The annealing observed in this sample is mainly due to the annealing of the cluster related defects detectable in the DLTS spectra shown in Fig. 6.21. This is the annealing of the defects attributed to the peaks at 204 K ($V_2^{(-/0)}$) and 170 K ($E(170K)$), which is proceeding in a similar way as it was observed in FZ material. Also the small increase of the peak at 118 K attributed to the doubly charged divacancy is due to the cluster annealing.

Another effect observed in this material is the increase of the defect labeled $E(40K)$. Its increase is finished after the same annealing step of 60 min as the decrease of the $E(170K)$.

The $E(35K)$, seen in the FZ sample, was not detected in this sample. Because of its very fast annealing as reported for the FZ sample it might be possible that the defect was already annealed out at the start of the annealing experiment.

A small contribution of the IO_2-defect observed at 67 K as the right shoulder of the peak attributed to the thermal donors is obviously annealed out after 1250 min as it is shown in the small inlay of Fig. 6.21. This is a bit faster than what will be presented in the next section for Cz-material but it might be only a problem of

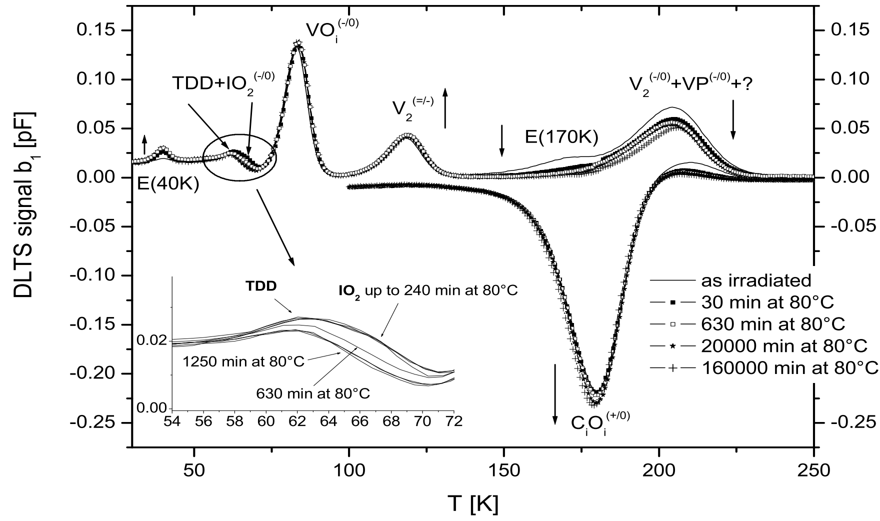

Figure 6.21: *DLTS spectra after electron injection (upside) and forward biasing (downside) of an DOFZ-diode irradiated with a fluence of* $\Phi_{eq} = 6.4 \cdot 10^{10}\ cm^{-2}$ *(900 MeV electrons). Measurement:* $U_R = -20\ V$, $U_{P,e} = -0.1\ V$, $U_{P,f} = 3\ V$, $t_P = 100\ ms$, $T_W = 200\ ms$.

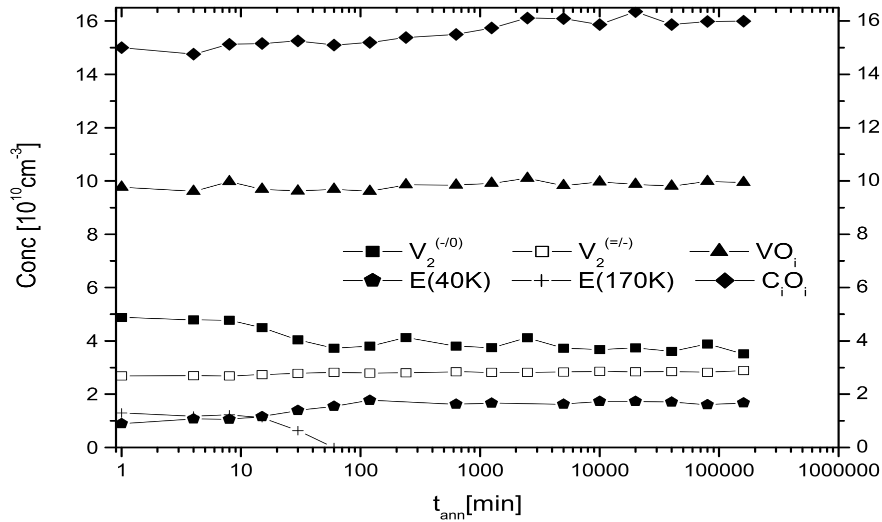

Figure 6.22: *Annealing behavior of different defects in a DOFZ sample detected after irradiation with 900 MeV electrons with a fluence of* $\Phi_{eq} = 6.4 \cdot 10^{10}\ cm^{-2}$. $T_a = 80^\circ C$.

detection of the very small contribution of this defect after 1250 min. Nevertheless the annealing behavior of this defect is in general as expected for the IO_2-defect [Sta04]. Unfortunately it is difficult to extract the correct concentration because the whole peak was first attributed to the thermal donors. Its identification as the IO_2-defect was only possible after its annealing out and therefore a maybe better investigation with the high resolution DLTS was not possible anymore.

The concentration of the VO_i-complex which is also shown in Fig. 6.22 is stable during the whole annealing procedure, while the C_iO_i-defect is slightly increasing. This increase of about 10^{10}cm^{-3} is roughly the same than the IO_2 concentration has

been before annealing. After the annealing out of the IO_2-defect no further build up of the C_iO_i concentration is observed.

An increase of the C_iC_s-defect concentration as observed in FZ material is not seen in the DOFZ sample. Which can be explained with the higher oxygen content and therefore with the higher probability of the C_iO_i formation compared with the FZ diode. As a result the formation of the C_iC_s is totally suppressed.

6.2.3 Isothermal annealing of Cz silicon

In Fig. 6.23 DLTS spectra obtained during an isochronal annealing at 80°C of a Cz diode irradiated with $\Phi_{eq} = 6.4 \cdot 10^{10}\ cm^{-2}$ of 900 MeV electrons are shown. Of special interest was the IO_2-defect which was also detected after gamma-irradiation in the same material [Sta04]. In Fig. 6.23 different annealing steps are presented

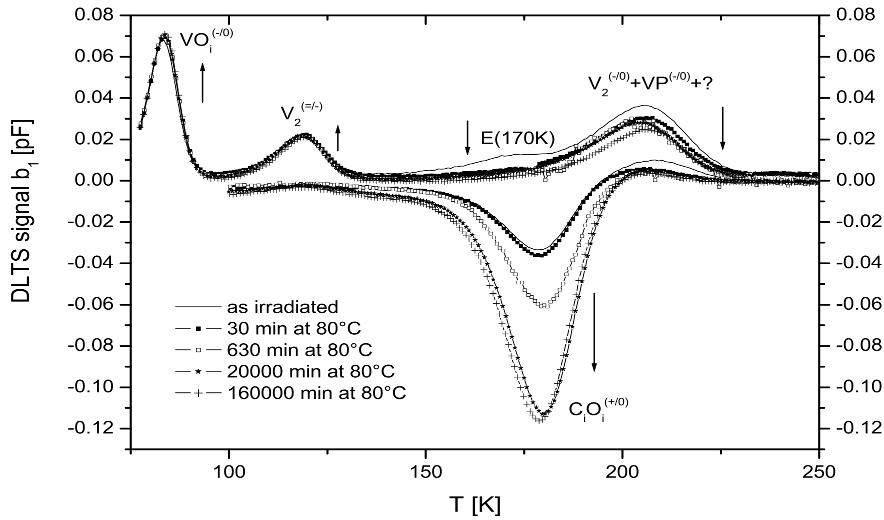

Figure 6.23: *Isothermal annealing at 80°C of a Cz-diode irradiated with a fluence of* $\Phi_{eq} = 6.4 \cdot 10^{10}\ cm^{-2}$ *(900 MeV electrons). Measurement:* $U_R = -20\ V$, $U_{P,e} = -0.1\ V$, $U_{P,f} = 3\ V$, $t_P = 100\ ms$, $T_W = 200\ ms$.

exemplarily. Only a part of the detectable changes are visible in these spectra. The main annealing effect is the strong increase of the peak related to the C_iO_i-defect. This is not correlated with any other change shown in these spectra. At temperatures below the lower limit of these spectra they are dominated by a large peak associated with the TDD's which were found even in unirradiated Cz-samples. The TDD-signal is overlapped by the IO_2-signal as shown in high resolution DLTS spectra in Fig. 6.24. The high resolution DLTS measurements have been employed to separate the IO_2-defect from the the thermal donors. The spectra presented in Fig. 6.24 have been taken at 60 K. Two components are visible in the spectra. The main one at shorter τ is attributed to the TDD's and the second one is attributed to the IO_2-defect. After about 1200 min at 80 °C about 50 % of the IO_2-concentration is annealed out while after 20000 min the component associated to the IO_2-defect vanished totally. The concentration of the TDD's stays stable which results in an almost identical peak-height before annealing and after annealing out of the IO_2-defect. The concentration of the VO_i shows a small increase during annealing. While

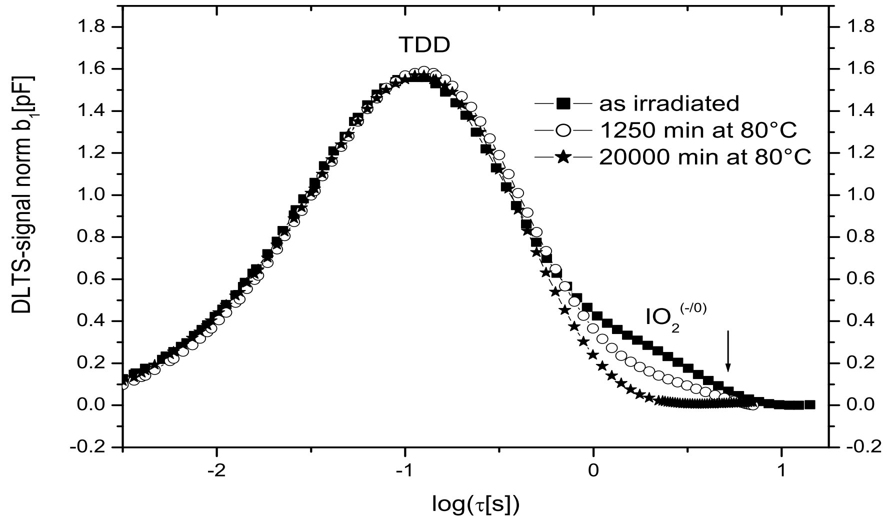

Figure 6.24: *Isothermal spectra of a Cz-diode irradiated with a fluence of* $\Phi_{eq} = 6.4 \cdot 10^{10}$ cm^{-2} *(900 MeV electrons) for different annealing times at 80° C. Measurement:* $U_R = -20$ V, $U_{P,e} = -0.1$ V, $T = 60$ K, $t_P = 100$ ms.

the singly charged state of the divacancy is deceasing as well as the $E(170K)$-defect the doubly charged divacancy is increasing during annealing.

The defects at 35 K, 40 K and 54 K presented in the annealing experiments of the FZ and DOFZ samples are not detectable due to the high concentration of the TDD's.

The time dependence of the defect-annealing detected in Cz-material is shown in Fig. 6.25. It can be seen that the decrease of the IO_2-concentration is correlated

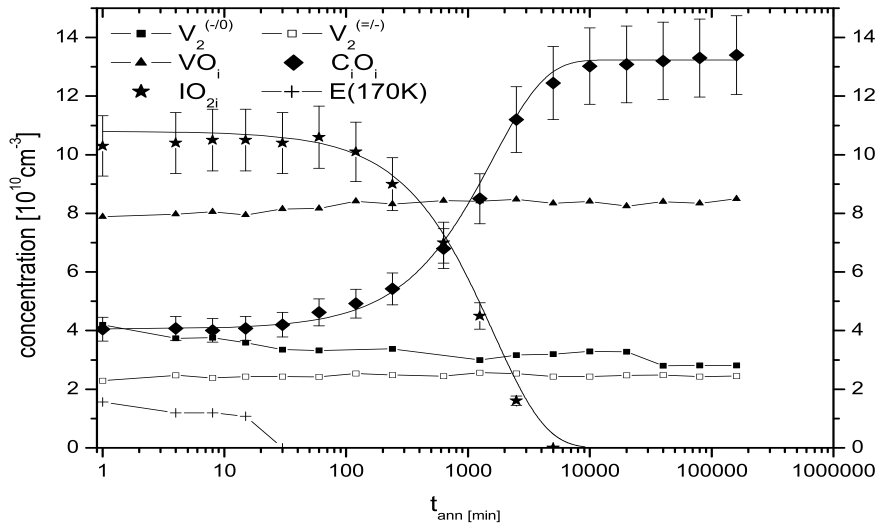

Figure 6.25: *Annealing behavior of different defects in a Cz sample detected after irradiation with 900 MeV electrons with a fluence of* $\Phi_{eq} = 6.4 \cdot 10^{10}$ cm^{-2}. $T_a = 80°C$.

with the increase of the C_iO_i-concentration. The time constants for the decrease of the IO_2 and the increase of the C_iO_i are about 1600 min for the correspond-

ing exponential functions. It was proven by [Lin01a], that the concentration of oxygen-dimers increases during the annealing of IO_2. If the defect dissociates also interstitials must be released. They are mobile at room temperature. Therefore they can replace carbon substitutionals (C_s) via the *Watkins Replacement mechanism*. The mobile C_i is captured by an oxygen atom forming the C_iO_i-complex. Another possible reaction for the interstitials would by to annihilate with a vacancy related defect like the VO_i or the divacancy. But at low fluences the concentration of these defects is to low to play a major role in the annealing of the IO_2-defect. Therefore their concentrations are not affected by this process. The formation of C_iC_s during the annealing of the IO_2 can be excluded because of the high oxygen content of the material which favors the capture of the C_i by an oxygen atom.

The annealing of the singly charged divacancy can be divided into two parts. One part at short times seems to be correlated with the decrease of the $E(170K)$-peak. The second part is attributed to the long term annealing of the clusters. As the clusters anneal out, the lattice strain relieves, and more divancancies can be filled with a second electron. This causes the increase of the signal from the $V_2^{(=/-)}$.

The vacancies escaping from the cluster could be responsible for the small increase of the VO_i-concentration via a capture by an oxygen atom (V + $O_i \rightarrow VO_i$).

6.2.4 Isothermal annealing of epitaxial silicon

An epi-50 diode was exposed to 900 MeV electrons and the achieved fluence was $\Phi_{eq} = 1.9 \cdot 10^{12}\ cm^{-2}$. In Fig. 6.26 the DLTS spectra after different annealing times are

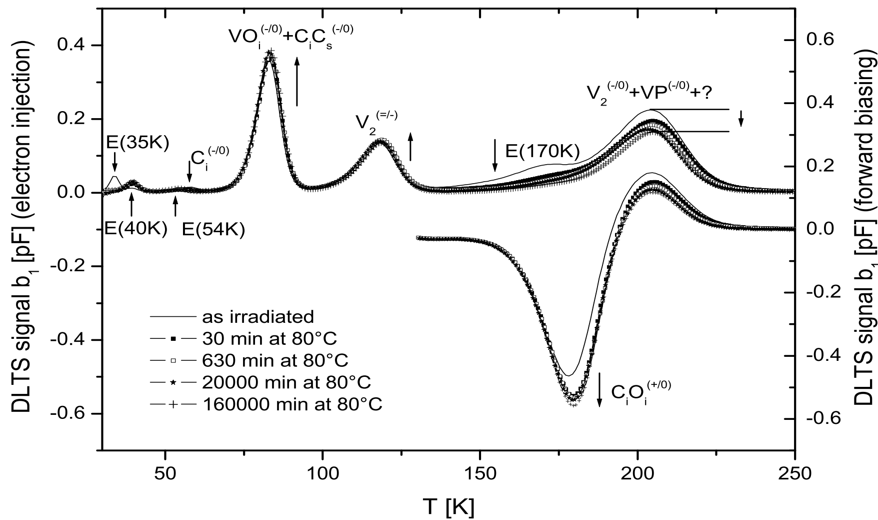

Figure 6.26: *DLTS spectra after electron injection (upside) and forward biasing (downside) of an epi-50-diode irradiated with a fluence of $\Phi_{eq} = 1.9 \cdot 10^{12}\ cm^{-2}$ (900 MeV electrons). Measurement: $U_R = -20\ V$, $U_{P,e} = -0.1\ V$, $U_{P,f} = 3\ V$, $t_P = 100\ ms$, $T_W = 200\ ms$.*

plotted. Already after the first annealing step (7 min - see Fig. 6.27) the $E(35K)$-defect is annealed completely. The increase of the the $E(40K)$-defect concentration can be observed at the same time. Nevertheless this increase cannot be correlated with the decay of the $E(35K)$-concentration since no similarity of time constants

and changes of concentration can be observed for both annealing channels. During the long term annealing the concentration of the $E(40K)$ stays unchanged.

It is surprising that the decrease of the $E(35K)$-level can be correlated with the first step of increase of the C_iO_i-defect concentration as shown in Fig. 6.27 since the change of $[C_iO_i]$ can be related to the change of $[E(35K)]$. Such a relation of the $E(35K)$ with the carbon related defect C_iO_i, C_iC_s and C_i was already supposed by [Mol99]. Nevertheless it is not clear whether the $E(35K)$ defect is a carbon related defect or an interstitial related defect since single interstitials can be transformed into C_i during annealing.

Beside this first annealing step the build up of the $[C_iO_i]$ can be explained by the annealing out of the C_i-defect.

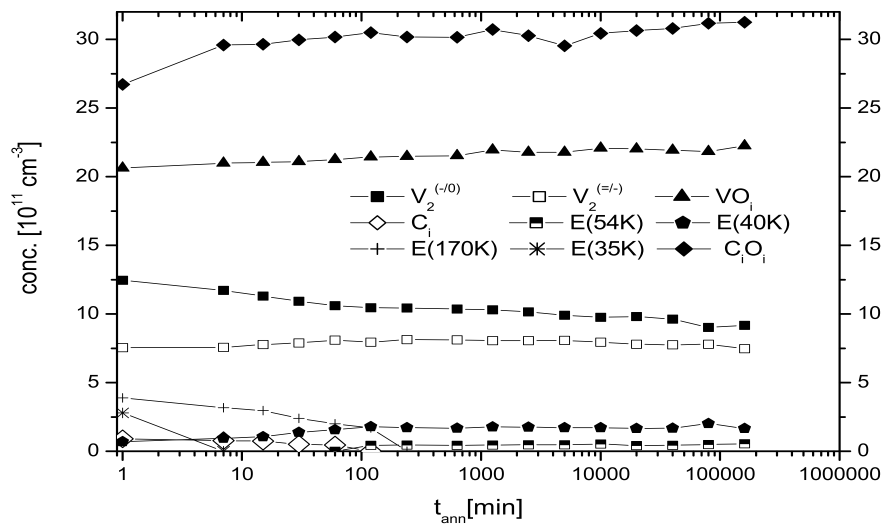

Figure 6.27: *Annealing behavior of different defects in an epi-50 sample detected after irradiation with 900 MeV electrons with a fluence of* $\Phi_{eq} = 19.1 \cdot 10^{11}\ cm^{-2}$. T_a *= 80°C.*

The time constants of this annealing can not only be correlated with the increase of the C_iO_i but also with an increase of the VO_i, which is due to a formation of C_iC_s overlapping the VO_i-defect. After the annealing out of the C_i the concentration of the C_iO_i and the VO_i+C_iC_s stays almost constant. Therefore a lack of interstitials is seen and another source for interstitials has to be assumed. After the annealing out of the C_i-defect a defect at 54 K, labeled $E(54K)$, is detectable. Its origin is not known. The cluster annealing still continues even after the annealing out of the $E(170K)$-peak and the correlated strong decrease of the $V_2{}^{(-/0)}$. This results in a smaller decrease of the $V_2{}^{(-/0)}$ and a continues increase of the $V_2{}^{(=/-)}$.

6.3 Defects after 26 MeV proton irradiation

In this section isochronal annealing studies with the DLTS method in a temperature range from 50 up to 300°C are presented. The studies have been performed on two types of epitaxial silicon devices with layer thicknesses of 72 μm. The samples have been irradiated with 26 MeV protons. The fluences are $8.1 \cdot 10^{11}\ cm^{-2}$ for the epi-

72-St sample and $4.8 \cdot 10^{11}$ cm^{-2} for the epi-72-DO diode. Both values are 1 MeV neutron equivalent values.

6.3.1 Isochronal annealing of epi-72-St-silicon

The changes in the defect concentrations observed during an isochronal annealing between 50 and 300 °C are displayed in Fig. 6.28.

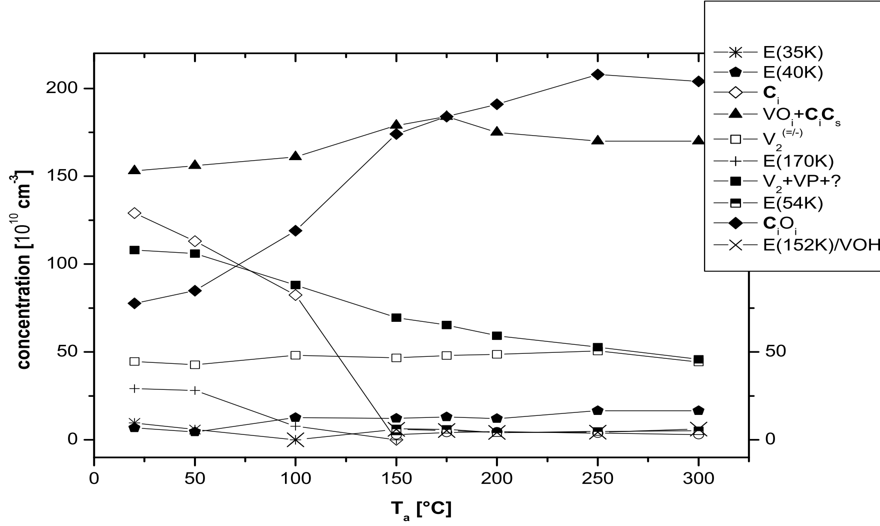

Figure 6.28: *Evolution of concentration during an isochronal annealing of defects detected in an epi-72-St diode irradiated with 26 MeV protons with a fluence of $\Phi_{eq} = 8.1 \cdot 10^{11}$ cm^{-2}. The annealing was performed between 50°C and 300°C for 20 min mainly every 50 K. Measurement: $U_R = -20\ V$, $U_{P,e} = -0.1\ V$, $U_{P,f} = 3\ V$, $t_P = 100\ ms$, $T_W = 200\ ms$.*

The evolution of the electron and hole trap spectra obtained on the epi-72-St diode during this isochronal annealing experiment is shown in Fig. 6.29.

The first defect that anneals out already during the two earliest annealing steps and whose peak in the spectra is vanished at 100°C is the $E(35K)$.

Due to its large initial peak height the C_i-defect can still be detected even after 20 min at 100°C with a concentration of more than 50 % of the initial one. At 150°C this peak is almost vanished. This behavior is not only observed for the $C_i^{(-/0)}$ but also for the $C_i^{(+/0)}$ in the lower part of Fig. 6.29.

In parallel to the decay of the C_i an increase mainly of the C_iO_i is seen. This finding has already been explained by the capture of the mobile C_is at O_i-sites. Due to its small concentration compared to the C_i a role of the $E(35K)$ in the formation of the C_iO_i, as shown before, can neither be accepted nor negated. Due to the relatively small oxygen concentration of this material also an increase of the peak at 84 K is observed. This is mainly associated with a formation of the C_iC_s defect. At higher annealing temperatures up to 250°C a subsequent decrease of the peak at 84 K is seen which is due to the annealing of the C_iC_s at these temperatures. The released C_is are immediately captured by O_is forming C_iO_i. Therefore the decay of the C_iC_s is accompanied by an increase of the C_iO_i peak-height.

Nevertheless the height of the peak at 84 K is larger after annealing than before. Since the C_iC_s is annealed out after 20 min at 250°C this difference is correlated

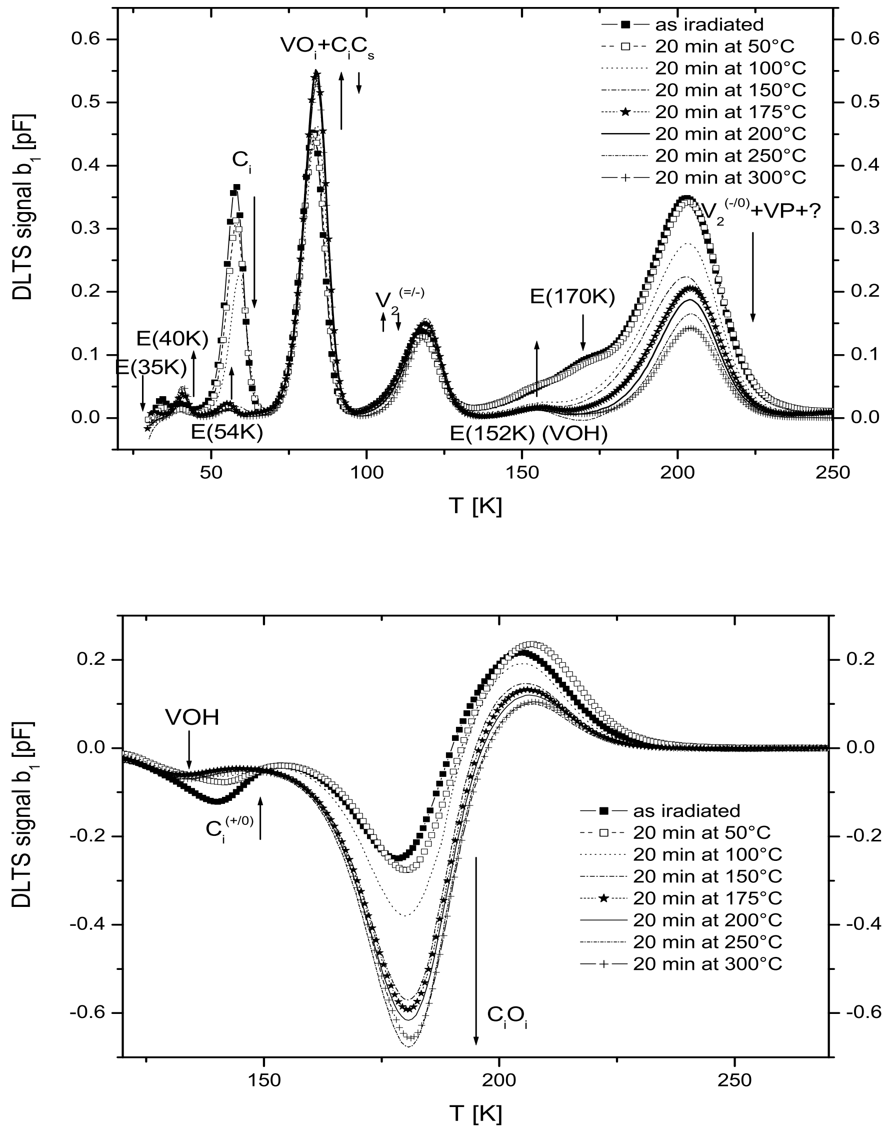

Figure 6.29: *Isochronal annealing of an epi-72 diode irradiated with 26 MeV protons with a fluence of* $\Phi_{eq} = 8.1 \cdot 10^{11}\ cm^{-2}$*. The annealing was performed between 50°C and 300°C for 20 min mainly every 50 K. Measurement:* $U_R = -20\ V$, $U_{P,e} = -0.1\ V$ *(top),* $U_{P,f} = 3\ V$ *(bottom),* $t_P = 100\ ms$, $T_W = 200\ ms$.

with an increase of the VO_i concentration, which can be explained by a release of vacancies from the clustered regions during the annealing. These vacancies are captured by O_is introducing more VO_is.

The main defect attributed to the clustered regions is the V_2. The increase of the $V_2^{(=/-)}$ concentration during annealing up to 250°C is due to cluster-annealing. The decrease of the $V_2^{(=/-)}$-peak after annealing at 300°C is correlated with the annealing out of the V_2 itself. Since no peak shift is observed for both charged states of the divacancy at high temperatures no transformation of the V_2 into the X-defect can be expected.

To describe the annealing of the $V_2^{(-/0)}+VP+?$-peak more considerations have to be taken into account. To visualize the different annealing behavior of this peak

at lower temperatures up to 150°C and higher temperatures up to 250°C difference spectra are shown. The annealing up to 150°C, represented by Fig. 6.30.a), is dominated by the annealing out of the $E(170K)$ and a defect labeled $E(210K)$ (see also [Mol99]). The annealing thereafter up to 250°C is dominated by a defect labeled $E(190K)$ (sometimes also labeled as $E(205a)$ [Mol99]). The corresponding difference spectrum of the two annealing stages of 20 min at 150°C and 250°C is shown in Fig. 6.30.b). After annealing at 250°C the peak heights of both charge states of the divacancy are equal. The annealing of the VP-defect can not be seen because of its very small initial concentration of about 1-2 % compared to the concentration represented by the whole $V_2^{(-/0)}$+VP+?-peak.

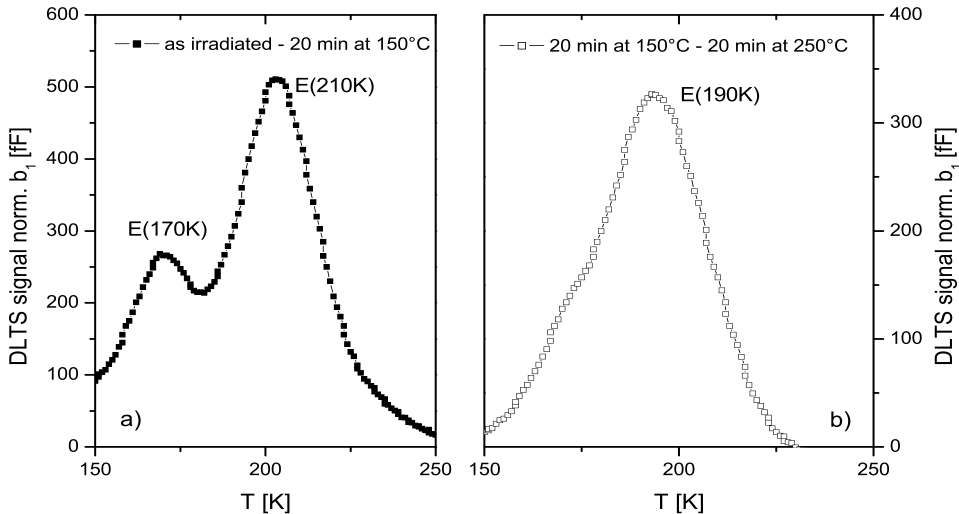

Figure 6.30: *Difference spectra of an epi-72-St diode irradiated with 26 MeV protons with a fluence of* $\Phi_{eq} = 8.1 \cdot 10^{11}$ cm^{-2}*. Measurement:* $U_R = -20$ V*,* $U_{P,e} = -0.1$ V *(top),* $U_{P,f} = 3$ V *(bottom),* $t_P = 100$ ms*,* $T_W = 200$ ms*.*

Already during the first annealing steps an unknown peak labeled $E(40K)$ emerges in the electron-trap spectra (upper part) of Fig. 6.29.

After the annealing out of the C_i-defect a defect already observed in previous sections and labeled as $E(54K)$ becomes visible.

At annealing temperatures higher than 100°C a peak at about 152 K becomes measurable. From the DLTS spectra it seems that this peak has already been there directly after irradiation but being overlapped by the cluster related peaks. This peak is most likely attributed to the $VOH^{(-/0)}$. Also the donor state of the VOH becomes detectable in the spectra of the lower part of Fig. 6.29.

6.3.2 Isochronal annealing of epi-72-DO-silicon

The evolution of defect concentrations observed during an isochronal annealing experiment between 50 and 300°C is shown in Fig. 6.31.

In Fig. 6.32 the different DLTS spectra after electron injection and forward biasing during the isochronal annealing experiment are presented.

Starting at low temperature in the spectra the first detected defect, the $E(35K)$, anneals out already during the first two annealing steps. At 100°C the related peak

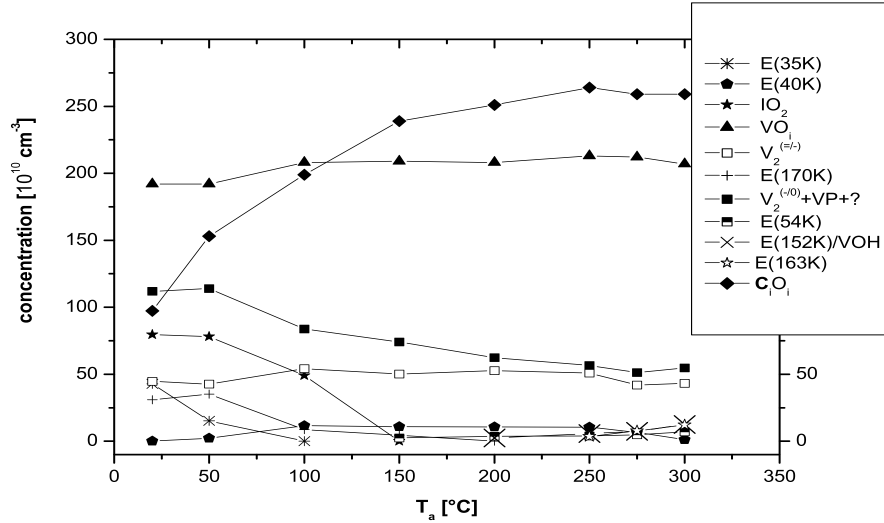

Figure 6.31: *Isochronal annealing behavior of defects detected in an epi-72-DO diode irradiated with 26 MeV protons with a fluence of* $\Phi_{eq} = 4.8 \cdot 10^{11}\ cm^{-2}$. *The annealing was performed between 50°C and 300°C for 20 min every 50 K. Measurement:* $U_R = -20\ V$, $U_{P,e} = -0.1\ V$, $U_{P,f} = 3\ V$, $t_P = 100\ ms$, $T_W = 200\ ms$.

is vanished. The decay of this peak coincides with the increase of the C_iO_i-peak in the lower spectra of Fig. 6.32. Therefore there is evidence to suggest that the $E(35K)$ is an interstitial or carbon-interstitial related defect.

The strong increase of the C_iO_i concentration during these first annealing steps would usually be explained by the decay of the IO_2 concentration. But up to 50°C no decay of the IO_2 is seen, and up to 100°C only 50 % of the increase of the C_iO_i concentration can be explained by the IO_2 while the second half can be explained by the $E(35K)$. Also after the annealing out of the IO_2 at 150°C the increase of the C_iO_i cannot be explained only by the IO_2, while two sources, IO_2 and $E(35K)$ can.

A formation of C_iC_s is not observed. This finding is due to the high oxygen concentration of this material which favors the formation of C_iO_i instead of C_iC_s.

The small increase of the VO_i concentration during the experiment can be explained by released vacancies from the clustered regions captured at O_i-sites.

The first parts of the annealing of the two negatively charged states of the V_2 are similar to what is presented for the epi-72-St diode. The increase of the $V_2^{(=/-)}$ is seen as well as the annealing of the peak $V_2^{(-/0)}$+VP+?, dominated by an annealing out of two defects, labeled $E(170K)$ and $E(210K)$ (see Fig. 6.33.a)), at low annealing temperatures and the annealing out of a defect, labeled $E(190K)$, at higher temperatures (see Fig. 6.33.b)). At temperatures above 250°C a shift of the $V_2^{(=/-)}$ towards lower and of the $V_2^{(-/0)}$ towards higher temperatures is detected. This effect which is is contrast to the observation in epi-72-St material is due to a transformation of the divacancy into the X-defect. The VP-defect is mentioned in the figures but is to small to play a role in the displayed spectra.

During the first annealing steps the $E(40K)$ emerges in the spectra. Up to 250°C no change in its concentration is observed. At higher temperatures this defect disappears. This finding has not been seen before. At the same time a defect

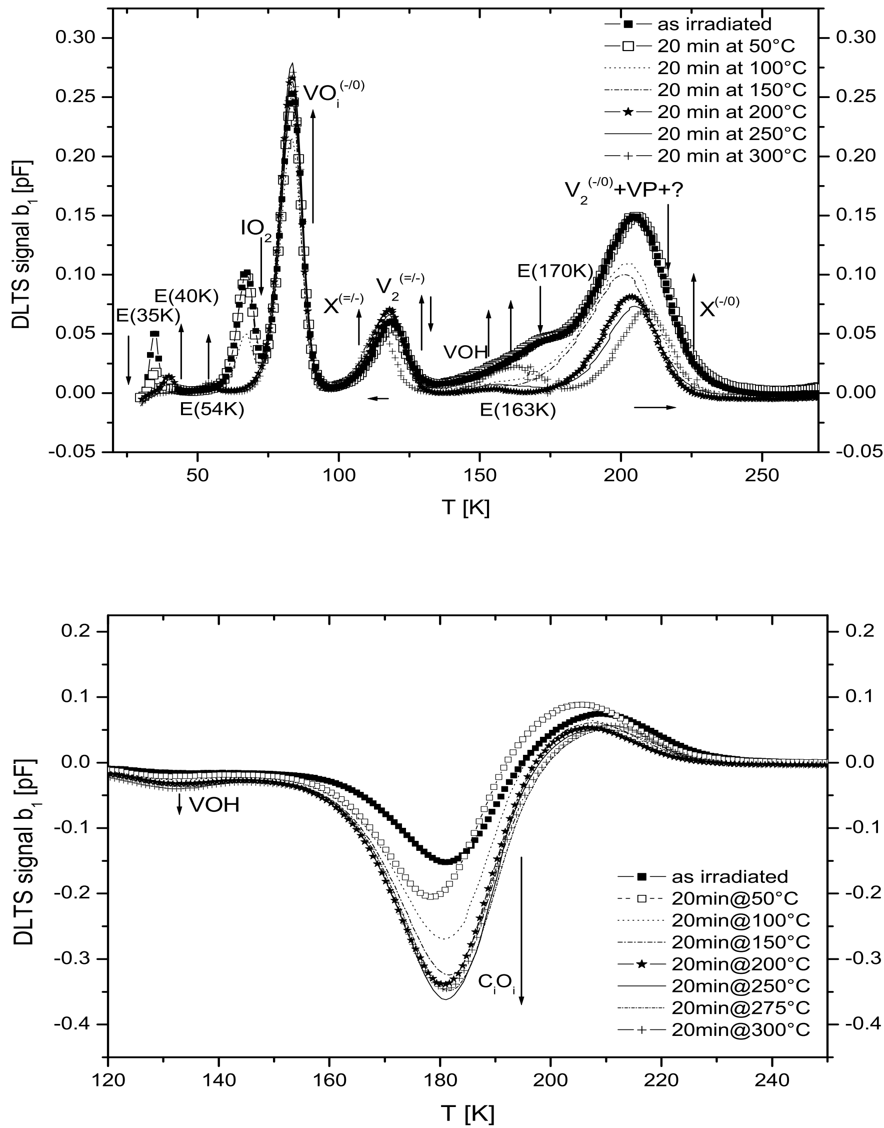

Figure 6.32: *Isochronal annealing of an epi-72-DO diode irradiated with 26 MeV protons with a fluence of* $\Phi_{eq} = 4.8 \cdot 10^{11}\ cm^{-2}$. *The annealing was performed between 50°C and 300°C for 20 min every 10 K. Measurement:* $U_R = -20\ V$, $U_{P,e} = -0.1\ V$ *(top),* $U_{P,f} = 3\ V$ *(bottom),* $t_P = 100\ ms$, $T_W = 200\ ms$.

labeled $E(163K)$ appears in similar concentration. But it is not known and can not be decided whether this coincidence leads to a correlation of these two defects or not.

Also the $E(152K)$ (most likely the $VOH^{(-/0)}$) is seen. Also its donor state is visible in the lower part of Fig. 6.32.

6.3.3 Comparison

Because both epi-diodes investigated in this section are not irradiated at the same time it is not known whether their history is identical or not. It was observed that the $E(35K)$ usually anneals out very fast already at low temperatures. The

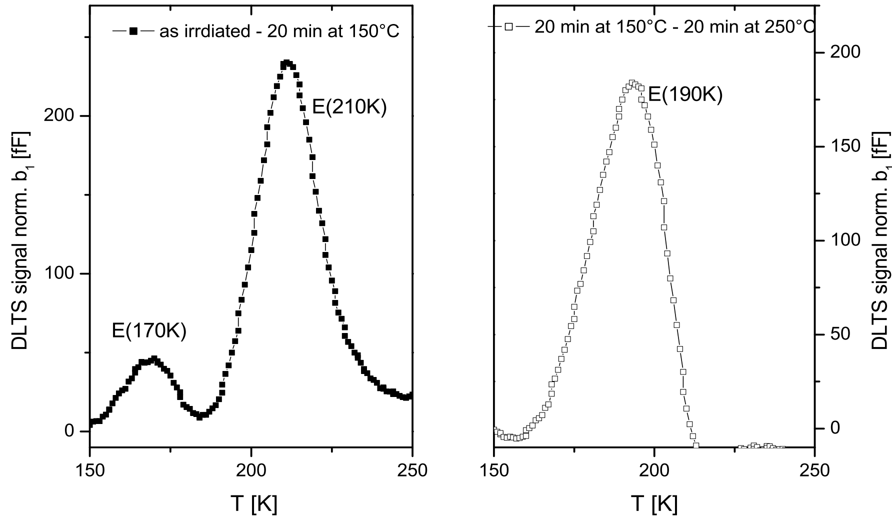

Figure 6.33: *Evolution of concentration during an isochronal annealing of defects detected in an epi-72-DO diode irradiated with 26 MeV protons with a fluence of* $\Phi_{eq} = 4.8 \cdot 10^{11}$ *cm^{-2}. The annealing was performed between 50°C and 300°C for 20 min mainly every 50 K. Measurement:* $U_R = -20\ V$, $U_{P,e} = -0.1\ V$, $U_{P,f} = 3\ V$, $t_P = 100\ ms$, $T_W = 200\ ms$.

$E(40K)$ usually emerges during the first annealing steps. In the epi-72-DO sample this typical behavior has been seen, while in the epi-72-St sample the $E(40K)$ has been detected already in the so-called as irradiated sample. Also the $E(35K)$ has been much smaller in this sample. Both observations leads to the suggestion that the annealing history of both samples is different from the beginning.

At higher temperatures this does not influence the annealing behavior. Most likely the annealing out of the $E(35K)$ influences the increase of the C_iO_i in principal in both samples.

The main difference in the annealing at lower temperatures is defined already by irradiation. The C_i defect which is seen only in the epi-72-St diode anneals out a bit faster than the IO_2, which is only seen in the epi-72-DO sample. Both defects are transformed into C_iO_i. In case of the epi-72-St diode also the C_iC_s is formed in a competitor reaction. This leads directly to another difference. Only in the epi-72-St sample the decay of the C_iC_s is observed between 150 and 250°C while in epi-72-DO no C_iC_s was introduced.

The annealing out of the clustered regions are independent of the used material. But the annealing of the V_2 itself strongly depends on the oxygen content of the material and leads to a transformation into the X-defect in case of epi-72-DO and to a simple dissociation of the V_2 in case of the epi-72-St sample.

Another annealing effect only observed in the oxygen rich sample is the formation of the $E(163K)$ defect. Also the decay of the $E(40K)$ at very high temperatures above 250°C has only been observed in the oxygen rich sample.

The formation of the VOH is similar in both samples.

Another defect observed in both materials is the $E(54K)$. It is seen after the annealing out of the C_i or the IO_2 respectively. For the epi-72-St sample it was not clear whether this defect was originally overlapped by the C_i or introduced during annealing, but in case of epi-72-DO it is clear that this defect emerges during the

annealing and is not radiation induced.

6.4 Defects after 23 GeV proton irradiation

Diodes processed on two different kind of epitaxial silicon with a layer-thickness of 25 and 75 μm were irradiated with 23 GeV protons. A fluence of $\Phi_{eq} = 7.3 \cdot 10^{11}$ cm^{-2} has been achieved. The samples were stored, after irradiation and a subsequent delay time at room temperature of about 30 minutes, in a freezer at temperatures below -20°C. An isochronal annealing was performed in a temperature range from 50°C to to 300°C to investigate the different annealing effects taken place. The heat treatment was performed in steps of 10°C with a duration of 20 min for each step.

6.4.1 Isochronal annealing of epi-25 silicon

In this section the results of the isochronal annealing experiment obtained on the epi-25 diode will be presented. The changes in the defect concentrations observed during the annealing is displayed in Fig. 6.34.

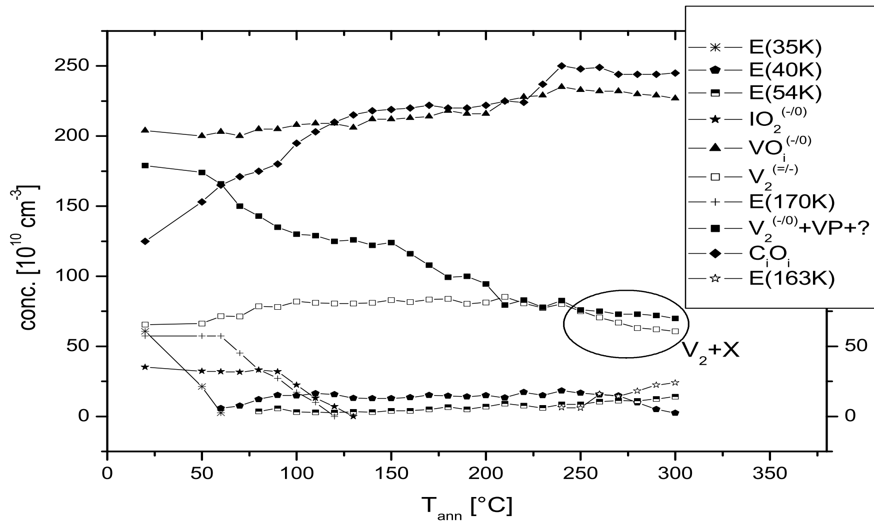

Figure 6.34: *Isochronal annealing behavior of defects detected in an epi-25 diode irradiated with 23 GeV protons with a fluence of* $\Phi_{eq} = 7.3 \cdot 10^{11}$ cm^{-2}. *Measurement:* $U_R = -20$ V, $U_{P,e} = -0.1$ V, $U_{P,f} = 3$ V, $t_P = 100$ ms, $T_W = 200$ ms.

In Fig. 6.35 the DLTS spectra after electron injection and forward biasing illustrating the annealing behavior of an epi-25 diode are shown. In case of hole emission only the C_iO_i-defect is seen. The peak associated with this defect is growing during the annealing. In contrast to the results after hole emission, electron emission lead to a wide range of different peaks visible in the spectra.

Close to the lower limit of the DLTS spectra a defect, $E(35K)$, can be observed. The defect is activated very fast during annealing and therefore its peak is vanished already after 20min at 60°C.

Afterwards a new defect at 40 K becomes detectable. This defect, $E(40K)$, is growing in concentration up to an annealing temperature of 100°C. Thereafter its

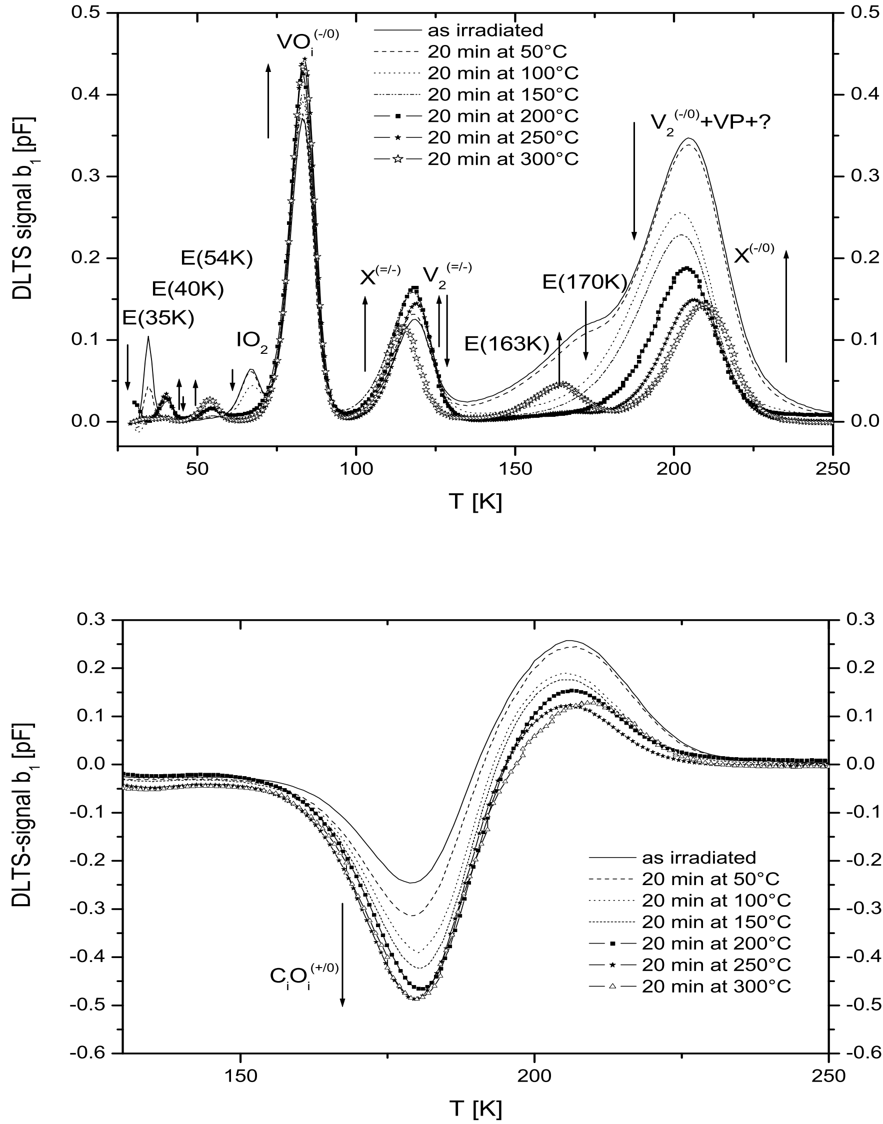

Figure 6.35: *Isochronal annealing of an epi-25 diode irradiated with 23 GeV protons with a fluence of* $\Phi_{eq} = 7.3 \cdot 10^{11}\ cm^{-2}$*. Measurement:* $U_R = -20\ V$*,* $U_{P,e} = -0.1\ V$ *(top),* $U_{P,f} = 3\ V$ *(bottom),* $t_P = 100\ ms$*,* $T_W = 200\ ms$*.*

concentration stays constant up to 250°C. Above this temperature it starts to anneal out and at 300°C it is almost disappeared.

Another main and radiation induced defect is the IO_2. It is shown in section 5.3 that the concentration of this defect strongly depends on the oxygen content in the material; or being more precise, on the oxygen-dimer content. Therefore an IO_2 depth-profile had been measured and already been demonstrated in Fig. 5.20. The IO_2-defect is stable up to 20 min at 80°C, while at higher temperatures the it anneals out. At 130°C its peak in the spectrum is disappeared.

In the lower part of Fig. 6.35 the only visible hole-trap is the C_iO_i. The strong increase of its concentration during the first two annealing steps cannot be explained by the decay of the IO_2 only because the $[IO_2]$ stays constant at the same time. Only the decay of the $E(35K)$ can explain this effect. Only the second part of the

increase of $[C_iO_i]$ between 70 and 130°C can be explained with the decrease of the $[IO_2]$. At higher temperatures the concentration is constant. The increase observed between 220 and 240°C can not be correlated with any known effect. A source for carbon interstitials in this temperature range, like the C_iC_s is not seen. The same increase will be shown for the epi-75 sample but amplified by a second effect.

Already at 80°C the $E(54K)$ appears. This defect slightly grows in concentration during the whole annealing experiment.

The largest peak after electron injection is caused by the VO_i-defect. During the annealing experiment the concentration of the VO_i increases continuously up to the annealing step at 240°C. Afterwards its concentration stays almost constant up to 300°C. The increase can be explained by a release of vacancies from the clustered regions. After the clusters have been annealed no further vacancies are released and therefore no increase of the VO_i concentration beyond 250°C is seen.

The doubly charged divacancy is attributed to the peak at 118 K. This peak increases during the annealing up to 200°C. Between 200 and 250°C its concentration becomes equal to the concentration of the singly charged divacancy. This indicates that at this annealing step the strain fields which are responsible for the cluster effect are relieved and all divacancies can be filled with a second electron. At higher annealing temperatures the peak starts to shift towards lower temperatures which is known from the transformation of the $V_2^{(=/-)}$ into the $X^{(=/-)}$-defect. While the X-defect is formed its annealing starts simultaneously. Above 250°C the peak is caused by an overlap of both defects. At temperatures higher than 250°C the ${V_2}^{(=/-)}$ anneals out very fast while the annealing of the X-defect takes much longer, therefore the peak at about 115 K in the presented spectrum after 20 min at 300°C can be associated to the X-defect only.

The annealing of the clustered regions associated with the two peaks $V_2^{(-/0)}+VP+?$ and $E(170K)$ is similar to what has been shown in case of irradiation with 26 MeV protons. The first part, which starts at 60 and ends at 150°C is dominated by the annealing of the $E(170K)$ and $E(210K)$ and the second part between 150 and 250°C is dominated by the annealing of the $E(190K)$. Above 200°C the concentration of the $V_2^{(-/0)}$ becomes equal to the one of the $V_2^{(=/-)}$. The VP-concentration is too small to be observable during this experiment.

A new defect at about 163 K becomes visible after annealing at 240°C. Its concentration is continuously growing up to 300°C. A simulation of the peak caused by this defect suggests an overlap of this peak by a second one at a deeper temperature.

6.4.2 Isochronal annealing of epi-75 silicon

The evolution of the defect concentrations during the isochronal annealing obtained on the epi-75 diode is presented in Fig. 6.36.

Several DLTS spectra after electron injection and forward biasing, taken during this experiment, are presented in Fig. 6.37. For a better identification of details in the spectra, only an assortment of spectra representing the measurements every 50 K are shown.

As observed for the epi-25 sample the first defect which anneals out up to 60°C is the $E(35K)$. Its decay coincides with an increase of the C_iO_i concentration.

The increase of the C_iO_i within this first annealing steps is stronger than the

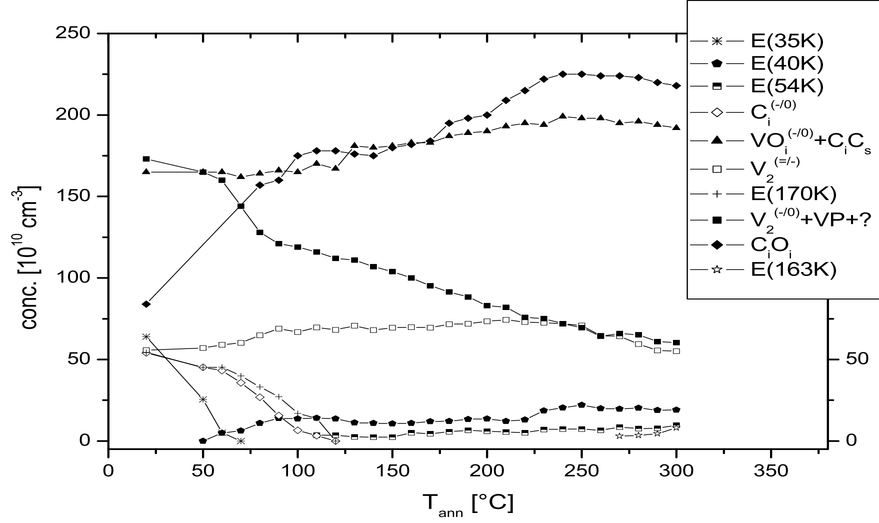

Figure 6.36: *Isochronal annealing behavior of defects detected in an epi-75 diode irradiated with 23 GeV protons with a fluence of* $\Phi_{eq} = 7.3 \cdot 10^{11}\ cm^{-2}$*. Measurement:* $U_R = -20\ V$, $U_{P,e} = -0.1\ V$, $U_{P,f} = 3\ V$, $t_P = 100\ ms$, $T_W = 200\ ms$.

decrease of the $E(35K)$. This is caused by the start of the C_i-annealing. Up to 120°C the C_i anneals out and the C_iO_i concentration reaches an intermediate maximum. A small amount of the C_i is also captured by C_s and C_iC_s is formed. This finding is monitored in a stronger increase of the peak at 84 K in comparison to the epi-25 sample.

Already in parallel to the C_iC_s-generation the cluster-annealing leads to a release of vacancies, which are captured at O_i-sites forming the VO_i. This defect is represented by the main part of the peak at 84 K. The annealing induced generation of VO_i is observed up to 250°C. Between 180 and 250°C this generation is overlapped by the decay of the C_iC_s generated before, which results in a smaller increase of the concentration attributed to the 84 K-peak compared to the epi-25 sample. Due to this overlap of two defects, the peak is labeled VO_i+C_iC_s in case of epi-75 and only VO_i in case of epi-25. The decay of the C_iC_s correlates with an increase of the C_iO_i.

Up to about 250°C the annealing of both negatively charged states of the divacancy is identical in both samples, epi-25 and epi-75. Therefore the defect, $E(170K)$, is vanished at 120°C as it is observed for the epi-25 diode.

At temperatures higher than 250°C the V_2 itself starts to anneal out. But in contrast to the epi-25 sample the shift of the $V_2^{(=/-)}$-peak towards lower temperatures is not seen in epi-75. Which is an indication for the V_2 to anneal out most likely by dissociation and not by transformation in the X-defect. The slight shift of the $V_2^{(-/0)}$ towards higher temperatures can be explained by an incomplete annealing of the clustered regions.

Although the oxygen content is much less in epi-75 than in epi-25, for which raison the introduction of VP should be larger, the VP-concentration is still to small to become a visible part in the evolution of the DLTS spectra during the annealing experiment.

As well as in epi-25 the $E(40K)$ and the $E(54K)$ emerge during the annealing.

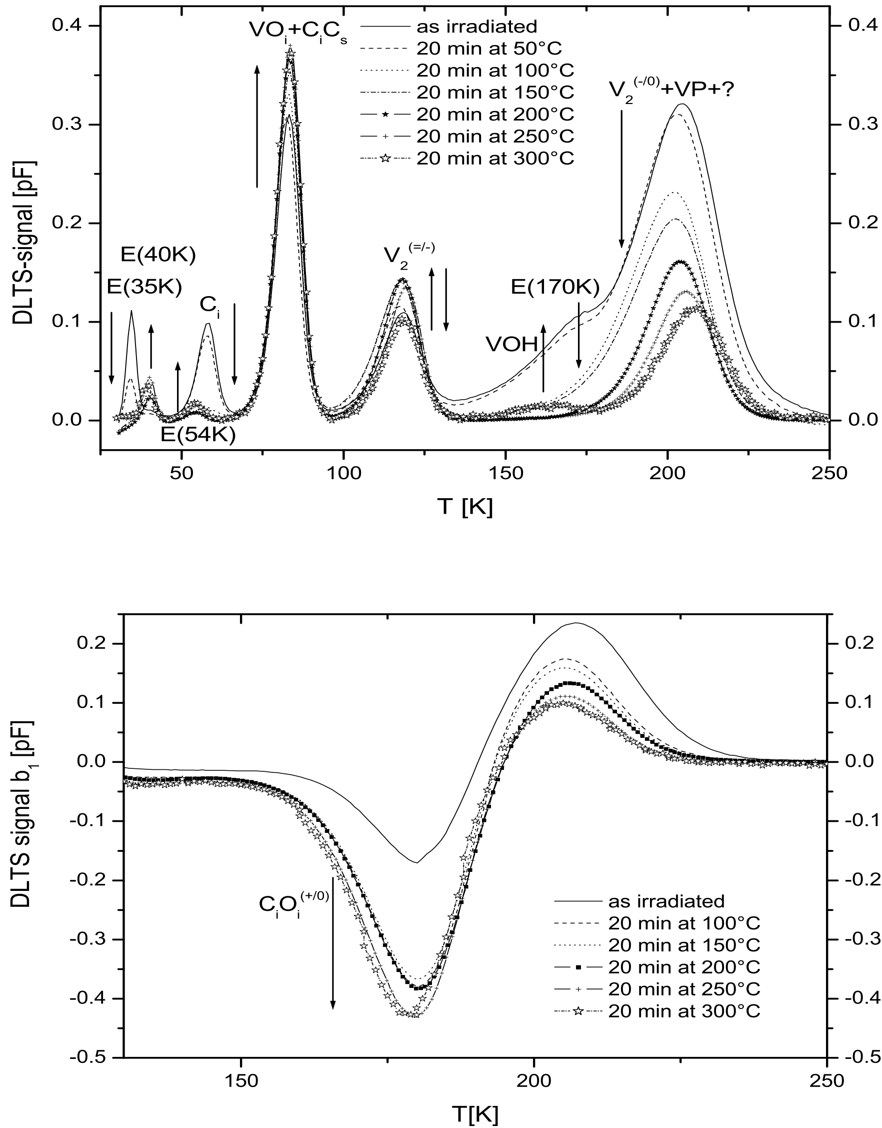

Figure 6.37: *Isochronal annealing of an epi-75 diode irradiated with 23 GeV protons with a fluence of* $\Phi_{eq} = 7.3 \cdot 10^{11}\ cm^{-2}$. *Measurement:* $U_R = -20\ V$, $U_{P,e} = -0.1\ V$ *(top),* $U_{P,f} = 3\ V$ *(bottom),* $t_P = 100\ ms$, $T_W = 200\ ms$.

Above 260°C the $E(163K)$ becomes visible, but in smaller concentration than in the epi-25 diode.

6.4.3 Comparison

Beside the oxygen content both epi-diodes, the epi-25 as well as the epi-75, should have the same impurities with similar concentrations. Therefore only those defects whose concentrations are influenced by the oxygen content show a different behavior during the annealing of both diodes. Both diodes were irradiated and stored always together to minimize differences caused by an unequal annealing history.

In both samples the obvious influence of the $E(35K)$-annealing on the C_iO_i concentration is seen in identical amount. Unfortunately it is not clear whether only

the $[C_iO_i]$ is influenced or also the $[C_iC_s]$. The answer to this open question would give more clues about the origin of the $E(35K)$ defect (only interstitial related or even interstitial and oxygen related).

An identical generation of the $E(40K)$ can be observed in both samples. But while this defect anneals out at high temperatures in the epi-25 sample, in epi-75 is not seen up to 300°C. The decay of the $E(40K)$ coincides with the increase of the E(163K) peak. This defect is seen in both samples but in much larger concentration in epi-25. This can be assessed as an indication that the E(163K) defect is oxygen related. A possible correlation of the decay of the $E(40K)$ and the increase of the E(163K) have to be shown by future high temperature annealing experiments.

Another defect observable in both materials with same annealing behavior is the $E(54K)$ defect. The only difference is, that in epi-25 the defect can already be detected at 90°C while in epi-75 it is first seen at 120°C. But this can be explained by the overlap of this defect by the C_i.

At this point the main difference between the two samples can be seen. In epi-25 the IO_2 is detected while in epi-75 this defect is not seen (at least in the investigated volume) but the C_i. On the other hand the C_i is not seen in epi-25. Both defects give rise to the C_iO_i concentration during annealing since both defects release carbon-interstitials. In epi-75 the annealing of the C_i also leads to a generation of C_iC_s which is not seen in epi-25 during the annealing of the IO_2. Since the C_iC_s anneals out roughly between 170 and 250°C, becoming a new source for the generation of C_iO_i, the C_iO_i concentration at high temperatures becomes similar in both materials.

The annealing of the clustered regions are identical in both materials as described above. But the annealing of the V_2 itself, starting at about 250°C is different in both materials. While the V_2 is transformed into the X-defect in epi-25 material, this effect is not seen in epi-75. Instead of this the competing reaction, the dissociation, is most likely observed. Since the subsequent annealing of the X-defect is slower than the dissociation of the V_2 the decay of the peak at about 205 K is faster in epi-75 than in epi-25. This effect has already been observed in case of standard FZ and DOFZ material [Sta04].

Due to the higher oxygen content the radiation induced generation of VO_i is larger in epi-25 than in epi-75, while the final increase at the end of the annealing experiment at 300°C compared with the beginning is equal.

6.5 Investigation of the IO_2-defect

In this section first the principal behavior of the IO_2-defect during DLTS measurements is investigated and afterwards its annealing behavior is shown.

6.5.1 Suppression of the IO_2-signal

A high concentration of the IO_2-defect has been detected in the epi-72-DO samples. Therefore an effect which leads to a suppression of the DLTS-signal from the IO_2-defect has been investigated in an epi-72-DO sample.

One sample has been irradiated with 26 MeV protons with a fluence of $\Phi_{eq} = 4.8 \cdot 10^{11}\ cm^{-2}$. Afterwards DLTS spectra have been taken. It has been detected that the DLTS signal attributed to the IO_2-defect is strongly suppressed when a forward bias has been applied to the diode at low temperatures. In order to characterize this phenomenon DLTS measurements have been performed from 30 K up to 110 K (U_R = -20 V, U_P = -0.1 V) after applying a forward bias of 3 V for a time of 100 s at different temperatures. In Fig. 6.38 the filled dots represent the normalized concentration of the IO_2 extracted from the obtained DLTS spectra. After each measurement the samples have been warmed up to room temperature to reverse the suppression of the IO_2. A further prolongation of the time used for applying the forward bias does not influence the results.

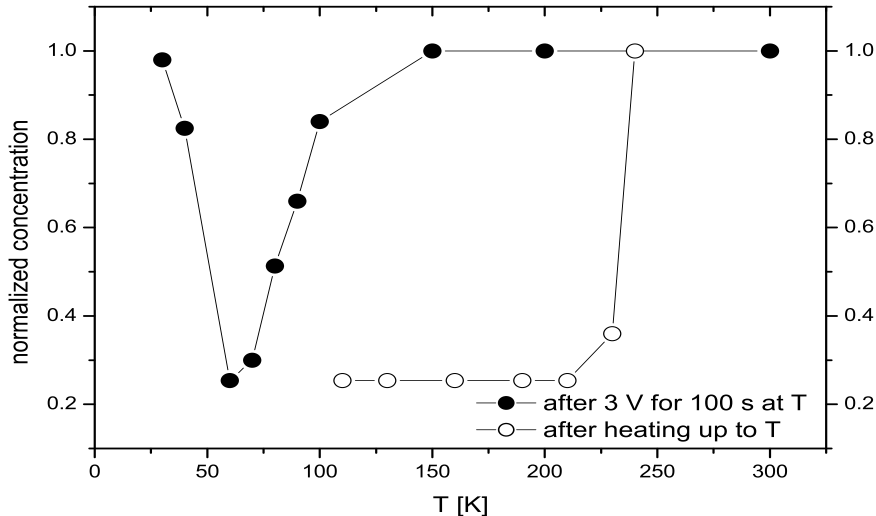

Figure 6.38: *Normalized concentration of the IO_2-defect after forward biasing (3 V) at different temperatures (filled dots) and after forward biasing at 60 K (3 V for 100 s) and subsequent heating up to different temperatures (open dots). U_R=-20V, U_P=-0.1V, t_p=100ms*

In a second experiment the sample has been cooled to 60 K and a the same forward bias of 3 V for 100 s has been applied. Afterwards the sample has been warmed up to different temperatures and a DLTS spectra down to 30 K has been taken. The normalized concentration of the IO_2 are plotted with open dots in Fig. 6.38. Also here the samples have been fully warmed up to room temperature after each measurement cycle.

It has been shown that the DLTS signal of the IO_2 defect can be suppressed by applying a forward bias to the investigated diode. The suppression reaches a maximum in the temperature range between 60 K and 70 K. This suppression is stable up to 230-240 K. At this temperature the suppression can be reversed. Unfortunately this experiment has been performed only with epi-72-DO samples in such detail, but it has also been detected in other thin epi diodes like the epi-25. Nevertheless this effect can up to now only be confirmed for thin epi-materials.

6.5.2 Annealing characteristics of IO_2

After irradiation with reactor neutrons only one kind of detector material underwent an annealing experiment which is presented in this work. The IO_2-defect is one of the main defects investigated in this work and an indicator for the presence of oxygen-dimers in silicon. In order to get more information about the annealing behavior of this defect isothermal annealing experiments of the defect have been performed at three different temperatures (80, 100 and 120°C). Informations about

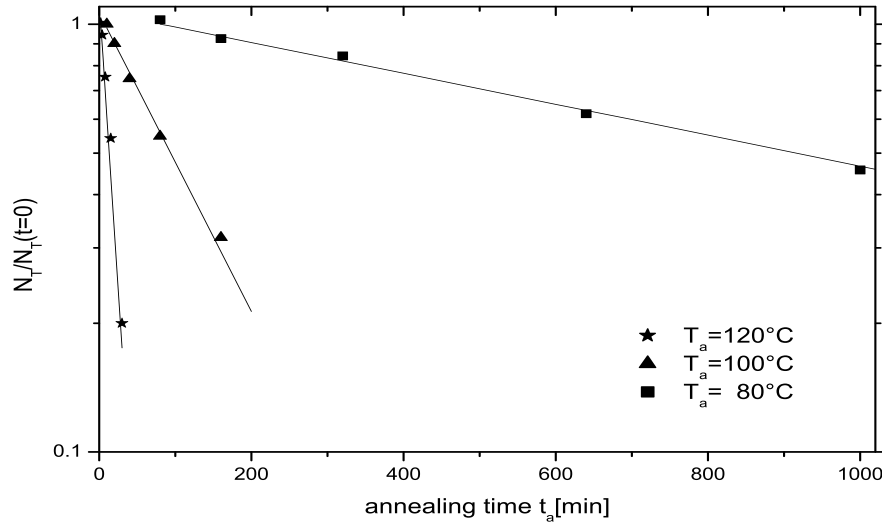

Figure 6.39: *Isothermal annealing of the IO_{2i} defect at different temperatures T_a. Measurement performed on an epi-25 detector irradiated with Φ_{eq}=$1 \cdot 10^{12}$ cm^{-2} reactor neutrons. U_R=-20V, U_P=-0.1V, t_p=100ms, T_W=200ms.*

the activation energy and the frequency factor can be evaluated when the annealing is performed at more than two different temperatures. For this experiment epi-25 diodes were used. The samples were irradiated with reactor neutrons with a fluence of $1 \cdot 10^{12}$ cm^{-2}. The data of the IO_2 concentrations were extracted from DLTS measurements performed with three time windows of 20 ms, 200 ms and 2 s. The normalized data and their fits are plotted in Fig. 6.39. The data are fitted with an exponential function.

$$N_t = N_{st} \cdot exp(-\frac{t - t_0}{\tau}), \tag{6.7}$$

where N_{st} is the starting concentration of the defect, τ is the time constant for the decrease, and t_0 is the starting time of the decrease. The time constants extracted

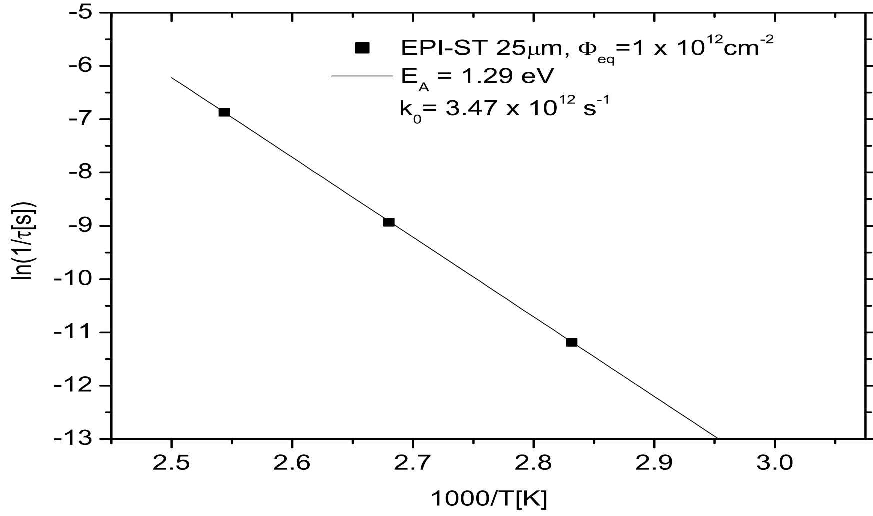

Figure 6.40: *Arrhenius plot for the thermal activation of the IO_{2i} defect after irradiation with Φ_{eq}=$1 \cdot 10^{12}$ cm^{-2} reactor neutrons. Epi-25 samples with 25μm thick layer.*

from these fits can be put in an Arrhenius plot as shown in Fig. 6.40. This plot revealed

$$\frac{1}{\tau} = k(T) = k_0 \cdot exp(\frac{-E_A}{k_B \cdot T}). \tag{6.8}$$

The evaluation of the time constants using this formula lead to an extraction of a frequency factor $k_0 = 3 \cdot 10^{12}$ s^{-1} and an activation energy $E_A = 1.29$ eV. Thus with a first order kinetics and a frequency factor k_0 close to the most abundant phonon frequency , it is very likely that the annealing of the IO_2 defect is due to dissociation.

Chapter 7

Comparison of Macroscopic Detector Properties and Microscopic Defects

Several radiation induced defects have been reported in the last chapters. But only a few of them have a significant impact on the macroscopic detector properties, like the effective doping concentration, the leakage current or the charge collection efficiency. In case of ^{60}Co-γ irradiation even a quantitative explanation for the effective doping concentration is possible (see e.g. [Pin02a, Pin03b]). This explanation bases on the E-center (VP), the I- and the Γ-level and the bistable donor (BD). In this work the model is extended towards hadronic irradiation (23 GeV protons and reactor neutrons). The main problem which has to be faced with is the huge generation of cluster damage. An even more basic problem is the extension of findings at low irradiation fluences, used for DLTS ($\approx 10^{12}$-10^{13} cm^{-2}) and TSC ($\approx 10^{14}$ cm^{-2}), towards high irradiation fluences up to 10^{16} cm^{-2} in case of macroscopic investigations.

7.1 High energy proton irradiation

Three types of epitaxial diodes with thicknesses of 25, 50 and 75μm had been irradiated with 23 GeV protons. Annealing experiments have been performed at elevated temperatures. A particular CERN scenario experiment, simulating the actual S-LHC conditions, with high fluence irradiation steps and intermittent annealing was carried out. For all three n-type epi-samples TSC measurements have been performed focusing on the defect concentration of the shallow donor, identified both in Cz and epi-diodes [Pin06]. Charge collection measurements have also been done for 5.8 MeV α-particles from a ^{244}Cm source using the time-resolved transient current technique (TCT) for recording current pulse shapes as described in [Fre97].

In contrast to FZ-silicon the effective doping concentration stays always positive immediately after irradiation [Lin06]. As known from studies with FZ-silicon-diodes part of this initial change, attributed to acceptor generation, is annealing out within a short time after irradiation such that a relative maximum of N_{eff} is observed at about 8 min (t_0).

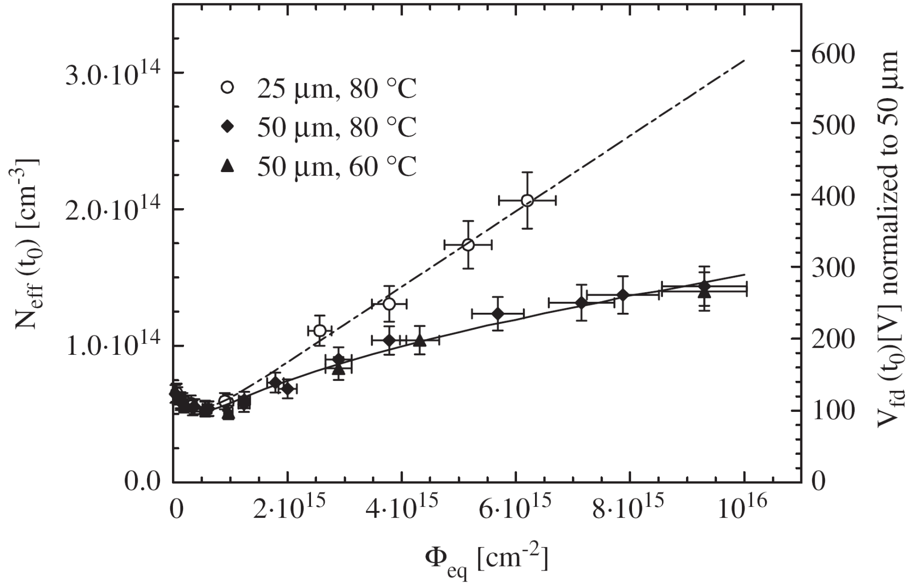

Figure 7.1: *Effective doping concentration and the corresponding full depletion voltage for epi-25 and epi-50 diodes as a function of equivalent fluence at annealing stage t_0. Values normalized to the same resistivity before irradiation and V_{FD} to a 50 μm thickness.*

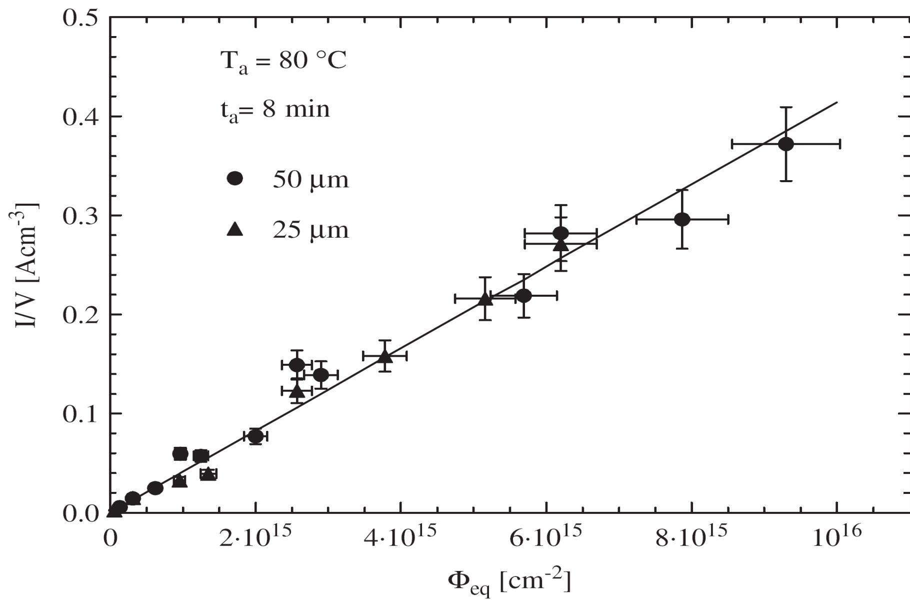

Figure 7.2: *Generation current per cm^{-3} as a function of equivalent fluence for epi-25 and epi-50 diodes, measured at t_0.*

Fig. 7.1 and 7.2 exhibit the fluence dependence of V_{FD} and the generation current for epi-25 and epi-50 diodes respectively up to $\Phi_{eq} = 1 \cdot 10^{16}\text{cm}^{-2}$. Both curves show results which are taken at the annealing time t_0. No type inversion was observed for the full fluence range. The dependance of the generation current on the fluence is almost identical to that known from FZ silicon devices [Mol99]. The extracted current-related damage constant α is $4.1 \cdot 10^{-17}$ A/cm.

A correlation of macroscopic findings with radiation induced defects has been introduced by [Pin06] after irradiation with 23 GeV protons.

The first part which has to be taken into account for such a correlation is the so called donor removal, e.g. the generation of the VP-defect complex. It has been shown in chapter 4 that an evaluation of the VP concentration after proton irradiation is not possible. Therefore an investigation has been performed after ^{60}Co-γ irradiation and a donor removal (or VP introduction) rate of 0.11 cm^{-1} has been extracted (see chapter 4. A comparison of the VP and the VO_i signal after ^{60}Co-γ-irradiation and the VO_i signal after 23 GeV proton irradiation leads to an introduction rate of VP in the order of 0.025 cm^{-1} after proton irradiation. This value is much smaller than the one given in [Pin06]. But due to the fact that less single vacancies are created after proton irradiation than after ^{60}Co-γ irradiation the value taken from chapter 4 has been used.

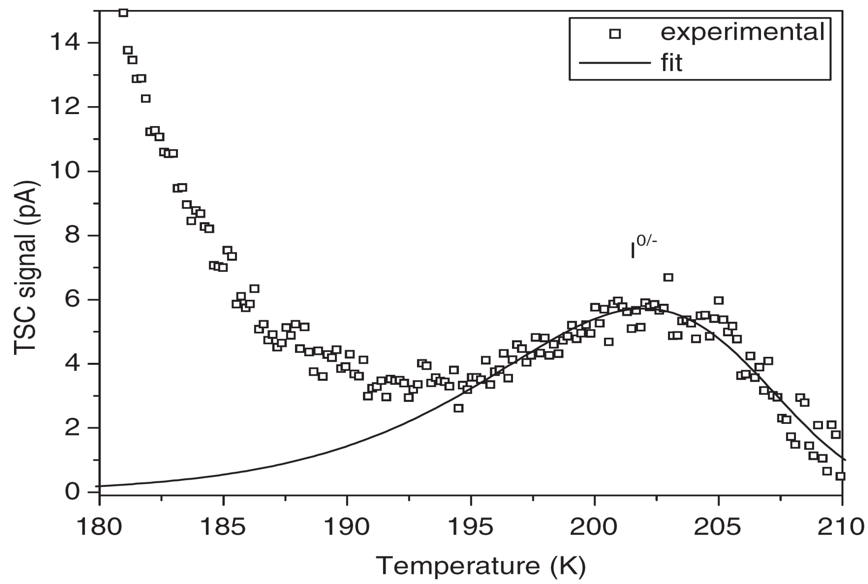

Figure 7.3: *The fit of the I-center TSC peak for epi-50 material after irradiation with 23 GeV protons with an equivalent fluence of 3.73 · 10^{14}cm^{-2} and after an annealing treatment at 60°C for 120 min.*

A second defect which contributes directly to the N$_{eff}$ is the I_p center. This defect has not been found by DLTS after proton irradiation within this work. On the one hand side the fluence of the investigated diodes has been too small to find a measurable amount of I_p centers and additionally the neighboring V_2-cluster make an investigation even more complicated. But it was possible to measure the I_p center with the TSC technique. An example of the fitting procedure is given in Fig. 7.3 for the experimental TSC peak corresponding to the acceptor state of the I_p center recorded on an fully depleted epi-50 diode. At has been shown in [Pin06] that this defect contributes with negative space charge to N$_{eff}$ with a value of 5.6 ·10^{12}cm^{-3} at room temperature (293 K) for an epi-50 diode irradiated with an equivalent fluence of 1.24 · 10^{14}cm^{-2} and subsequent annealing for 120 min at 60°C.

A third level that contributes to the N$_{eff}$ is the BD defect (bistable donor). This defect starts to be generated after high irradiation fluences where the DLTS method

can no longer be applied. It was described in [Pin03b] that the BD is detectable via two TSC signals, $BD(98K)$ and $BD-tail$, indicating that the BD center can exist in two configurations, labeled as BD_A and BD_B, respectively. The formation of the BD center is enhanced in material with high concentration of oxygen-dimer. After low fluences these dimers can typically be identified by means of the IO_2 defect. The contribution of the BD to the N_{eff} is $1.3 \cdot 10^{12}\text{cm}^{-3}$.

Very recently new TSC experiments performed in our lab [Pin07] revealed that the $H(116K)$, $H(140K)$ and $H(152K)$ presented in Fig. 7.4 are hole traps with a significant electric field enhanced emission. This means that these defects are acceptors in the lower half of the bandgap and therefore they contribute with negative space charge in their full concentration to the effective space charge in n-type diodes. A rough estimation of the contribution of these defects to N_{eff} leads to a value in the order of $6.0 \cdot 10^{12}\text{cm}^{-3}$.

The change in N_{eff} due to proton irradiation can be partly explained by these TSC evaluations.

The following equation can be written for N_{eff} at room temperature:

$$N_{eff} = N_{eff,0} + [BD] - [E] - [I_p^-] - [Y] - [Z], \tag{7.1}$$

where the [BD] term represents the concentration of positive space charge introduced by the ionized BD centers, [E] the concentration of the E-center (VP, removal of P donors), $[I_p^-]$ the concentration of negatively charged I_p centers, [Y] the concentration of new acceptors [Pin07] and [Z] the concentration of negative space charge introduced by clusters or other unknown defects at room temperature.

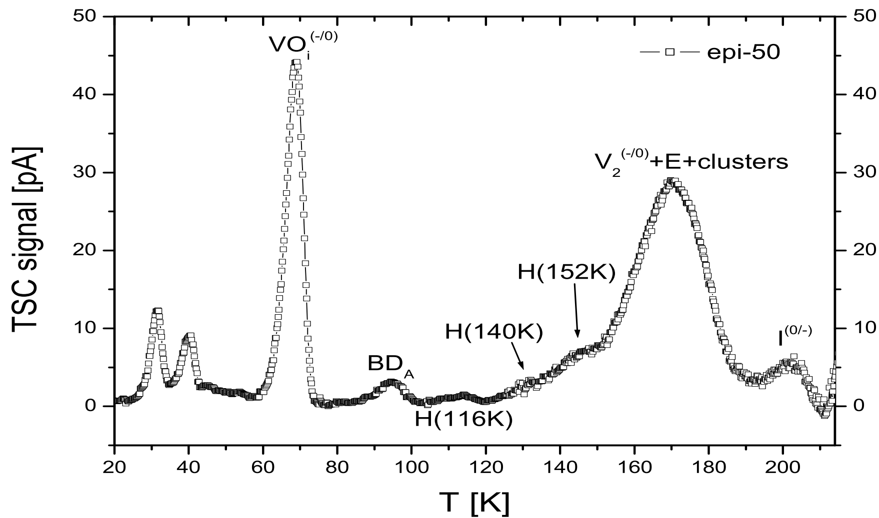

Figure 7.4: *TSC spectra after irradiation with 23 GeV protons with an equivalent fluence of $1.24 \cdot 10^{14}\text{cm}^{-2}$ recorded on epi-50 material after an annealing treatment at 60°C for 120 min. Forward injection was performed at 15 K for filling the traps.*

In case of the epi-50 sample irradiated with $\Phi_{eq}(23\text{ GeV protons}) = 1.24 \cdot 10^{14}\text{cm}^{-2}$ the donor removal is $[E] = 3.1 \cdot 10^{12}\text{cm}^{-3}$. This value and the evaluations above predict a change of the initial N_{eff} of $7.24 \cdot 10^{13}\text{cm}^{-3}$ before irradiation to a value of about $5.90 \cdot 10^{13}\text{cm}^{-3}$, compared with $5.70 \cdot 10^{13}\text{cm}^{-3}$ as measured by C/V.

The missing part represents a negative charge concentration of about $2.0 \cdot 10^{12}\text{cm}^{-3}$ which may be due to clusters or other deep defects ([Z]) not detected so far.

A TSC spectrum showing the different relevant defects is given in Fig. 7.4.

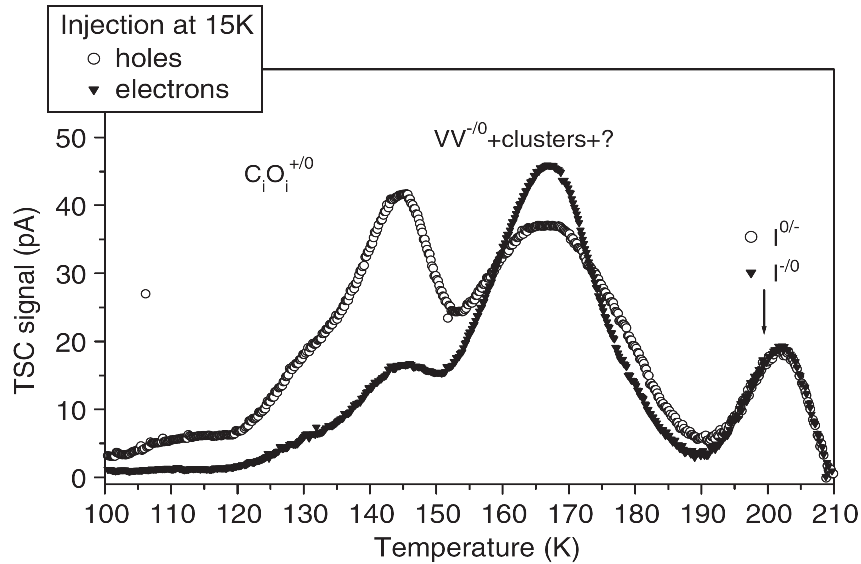

Figure 7.5: *TSC spectra just after irradiation with 23 GeV protons with an equivalent fluence of $3.73 \cdot 10^{14}\text{cm}^{-2}$ recorded on epi-50 material after holes and electron injection at 15 K.*

Nevertheless, with a generation rate of the BD smaller than the one of Z, type-inversion should be expected. But no type inversion has been detected. One raison might be the observation that the percentage of stady state electron occupancy of the I_p center is decreasing with increasing irradiation fluence, i.e. with increasing leakage current. In Fig. 7.5, the TSC spectra obtained after only electron or only hole injection on an epi-50 diode irradiated with an equivalent fluence of $3.73 \cdot 10^{14}\text{cm}^{-2}$ are given. As can be seen, the TSC peaks corresponding to the electron/hole emission from the I_p center have the same amplitude. This fact indicates that the steady state occupancy of the I_p center is ∼50%. An example of high occupancy (∼85%) with electrons of the I_p centers is given in [Pin03a] for diodes with very low leakage currents. The result of decreasing steady state electron occupancy percentage with increasing the fluence of the I_p-center is that the quadratic fluence dependence of I_p centers concentration will not be reflected in the steady state electron occupancy of the I_p centers, i.e. N_{eff} at room temperature.

But even if one would disregard the I_p center at all type inversion should occur. Therefore two other possibilities have to be taken into account. One might be a dependence of [BD] stronger than linear on the fluence ([BD](Φ)$\propto \Phi^{\gamma}$ with $\gamma > 1$). A second might be non constant introduction rates for g[Z] and g[Y] at higher fluences.

In Fig. 7.6 the effective doping concentration after 10 min at 80°C is displayed as a function of equivalent fluence. Due to experimental difficulties with C/V measurements at 10 kHz for the epi-75 diodes, all data in Fig. 7.6 are obtained with

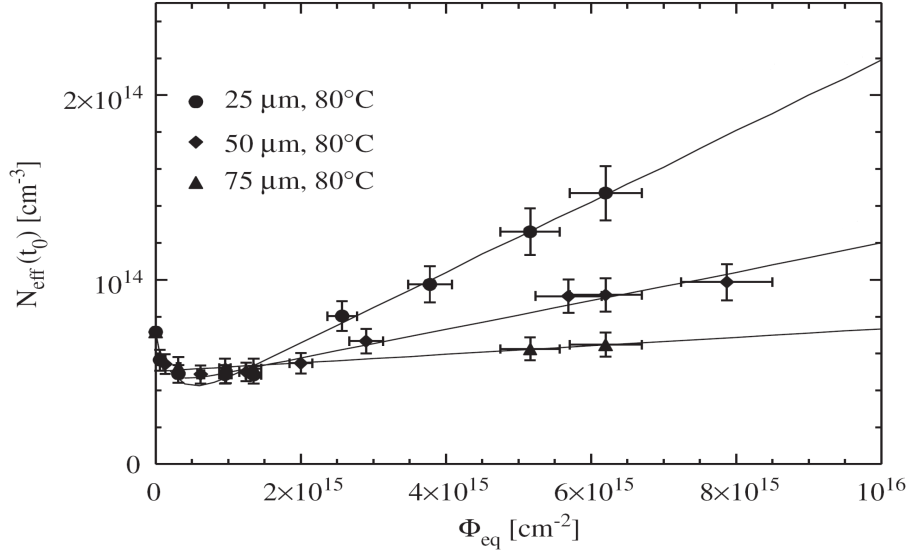

Figure 7.6: *Effective doping concentration, as measured after the end of the beneficial annealing as function of fluence after 23 GeV proton irradiation. Solid lines represent fits to the given model.*

100 kHz. Contrary to the damage effects in FZ silicon the effective doping concentration stays always positive and after reaching a slight minimum even increases almost linearly with fluence. For the chosen annealing stage both the beneficial annealing and the reverse annealing effects do not play a significant role. The values plotted in Fig. 7.6 are therefore approximately only caused by the change from the initial effective doping concentration due to the stable damage component. Mainly two effects attribute to the stable damage. The donor removal reduces the positive space charge by formation of E-centers (VP). This component, responsible for the first part of the fluence dependence, is exponentially saturating due to the exhaustion of P-donors. The donor removal has been observed in n-type FZ as well as in epi silicon diodes. A large value of the doping concentration, as possible in thin diodes, will however delay this exhaustion. For larger fluences in epi-diodes the possible creation of acceptors is obviously always overcompensated by donors causing the almost linear increase of N_{eff} with fluence.

It is however remarkable that the effect of stable donor generation largely depends on the thickness of the device. The differences seen in Fig. 7.6 between epi-25 and epi-75 diodes are obviously correlated with the oxygen concentration profiles shown in Fig. 3.2. A direct correlation has to be excluded, because a similar effect was not observed in oxygen enriched FZ silicon (DOFZ) diodes with the same average oxygen-concentration. A first understanding was provided by defect spectroscopy experiments, where a shallow donor at E_C-0.23 eV has been seen, which is not detectable in FZ diodes [Pin06]. In Fig. 7.7 TSC-spectra for the three epi diodes are presented. While the well known point defects like e.g. C_iO_i, the double vacancy as well as the the peak at 116 K, known from previous work on FZ diodes [Mol99], are measured with concentrations independent of the diode type and therefore independent of the O-concentration, the TSC signal due to the shal-

low donor (denoted as $BD^{(0/++)}$) has a similar dependence on the material as the average oxygen-concentration and the stable damage generation.

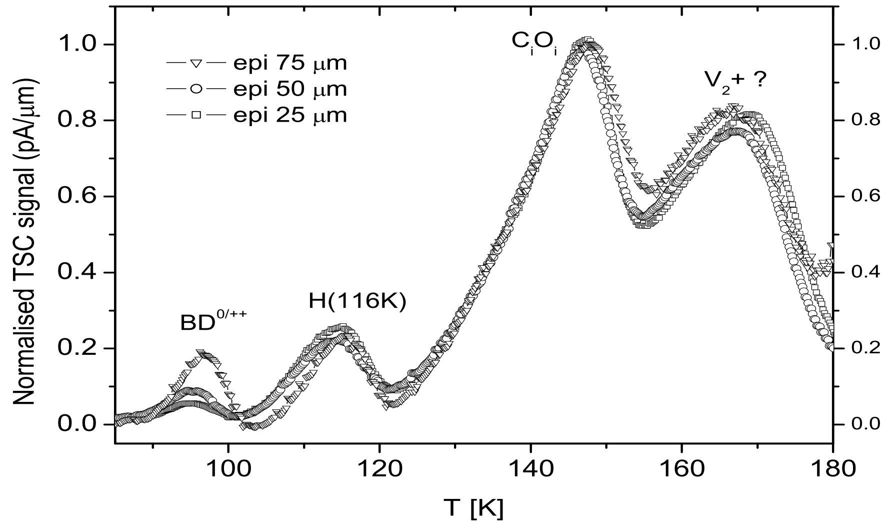

Figure 7.7: *TSC spectra for epi-25, epi-50 and epi-75 diodes after 23 GeV proton irradiation with Φ_{eq} = 1.8 · 10^{14}cm^{-2} and 120 min annealing at 60°C (top curve: epi-25, bottom one: epi-75).*

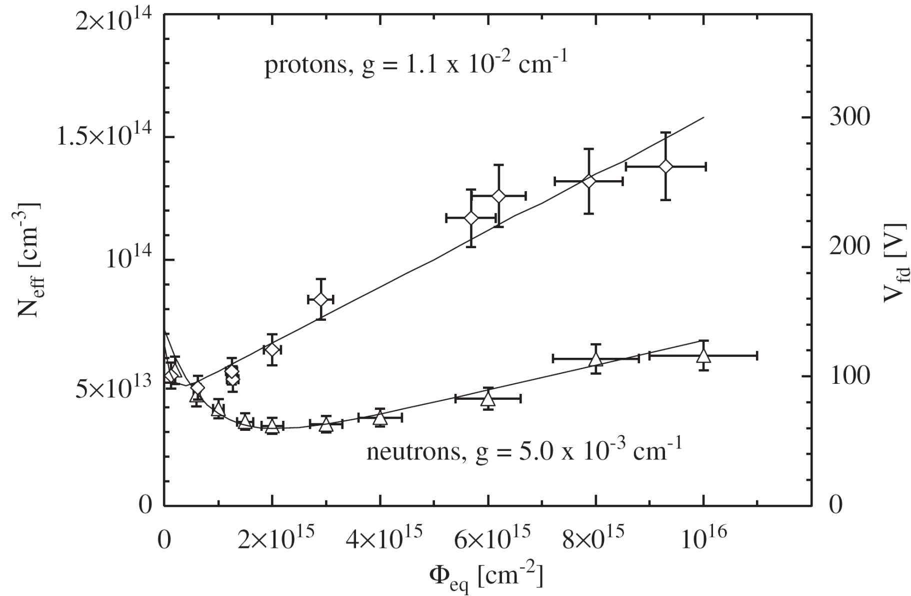

Figure 7.8: *Comparison of the donor generation in epi-50 diodes after irradiation with 23 GeV protons and reactor neutrons, measured at the end of the beneficial annealing. Solid lines represent fits to the given model, slope values assigned to the curves represent the donor generation rates.*

In Fig. 7.8 a comparison of the effect after proton and neutron irradiation is displayed for epi-50 diodes. It has been shown that, due to Coulomb interaction, the

generation of point defects after proton irradiation is much larger than for neutron damage, even after normalizing both to NIEL equivalent fluence values (see e.g. [Huh02] or chapter 4). It is therefore no surprise, that the positive space charge build up after proton irradiation is much larger than for neutron damage. It is also obvious from Fig. 7.8 that in case of proton damage the initial donor removal is faster than after neutron irradiation. This fact is also a result of the larger point defect generation.

A tentative explanation for the generation of the BD and hence the superior radiation tolerance of n-type epi diodes had been proposed e.g. in [Pin06]. A strong similarity of the BD-complex to thermal donors and the well known fact that oxygen dimers (O_{2i}) are precursors for the formation of thermal donors [Lee02] leads to the assumption that dimers are involved in the damage related BD production. It has been shown in section 5.3 that the oxygen-dimer concentration is strongly correlated with the oxygen concentration of the diodes.

Taking the differences in the oxygen profiles in Fig. 3.2 into account it is very likely that the BD-complex, found in epi-silicon after irradiation, is indeed responsible for the dominating positive space charge build up in these devices and that this donor is generated via the oxygen dimers.

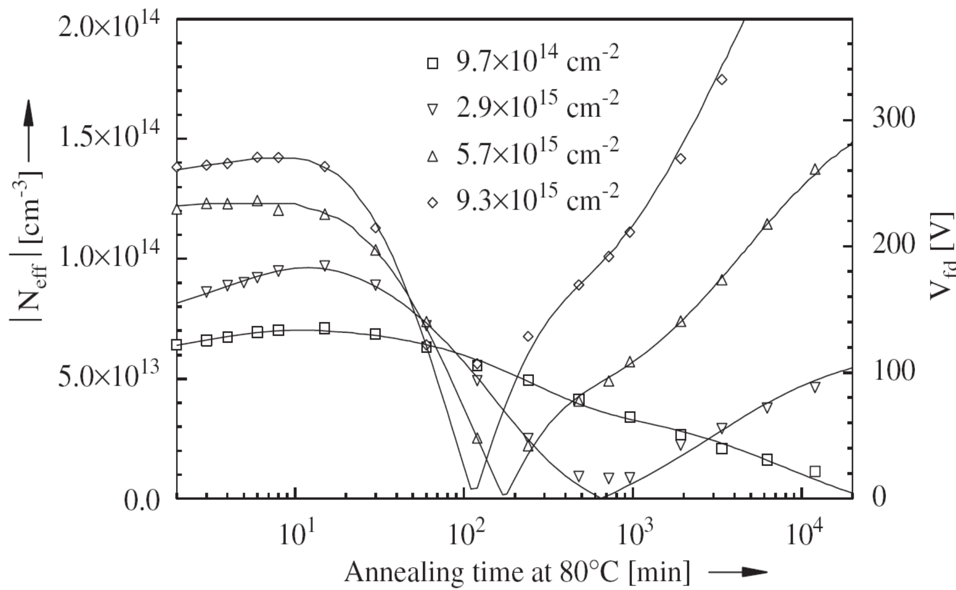

Figure 7.9: *Examples of annealing functions for epi-50 diodes at 80°C after irradiation with different 1 MeV neutron equivalent fluences of 23 GeV protons. Lines represent model fits.*

In Fig. 7.9 it is shown that the effect of a fluence depending increased positive space charge creation could be partly compensated by the generation of acceptors during annealing. This effect finally leads to type inversion. For an irradiation with $\Phi_{eq} = 9 \cdot 10^{15}\text{cm}^{-2}$ this occurs however only at about 100 min, which would correspond to a storage time of 500 days at room temperature [Mol99]. Therefore in contrast to FZ detectors which would always have to be stored at low temperatures in order to avoid an intolerable increase of the depletion voltage, in case of epi-detectors such low temperature storage is not necessary. In addition keeping the

detectors at room temperature during the beam off periods could be rewarding because the increase of the depletion voltage resulting from the donor generation during the beam period would be partly compensated by annealing induced acceptor generation. In order to prove this suggestion the following dedicated experiment

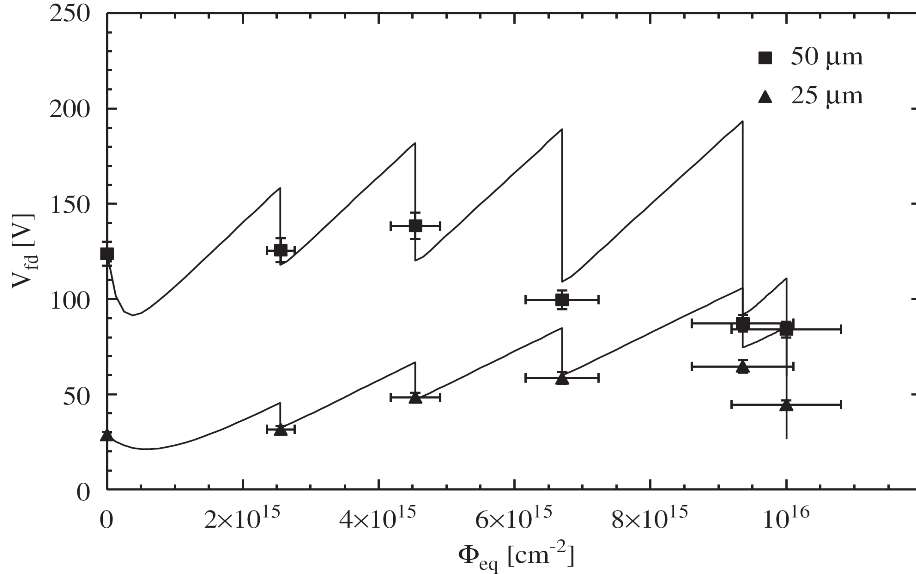

Figure 7.10: *Results of succesive irradiation with 23 GeV protons with steps of $\Phi_{eq} = 2.2 \cdot 10^{15}cm^{-2}$ followed by annealing for 50 min at 80°C. Symbols: experimental points, solid lines: simulations.*

had been performed. Both epi-25 and epi-50 diodes had been irradiated with 23 GeV protons fluence steps of about $\Phi_{eq} = 2.2 \cdot 10^{15}\text{cm}^{-2}$. After each damage step the diodes were annealed for 50 min at 80°C corresponding approximately to the 265 days beam off period at room temperature at the S-LHC. The compression factor between 20°C and 80°C was taken to be 7500 for this evaluation, according to an activation energy for the involved kinetics of 1.31 eV [Mol99]. On the other hand a simulation was performed calculating the depletion voltage along the full irradiation and annealing cycles. Values extracted from a detailed parametrization fit of extensive annealing experiments at 60°C and 80°C had been employed [Lin06]. After each annealing step the depletion voltage had been measured followed by the next irradiation step. The measured data of this experiment as well as the simulations are shown in Fig. 7.10. An excellent agreement was obtained for both the epi-25 and the epi-50 diodes. It is clearly seen that the depletion voltage of the epi-25 diode is increasing with fluence (by roughly a factor of 2) while that of the epi-50 diode is even slightly decreasing. This is of course due to the fact that in case of the thin epi-25 diode the positive space charge is much more increasing with fluence and hence less compensating by the annealing induced acceptors than in case of the epi-50 one.

For the application of silicon detectors in the tracking area of elementary particle physics experiments, a good signal-to-noise ratio for minimum ionizing particles (mip's) is essential. The electronic noise can be sufficiently reduced if the detectors are operated at low temperature and provided the capacitance is adequately low,

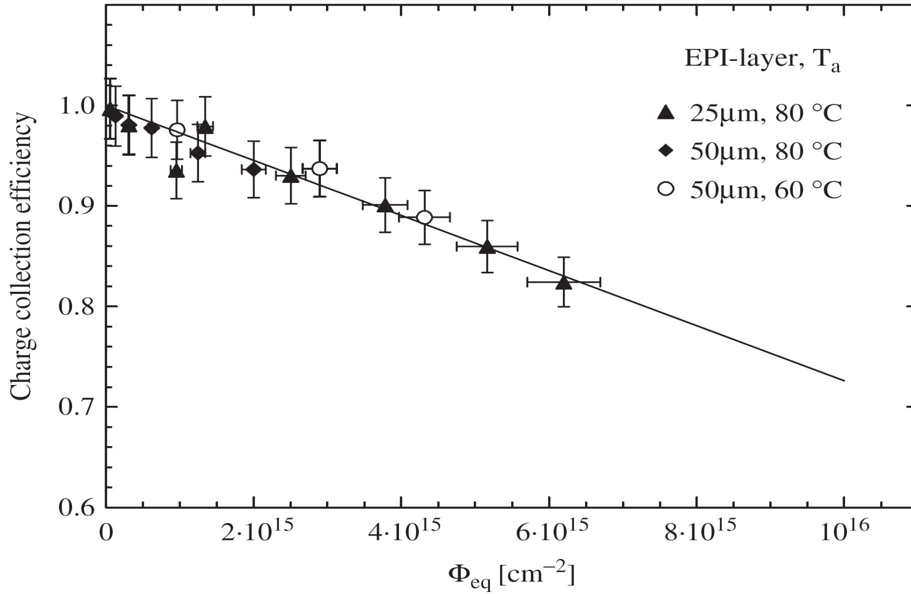

Figure 7.11: *Charge collection efficiency (CCE) as a function of equivalent fluence after 23 GeV proton irradiation for epi-25 and epi-50 diodes as measured with 5.8 MeV α-particles.*

possible for thin epi-diodes if used as small area pixel devices. Hence the most important issue is the charge collection efficiency (CCE). As discussed, the required electric field strength throughout the sensitive volume can be readily achieved for epi-diodes within the full S-LHC fluence range using moderate voltages. Degradation effects of the charge collection due to the loss of drifting charge carriers by trapping is therefore the major problem. Charge collection properties of irradiated epi-diodes were extensively investigated in a study for mip's [Kra05]. Here, measurements had been performed using a collimated beam of 5.8 MeV α-particles. As their penetration depth is 24μm (taking an air gap of 3 mm between the source and the detector into account), both holes and electrons contribute to the induced charge. The bias voltage was always kept sufficiently above the depletion voltage such that the drift velocity of the charge carriers approaches nearly the saturation values and as a consequence, the drift time becomes independent of the bias voltage. This leads to a saturating loss of the collected charge by trapping. From these voltage scans, performed very similar to what is shown in [Kra05] the collected charge is measured at a constant bias voltage for all investigated diodes. The CCE is plotted as a function of fluence in Fig. 7.11. The solid line presents a fit to the experimental data according to: CCE = 1-$\beta_c\Phi_{eq}$. For the parameter β_c a value of $2.7 \cdot 10^{-17}$cm^2 is derived which leads to an extrapolated CCE value of 75% at $\Phi_{eq} = 1 \cdot 10^{16}$cm^{-2}. Measurements on proton irradiated epi-50 samples performed with a ^{90}Sr-β source (representing mip's) have resulted in a quite similar value of 60% at $8 \cdot 10^{15}$cm^{-2} [Kra05]. Unfortunately no correlation of the trapping effects with specific defects have been found so far. But it has been shown that the trapping is independent of the the used silicon material and therefore it is suggested that the differences in e.g. oxygen or carbon content of the diodes do not influence the trapping behavior.

7.2 Reactor neutron irradiation

Epi-72-St and epi-72-DO as well as MCz diodes were irradiated with reactor neutrons. Equivalent fluences of up to 10^{16}cm^{-2} have been achieved. For both epi-materials and the MCz-silicon TSC measurements were performed with special attention on the radiation induced BD-generation, as it has been shown in the last section. CCE measurements with α-particles from a ^{244}Cm source were performed for both types of epi-silicon. Additional charge collection studies with 670 nm laser light pulses were done in order to prove whether the irradiated devices had undergone a space charge sign inversion after a certain fluence or not.

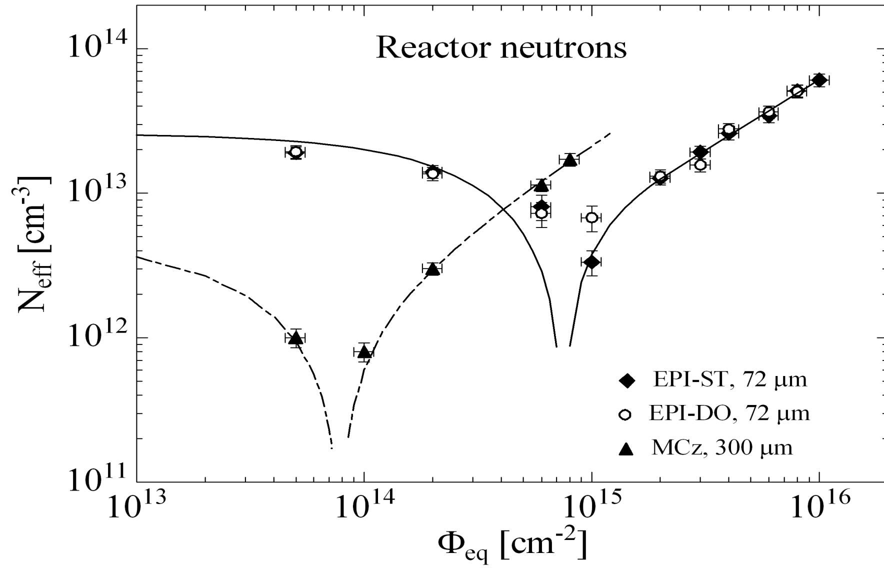

Figure 7.12: *Effective doping concentration as function of fluence, as measured after annealing for 8 min at 80°C. Lines represent fits according to Eq. 7.2*

The development of N$_{eff}$ in relation to the achieved equivalent fluence for both epi-materials and MCz detectors is presented in Fig. 7.12. The values are taken after an annealing period of 8 min at 80°C, therefore they correspond roughly to the stable damage component N$_C$. Because of its thickness of 300 μm the largest fluence for the MCz samples was limited to $8 \cdot 10^{14}$cm^{-2} due to the resulting increase of the V$_{FD}$, which is limited by the used voltage source. The highest fluence achieved for the epi-samples results in a V$_{FD}$ of 300 V. The solid and the dashed lines in Fig. 7.12 represent fits to the epi- and MCz-data according to

$$N_{eff}(\Phi_{eq}) = |N_{eff,0} \cdot exp(-c \cdot \Phi_{eq}) - g_{eff} \cdot \Phi_{eq}| \quad (7.2)$$

where N$_{eff,0}$ is the initial doping concentration, c is the donor removal coefficient and g$_{eff}$ is the effective introduction rate of defects which are charged in the space charged region. It is assumed that g$_{eff}$ represents an effective introduction of negative space charge leading to type inversion above about $8 \cdot 10^{13}$cm^{-2} for MCz and $8 \cdot 10^{14}$cm^{-2} for the epi-materials. Mainly two reasons cause this difference. At first, the lower initial doping of the MCz-samples ($4.9 \cdot 10^{12}$cm^{-3}) compared to the epi-samples ($2.5 \cdot 10^{13}$cm^{-3}) results in an earlier exhaustion of donors in MCz-material

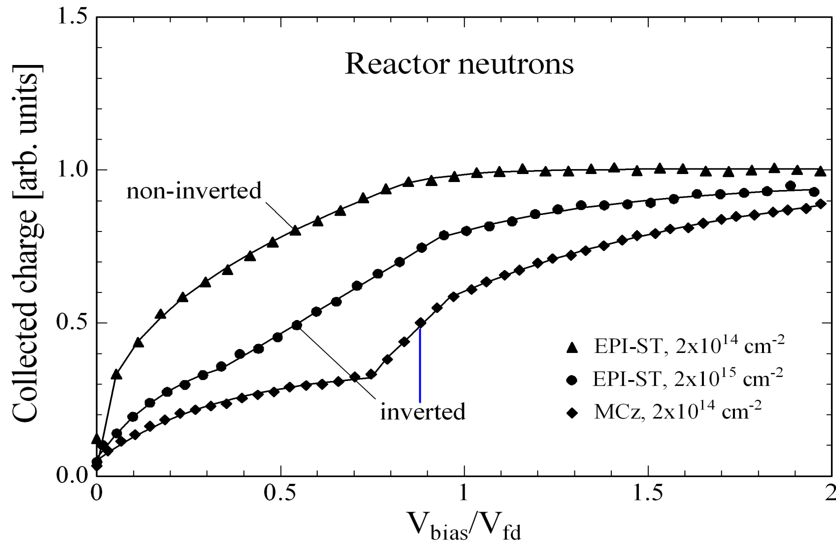

Figure 7.13: *Collected charge as function of normalized bias V_{bias}/V_{FD} for an inverted MCz, a non-inverted and an inverted epi-72-St diode. The charge carriers were created by illuminating the p^+-electrode with 670 nm laser light pulses.*

and secondly the introduction rate for MCz ($g_{eff} = 2.3 \cdot 10^{-2}\text{cm}^{-1}$) is much larger compared to both epi-materials ($g_{eff} = 6.0 \cdot 10^{-3}\text{cm}^{-1}$). At the same annealing time of 8 min the generation current has been investigated. A linear increase has been found up to an equivalent fluence of 10^{16}cm^{-2}. A current-related damage constant α of about $4 \cdot 10^{-17}$ A/cm has been extracted [Fre07].

To prove the appearance of type inversion measurements were performed by illuminating the p^+ contact with 670 nm laser light pulses. It's small absorption length of about 3 μm in silicon causes a creation of electron hole pairs near the p^+ surface. The charge collection for an inverted device should only become efficient when the applied bias voltage is close to the value for full depletion. In Fig. 7.13 the collected charge of two epi-72-St-diodes and a MCz-device is shown as a function of the bias normalized to the individual full depletion voltage. The epi-devices are irradiated with $2 \cdot 10^{14}\text{cm}^{-2}$ (non-inverted) and $2 \cdot 10^{15}\text{cm}^{-2}$ (inverted) while the MCz-sample is irradiated with $2 \cdot 10^{14}\text{cm}^{-2}$ (inverted). In case of the non inverted sample the collected charge follows approximately an square root dependence on the voltage. This is expected for highly irradiated but not inverted diodes where the charge carriers are created near the p^+-electrode. In contrast to that, for both inverted samples the voltage dependence of the collected charge can be segmented into three parts. In the first region the increase of the collected charge can be described by a saturating development followed in the second region by a nearly linear increase. Finally in the region where $V_{bias} > V_{FD}$ a further rise is observed. The voltage dependance in the first two parts is typically observed for inverted samples and can be explained by the double junction effect [Li92]. On the other hand the behavior in the third region can be attributed to charge carrier trapping. This is more pronounced in the MCz-diode due to the larger thickness and thus longer collection time compared to the inverted epi-device.

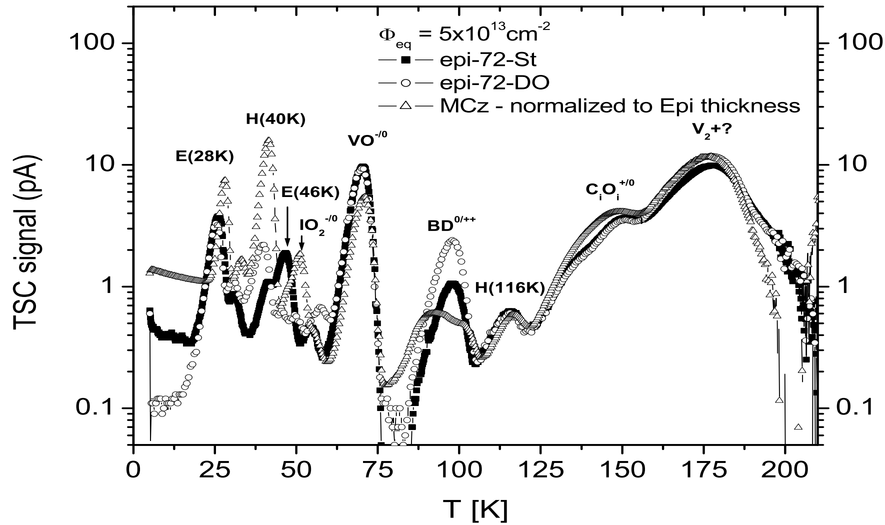

Figure 7.14: *TSC spectra after irradiation with reactor neutrons ($\Phi_{eq} = 5 \cdot 10^{13}cm^{-2}$) recorded on an epi-72-St, epi-72-DO and MCz diode with a reverse bias of 150 V for the epi-diodes and 300 V for the MCz diode. The TSC current of the 300 μm thick MCz is normalized to the thickness of the epi-diodes (72 μm). Injection of charge carriers for filling the traps was performed by forward biasing at 5 K.*

In the last section it was demonstrated that epi-50 material does not undergo type inversion during irradiation with 23 GeV protons or reactor neutrons up to fluences of 10^{16}cm^{-2}. An explanation was given by an introduction of shallow donors which always overcompensate the creation of deep acceptors (see also [Lin06a]). Thus the question is why do the both 72 μm epi-samples undergo type-inversion. An explanation would be that the introduction rate for shallow donors is suppressed or strongly reduced to a level below that of acceptors. TSC measurements on all materials demonstrate that shallow donor (denoted as $BD^{0/++}$) are generated in both epi-materials but in much lower concentration in MCz-material. All spectra shown in Fig. 7.14 are taken for a reverse bias voltage which is high enough so that the diodes stay fully depleted in the total TSC temperature range.

While the well known point defects like the C_iO_i, the V_2 or the H(116K) are measured with similar concentrations in all diode-types, the signal attributed to the VO_i-defect has a smaller peak height for the MCz diode than for both epi-diodes. This is due to the incomplete filling of the VO_i center due to the much lower doping concentration of the MCz material compared with the epi samples. Strong differences between the TSC spectra of the diodes are observed in the low temperature range. In case of the MCz a signal labeled IO_2 is observed. It was already mentioned that the oxygen-dimer, for whose presence the IO_2-defect is an indicator, is known to be a precursor for the formation of shallow donors like the early thermal donors TDD1 and TDD2 [Lin97, Lee02]. At very low temperature the spectra for the MCz and the epi-72-St show a "tail" in the TSC current. This tail, which is more pronounced in the MCz-diode, might be attributed to the existence of the BD-center in another configuration [Pin06]. The bistability of the BD-center could be directly observed in epi-72-DO material (see Fig. 7.15). In the TSC spectrum measured directly after irradiation a peak at 49 K (labeled $BD^{+/++}$) is shown which disappears

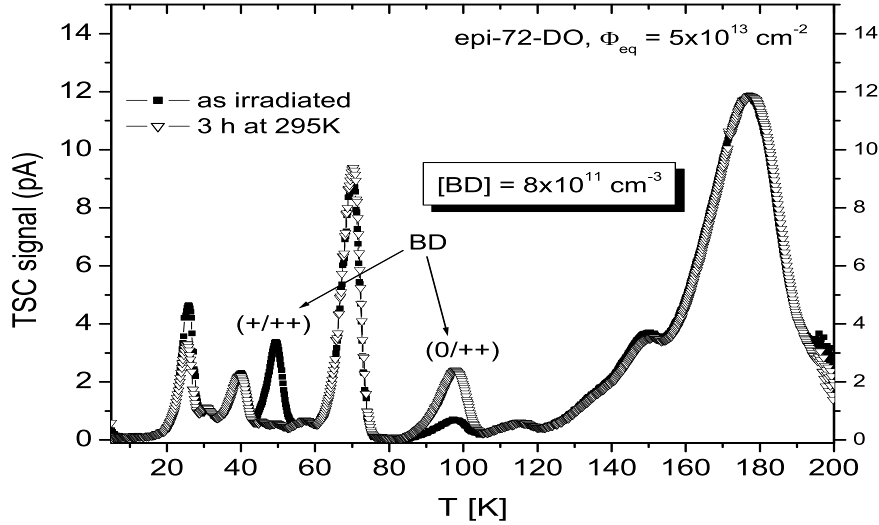

Figure 7.15: *TSC spectra of an epi-72-DO diode irradiated with reactor neutrons (Φ_{eq} = $5 \cdot 10^{13} cm^{-2}$) and after storage for 3 h at 295 K. The applied reverse bias and the filling of the traps are the same as given in the caption of Fig. 7.14.*

after a short storage time of three hours at room temperature. Thereafter a strong increase of the $BD^{0/++}$-transition is observed. The donor activity of both BD transition had been proven by the temperature shift of the peak position as function of the applied voltage (Poole-Frenkel effect). This effect is shown in Fig. 7.16 for the $BD^{+/++}$ transition. For the epi-72-DO diode the BD introduction rate could be accurately evaluated ($g(BD^{0/++}) = 1.7 \cdot 10^{-2}cm^{-1}$). This value represents the rate of positive charge introduced by the BD in the space charge region. Since the BD is assigned as a double donor the introduction for the BD concentration is half of the value given above.

In order to get an insight into the influence of the BD on the development of N_{eff} as function of fluence for the epi-72-DO material as presented in Fig. 7.12 the equation 7.2 can be rewritten as [Pin06]:

$$N_{eff} = N_{eff,0} + [BD] - [E] - [Z] \tag{7.3}$$

where [BD] represents the concentration of positive charge introduced by the ionized BD centers, [E] the concentration of the E-center (VP-defect) and [Z] the concentration of negative space charge at room temperature introduced e.g. by the deep acceptor I_p [Pin02a], clusters or other unknown defects. Unfortunately a quantitative evaluation for [Z] from TSC- or DLTS-studies could not be given so far. Therefore for a first guess the introduction rate of [Z] has been deduced from $N_{eff}(\Phi_{eq})$ measurements for neutron irradiated high purity FZ devices. In [Lin01b] a value of $g([Z]) = 2 \cdot 10^{-2}cm^{-1}$ is reported for standard FZ as well as oxygen enriched FZ (DOFZ) material. At high fluences, when all P donors are exhausted due to the formation of E-centers, N_{eff} is determined by the difference [BD]-[Z] only. For the epi-72-DO material with an effective introduction rate for negative space charge of $g_{eff} = 6 \cdot 10^{-3}cm^{-1}$ an introduction rate for positive space charge of $g([Z]) - g_{eff} = 1.4 \cdot 10^{-2}cm^{-1}$ is expected. This value is in sufficiently good agreement with the measured introduction rate for the BD-center presented above.

The comparison with the results after proton irradiation of the epi-50 samples, presented in the previous section, shows that although the introduction of BD is stronger after neutron irradiation and although the introduction of I_p is not observed in the TSC spectra type inversion takes place. Different raisons likely be responsible for this finding. One is the known higher introduction of clustered regions after neutron irradiation. Also a non constant introduction rate for [Z] (or [Z] + [Y]) might be a raison. But also other possibilities have to be taken into account. One is the recovery of P-doping at high fluences due to annihilation of VP by interstitials, which is more likely for the epi-50 samples because of its higher P concentration than for the epi-72-DO or epi-72-St samples. Nevertheless this would rather more explain why the epi-50 does not invert, but it would also explain why the inversion of the different epi-72 samples is more likely than the inversion of the epi-50 samples. Another very basic raison might be found in the assumption of a homogeneous electric field distribution used for the extraction of N_{eff}. This assumption might not be true anymore in case of a high and inhomogeneous cluster generation as it is known from both proton and neutron irradiation. But nevertheless the higher introduction of clustered regions after neutron irradiation can also be a raison for differences between proton and neutron irradiation.

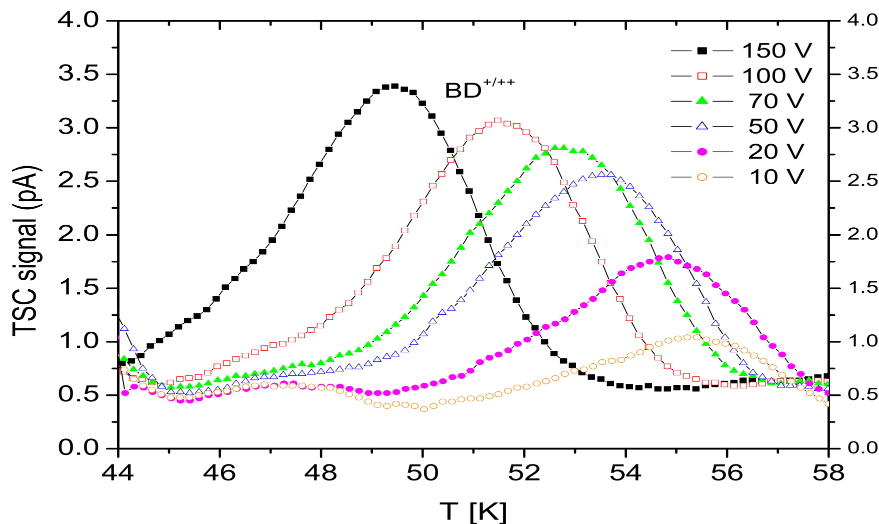

Figure 7.16: *Donor activity of the $BD^{(+/++)}$ transition. The TSC peak is shifting towards lower temperatures with increasing reverse bias applied during the TSC measurement.*

For the epi-72-St material an evaluation of the BD-concentration can not be done with sufficient accuracy and, therefore, a quantitative comparison between g_{eff} and the introduction rate of BD's could not be given.

It was already mentioned that one of the most important issues for the application of silicon sensors in the innermost part of the tracking area of the future S-LHC experiments will be the charge collection efficiency. The required electric field strength throughout the sensitive volume can readily be achieved for epi-devices within the S-LHC fluence range using moderate bias voltages. Degradation of the charge collection due to trapping of the drifting carriers is therefore a major problem. 5.8 MeV α-particles had been used to perform charge collection measurements as described in the last section. The collected charge is extracted from voltage scans

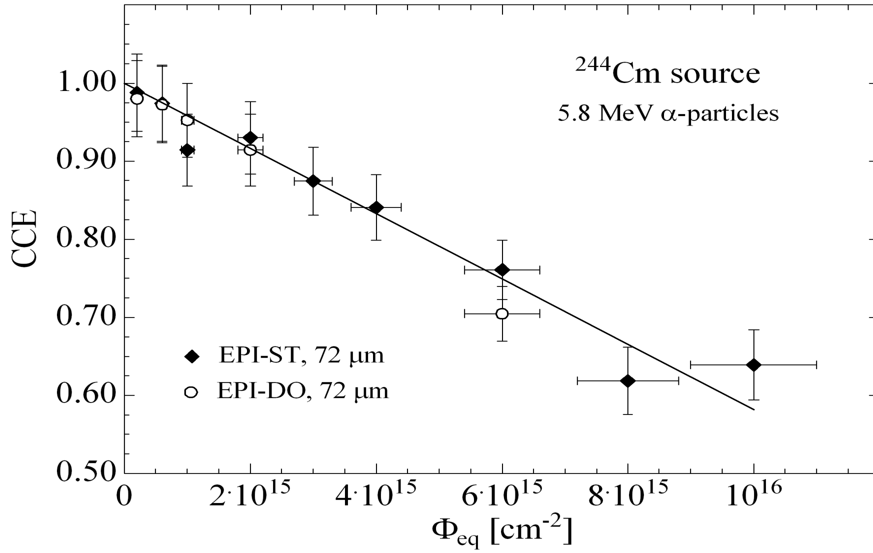

Figure 7.17: *Charge collection efficiency as function of fluence for epi-72-St and epi-72-DO diodes as measured with 5.8 MeV α-particles.*

performed very similar to what is shown in [Kra05]. The maximal bias voltage was kept above the value for full depletion such that the drift velocity of the charge carriers approaches nearly the saturation values. As a consequence, the collection time becomes independent of the bias voltage leading finally to a saturation of the charge loss by trapping. The CCE is plotted as function of fluence in Fig. 7.17. The solid line presents a fit to the experimental data according to CCE = 1 - $\beta_c \Phi_{eq}$. For the parameter β_c a value of $4.2 \cdot 10^{-17}$cm^2 is derived, resulting in a CCE value of 58% at 10^{16}cm^{-2}. From charge collection measurements with β-particles of a ^{90}Sr source, representing mip's, a charge collection of 3200 e was measured at $8 \cdot 10^{15}$cm^{-2} for epi-devices from the same production batch [Cin06]. This correspond to a CCE value of 56% which is quite similar to the value observed for α-particles. Both are also in good agreement with those data presented in the last section for epi-50 samples after irradiation with 23 GeV protons with the same equivalent fluence.

Chapter 8

Summary

Different silicon diodes fabricated on standard (StFZ) and diffusion oxygenated float zone (DOFZ), Czochralski (Cz), Magnetic Czochralski (MCz) and epitaxial silicon (EPI) with different oxygen content, resistivity and thickness were irradiated with different particles (^{60}Co-γ, 6 and 900 MeV electrons, 26 MeV and 23 GeV protons and reactor neutrons). The oxygen concentration in these materials varied between a few 10^{16}cm^{-3} in case of the StFZ and up to $8 \cdot 10^{17}$cm^{-3} for the Cz material.

Microscopic investigations with the *Deep Level Transient Spectroscopy* (DLTS) and partly with the *Thermally Stimulated Current* (TSC) method have been performed to compare the behavior of the different device-materials after irradiation with different particles.

Particle dependence of radiation induced defects

Devices manufactured on epitaxial silicon with a thickness of 50μm grown on a very low resistivity Cz-silicon substrate have proven to be radiation harder than conventional thick FZ-sensors with respect to the change of effective doping. Therefore such devices were irradiated with all kinds of particles mentioned above to compare the defect generation by using the DLTS method.

The main result of this comparison was the detection of differences in the ratio of point- and cluster related defects. After ^{60}Co-γ irradiation only point defects were measurable while after all other irradiations characteristic cluster related defects were seen too. These defects are observable in the suppression of the doubly charged divacancy ($V_2^{(=/-)}$), the presence of the E(170K)-defect, the broadening of the peak associated with the singly charged divacancy ($V_2^{(-/0)}$) and the decrease of the ratio of the vacancy-oxygen (VO_i) and the divacancy (V_2) defect. These cluster related effects become more and more significant with increasing energy of the *Primary knock-on atoms* (PKA's).

Beside the V_2 and the $E(170K)$ also the $VO_i^{(-/0)}$, the carbon-interstitial-oxygen interstitial ($C_iO_i^{(+/0)}$), the carbon interstitial ($C_i^{(-/0)}$) and the vacancy-phosphorus ($VP^{(-/0)}$) complex have been detected. The oxygen concentration was high enough to suppress the formation of the carbon-interstitial-carbon-substitutional (C_iC_s) complex. Only a small introduction of the C_i was detected. Although the phosphorus concentration is very high in the EPI-samples the VP defect was only visible after ^{60}Co-γ irradiation. This finding is due to the much lower generation of single

vacancy related defects after all other irradiations. However the DLTS method is only applicable at low radiation doses and at higher fluences the generation of VP plays a large role (donor removal).

The introduction of the C_iO_i, the defect which represents almost all defects related to single interstitials (via the chain $I + C_s \rightarrow C_i$; $C_i + O_i \rightarrow C_iO_i$), is similar to the introduction of the VO_i. This finding combined with the values for the introduction of divacancies leads to an increasing ratio of generated vacancies and interstitials with increasing energy of the PKA's. This effect indicates the also increasing presence of other interstitial related defects, like the di-interstitial (I_2) or the di-interstitial-oxygen (I_2O) complex, which are detectable with Infra-Red (IR) absorbtion measurements.

The interstitial-oxygen-dimer (IO_2), which is a good indicator for oxygen-dimers, was expected but not detected in the investigated volume of the devices. This finding is explained by a strong inhomogeneity not only of the oxygen but also of the oxygen-dimer concentration in the samples.

Material dependence of radiation induced defects

Diodes processed from different silicon materials were irradiated with ^{60}Co-gammas, 900 MeV electrons, 26 MeV protons, 23 GeV protons and reactor neutrons.

After ^{60}Co-γ irradiation in all samples the VO_i defect was detected in a large concentration and similar to the C_iO_i concentration. The introduction rates of the two negatively charged states of the divacancy were found with identical values in all samples.

The detection of the C_i and IO_2 defects were found to depend strongly on the oxygen content. In samples with high oxygen content the IO_2 defect was detected while in samples with low oxygen content the C_i was seen. The oxygen concentration was also influencing the VP-generation. In case of high oxygen content this so-called donor-removal, the removal of the phosphorus doping, was strongly suppressed by the competing formation of the VO_i-defect.

After 900 MeV electron irradiation a suppression of the $V_2^{(=/-)}$ concentration was detected in all materials with similar rate. This cluster related effect as well as the peak-broadening of the $V_2^{(-/0)}$ defect was observed. In addition, the E(170K)-defect was seen with similar introduction rate in all samples. The generation of impurity related defects did strongly depend on the oxygen content with similar findings as after ^{60}Co-γ irradiation. Nevertheless the introduction of single interstitial and vacancy related defects is much smaller than after ^{60}Co-γ irradiation. In case of the StFZ sample also the C_iC_s defect and the donor state of the C_i were present. In the float-zone- and EPI-materials additionally the shallow defects E(35K) and E(40K) were detected.

After 26 MeV proton irradiation different kinds of epitaxial as well as MCz silicon devices were investigated. The cluster formation was found to be independent of the used material, as expected from the experiments above. Differences are found for the introduction of impurity related defects. The introduction of the VO_i is similar in all EPI-materials except the oxygenated one and the MCz sample where a slightly higher concentration was found. Depth profiles of the IO_2 defect concentration were measured and compared with those of the oxygen concentration. A

quadratic dependence can be suggested from these results. A depth profile of the C_i concentration in an EPI-sample with a strong oxygen inhomogeneity was also measured. A clear correlation of C_i-maxima and oxygen-minima were found. This is in good agreement with the oxygen enhanced formation of the C_iO_i defect.

The same results were found for three different EPI-samples (25, 50 and 75 μm thickness) after irradiation with 23 GeV protons. No differences were seen for the cluster introduction. Inhomogeneous profiles for the C_i and the IO_2 defects were found due to the oxygen inhomogeneity.

The depth profiles of the IO_2 concentration taken after these two proton (26 MeV and 23 GeV) irradiation experiments suggest a strong correlation of the oxygen and oxygen-dimer concentration which is in contrast to a former suggestion of a homogeneous dimer concentration in EPI-samples due to their high mobility during the production of the samples and their out-diffusion from the Cz-substrates.

Several EPI-diodes with different thicknesses and oxygen profiles as well as a MCz sample were irradiated with reactor neutrons. In this experiment the highest introduction of clustered regions compared to all other performed irradiation experiments was seen. At the same time the generation of point defects was reduced. Nevertheless the same mechanism for the generation of impurity defects has been observed as after irradiation with charged hadrons. This can be summarized in the following way. A very high oxygen concentration leads to a high corresponding content of oxygen-dimers and therefore a lot of generated interstitials are trapped by dimers before getting transformed into C_i. But still a lot of C_i's are formed and afterwards captured by O_i and C_iO_i is formed. With decreasing oxygen content first the generation of IO_2 becomes smaller, than the generation of C_iO_i which leads to the highest C_i concentration in case of the lowest oxygen content.

Annealing of radiation induced defects

Isochronal annealing studies were performed on different materials after ^{60}Co-gamma, 26 MeV and 23 GeV proton irradiation. In the first case only the annealing of point defects can be observed, while after hadron irradiation also the cluster annealing is seen. The cluster annealing was found to be independent of the irradiation type and also of the used material. At temperatures between 250 and 300°C the clusters are annealed out.

Differences are observed for point defects. While the type of irradiation is only responsible for the introduction rate the defect annealing strongly depends on the investigated material.

A new defect, the $E(35K)$, had been identified as an interstitial related defect which influences the C_iO_i concentration during annealing. Two other interstitial related defects are also annealing below 100°C. First the C_i due to migration and afterwards the IO_2 by dissociation. The annealing leads to the formation of the C_iO_i and in case of low oxygen content also to the C_iC_s. While the C_iO_i defect is stable up to 300°C, the C_iC_s anneals out between 200 and 250°C. Above 300°C also the C_iO_i anneals out as well as the VO_i. Most likely the annihilation of C_iO_i and VO_i ($C_i + V \rightarrow C_s$) is responsible for this mechanism. In some cases also a formation of the VOH-defect was observed at this high temperatures.

The annealing of the divacancies strongly depends on the oxygen content of the

devices. In case of a high content the formation of the so-called X-defect was observed. Two charged states of this defect, the $X^{(=/-)}$ as well as the $X^{(-/0)}$, were seen with properties similar to the ones of the $V^{(=/-)}$ and the $V^{(-/0)}$ respectively. Up to now it is not clear wether the X-defect can be associated with the V_2O (depending on the oxygen content) or the V_2O_2 (depending on the oxygen-dimer content). For a better insight into this question detailed annealing experiments after ^{60}Co-γ-irradiation were performed using the DLTS as well as the TSC method. Although the results suggested an identification with the V_2O_2-defect, such a clear statement was not possible to give.

An isothermal annealing experiment at 80°C was performed on float zone, Czochralski and epitaxial silicon after irradiation with 900 MeV electrons. At this temperature mainly the annealing of the interstitial related defects C_i and IO_2 were observed. But also the annealing of cluster was studied.

After irradiation with reactor neutrons the annealing of the IO_2 was studied at different temperatures and an activation energy of the annealing $E_A = 1.29$ eV was extracted as well as a frequency factor of about $3 \cdot 10^{12} s^{-1}$. This frequency factor indicates that the annealing is due to dissociation.

Relation of microscopic and macroscopic features

Epitaxial (EPI) as well as MCz silicon was investigated regarding the relation of microscopic defects and macroscopic findings after irradiation with 23 GeV protons and reactor neutrons. A model for a quantitative explanation of the effective doping concentration, as introduced after ^{60}Co-γ irradiation, had been extended for a description after proton and neutron irradiation.

In case of proton irradiation it is shown, that thin, low resistivity epitaxial devices exhibit a large radiation tolerance up to more than 10^{16}cm^{-2} equivalent fluence. This effect is mainly attributed to the damaged induced generation of shallow bistable donors, which are most likely created via the presence of oxygen dimers. While the positive space charge build up strongly depends on the large oxygen content of the EPI-samples the acceptor creation during annealing is similar to what had been observed in FZ diodes. A dedicated experiment with 23 GeV proton irradiation steps and intermittent room temperature equivalent annealing had been performed and a comparison with simulations for a realistic 5 year's operational scenario of the S-LHC had supported the assumption that such thin epitaxial devices can withstand the damage during low temperature operational time and room temperature beam off periods at the future S-LHC.

After neutron irradiation of 72 μm thick 150 Ωcm standard and oxygen enriched EPI-devices as well as MCz-silicon detectors type inversion was seen and proven by charge collection measurements with 670 nm laser light pulses. From the analysis of the doping concentration generation rates for the introduction of negative space charge were evaluated. TSC measurements had shown that in EPI material the introduction of negative space charge is partly compensated by the generation of shallow donors (BD).

After proton- as well as neutron-irradiation charge collection efficiency measurements were performed with α-particles which resulted in similar fluence dependence.

Chapter 9

Outlook

The experimental data presented in this work gives information about the generation as well as the evolution of defects in different silicon materials. According to these data it is possible to understand the important role of oxygen and oxygen-dimer in the defect generation. Especially the measurements regarding the oxygen dimer lead to a deeper understanding in the relation between the oxygen and oxygen-dimer distribution. The oxygen-dimer is identified to be of major importance for the radiation hardness of silicon devices.

Although a model for a relation between microscopic defects and macroscopic detector properties has been established including the dimer related BD-defect the recent discovery of the new acceptor levels by TSC measurements have shown that this model might not be final and more investigations have to be undertaken.

The DLTS as well as the TSC methods are used for systematic studies of low irradiated devices. But the achieved fluences in future experiments reach values which are several orders of magnitude higher, therefore other experiments have to be performed to give a more detailed picture of the defects generation at high fluences. For this purpose different other techniques have to be combined.

This combination of different techniques is also necessary to identify the defects responsible for the main open problem for the future experiments, the charge trapping. It would be an invaluable progress if one could identify these defects and would open doors for an appropriate defect engineering. This might also include even more detailed investigations of the formation and annealing of the clustered regions.

Another open question is the influence of the doping in combination with the thickness of the devices. For such investigations devices with different thicknesses and identical impurities should be used.

Some open questions regarding the fundamental structure of defects are the controversy about the X-defect which is not finally solved. The defect E(35K) has been identified as interstitial related but no further information is extracted about its structure so far.

Appendix A

Constants and Silicon properties

In this section the fundamental constants and the properties of silicon which were used in this work are given. The values and equations in this section are taken from the PhD thesis of M.Moll [Mol99].

Property	Si	diamond	SiC
Atomic number (Z)	14	6	14+6
Density [g/cm^3]	2.33	3.52	3.22
Lattice constant [Å]	5.43	3.57	3.08
Bandgap [eV]	1.12	5.47	2.99
Energy to create e-h pair [eV]	3.6	13	8
Electron mobility [$cm^2/V/s$]	1450	1800	400
Hole mobility [$cm^2/V/s$]	450	1200	50
Displacement energy [eV]	20	43	25
Average signal (mips) [e-h/μm]	110	36	53

Table A.1: *Properties of different materials used for detector fabrication (after [Lut99],[Mol99],[Bru03]).*

Quantity	Symbol	Value
Boltzmann constant	k_B	$1.380658(12) \cdot 10^{-23}$ J/K
Elementary charge	q_0	$1.60217733(49) \cdot 10^{-19}$ C
Permittivity in vacuum	ϵ_0	$8.854187817 \cdot 10^{-14}$ F/cm
Electrical constant of Si	ϵ_{Si}	11.9
Electron rest mass	m_0	$9.1093897(54) \cdot 10^{-31}$ kg

Table A.2: *Fundamental constants*

The bandgap between the conduction and the valence band is temperature dependent. For this work the following temperature dependence was used:

$$E_g(T) = E_g(0) - \frac{\alpha_g \cdot T^2}{T + \beta_g} \tag{A.1}$$

with $E_g(0)$=1.1692 eV, α_g=$4.9 \cdot 10^{-4}$ eV/K and β_g=655 K.

For the density-of-state effective masses for electrons m^*_{dC} and holes m^*_{dV} the following parametrizations have been used:

$$m^*_{dC} = 6^{2/3}(m_t^{*2} m_l^*)^{1/3} \tag{A.2}$$

$$\textit{with} \qquad m_t^*/m_0 = 0.1905 \cdot \frac{E_g(0)}{E_g(T)} \qquad \textit{and} \qquad m_l^*/m_0 = 0.9163 \tag{A.3}$$

and

$$m^*_{dV}/m_0 = (\frac{a + bT + cT^2 + dT^3 + eT^4}{1 + fT + gT^2 + hT3 + iT^4})^{2/3} \tag{A.4}$$

with the constants

a=0.4435870	b=$0.3609528 \cdot 10^{-2}$	c=$0.1173515 \cdot 10^{-3}$
d=$0.1263218 \cdot 10^{-5}$	e=$0.3025581 \cdot 10^{-8}$	f=$0.4683382 \cdot 10^{-2}$
g=$0.2286895 \cdot 10^{-3}$	h=$0.7469271 \cdot 10^{-6}$	i=$0.1727481 \cdot 10^{-8}$

With these equations and the ones given in section 2.4 the occupation of a defect at room temperature and the generation current can be calculated.

Appendix B

Discrete Fourier Transformation

B.1 Signal processing

B.1.1 Fourier transformation

Fourier transformation is of fundamental use in physics. For electronic applications it is used to transform a time depending function f(t) into a function $F(i\omega)$ depending on frequency. Both functions contain the same information. If the integral of the function f(t), $\int_{-\infty}^{\infty} |f(t)|dt$ converges the function $F(i\omega)$ can be calculated

$$F(i\omega) = \int_{-\infty}^{\infty} f(t)exp(-i\omega t)dt. \tag{B.1}$$

It is also possible to transform this function back into the original function. This procedure is called inverse Fourier transformation.

$$f(t) = \int_{-\infty}^{\infty} F(i\omega)exp(i\omega t)d\omega. \tag{B.2}$$

For digital systems the values of the function f(t) are sampled, i.e. the data points are taken at discrete times $t_k = k\Delta t$. The difference in time between two points is called the sampling interval Δt. The function f_k consists of a finite number of discrete points $f_k = f(k\Delta t)$. In this case the continuous transformation cannot be used anymore. The discrete Fourier transformation (DFT) is defined as:

$$F_n = \sum_{k=0}^{N-1} f_k exp(-2\pi i\omega nk)/N), n = 0, 1, ..., N-1. \tag{B.3}$$

Also for the discrete Fourier transformation (DFT) the inverse transformation (IDFT) exists:

$$f_k = \sum_{k=0}^{N-1} F_n exp(2\pi i\omega nk)/N), n = 0, 1, ..., N-1. \tag{B.4}$$

The calculation of the DFT and the IDFT is done by a processor. If the sampled data rows contain a large number of points long CPU times are needed. Fortunately an algorithm exists which takes much less calculations and is used in nearly all applications using digital Fourier transformations. It is called FFT, which stands for Fast Fourier Transformation.

B.2 Folding

Another relevant operation is the so-called folding of two functions f(t),h(t):

$$g(t) = f(t) * h(t) = \int_{-\infty}^{\infty} h(t-\tau) f(\tau) d\tau, \quad \text{(B.5)}$$

where $f(t)$ is the unfolded function, $h(t)$ the folding function. The folding operation is commutative, i.e. $f(t)*h(t) = h(t)*f(t)$. A simplification of the folding operation can be achieved by using the Fourier transformation, because the folding of two functions is equal to a multiplication of the Fourier transformed functions:

$$G(i\omega) = H(i\omega) G(i\omega). \quad \text{(B.6)}$$

Considering a discrete number of values, the integrals have to be exchanged again:

$$g_k = \sum_{n=0}^{N-1} \bar{h}_{k-n} f_n \quad \text{(B.7)}$$

$$G_n = H_n F_n. \quad \text{(B.8)}$$

From (B.6) the transmission function $H(i\omega)$ transforms the function $f(t)$ with the spectra $F(i\omega)$ into the function $g(t)$ with the spectra $G(i\omega)$. An example for the folding operation in digital signal processing is the use of a digital filter. For a FIR (finite impulse response) filter the sampled values f_k are folded with the filter function, with the filter coefficients h_k:

$$g_k = \sum_{n=-N}^{N} h_n f_{k-n}. \quad \text{(B.9)}$$

B.3 Correlator functions

The calculation of the Fourier-coefficients or of the DLTS-signal can be taken as a special case of a correlator. The transient $f(t)$ is multiplied with a weighting function $h(t)$. The analogue correlator signal d^K is then the integral:

$$d^K = \int_0^{T_W} h(t) f(t) dt \quad \text{(B.10)}$$

For a discrete system this integral turns into a sum:

$$d = \sum_{n=0}^{N-1} h_n f_n \quad \text{(B.11)}$$

This summation can be written as folding:

$$g_k = \sum_{n=0}^{N-1} h_{k-n} f_n = \frac{1}{N} \sum_{n=0}^{N-1} H_n F_n exp(2\pi ink/N) \quad \text{(B.12)}$$

For more information about signal processing, folding and the correlator functions see also [Wei91].

Appendix C

Used devices

In this section an overview of the identification of the used devices and the measurements they were used for is given.

Label	irradiation	annealing	Wafer type
5856-01-10	^{60}Co-γ	isochronal 120-320°C	epi-50
8364-03-26	^{60}Co-γ	isochronal 120-320°C	epi-72-St
8364-03-18	^{60}Co-γ		epi-72-St
8364-06-53	^{60}Co-γ	isochronal 120-320°C	epi-72-DO
8364-06-60	^{60}Co-γ		epi-72-DO
WB-05-D08	^{60}Co-γ	isochronal 120-320°C	FZ-50
WB-05-C05	^{60}Co-γ		FZ-50
8556-09-24	^{60}Co-γ	isochronal 120-300°C	MCz-100
8556-09-15	^{60}Co-γ		MCz-100
6336-05-24	6 MeV electrons		epi-50
5856-02-38	900 MeV electrons	isothermal at 80°C	epi-50
ca0333	900 MeV electrons	isothermal at 80°C	StFZ
cd2022	900 MeV electrons	isothermal at 80°C	DOFZ
5337-04-38	900 MeV electrons	isothermal at 80°C	Cz
5856-08-32	26 MeV protons		epi-50
8364-01-25	26 MeV protons	isochronal 50-300°C	epi-72-St
8364-06-16	26 MeV protons	isochronal 50-300°C	epi-72-DO
6837-13-17	26 MeV protons		epi-75
6837-02-35	26 MeV protons		epi-25
8556-05-7	26 MeV protons		MCz
5856-07-60	23 GeV protons		epi-50
6837-03-35	23 GeV protons	isochronal 50-300°C	epi-25
6837-07-56	23 GeV protons	isochronal 50-300°C	epi-75

Table C.1: Used materials I

Label	irradiation	annealing	Wafer type
5856-01-26	reactor neutrons		epi-50
6837-01-07	reactor neutrons	isothermal at 100°C	epi-25
6837-01-08	reactor neutrons	isothermal at 80°C	epi-25
6837-01-10	reactor neutrons	isothermal at 120°C	epi-25
8364-02-26	reactor neutrons		epi-72-St
8364-05-24	reactor neutrons		epi-72-DO
8556-05-27	reactor neutrons		MCz
cb0241	^{60}Co-γ	isothermal at 250°C	DOFZ
cc1542	^{60}Co-γ	isothermal at 250°C	DOFZ
cd2041	^{60}Co-γ	isothermal at 250°C	DOFZ

Table C.2: Used materials II

Appendix D

Detected defects

In this section the parameters of the detected defects by the DLTS method are given. Defects with a negative activation energy are in relation to the edge of the conduction band, defects with a positive activation energy are in relation to the edge of the valence band.

Defect	$\Delta H'$ [eV]	$\sigma_{n,p}$ $[cm^2]$	$T(T_w = 200$ ms) [K]
$E(35K)$	-0.075	$2.0 \cdot 10^{-13}$	35
$E(40K)$	-0.078	$1.4 \cdot 10^{-14}$	40
$C_i^{(-/0)}$	-0.105	$1.4 \cdot 10^{-15}$	58
IO_2	-0.143	$3.8 \cdot 10^{-14}$	67
VO_i	-0.172	$1.2 \cdot 10^{-14}$	84
$V_2^{(=/-)}$	-0.259	$6.2 \cdot 10^{-15}$	118
$V_2^{(-/0)}$	-0.415	$1.5 \cdot 10^{-15}$	204
$C_i^{(+/0)}$	+0.287	$3.5 \cdot 10^{-15}$	140
C_iO_i	+0.351	$7.0 \cdot 10^{-16}$	179
BD	-0.225		95 (TSC)

Table D.1: *Radiation induced defects*

Defect	$\Delta H'$ [eV]	$\sigma_{n,p}$ $[cm^2]$	$T(T_w = 200$ ms) [K]
$E(54K)$	-0.096	$1.1 \cdot 10^{-15}$	54
Q	-0.232	$1.5 \cdot 10^{-14}$	110
$E(140K)$	-0.300	$5.0 \cdot 10^{-15}$	140
$VOH^{(-/0)}$	-0.322	$4.4 \cdot 10^{-15}$	152
$E(163K)$	-0.311	$6.2 \cdot 10^{-16}$	163
$E(175K)$	-0.357	$1.5 \cdot 10^{-15}$	175
$X^{(=/-)}$	-0.241	$1.1 \cdot 10^{-14}$	114
$X^{(-/0)}$	-0.467	$1.1 \cdot 10^{-14}$	211
$VOH^{(+/0)}$	+0.285	$1.6 \cdot 10^{-14}$	130

Table D.2: *Defects generated during annealing*

List of Figures

2.1 Introduced damage by 1 MeV neutron 4
2.2 Distribution of vacancies for different particles 5
2.3 Displacement damage functions D(E) normalized to 95 MeVmb 7
2.4 Defect states in the bandgap 7
2.5 SRH statistics 12
2.6 Oxygen interstitial 18
2.7 Oxygen dimer 19
2.8 Annealing temperatures of V-related defects 21
2.9 VO_i and VP 22
2.10 V_2O and V_2O_2 24
2.11 Annealing temperatures of I-related defects 25
2.12 Fluence dependence of the effective doping 28

3.1 SIMS of DOFZ and Cz silicon 32
3.2 SIMS of epi and MCz silicon 33
3.3 C/V characteristics 36
3.4 DLTS principle 39
3.5 Emission transient 40
3.6 Double boxcar method 41
3.7 Correlator functions 42
3.8 Temperature scan 43
3.9 Lambda correction 44
3.10 DLTS spectrum of two levels with similar properties 46
3.11 Normalized b1 coefficient 47
3.12 TSC principle 49
3.13 TSC spectrum 50
3.14 DLTS set-up 52
3.15 Electrical setting 53

4.1 DLTS spectra after ^{60}Co-γ irradiation 56
4.2 DLTS spectra after 6 MeV electron irradiation 58
4.3 DLTS spectra after 900 MeV electron irradiation 59
4.4 DLTS spectra after 26 MeV proton irradiation 61
4.5 DLTS spectra after 23 GeV proton irradiation 62
4.6 DLTS spectra after reactor neutron irradiation 63
4.7 Introduction rates of the $VO_i^{(-/0)}$-defect 65
4.8 DLTS spectra illustrating the cluster effect 66
4.9 Divacancy-ratio in epi50 66
4.10 Introduction rates of the divacancy 67
4.11 Ratio of VO_i and V_2 68

4.12 Introduction rates of the E(170K)-defect 69
4.13 Introduction rates of the $C_iO_i^{(+/0)}$-defect 70
4.14 Ratio of VO_i and CO_i 71
4.15 VP-defect 72

5.1 DLTS spectra after ^{60}Co-γ-irradiation (epi-50, epi-72-St, epi-72-DO) 75
5.2 DLTS spectra after ^{60}Co-γ-irradiation (DLTS spectra after ^{60}Co-γ-irradiation (FZ-50 and MCz-100) 76
5.3 Introduction rates of different defects after ^{60}Co-γ-irradiation 78
5.4 DLTS spectra after 900 MeV electron irradiation (FZ and DOFZ) 80
5.5 DLTS spectra after 900 MeV electron irradiation (epi-50) 81
5.6 DLTS spectra after 900 MeV electron irradiation (Cz) 82
5.7 Isothermal spectra of a Cz-diode 82
5.8 Introduction rates after irradiation with 900 MeV electrons 83
5.9 DLTS spectra after 26 MeV proton irradiation (epi-25, epi-50, epi-75) . . . 85
5.10 Depth profile of the C_i concentration in an epi-72-St detector 86
5.11 DLTS spectra for epi-72-St irradiated with 26 MeV protons 87
5.12 DLTS spectra for epi-72-St and epi-72-DO irradiated with 26 MeV protons 88
5.13 DLTS spectra for MCz material before and after irradiation with 26 MeV protons 88
5.14 Depth profiles of IO_{2i} defect concentration in epi-72-St, epi-72-DO and MCz devices after irradiation with 26 MeV protons 89
5.15 Concentration of the IO_{2i} defect in epi-72-St, epi-72-DO and MCz detectors as function of the oxygen concentration 90
5.16 Introduction rates after irradiation with 26 MeV protons 91
5.17 DLTS spectra after 23 GeV irradiation (epi-25) 92
5.18 DLTS spectra after 23 GeV irradiation (epi-50) 93
5.19 DLTS spectra after 23 GeV irradiation (epi-75) 93
5.20 Depth profiles of several defects 94
5.21 Introduction rates after irradiation with 23 GeV protons 95
5.22 DLTS spectra after reactor neutron irradiation (epi-25) 96
5.23 DLTS spectra after reactor neutron irradiation (epi-50) 97
5.24 DLTS spectra after reactor neutron irradiation (epi-72-St) 97
5.25 DLTS spectra after reactor neutron irradiation (epi-72-DO) 98
5.26 DLTS spectra after reactor neutron irradiation (MCz) 99
5.27 Introduction rates after irradiation with reactor neutrons 100

6.1 DLTS spectra, after ^{60}Co-γ-irradiation, of epi-72-St during annealing. . . . 103
6.2 DLTS spectra (holes), after ^{60}Co-γ-irradiation, of epi-72-St during annealing.104
6.3 Annealing of epi-72-St after gamma irradiation. 105
6.4 Annealing of epi-72-DO after gamma irradiation. 106
6.5 DLTS spectra after ^{60}Co-γ-irradiation of epi-72-DO during annealing. . . . 107
6.6 DLTS spectra (holes) after ^{60}Co-γ-irradiation of epi-72-DO during annealing.108
6.7 Evolution of the defect concentrations in a MCz-100 diode 109
6.8 DLTS spectra after electron injection of a MCz-100-diode 110
6.9 DLTS spectra after forward biasing of a MCz-100-diode 111
6.10 Evolution of the defect concentrations during an isochronal annealing of FZ-50 112
6.11 DLTS spectra after electron injection of an FZ-50-diode 113
6.12 DLTS spectra after forward biasing of an epi-72-diode 114

6.13 DLTS spectra illustrating the annealing out of the divacancy and the generation of the X-defect 115
6.14 Divacancy concentration of all three DOFZ materials during isothermal annealing 117
6.15 X-center concentration of all three DOFZ materials during isothermal annealing 117
6.16 DLTS spectra illustrating the annealing out X-defect 119
6.17 TSC spectra illustrating an isothermal annealing at 300°C of the divacancy 121
6.18 Evolution and simulation of the X-defect concentration during an isothermal annealing at 300°C for an epi-50 diode 122
6.19 DLTS spectra after electron injection (upside) and forward biasing (downside) of an FZ-diode during annealing (900 MeV electrons) 123
6.20 Annealing behavior of different defects in an FZ sample detected after irradiation with 900 MeV electrons 123
6.21 DLTS spectra after electron injection (upside) and forward biasing (downside) of an DOFZ-diode during annealing (900 MeV electrons) 125
6.22 Annealing behavior of different defects in a DOFZ sample detected after irradiation with 900 MeV electrons 125
6.23 Isothermal annealing at 80°C of a Cz-diode irradiated with 900 MeV electrons 126
6.24 Isothermal spectra of a Cz-diode (IO_2 and TDD) irradiated with 900 MeV electrons 127
6.25 Annealing behavior of different defects in a Cz sample detected after irradiation with 900 MeV electrons 127
6.26 DLTS spectra after electron injection and forward biasing of an epi-50-diode 128
6.27 Annealing behavior of different defects in an epi-50 sample detected after irradiation with 900 MeV electrons 129
6.28 Evolution of concentration during an isochronal annealing of defects detected in an epi-72-St diode irradiated with 26 MeV protons 130
6.29 Isochronal annealing of an epi-72 diode irradiated with 26 MeV protons . . 131
6.30 Difference spectra of an epi-72-St diode irradiated with 26 MeV protons . . 132
6.31 Isochronal annealing behavior of defects detected in an epi-72-DO diode irradiated with 26 MeV protons 133
6.32 Isochronal annealing of an epi-72-DO diode irradiated with 26 MeV protons 134
6.33 Evolution of concentration during an isochronal annealing of defects detected in an epi-72-DO diode irradiated with 26 MeV protons 135
6.34 Isochronal annealing behavior of defects detected in an epi-25 diode irradiated with 23 GeV protons 136
6.35 Isochronal annealing of an epi-25 diode irradiated with 23 GeV protons . . 137
6.36 Isochronal annealing behavior of defects detected in an epi-75 diode irradiated with 23 GeV protons 139
6.37 Isochronal annealing of an epi-75 diode irradiated with 23 GeV protons . . 140
6.38 Suppression of the IO_2-defect 142
6.39 Isothermal annealing of the IO_{2i} defect at different temperatures T_a 143
6.40 Arrhenius plot for the thermal activation of the IO_{2i} defect after irradiation with reactor neutrons 144

7.1 Effective doping concentration versus fluence 146
7.2 I/V versus fluence 146
7.3 TSC fit of I center 147
7.4 TSC-spectrum after proton irradiation 148

7.5 TSC-comparison I electrons/holes 149
7.6 Effective doping concentration, as measured after the end of the beneficial annealing 150
7.7 TSC spectra for epi-25, epi-50 and epi-75 diodes 151
7.8 Comparison of the donor generation in epi-50 diodes after irradiation with 23 GeV protons and reactor neutrons 151
7.9 Examples of annealing functions 152
7.10 S-LHC scenario 153
7.11 Charge collection efficiency (CCE) 154
7.12 Effective doping concentration as function of neutron-fluence 155
7.13 Collected charge as function of normalized bias V_{bias}/V_{FD} 156
7.14 TSC spectra after irradiation with reactor neutrons 157
7.15 TSC spectra of an epi-72-DO diode irradiated with reactor neutrons 158
7.16 Donor activity of the $BD^{(+/++)}$ transition 159
7.17 Charge collection efficiency as function of fluence for epi-72-St and epi-72-DO diodes 160

List of Tables

2.1 Hardness factors 5
2.2 Davies model 26

3.1 Properties and labeling of the used materials 32

4.1 Introduction rates (IR) after ^{60}Co-γ irradiation. 57
4.2 Introduction rates (IR) after 6 MeV electron irradiation. 59
4.3 Introduction rates (IR) after 900 MeV electron irradiation. 60
4.4 Introduction rates (IR) after 26 MeV proton irradiation. 61
4.5 Introduction rates (IR) after 23 GeV proton irradiation. 62
4.6 Introduction rates (IR) after reactor neutron irradiation. 64
4.7 Ratio of introduction rates for the E(170K)-defect and the ${V_2}^{(-/0)}$+?-defect. 69
4.8 Ratio of introduction rates of vacancy and interstitial related defects. . . . 72

5.1 Introduction rates (IR) after ^{60}Co-γ-irradiation. 78
5.2 Ratio of the VO_i-defect and the divacancy. 79
5.3 Ratio of the sum of interstitial and vacancy related defects. 79
5.4 Introduction rates (IR) after 900 MeV electron-irradiation. 83
5.5 Sum of the introduction rates of the interstitial related defects after 900 MeV electron-irradiation. 84
5.6 Introduction rates (IR) after 26 MeV proton-irradiation. 90
5.7 Sum of the introduction rates of the interstitial related defects after 26 MeV proton-irradiation. 91
5.8 Introduction rates (IR) after 23 GeV proton-irradiation. 95
5.9 Sum of the introduction rates of the interstitial related defects after 23 GeV proton-irradiation. 96
5.10 Introduction rates (IR) after reactor neutron-irradiation. 99
5.11 Sum of the introduction rates of the interstitial related defects after neutron irradiation. 100

6.1 Defect reactions at higher temperatures. 101
6.2 Time constants for annealing of VV 116
6.3 Time constants for formation and annealing of X 118
6.4 Time constants for formation and annealing of X assuming X to be V_2O and with oxygen contents 10 - 30 % higher than after SIMS. 120
6.5 Reactions used for simulation of TSC results after gamma irradiation 121

A.1 Material properties 166
A.2 *Fundamental constants* 166

C.1 Used materials I 170
C.2 Used materials II 171

D.1 *Radiation induced defects* 172
D.2 *Defects generated during annealing* 172

Bibliography

[Abe98] D. Åberg, B.G. Svensson, T. Hallberg, J.L. Lindström. Kinetic study of oxygen dimer and thermal donor formation in silicon. Physical Review B, 58, 12944 (1998).

[Akk01] Akkerman et al.. Rad. Phys. and Chemistry 62: 301-310, 2001.

[And75] P.W. Anderson. Model for the Electronic Structure of Amorphous Semiconductors. Physical Review Letters, Volume 34, Number 15: 953-955, 1975.

[And04] L. Andricek et. al., IEEE Trans Nucl. Sci. Vol 51 No 3 (2004) 1117.

[ATL] ATLAS. Pixel Detector- Technical Design Report. CERN/LHCC/98-13, 1998.

[Bar03] A. Barcz, M. Zielinski, E. Nossarzewska, G. Lindstroem. Extremely deep SIMS profiling: oxygen in FZ silicon. Applied Surface Science 203-204: 396-399, 2003.

[Bru03] M. Bruzzi. Development of Radiation Hard Sensors for Very High Luminosity Colliders -CERN-RD50 project-. Presented at 2003 IEEE NSS MIC Portland, Oregon, USA, October 19-24, 2003.

[Cas00] R.A. Casali, H. Ruecker, and M. Methfessel. Interaction of vacancies with interstitial oxygen in silicon. Applied Physics Letters, Volume 78, Number 7, 2000.

[Cin06] V. Cindro, G. Kramberger, I. Mandic, M. Mikuz, M. Zavrtanik, G. Lindström, E. Fretwurst, V. Khomenkov, CCE measurements with epi-Si detectors, 8th RD50-Workshop on Radiation hard semiconductor devices for very high luminosity colliders, Prague,Czech Republic, 25-28th June 2006

[CiS] CiS, Institut für Mikrosensorik GmbH, Erfurt, Germany

[CMS] CMS. CMS Technical Proposal. CERN/LHCC94-38,1994, 1994.

[Cor61] J.W. Corbett, G.D. Watkins, R.M. Chrenko, and R.S. McDonald. Defects in irradiated Silicon. II. Infrared Absorption of the Si-A Center. Physical Review, Volume 121, Number 4: 1015-1022, 1961.

[Cor64] J.W. Corbett, G.D. Watkins, and R.S. McDonald. New Oxygen Infrared Bands in Annealed Irradiated Silicon. Physical Review, Volume 135, Number 5A: 1381-1385, 1964.

[Cor65] J.W. Corbett and G.D.Watkins. Production of Divacancies and Vacancies by Electron Irradiation of Silicon. Physical Review A, 138: 555-, 1965.

[Cor66] J.W. Corbett. Electron Radiation Damage in Semiconductors and Metals. Academic Press, New York and London, 1966.

[Cou00] J. Coutinho, R. Jones, P.R. Briddon, S. Öberg. Oxygen and dioxygen centers in Si and Ge; Density-functional calculations. Physical Review B, Volume 62, Number 16, 2000.

[Cou01] J. Coutinho, R. Jones, L.I. Murin, V.P. Markevich, J.L. Lindström, S. Öberg, P.R. Briddon. Thermal Double Donors and Quantum Dots. Pysical Review Letters, Volume 87, Number 23: 235501-1-4, 2001.

[Cou03] J. Coutinho, R. Jones, S. Öberg, P.R. Briddon. The formation, dissociation and electrical activity of divacancy oxygen complexes in Si. Physica B 340-342: 523-527, 2003.

[Dav87] G. Davies, E.C. Lightowlers, R.C. Newman and A.S. Oates. A model for radiation damage effects in carbon-doped crystalline silicon. Semicond. Sci Technol, 2: 524-532, 1987.

[Dav06] G. Davies, S. Hayama, L. Murin, R. Krause-Rehberg, V. Bondarenko, A. Sengupta, C. Davia, A. Karpenko. - Radiation damage in silicon exposed to high-energy protons. Phys. Rev. B Vol. 73, N 16. p. 165-202 (1-10). 2006

[Dez97] B. Dezillie. Radiation hardness studies of epitaxial silicon particle detectors for applications at the CERN Large Hadron Collider. PhD thesis, University Joseph Fourier-Grenoble 1, 1997.

[Ewe96] C.P. Ewels, R. Jones, S. Öberg, J. Miro, and P. Deak. Shallow Thermal Donor Defects in Silicon. Physical Review Letters, Volume 77, Number 5: 865-868, 1996.

[Fei97] H. Feick. Radiation Tolerance of Silicon Particle Detectors for High-Energy Physics experiments. PhD thesis, Universtity of Hamburg, 1997.

[Fek97] O.V. Feklisova and N.A. Yarykin. Transformation of deep-level spectrum of irradiated silicon due to hydrogenation under wet chemical etching. Semicond. Sci. Technol. 12: 742-749, 1997.

[Fre97] E. Fretwurst, V. Eremin, H. Feick, J. Gerhardt, Z. Li, G. Lindström. Nucl. Instr. & Meth. in Phys. Res. A, 388: 356, 1997.

[Fre07] E. Fretwurst, L. Andricek, F. Hönniger, K. Koch, G. Kramberger, G. Lindstöm H.G. Moser, I. Pintilie, R. Richter, R. Rder. Comparison of neutron damage in thin FZ, MCz and epitaxial silicon detectors, presented on the RD50 workshop in Vilnius, 4th to 6th of June 2007

[Ful54] C.S. Fuller, N.B. Ditzenberger, N.B. Hannay and E. Buehler. Physical Review, 96: 833, 1954.

[Gar48] G.F.J Garlick and A.F. Gibson. The Electron Trap Mechanism of Luminescence in Sulphide and Silicate Phosphors. Proc. Phys. Soc. (London) 60: 574-578, 1948.

[Gil97] K. Gill, G. Hall, B. MacEvoy. Bulk damage effects in irradiated silicon detectors due to clustered divancancies. J. Appl. Phys., 82 (1): 126-136, 1997.

[Gos59] B.R. Gossik. Disordered Regions in Semiconductors Bombarded by Fast Neutrons. Journal of Applied Physics, Volume 30, Number 8: 1214-1218, 1959.

[Gur92] E. Guerer, B.W. Benson, G.D. Watkins. Configurational Metastabilty of Carbon-Phosphorous Pair Defects in Silicon. Materials Science Forum. Vol. 83-87: 339-344, 1992.

[Gri96] P. Griffin et al. SAND92-0094 (SANDIA Natl. Lab., Nov 1996), neutron cross sections taken from ENDF/B-VI, ORNL, unpublished but available from G. Lindström, Hamburg (gunnar.lindstroem@desy.de)

[Hal99] Anders Hallen, Niclas Keskitalo, Lalita Josyula and Bengt G. Svensson. Migration energy for the silicon self-interstitial. Journal of Applied Physics, Volume 86, Number 1: 214-216, 1999.

[Has97] J.L. Hastings, S.K. Estreicher, P.A. Fedders. Vacancy aggregates in silicon. Physical Review B, 56(16):10215-10220, 1997.

[Her01] J. Hermansson, L.I. Murin, T. Hallberg, J.L. Lindström, M. Kleverman, B.G. Svensson. Complexes of the self-interstitial with oxygen in irradiated silicon: a new assignment of the 936 cm^{-1} band. Physica B 302-303: 188-192, 2001.

[Huh02] M. Huhtinen. Simulation of non-ionising energy loss and defect formation in silicon. Nucl. Instr. & Meth. in Phys. Res. A, 491: 194-215, 2002.

[Huh93a] M. Huhtinen an P. Aarino. Estimation of pion induced displacement damage in silicon. HU-SEPT R 1993-02, 1993

[Huh93b] M. Huhtinen and P.A. Aarnio. Pion induced displacement damage in silicon devices. Nucl. Inst. & Meth. in Physics Research, A 335:580, 1993 (See also [Huh93a])

[ITM] Institute of Electronic Materials Technology (ITME), ul Wolczynska 133, 01-919 Warsaw, Poland.

[ITR] International Technology Recommendation Panel (ITRP), Final International Technology Recommendation Panel Report, Sep. 2004, available at http://www.ligo.caltech.edu/ BCBAct/ITRP/

[Jag93] C. Jagadish, B.G. Svensson and N. Hauser. Point defects in n-type silicon implanted with low doses of MeV boron and silicon ions. Semicond. Sci. Technol. 8: 481-487, 1993.

[Kem80] J. Kemmer. Fabrication of Low Noise Silcion Radiation Detectors by the Planar Process. Nuclear Instruments and Methods, 169: 499-502, 1980.

[Khi01] L.I. Khirunenko, L.I. Murin, J.L. Lindström, M.G. Sosnin, Yu.V. Pomozov. Self-interstitial-oxygen related defects in low-temperature irradiated Si. Physica B 308-310: 458-461, 2001.

[Kim76] L.C. Kimerling. New Developments in Defect Studies in Semiconductors. IEEE Transactions on Nuclear Science, Vol.NS-23, No.6: 1497-1505, 1976.

[Kon92] A. Yu. Konobeyev et al. Neutron sisplacemant cross-sections for structural materials below 800 MeV. J. Nucl. Mater., 186:117, 1992

[Kra01] G. Kramberger. Signal Developement in irradiated silicon detectors. PhD thesis, Universtity of Ljubljana, 2001.

[Kra03] G. Kramberger. D. Contarato, E. Fretwurst, F. Hönniger, G. Lindström, I. Pintilie, R. Röder, A. Schramm, J. Stahl. Superior radiation tolerance of thin epitaxial silicon detectors. Nucl. Instr. & Meth. in Phys. Res. A, 515: 665-670, 2003.

[Kra05] G. Kramberger, V. Cindro, I. Dolenc, et al., Charge collection properties of heavily irradiated epitaxial silicon detectors, Nucl. Inst. & Meth. A 554, 212-219 (2005).

[Kuh01] M. Kuhnke. Microscopic Investigations on Various Silicon Materials Irradiated with Different Particles with the DLTS Method. PhD thesis, Universtity of Hamburg, 2001.

[Lan74] D.V. Lang. Deep-level Transient Spectroscopy: A new method to characterize traps in semiconductors. J. Appl. Phys., 45:3023, 1974.

[Laz87] M.S. Lazo, D.M. Woodall and P.J. McDaniel. Silicon and silicon dioxide neutron damage functions. In Proc. Fast Burt React. Workshop, 1986. Sandia National Laboratories, 1987. [Tech.Rep.] SAND, SAND87-0098 Vol.1., pages 85-103, 1987.

[Lea98] P. Leary, R. Jones, S. Öberg. Interaction of hydrogen with substitutional and interstitial carbon defects in silicon. Physical Review B, Volume 57, Number 7: 3887-3899, 1998.

[Lee73] Y. H. Lee and J. W. Corbett. EPR Studies in Neutron-Irradiated Silicon: A Negative Charge State of a Nonplanar Five-Vacancy Cluster (V_5^-). Physical Review B, 8(6):2810, 1973.

[Lee76] Young-Hoon Lee and James W. Corbett. EPR studies of defects in electron irradiated silicon: A triplet state of vacancy-oxygen complexes. Physical Review B, Volume 13, Number 6: 2653-2666, 1976.

[Lee01] Y.J. Lee, J. von Boehm, M. Pesola, and R.M. Nieminen. Aggregation kinetics of Thermal Double Donors in Silicon. Physical Review Letters, Volume 86, Number 14: 3060-3063, 2001.

[Lee02] Y.J. Lee, J. von Boehm, M. Pesola, and R.M. Nieminen. First-principles study of migration, restructuring, and dissociation energies of oxygen complexes in silicon. Physical Review B, Volume 65: 085205-1-12, 2002.

[Lee03] Y.J. Lee, J. von Boehm, M.Pesola, and R.M. Nieminen. Comparison of oxygen-chain models for late thermal double donors in silicon. Applied Physics Letters, Volume 82, Number 13: 2094-2096, 2003.

[Li92] Z. Li, H. W. Kramer, J. Electron Mater. 21 (1992) 701

[Li98] Z. Li. Systematic modelling and comparisons of capacitance and current-based microscopic defect analysis techniques for measurements of high-resistivity silicon detectors after irradiation. Nucl. Instr. & Meth. in Phys. Res. A, 403: 399-416, 1998.

[Lin80] V.A.J. van Lint, T.M. Flanagan, R.E. Leadon, J.A. Naber, V.C. Rogers. Mechanisms of Radiation Effects in Electronic Materials. John Wiley & Sons, 1980.

[Lin94] J.L. Lindström and T. Hallberg. Clustering of Oxygen Atoms in Silicon at 450°C: A New Approach to Thermal Donor Formation. Physical Review Letters, Volume 72, Number 17: 2729-2732, 1994.

[Lin97] J.L. Lindström et al., Mater. Sci. Forum 258-263: 367, 1997.

[Lin01] G. Lindström et al.. Developments for radiation hard silicon detectors by defect engineering-results by the CERN RD48 (ROSE) Collaboration. Nucl. Instr. & Meth. in Phys. Res. A, 465: 60-69, 2001.

[Lin01a] J.L. Lindström, T. Hallberg, J. Hermansson, L.I. Murin, B.A Komarov, V.P. Markevich, M. Kleverman, B.G. Svensson. Interaction between self-interstials and the oxygen dimer in silicon. Physica B 308-310: 284-289, 2001.

[Lin01b] G. Lindström et al., Nucl. Instr. & Meth. A 466 (2001) 308-326

[Lin03] J.L. Lindstöm, L.I. Murin, B.G. Svensson, V.P. Markevich, T. Hallberg. The VO_2^* defect in silicon. Physica B 340-342: 509-513, 2003.

[Lin03a] G. Lindström. Radiation damage in silicon detectors. Nucl. Instr. & Meth. in Phys. Res. A, 512: 30-43, 2003.

[Lin06] G. Lindström, E. Fretwurst, F. Hönniger, G. Kramberger, M. Möller-Ivens, I. Pintilie, A. Schramm. Radiation tolerance of epitaxial silicon detectors at very large proton fluences. Nuclear Instruments & Methods in Phys. Rev. A, 556: 451-458, 2006

[Lin06a] G. Lindstöm, I. Dolenc, E. Fretwurst, F. Hönniger, G. Kramberger et al.,Epitaxial Silicon Detectors for Particle Tracking -Radiation Tolerance at Extreme Hadron Fluences-, Nucl. Instr. & Meth. A 568 (2006) 66-71

[Lut96] G. Lutz. Effects of deep level defects in semiconductor detectors. Nucl. Instr. & Meth. in Phys. Res. A, 377: 234-243, 1996.

[Lut99] Gerhard Lutz. Semiconductor Radiation Detectors. Springer-Verlag. ISBN 3-540-64859-3, 1999.

[Mac95] B.C. MacEvoy, G. Hall, K. Gill. Defect evolution in irradiated silicon detector material. Nucl. Instr. & Meth. in Phys. Res. A, 374: 12-26, 1996.

[Mac96] B.C. MacEvoy, Defect kinetics in silicon detector material for applications at the Large Hadron Collider. PHD Thesis Imperial College, London UK, RAL-TH-97-003, Nov 1996.

[Mac99] B.C. MacEvoy, A. Santocchia, G. Hall. Defect-engineering rad-hard particle detectors: the role of impurities and inter-defect charge exchange. Pysica B 273-274: 1045-1049, 1999.

[Mac00] B.C. MacEvoy, G. Hall. Defect kinetics in novel detector materials. Materials Science in Semiconductor Processing 3: 243:249, 2000.

[Mac02] B.C. MacEvoy, G. Hall, A. Santocchia. Cryogenic investigations and modelling of inter-defect charge exchange in silicon particle detectors. Nucl. Instr. & Meth. in Phys. Res. B, 186:138-143, 2002.

[Mak03] L.F. Makarenko, F.P. Korshunov, S.B. Lastovskii, and N.I. Zamyatin. Detection of Hydrogen Impurity in Silicon Radiation Detectors. Semiconductors, Vol. 37, No. 5: 611-615, 2003.

[Mik05] M. Mikelsen, E.V. Monakhov, G. Alfieri, B.S. Avset, B.G. Svensson. Kinetics of divacancy annealing and divacancy-oxygen formation in oxygen-enriched high-purity silicon. Physical Review B 72, 295207 (2005).

[Mik07] M. Mikelsen, J.H. Bleka, J.S. Christensen, E.V. Monakhov, B.G. Svensson. Annealing of the divacancy-oxygen and vacancy-oxygen complexes in silicon. Phys. Rev. B 75, 155202 (2007).

[Mol99] M. Moll. Radiation Damage in Silicon Particle Detectors. PhD thesis, University of Hamburg, 1999.

[Mol02] M.Moll, E. Fretwurst, M. Kuhnke, G.Lindström. Relation between microscopic defects and macroscopic changes in silicon detector properties after hadron irradiation. Nucl. Instr. & Meth. in Phys. Res. B, 186: 100-110, 2002.

[Mon02] E.V. Monakov, B.S. Avset, A. Hallen and B.G. Svensson. Formation of a double acceptor center during divacancy annealing in low-doped high purity oxygenated Si. Physical Review B, Volume 65, 233207:1-4, 2002.

[MPI] MPI Halbleiterlabor; Otto-Hahn-Ring 6, D-81739 München, Germany.

[Mur98] L.I. Murin, T. Hallberg, V.P. Markevich, and J.L. Lindström. Experimental Evidence for the Oxygen Dimer in Silicon. Physical Review Letters, Volume 80, Number 1: 93-96, 1998.

[Mur06] L.I. Murin, J.L. Lindström, G. Davies, V.P. Markevich. Evolution of radiation-induced carbon-oxygen-related defects in silicon upon annealing: LVM studies. Nucl. Instr. & Meth. in Phys. Rev. B 253 210-213, 2006.

[Mur07] L.I. Murin, B.G. Svensson, Interaction of intrinsic defects with oxygen in neutron irradiated MCz-Si: An infrared absorbtion study, Presentation at WODEAN Conference June 2007, Vilnius, Lithuania

[Obe98] S. Öberg, C.P. Ewels, R. Jones, T. Hallberg, J.L. Lindström, L.I. Murin, P.R. Briddon. First Stage of Oxygen Aggregation in Silicon: The Oxygen Dimer. Physical Review Letters, Volume 81, Number 14, 1998.

[OKM] Okmetic Oy, Finland

[Pan91] Jacques I. Pankove, Noble M. Johnson, editors. Hydrogen in semiconductors, volume 34 of Semiconductors and Semimetals. Academic Press, INC., 1991. ISBN 0-12-752134-8.

[Pel01] P. Pellegrino, P. Leveque, J. Lalita, A. Hallen, C. Jagadish, B.G. Svensson. Annealing kinetics of vacancy-related defects in low-dose MeV self-ion-implanted n-type silicon. Physical Review B, Volume 64, 195211: 1-10, 2001.

[Pin00] I. Pintilie, L. Pintilie, M. Moll, E. Fretwurst and G. Lindström. Thermally stimulatated current method applied on diodes with high concentration of deep trapping levels. Applied Physics Letters, Volume 78, Number 4: 550-552, 2001.

[Pin02] I. Pintilie, C. Tivarus, L. Pintilie, M. Moll, E. Fretwurst, G. Lindström. Thermally stimulated current method applied to highly irradiated silicon diodes. Nucl. Instr. & Meth. in Phys. Res. A, 466:652-657, 2002.

[Pin02a] I.Pintilie, E. Fretwurst, G. Lindstroem, J. Stahl. Close to midgap trapping level in ^{60}Co gamma irradiated silicon detectors. Appl. Phys. Lett. 81 (1): 165, 2002.

[Pin03a] I.Pintilie, E. Fretwurst, G. Lindstroem, J. Stahl. Second order generation of point defects in gamma irradiated float zone silicon, an explanation for "type inversion". Appl. Phys. Lett. 82 (13): 2169, 2003.

[Pin03b] I.Pintilie, E. Fretwurst, G. Lindstroem, J. Stahl. Results on defects induced by ^{60}Co gamma irradiation in standard and oxygen-enriched silicon. Nucl. Instr. & Meth. in Phys. Res. A, 514: 18-24, 2003.

[Pin03c] I. Pintilie, E. Fretwurst, G. Kramberger, G. Lindström, Z. Li, J. Stahl. Second-order generation of point defects in highly irradiated float zone silicon - annealing studies. Physica B, 340-342: 578-582, 2003.

[Pin05] I. Pintilie, E. Fretwurst, F. Hönniger, G. Lindström. J. Stahl, Nucl. Instr. and Meth. A 552 (2005) 56-60

[Pin06] I. Pintilie, M. Buda, E. Fretwurst, G. Lindström, J. Stahl, Stable radiation-induced donor generation and its influence on the radiation tolerance of silicon diodes. Nucl. Instr. and Meth. A 556 (2006) 197-208

[Pin06b] I. Pintilie, E. Fretwurst, F. Hönniger, G. Lindström, B.G. Svensson, Defect kinetics in Epi/Cz silicon after ^{60}CO-γ irradiation, Presentation at the 8th CERN-RD50 collaboration workshop, 26th June 2006, Praque

[Pin06c] I. Pintilie, CERN-RD50 WODEAN Meeting Hamburg, Thermally Stimulated Currents Method, August 2006

[Pin07] I. Pintilie, private communication.

[PHYS] http://www.phystech.de; Company homepage

[Ram98] M. Ramamoorty and S.T. Pantelides. Enhanced Modes of Oxygen Diffuison in Silicon. Solid State Communications, Vol 106, No. 5: 243-248, 1998.

[RD50] http://rd50.web.cern.ch/rd50; Collaboration homepage

[Sch03] A. Schramm. Strahlenhärte von epitaktischen Siliziumdetektoren. Diploma thesis, University of Hamburg, 2003.

[Shi90] Y. Shi, D.X. Shen, F.M. Wu, and K.J. Cheng. A numerical study of cluster center formation in neutron- irradiated silicon. J. Appl. Phys., 67 (2): 1116-1118, 1990.

[Shi94] F. Shimura, editor. Oxygen in silicon, volume 42 of Semiconductors and Semimetals. Academic Press, INC., 1994. ISBN 0-12-752142-9.

[SLHC] F. Gianotti, et al., hep-ph/0204087, 2002.

[SIT] Somitomo/Sitix, Japan

[Son88] L.W. Song, X.D. Zhan, B.W. Benson, and G.D. Watkins. Bistable Defect in Silicon: The Interstitial-Carbon- Substitutional-Carbon Pair. Physical Review Letters, Volume 60, Number 5: 460-463, 1988.

[Son90] L.W. Song, X.D. Zhan, B.W. Benson, and G.D. Watkins. Bistable interstitial-carbon-substitutional-carbon pair in silicon. Physical Review B, 42 (9): 5765, 1990.

[Sum93] G.P. Summers et al. Damage correlations in semiconductors exposed to gamma, electron and proton radiations. IEEE Transactions on Nuclear Science, NS-40:1372, 1993

[Sta04] J. Stahl Defect Characterisation in High-Purity Silicon after γ- and Hadron Irraditation. PhD thesis, University of Hamburg, 2004.

[Sve86] B.G. Svensson and J.L. Lindström. Kinetic study of the 830- and 889-cm^{-1} infared bands during annealing of irradiated silicon. Physical Review B, Volume 34, Number 12: 8709-8717, 1986.

[Sve91] B.G. Svensson, B. Mohadjeri, A. Hallen, J.H. Svensson, J.W. Corbett. Divacancy acceptor levels in ion-irradiated silicon. Physical Review B, Volume 43, Number 3: 2292-2298, 1991.

[Sve92] B.G. Svensson, J.L. Lindström. Generation of divacancies in silicon by MeV electrons: Dose rate dependence and influence of Sn and P. J. Appl. Phys. 72(12): 5616-5621, 1992.

[Sve97] B.G. Svensson, C. Jagadish, A. Hallen, J. Lalita. Generation of vacancy-type point defects in single collision cascades during swift-ion bombardment of silicon. Physical Review B, Volume 55, Number 16: 10498-10507, 1997.

[Sze81] S.M. Sze. Physics of semiconductor devices. John Wiley & Sons, 2nd edition, 1981.

[Sze85] S.M. Sze. SEMICONDUCTOR DEVICES Physics and Technology. John Wiley & Sons, 1985.

[Vas97] A. Vasilescu. The NIEL scaling hypothesis applied to neutron spectra of irradiation facilities and in the ATLAS and CMS SCT. ROSE Internal Note, ROSE/TN 97/2, 1997

[Vec76] J.A. van Vechten, C.D. Thurmond. Entropy of ionization and temperature variation of ionization of defects in semiconductors. Physical Review B, Volume 14, Number 8: 3539-3550, 1976.

[WAC] Wacker Siltronic, Burghausen, Germany.

[Wai57] T.R. Waite, Phys. Rev. 107, 463 (1957).

[Wat60] G.D. Watkins and J.W. Corbett. Defects in Irradiated Silicon. I. Electron Spin Resonance of the Si-A Center. Physical Review, Volume 121, Number 4: 1001-1014, 1960.

[Wat64] G.D. Watkins and J.W. Corbett. Defects in Irradiated Silicon: Electron Paramagnetic Resonance and Electron- Nuclear Double Resonance of the Si-E Center. Physical Review, Volume 134, Number 5A: 1359-1377, 1964.

[Wat65] G.D. Watkins and J.W. Corbett. Defects in Irradiated Silicon: Electron Paramagnetic Resonance of the Divacancy. Physical Review, Volume 138, Number 2A: 543-555, 1965.

[Wat81] G.D. Watkins and J.R. Troxell. Negative-U Properties for Point Defects in Silicon. Physical Review Letters, Volume 44, Number 9, 593-596, 1980.

[Wat96] S.J. Watts et al. A new model for generation and recombination in silicon depletion regions after neutron irradiation IEEE NS-43 2587 (1996)

[Wat00] G.D. Watkins. Intrinsic defects in silicon. Materials Science in Semiconductor Processing, 3: 227-235, 2000.

[Wei68] L.R. Weisberg and H. Schade. A Technique For Trap Determinations in Low-Resistivity Semiconductors. J. Appl. Phys., 39(11): 5149-5151, 1968.

[Wei91] S. Weiss. Halbleiteruntersuchungen mit dem DLTFS- (Deep-Level Transient Fourier Spectroscopy-) Verfahren. PhD thesis, University of Kassel, 1991.

[Wun92] R. Wunstorf. Systematische Untersuchungen zur Strahlenresistenz von Silizium-Detektoren für die Verwendung von Hochenergie-Experimenten. PhD thesis, Universtity of Hamburg, 1992.

[Zon98] D. Zontar, Study of radiation damage in silicon detectors for high luminosity experiments at LHC, PhD thesis, Ljubljana 1998

Acknowledgements

First of all I like to express my thanks to Prof. Dr. Robert Klanner and Prof. Dr. Peter Schleper for giving me the opportunity to work in their group at the Hamburg University. Very special thanks go to Prof. Dr. Dr. h.c. Gunnar Lindström and Dr. Eckhart Fretwurst for their daily great support and many useful advice. I am also grateful to Dr. Stefan Stonjek who had introduced me to the group.

A special thank goes to Prof. Dr. Ioana Pintilie and Dr. Jörg Stahl for introducing me into the field I worked on for the last years and for giving me support and advice. Thanks to Dr. Gregor Kramberger for the support of the measurement software.

I like to thank Dipl. Ing. Uwe Pein and Peter Buhmann for keeping the technical equipment running.

Among the several students over the years, I like to mention and to thank especially the office mates I shared with for quite a lot of discussions. Dr. Devis Contarato, Manfred Möller-Ivens, Alexandra Junkes, Kathrin Koch, Benedikt Mura and Alexander Clahes.

I also wish to thank all the people that provided the irradiation facilities. Many thanks to Dr. Zheng Li for the γ-irradiation at BNL, to Dr. Michael Moll and Maurice Glaser for their help at CERN, to Dr. Vlado Cindro for the neutron irradiation in Ljubljana, to Dr. Luciano Bosisio and Dr. Selena Dittongo for the work on the high energy electron irradiation, to Dr. Alexander Furgeri for the proton irradiation at Karlsruhe and to Prof. Dr. Bengt Gunnar Svensson for making the electron irradiation at Stockholm possible. I am also grateful to Dr. Ralf Röder and CiS for the device production and to the people at ITME for doing the SIMS measurements.

I like to thank the members of the RD-50 collaboration for interesting workshops and discussions.

Finally many thanks to all those members of the group I did not mention personally but who also contributed to the nice atmosphere in the group.